# Mathematical Modelling of Combustion in Confinement and Autoignition


James Paul Harris

Christ Church

University of Oxford

A thesis submitted for the degree of

*Doctor of Philosophy*

January 2025

This thesis is dedicated to my parents and grandparents. Your love and support mean the world to me.

# Acknowledgements

I have so many people to thank for their support and encouragement over the course of my DPhil studies, but compiling a complete list has proven to be impossible for fear of accidentally missing someone out. I will therefore keep what I write here to a minimum, safe in the knowledge I can thank people individually at a later date.

I would like to take this opportunity to thank my supervisors—Colin Please, David Allwright, Jon Chapman and John Ockendon—for their advice and guidance. A special thanks must go to Colin and David, who have been there for me since the beginning of this project and have seen it through to the end.

I also owe my thanks to BP for sponsoring my thesis. Thank you to Rana Ali, Adnan Mahmood and the rest of the team in Pangbourne for their insights into internal combustion and octane numbers, and to Brian Macey for introducing me to engine knock in the first place.

This thesis would not have been possible without InFoMM, and InFoMM would not have been possible without Colin Please and Chris Breward. My thanks go to Colin and Chris for bringing together a family of applied mathematicians, and so much more. Thanks also to Sophie Hurden, Sarah Howle, Jonathan Mason, Helen Cullen and the rest of the wonderful team of support staff (past and present) in the Mathematical Institute.

Last, but by no means least, I would like to thank my family. Mum, Dad, Nana and Grandad, you have believed in me for every step of this journey, and for that I am truly grateful.

# Abstract

Knock in spark-ignited internal combustion engines is a result of an explosion, known as autoignition, in the unburnt end-gas ahead of the flame. Autoignition is first apparent at hot spots, which develop suddenly at localised points in the end-gas after a period of seemingly normal combustion. We use perturbation methods to analyse a one-dimensional model of premixed gaseous combustion in confinement, to demonstrate the role acoustic waves play in the development of hot spots.

Acoustic waves are an inherent feature of combustion in confinement. Flames are subsonic combustion waves, meaning they affect the gas either side of them through the production of acoustic waves. When the combusting gas is enclosed in a finite volume, the acoustic waves produced at the flame reflect from the boundaries and subsequently interact with the flame. We use the Chapman–Jouguet conditions to formulate a free-boundary problem for the flame position, treating the flame as a discontinuity between two regions of inviscid gas. Using ideas from the method of multiple scales and WKBJ theory in the limit of small Mach number, we model the 'compression stage' where the reaction rate in the end-gas is negligible. We find that the acoustic waves in the gas either side of the flame can be expressed as a series of modes, whose amplitude, frequency and spatial structure evolve slowly as the flame moves. We present numerical solutions of our multiple scales model for a simple three-step chain branching reaction mechanism that is representative of premixed hydrogen combustion. The multiple scales framework we develop can be generalised to other chemical reaction mechanisms, provided a suitable model for the mass flux through the flame can be identified.

For the same three-step reaction, we find that the flame crosses the entire region and autoignition does not occur if the temperature in the end-gas remains below a critical temperature. We determine an explicit expression for the critical temperature in terms of the dimensionless parameters of the system. In agreement with numerical simulations of autoignition in the literature, we observe that the critical temperature decreases as the size of the combustion chamber increases.

For a parameter regime where autoignition occurs, we use activation energy asymptotics to derive a simplified model for the 'induction stage', which is the period of time where the temperature in the end-gas is close to the critical temperature. We focus on the distinguished limit where the gas dynamics and chemistry in the end-gas are fully coupled during the induction stage, and find that the behaviour of the end-gas during the induction stage is governed by Clarke's equation. To identify suitable initial data to solve Clarke's equation numerically, we use an intermediate variable to systematically match with the multiple scales solution during the compression stage.

We solve for the behaviour of the gas either side of the flame during the induction period for a range of different initial conditions and different parameter values. We find that hot spots can develop at the flame, at the cold wall, or in the bulk of the end-gas. We

observe the variation in the time and position at which the hot spot appears decreases as the amplitude of the acoustic waves in the end-gas decreases, with the hot spot occurring preferentially at the wall for small amplitude acoustic waves.

# Contents

# List of Figures

# Chapter 1

# Introduction

When a petrol car is operating normally, you will hear a low-pitched, continuous engine noise. However, under certain circumstances, a spark-ignited engine can make a knocking sound, quite different to normal. This sound is known as *knock*. The underlying combustion processes which lead to knock can be particularly damaging to an engine, so knock must be carefully controlled to avoid engine damage.

Knock is believed to be caused by a localised explosion, known as autoignition, of the unburnt fuel within the engine cylinder. What causes autoignition, and why it is first apparent at localised points away from the hottest parts of the engine, is not well understood. We use perturbation methods to analyse a mathematical model for gaseous combustion, to shed light on the role acoustic waves play during normal combustion (when autoignition does not occur) and during autoignition.

In this introductory chapter, we give a definition of what knock is and how its intensity is quantified based on the trace created by a pressure transducer exposed to the inside of the cylinder. We discuss the industrial motivation behind studying knock, and, based on photographic techniques and numerical simulations, give a description of the combustion processes which lead to knock. Finally, we summarise the modelling approach we take to better understand autoignition.

## 1.1 What is knock?

In the context of internal combustion engines, *knock* is an 'objectionable noise' heard outside of an engine, which is distinct to the sound of normal combustion [11]. This definition is rather vague, as it requires a set of well-tuned ears to tell if knock is occurring or not. Measures to quantify the intensity of knock can be based on measurements of vibration of the engine or on the filtered signal from a pressure transducer exposed to the inside of the cylinder. The latter is preferred in research [69, §3.2.1].

During a normal cycle of a spark-ignited internal combustion engine, such as that found in a petrol car, a mixture of air and vaporised fuel, known as the charge, is ignited by a spark during the compression stroke, causing a flame front to propagate across the cylinder. The combustion of the fuel results in a rise in pressure, which pushes the piston down after it has reached top dead-centre (TDC, see Figure 1.1), providing power to the

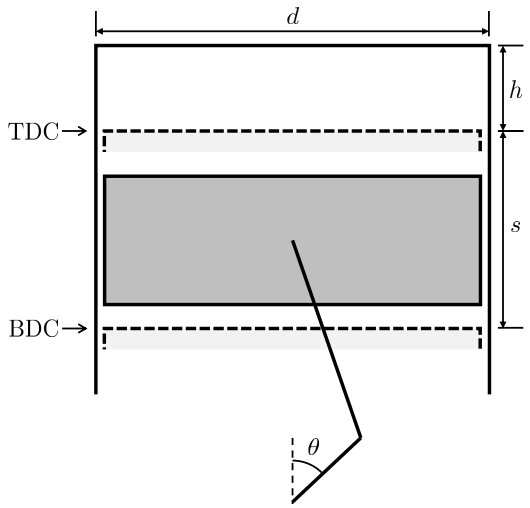


**Figure 1.1:** *A simplified diagram of a cylinder of an internal combustion engine. Top dead-centre (TDC), bottom dead-centre (BDC), crank angle ($\theta$), stroke ($s$), cylinder height ($h$), and cylinder diameter ($d$) are indicated. The compression ratio is the volume of the cylinder at BDC divided by the volume of the cylinder at TDC.*

engine. A typical pressure trace for a normal engine cycle is shown in red in Figure 1.2. Note that this pressure trace appears to be smooth.

By contrast, during an engine cycle when knock occurs, the pressure trace exhibits a sharp pressure rise, followed by high frequency pressure oscillations, as seen in the blue curve of Figure 1.2. The two pressure traces presented in Figure 1.2 are taken from the same variable compression ratio engine, running at the same speed and on the same fuel-air mixture. Knock occurs when the compression ratio is increased from 8.0 to 9.0. Although there is no universally accepted index for knock intensity [69, §3.2.1], it will be sufficient for our discussions to think of knock intensity as the amplitude of these rapid pressure oscillations.

## 1.2 Why study knock?

As well as being objectionable to the engine operator, knock is a warning sign that damaging abnormal combustion is occurring within the cylinder. The gas within a knocking engine cylinder reaches much higher temperatures and pressures than during a normal engine cycle. These high temperatures can cause engine components to melt or crack [89]. It is therefore very important to control knock to avoid potentially catastrophic engine failure.

Many factors are known to affect knock intensity [69, 98]: Increasing the air-fuel ratio, decreasing the intake temperature of the air and fuel, retarding (delaying) the spark timing and changing the cylinder design, particularly reducing the compression ratio, are all known to decrease the intensity of knock. However, these factors also affect the efficiency of the engine. Thus, knock limits the efficiency that can be achieved through engine design and operation [44, §9.6.1].

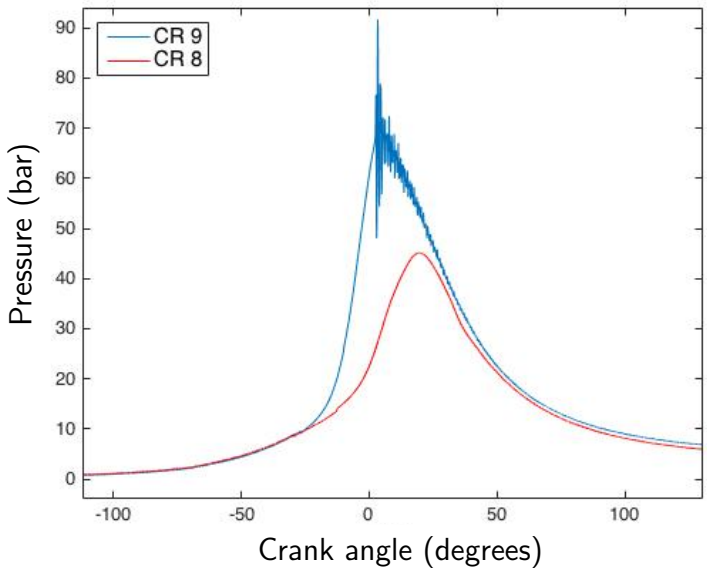


**Figure 1.2:** *Pressure traces from a pressure transducer exposed to the inside of the cylinder of a variable compression ratio spark ignited internal combustion engine running at 600 RPM with a stoichiometric mixture of iso-octane and air. The red curve is typical of a normal cycle, whereas the blue curve is typical of a cycle where knock occurs. The red and blue curves were produced when the compression ratio was 8.0 and 9.0, respectively. The spark plug fired at* $30^\circ$ *before TDC for both cycles. Reprinted from [69] with permission from the author.*

The choice of fuel used in an engine is another factor known to affect whether knock occurs or not. The *octane number* of a fuel is an indirect measurement of a fuel's propensity to cause knock; a high octane number fuel will cause lower intensity knock than a low octane number fuel in the same engine under the same operating conditions. There are two key international industrial standards defining octane number: the *Motor Octane Number* (MON) and the *Research Octane Number* (RON) [1, 2]. The test procedures for each standard are similar, with a fuel's octane number being determined by testing its performance in a specific test engine against that of a primary reference fuel. Comparing back to a reference fuel in this way offers a robustness which allows the MON and RON of a fuel to be determined consistently at refineries and research facilities around the world.

Despite the shift towards electric passenger cars in recent years, petrol cars will still be on the roads for many years to come. Furthermore, electrification is not suitable for all applications where internal combustion engines are currently used. For example, lithium ion batteries are unsuitable for use in aircraft and heavy-duty trucks due to low energy density [47].

The automotive industry is starting to experiment with the use of alternative fuels in internal combustion engines in an effort to address our transportation needs while also reducing the impact on the environment. For example, fuel manufacturers have started blending sustainable fuel components, such as ethanol derived from sugar cane, into petrol. Because the choice of fuel influences the conditions under which knock occurs, care must be taken when developing new fuel blends to ensure that the fuel blend's MON and RON are compatible with vehicles already on the road.

The relationship between fuel composition and octane number is not straightforward. For example, Foong et al. [38] show that a binary mixture composed of 40% ethanol and 60% iso-octane by volume has a RON greater than either of the pure components themselves. Furthermore, a primary reference fuel with octane number, $ON$, in the range $0 \leq ON \leq 100$ is fundamentally different to a primary reference fuel with $ON > 100$ [1, 2]. While we may think of octane number as one scale, the difference in the reference fuels may cause distortions in any patterns observed in octane number. Existing models [e.g. 39], used to understand the relationship between fuel composition and octane number based on regression are limited by their training data. As new and varied fuel components begin to be blended into our fuels, a comprehensive experimental regime would be needed to gather the data required to refit a regression model.

Hydrogen internal combustion engines are also being considered as an alternative method of powering heavy-duty trucks [43]. Spark-ignited internal combustion engines running on hydrogen suffer from pre-ignition [92] and autoignition [87], which are abnormal combustion processes that can lead to knock. Therefore, before hydrogen can be adopted as a fuel, engine manufacturers must consider how to mitigate knock through engine design and choice of operating conditions.

A model that enables prediction of how knock intensity depends on fuel composition, engine design and engine operating conditions would be of great interest and expedite the development and adoption of new, more environmentally-friendly fuels. In this thesis, we use perturbation methods to analyse a physics-based model of gaseous combustion in confinement, to provide insights into how the occurrence of knock depends on the

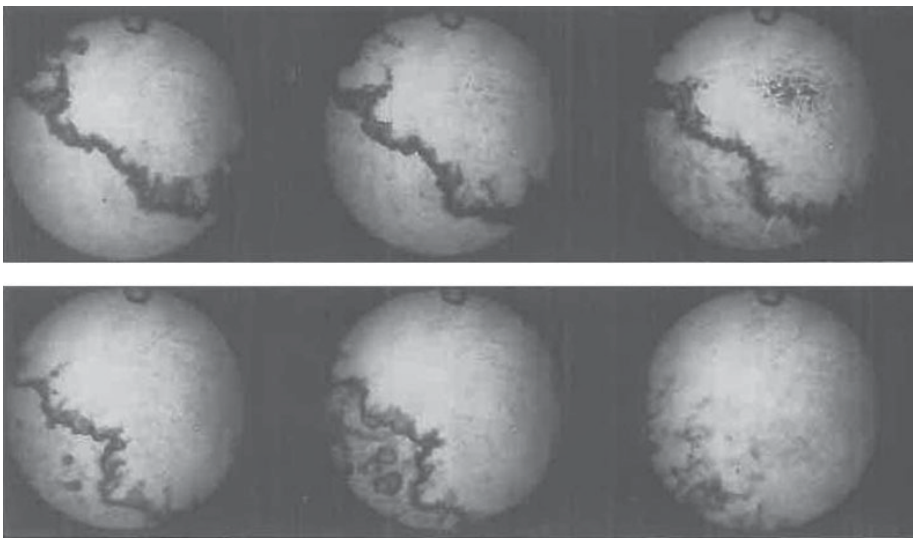

**Figure 1.3:** *Schlieren images of a knocking cycle of an internal combustion engine. Time advances from left to right, along the first row and then the second row. Reprinted from [11] with permission from the Royal Society.*

physical and chemical properties of the fuel-air mixture and the size of the cylinder. In the next section, we discuss the underlying combustion processes that contribute to knock to understand the behaviour we should expect to capture with our model.

## 1.3 What is autoignition?

Knock is generally understood to be brought about by autoignition of the unburnt gas, known as the end-gas, ahead of the flame [98]. In this section, we use experimental observations and results from numerical simulations from the literature to provide a description of autoignition. We will also briefly describe other related abnormal combustion processes including pre-ignition.

### 1.3.1 Experimental observations in the literature

Engines fitted with windows into the cylinder allow us to use natural light and schlieren[1] photography to observe the abnormal combustion processes responsible for knock. An engine cycle where knock occurs starts in much the same way as a normal engine cycle; the charge is compressed by the piston before being ignited by the spark plug. The resulting flame front starts to propagate across the cylinder. In the first three frames of Figure 1.3, the flame appears as a dark surface travelling towards the bottom left. In a normal cycle, the flame front completely crosses the combustion chamber. However, in the fourth frame of Figure 1.3, two dark 'hot spots' appear in the end-gas at the bottom

[1]Schlieren photography is a photographic technique which is sensitive to gradients of refractive index, which correspond to gradients of density [26].

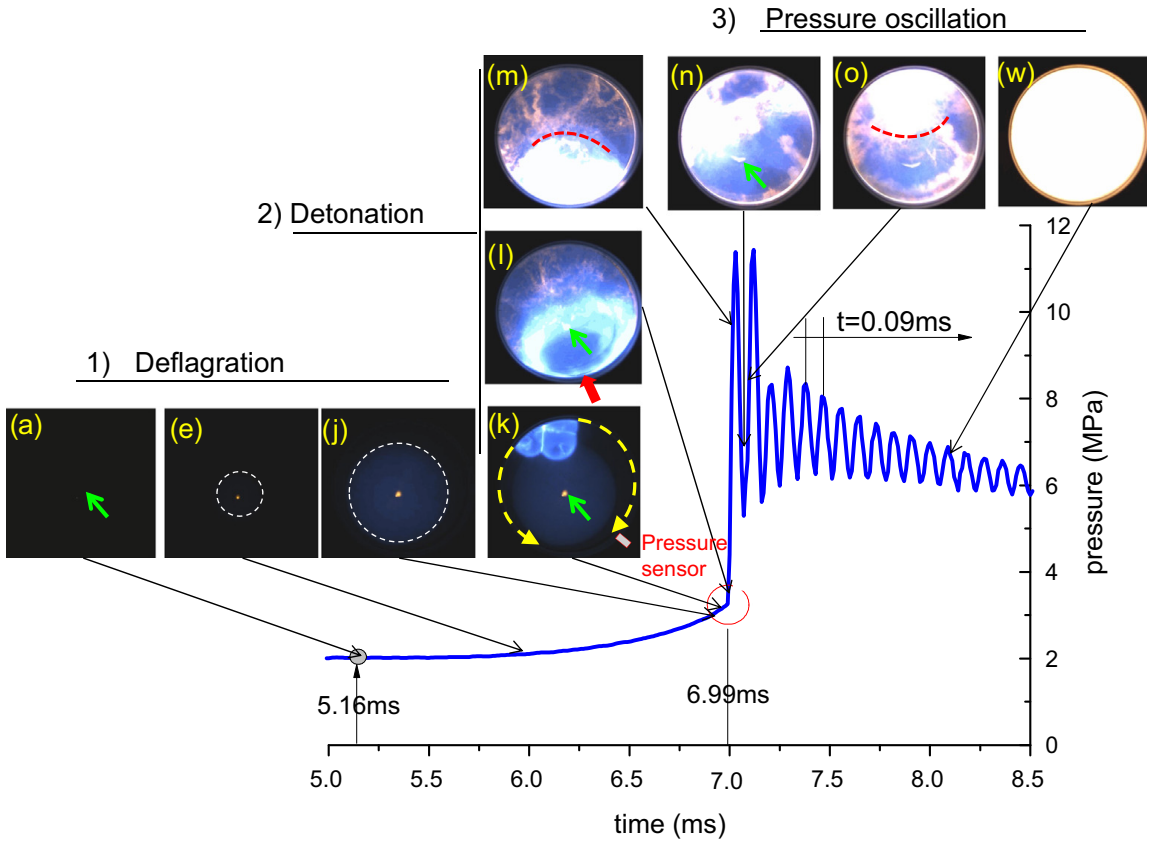


**Figure 1.4:** *Stages of knock, captured in a rapid compression machine. Adapted from [90] with permission from Elsevier.*

left, and the remaining unburnt fuel rapidly burns over the next two frames. The rapid reaction in the end-gas is known as autoignition.

Wang et al. [90] observe what they call super-knock in a rapid compression machine, which is a research device used to emulate the conditions inside a single engine cycle. Selected frames from their natural light film are shown in Figure 1.4, together with the pressure trace recorded by a pressure sensor, whose location is indicted by the grey rectangle in frame (k). The flame in their experiment is not initiated by a spark plug, but by a hot particle in the gas, whose position is indicated by a green arrow in selected frames of Figure 1.4. The flame, also known as a deflagration (see Section 2.2.1), propagates through the unburnt gas radially, starting from the hot particle. The flame position is indicated by the white dashed line in frames (e) and (j) of Figure 1.4. The expansion of the gas burning at the flame compresses the unburnt gas, as demonstrated by the slow rise in pressure between 5.16 ms and 6.99 ms. In frame (k), a detonation[2] is initiated at the wall of the cylinder. The detonation propagates at supersonic speeds through the unburnt gas. As the detonation passes the pressure sensor, there is a rapid rise in pressure. By frame (m), almost all the reactant has been used up, and pressure oscillations continue

[2] *Warning: Knock is sometimes known as 'detonation' in the literature.* For the avoidance of doubt, we will only use detonation to refer to supersonic combustion waves, see Section 2.2.1.

in the burnt gas.

Despite the difference in experimental set up in the studies described in the previous two paragraphs, the qualitative description is the same. A flame front propagates across the combustion chamber. Before the flame completely crosses the cylinder, a reaction occurs in the end-gas, which is more violent than the reaction in the flame. The resulting difference in pressure causes the oscillations observed in the pressure trace.

It should be pointed out that autoignition does not always lead to knock; König and Sheppard [63] do not measure any discernible pressure oscillations when they observe autoignition towards the end of the engine cycle. Nevertheless, they found that autoignition preceded knock in each knocking cycle they analysed.

Autoignition rarely occurs homogeneously throughout the end-gas. Rather, autoignition is first apparent at localised reaction centres, known as hot spots, which can be variably located near the wall, near the spark-ignited flame or in the bulk of the end-gas [63]. In some experiments, these hot spots are artificially brought about by including hot aluminium particles in the charge [62]. However, this modification is not necessary to see autoignition develop from hot spots [63, 86]. In general, the reason for the localisation of autoignition is not well understood [13].

A number of possible mechanisms have been suggested that could lead to the development of a hot spot by producing a local variation in temperature or chemical composition [85]. Temperature variations can be produced by reflecting pressure waves, turbulence or by the end-gas coming into contact with something hot (or cold). Candidates include the hot exhaust value, the (relatively) cool sides of the cylinder, hot gases remaining from the previous cycle, or hot particles or droplets of, for example, soot or oil. Inadequate mixing of the fuel and air could lead to variations in the chemical composition. Furthermore, reactive species left over from a previous cycle, either in the gas or as deposits on the cylinder wall, could alter the chemistry of the end-gas, resulting in faster reaction.

It is possible that more than one of these mechanisms contributes to the formation of hot spots in internal combustion engines. After all, an engine cylinder is a complex system, with moving parts, turbulent gas and many reactive species. However, autoignition is not solely associated with engines. For instance, we have already discussed how autoignition can occur in rapid compression machines [90]. It would be prudent to study models of combustion in systems that are much simpler than an engine, but which exhibit similar behaviour. We therefore now consider the behaviour exhibited by numerical simulations of combustion in confinement from the literature.

### 1.3.2 Numerical simulations from the literature

Autoignition is not only an aspect of combustion within internal combustion engines and rapid compression machines, but is more generally a feature of combustion in gas confined within an enclosed volume. There is a large body of literature, but here we present two particular numerical studies that demonstrate the behaviour seen during autoignition. In this section, we discuss the 2D numerical simulations by Liberman et al. [66], which suggest that autoignition is possible in a system with much simplified chemistry and geometry. We also examine the numerical simulations of the combustion of hydrogen by Yu and

Chen [95], which demonstrate the range of phenomena we may expect from a 1D model of combustion in confinement.

#### 1.3.2.1 Simple chemistry in 2D

The model Liberman et al. [66] study describes a gas undergoing a simple, one-step chemical reaction in a thin rectangular domain, with thermally-insulated slip walls [66]. They choose initial conditions to represent a flame initiated at one of the short sides of the rectangle. The reaction rate they use has an Arrhenius temperature dependence. We will discuss the Arrhenius law in more detail in Section 2.1.1, but, for now, we can consider the model Liberman et al. [66] use to be a simple model of combustion.

The simplicity of the model in [66] precludes many of the mechanisms of hot spot development described at the end of Section 1.3.1: the walls are insulated so there is no wall heating or cooling; the temperature and chemical composition of the end-gas is initially uniform; there is no evidence of turbulence in their simulations. Yet, after a period of normal flame propagation, Liberman et al. [66] observe a sudden local rise in temperature and pressure ahead of the flame. Based on the numerical simulations by Liberman et al. [66], Sivashinsky [85] suggests that a purely gas dynamical mechanism based on heating by reflected pressure waves is sufficient to capture the 'salient features' of autoignition. This is not to say that other mechanisms are unimportant in the development of hot spots in internal combustion engines. Rather, we recognise that compressive heating by acoustic waves is a fundamental mechanism that can bring about autoignition, even in the absence of other sources of ignition.

#### 1.3.2.2 Hydrogen combustion in 1D

Numerical simulations of a model for the combustion of hydrogen in 1D by Yu and Chen [95] exhibit a plethora of interesting behaviours, including autoignition. We present their results, as they provide a clear picture of the behaviour of flames and the sequence of events during autoignition.

We will not dwell on the details of the model Yu and Chen [95] use, which can be found in the supplementary material of [19]. Briefly, they simulate the combustion of a stoichiometric mixture of hydrogen and air (accounting for numerous intermediate reactions) between two parallel rigid, insulating, impermeable walls at $x = 0$ and $x = \bar{L}$. They choose initial conditions for the temperature and mass fractions that are representative of a premixed planar flame at the left-hand wall of the combustion chamber. Apart from close to the left-hand wall, the temperature of the gas is approximately $\bar{T}_{\mathsf{init}}$ initially. The initial pressure, $\bar{p}_{\mathsf{init}}$, is taken to be uniform throughout the combustion chamber and the initial velocity is taken to be equal to zero.

Yu and Chen [95] observe a trio of possible outcomes following the initiation of the flame: (i) normal combustion, where the flame crosses the combustion chamber and reaches the far wall; (ii) autoignition, where the end-gas explodes before the flame reaches the far wall; and (iii) 'detonation development', which we will discuss in Section 1.3.3. They find that the length, $\bar{L}$, of the combustion chamber, the initial pressure, $\bar{p}_{\mathsf{init}}$, and the characteristic initial temperature, $\bar{T}_{\mathsf{init}}$, of the end-gas, affect the behaviour observed.

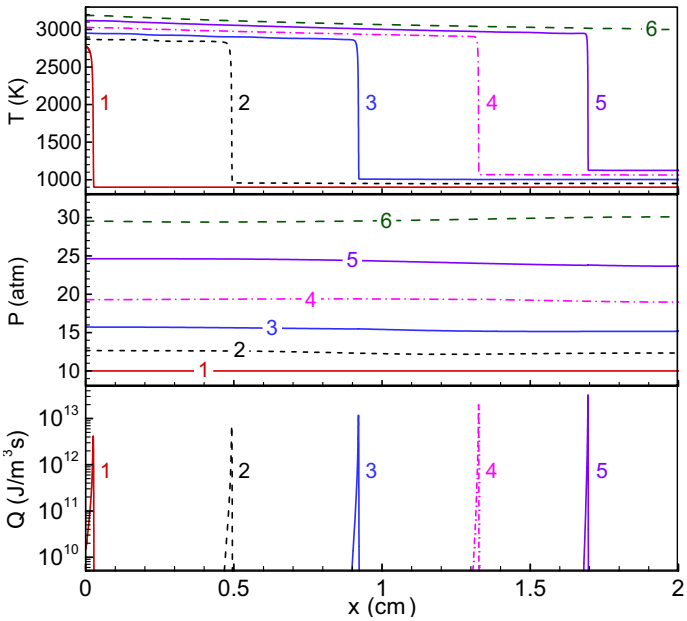


**Figure 1.5:** *Temperature, pressure and heat release rate profiles during normal combustion of a well-mixed stoichiometric mixture of hydrogen and air, plotted at (approximately)* 120 µs *intervals. The parameter values are* $\bar{L} = 2\,\text{cm}$, $\bar{p}_{init} = 10\,\text{atm}$, *and* $\bar{T}_{init} = 900\,\text{K}$. *Reprinted from [95] with permission from Elsevier.*

The behaviours (i) and (ii) are most relevant to understanding autoignition, so we discuss them in detail now.

**1.3.2.2.1 Case (i) — Normal combustion** The first possibility is that the flame initiated at the left-hand wall propagates across the chamber and reaches the far wall at $x = \bar{L}$. This is observed when $\bar{L} = 2\,\text{cm}$, $\bar{p}_{\text{init}} = 10\,\text{atm}$, and $\bar{T}_{\text{init}} = 900\,\text{K}$.

Yu and Chen [95] define the flame position as the position of the local maximum heat release rate. The flame is characterised by a thin region of chemical activity moving to the right, across which there is a rapid rise in temperature, as seen in Figure 1.5. The combustion process occurring at the flame is almost constant pressure, resulting in no discernible pressure jump at the flame position in Figure 1.5.

The flame is subsonic (the speed of sound in the end-gas is approximately $700\,\text{m}\,\text{s}^{-1}$) meaning the flame sends pressure waves into the gas ahead of it. The pressure trace at the right-hand wall at $x = 2\,\text{cm}$, shown in Figure 1.6a, provides evidence of pressure waves with small amplitudes relative to the ambient pressure. The pressure profile is initially spatially uniform, so these pressure waves must be produced by the flame. Since the gas is confined between rigid walls, the pressure waves reflect from the walls and subsequently interact with the flame. The pressure rise at the wall is not monotonic, due to the reflection and transmission of the pressure waves at the flame. We note that there is not similar evidence of acoustic waves in the pressure traces in Figures 1.2 and 1.4 prior to the onset of knock. We speculate that acoustic waves are present in physical systems, but are sufficiently small that either they are not detected by the pressure transducer or

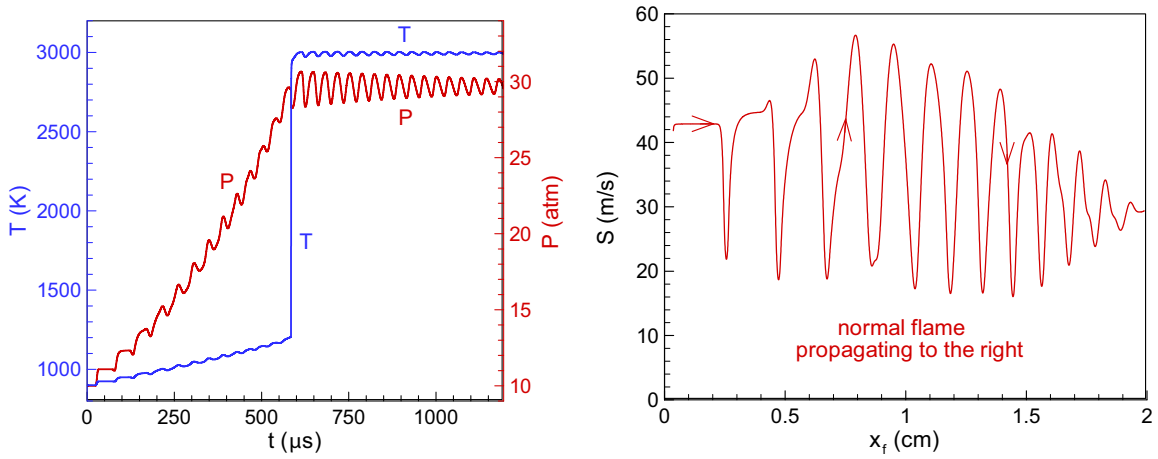


**Figure 1.6:** *The effect of pressure waves during normal combustion: (a) Evolution of pressure and temperature with time at the right-hand wall, $x = 0$; (b) Variation in flame speed, $S$, with flame position, $x_f$. The parameter values are $\bar{L} = 2\,\text{cm}$, $\bar{p}_{init} = 10\,\text{atm}$, and $\bar{T}_{init} = 900\,\text{K}$. Reprinted from [95] with permission from Elsevier.*

they are filtered out as noise.

The pressure waves also have an effect on the flame speed. In Figure 1.6b, the flame speed, $S$, is plotted against flame position. To an observer external to the system—that is, in the Eulerian or lab reference frame—the flame speed is oscillatory. However, Yu and Chen [95] note that the flame speed relative to the gas velocity increases monotonically in time. In physical experiments, flames in channels have been observed to exhibit oscillatory behaviour [41], similar to that depicted in Figure 1.6b. The interaction between flames and pressure waves in an enclosed volume is not well understood theoretically, even in 1D. The rising temperature either side of the flame observed in Figure 1.5 results in an increase in sound speed which complicates the description of the pressure waves. We investigate this problem thoroughly in Chapter 3, exploiting the small Mach number of the flame. We discuss previous studies taking a similar approach in Section 2.2.5.

**1.3.2.2.2 Case (ii) — Autoignition** The second case Yu and Chen [95] identify is when the end-gas autoignites. They find this can be brought about by increasing the length of the chamber, or increasing the initial temperature or pressure. We present their results in Figure 1.7a for a simulation with a increased initial temperature compared to the simulation discussed in Section 1.3.2.2.1, so that $\bar{L} = 2\,\text{cm}$, $\bar{p}_{\text{init}} = 10\,\text{atm}$, and $\bar{T}_{\text{init}} = 1000\,\text{K}$. Note that Figure 1.7a does not show the whole of the domain from $x = 0$ to $x = 2\,\text{cm}$.

In this case, the flame initially propagates in the same subsonic, oscillatory way as it does for normal combustion. However, before the flame reaches the right-hand wall, the end-gas undergoes a sudden and rapid chemical reaction, resulting in a large local increase in temperature and pressure. In contrast to the nearly constant pressure combustion across the flame, the explosion in the end-gas is nearly constant volume.

Autoignition is first apparent at approximately $x = 1.97\,\text{cm}$ in Figure 1.7a. From this point, the temperature and pressure quickly rise throughout the end-gas in a wave that Yu and Chen [95] call an autoignition front. Defining the position of the autoignition front as the position of the local maximum heat release rate, the autoignition front travels much faster than the speed of sound, or indeed the Chapman–Jouguet speed, which we introduce in Section 2.2.1.

The pressure trace at the right-hand wall exhibits large pressure oscillations following autoignition, similar to the pressure trace recorded from a knocking engine cylinder. We speculate that these waves are a result of the pressure imbalance as the autoignition front meets the flame.

Modelling ignition in gases is not straightforward. How much of the chemical energy released from the fuel is converted to thermal energy and how much is converted to kinetic energy depends on the rate at which the energy is released [60]. As we see from Figure 1.7a, the reaction rate in the end-gas changes through orders of magnitude during autoignition. At its maximum, the reaction rate in the end-gas is an order of magnitude higher than the peak reaction rate within the nearly constant-pressure spark-ignited flame. In Section 2.2.4, we recognise that the autoignition front in Figure 1.7a is a weak detonation and discuss how weak detonations are formed during ignition from spatially inhomogeneous initial conditions. While there is a significant body of literature looking at how a gas ignites from a fixed temperature profile, very little has been done to explain what role acoustic waves play in preconditioning the gas prior to autoignition. In Chapter 4, we identify a critical temperature, below which the reaction rate in the end-gas has a negligible effect on the gas dynamics, and investigate how the acoustic waves generated during the early stages of combustion lead to the formation of a hot spot when the reaction rate in the end-gas becomes significant.

### 1.3.3 Other abnormal combustion processes

The experimental and numerical results presented in Sections 1.3.1 and 1.3.2, give an overview of the general behaviour seen during autoignition. We have seen that autoignition is a nearly constant volume explosion of the unburnt gas ahead of the flame, following a period of seemingly normal combustion. There are, however, two other abnormal combustion phenomena of relevance we should discuss briefly: the deflagration to detonation transition and spontaneous ignition.

The third behaviour Yu and Chen [95] identify is what they call detonation development, which they observe if they further increase the initial temperature, initial pressure or length of the domain. In this case, either the flame accelerates or the autoignition front decelerates, resulting in a detonation travelling at the Chapman–Jouguet speed. We will discuss the theory behind detonations, which are supersonic combustion waves, in more detail in Section 2.2.1.

In general, detonations can be initiated in one of two ways [64]: directly using a powerful enough ignition source, or indirectly via the so-called deflagration to detonation transition (DDT), whereby a deflagration (a flame) initiated near the closed end of a tube accelerates to a detonation. The numerical simulation by Yu and Chen [95] shown in Figure 1.7b is an example of DDT. As the flame accelerates, the pressure rises at the

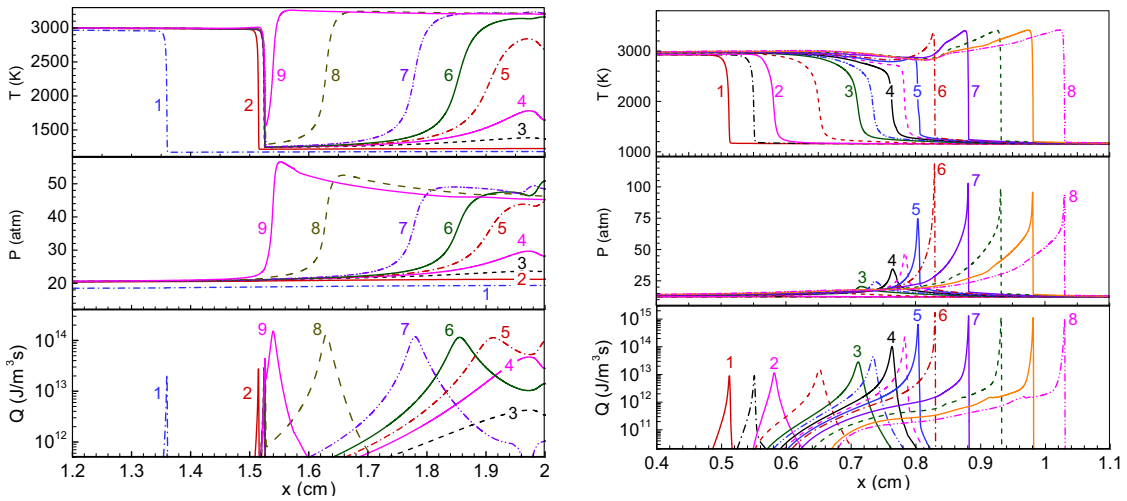


**(a)** *Autoignition.* **(b)** *Detonation development.*

**Figure 1.7:** *Temperature, pressure and heat release rate profiles during abnormal combustion. (a) Autoignition: The time between profile 1 and 2 is* 38.02 µs*, whereas the time between profile 3 and 9 is* 1.34 µs*. (b) Detonation development: The time between profile 1 and 2 is* 8.01 µs*, whereas the time between profile 3 and 8 is* 1.81 µs*. The parameter values are* $\bar{L} = 2\,\text{cm}$ *and* $\bar{p}_{init} = 10\,\text{atm}$ *for both cases, and (a)* $\bar{T}_{init} = 1000\,\text{K}$ *and (b)* $\bar{T}_{init} = 1100\,\text{K}$*. Reprinted from [95] with permission from Elsevier.*

flame, evolving to form a spike in pressure at the front of the detonation wave. Note that Figure 1.7b does not show the whole of the domain from $x = 0$ to $x = 2\,\text{cm}$.

Such acceleration is observed by Urtiew and Oppenhiem [88]. The cause of DDT is not fully understood, and is postulated to be caused by multi-dimensional effects, such as turbulence, frictional heating and the Darrieus–Landau instability of a flame [13]. The fact DDT is observed in 1D simulations [e.g. 83, 95] therefore warrants further investigation.

DDT is not generally believed to contribute to knock in internal combustion engines [98]. In their experiments, Spicher et al. [86] never observe significant acceleration of the spark-ignited flame in a knocking engine cycle, and they do not observe autoignition adjacent to the flame. On the other hand, König and Sheppard [63] do observe autoignition at the flame, which increases the apparent velocity of the flame. However, they observe no meaningful acceleration of the flame prior to the onset of autoignition.

At the end of Section 1.3.1, we discussed several mechanisms that have been proposed in the literature for how a hot spot forms. Apart from pressure waves and turbulence, which are gas dynamical effects, most of the mechanisms presented could be described as spontaneous ignition due to an external influence. For example, the end-gas could ignite due to the presence of a hot particle in the charge, or a hot surface in the engine [89]. We will refer to this as spontaneous ignition.

Spontaneous ignition could occur at any point when there is unburnt fuel and oxygen in the engine cylinder. When spontaneous ignition occurs before the spark plug fires, it is known as pre-ignition [45, §9.6.1]. Pre-ignition results in the creation of a flame in the same way as ignition by the spark plug, but with ignition coming earlier in the engine

cycle. The effect of pre-ignition on knock is therefore equivalent to advancing the spark timing, i.e. the intensity of knock increases. Pre-ignition does not necessarily result in autoignition, but when it does the mechanism for hot spot development in the end-gas is exactly the same as for a spark-ignited flame, except, perhaps there are multiple flame fronts instead of just one. Wang et al. [90] refer to the knock they observe in a rapid compression machine as super-knock because it is a result of autoignition following pre-ignition due to a hot particle. Pre-ignition can occur sporadically, due to, for example, oil being ejected from the crevice between the piston and the wall, or occur recurrently, due to a hot surface within the engine, such as the exhaust valve [89]. To the engine operator, the difference between knock caused by autoignition following ignition by the spark plug and knock caused following pre-ignition is that the intensity of the former can be controlled by changing the spark timing.

It is also possible for spontaneous ignition to occur in the end-gas after ignition by the spark plug. However, unless the rate of reaction increases significantly throughout a region of the end-gas, it is most likely that spontaneous ignition would result in an additional flame front emanating from the point at which spontaneous ignition occurs [45, §9.6.1]. The additional flame would generate small acoustic waves in the combustion chamber, but would not lead to the large amplitude pressure oscillations characteristic of knock without further autoignition of the end-gas.

The description of autoignition remains the same, regardless of whether the flame (or flames) are initiated by spontaneous ignition or by a spark plug. Therefore, from now on, we focus our attention on understanding the interplay between flames and acoustic waves to better understand the fundamental mechanism behind autoignition.

## 1.4 Thesis summary

Results from experimental studies suggest that knock in internal combustion engines is a result of autoignition, which is an explosion of the end-gas, first apparent at discrete points known as hot spots. Autoignition is not solely associated with internal combustion engines. As we have seen, numerical simulations of combustion in confinement exhibit autoignition despite having significantly simpler geometries and chemical reaction mechanisms. To better understand the mechanisms that lead to autoignition, it is prudent to study a model for combustion in a system that exhibits autoignition but is much simpler than an internal combustion engine.

In Chapter 2, we write down a model for combustion in a gas confined between two rigid, impermeable, insulating walls in 1D. We consider two simple chemical models: a one-step reaction with an Arrhenius temperature dependence, and a three-step chain branching reaction. Ultimately, we conclude that the one-step reaction is unsuitable for studying autoignition. However, it is important that we discuss the one-step reaction, because it is central to many of the advances in the theoretical understanding of combustion. The three-step reaction we study captures the salient features of the chain branching reaction mechanisms typical of real combustion, but with a reduced number of chemical reactions and species. Of course, by considering chemical reaction mechanisms with only a few reactions, we lose accuracy in modelling combustion of real fuels. However, we take the

pragmatic view that by simplifying the chemistry we are able to more easily use asymptotic analysis to identify structures in the combusting gas and gain theoretical insights into the mechanisms that lead to autoignition.

In Section 2.2, we discuss key results from the mathematical literature on combustion. There is a vast literature, so we chose to focus upon specific examples which are pertinent to understanding autoignition in 1D. Broadly, we focus on two areas: combustion waves and ignition. In particular, we discuss the Chapman–Jouguet theory of deflagrations and detonations, and look at how asymptotic analysis in the limit of large activation energy and small Mach number can be used to determine the mass flux through a flame. We summarise the stages of ignition from homogeneous initial conditions, and discuss asymptotic and numerical studies into ignition with spatial variations. At the end of Chapter 2, we review previous theoretical studies on combustion in confinement and discuss a simple model for autoignition from the literature.

In the experimental and numerical results presented in Section 1.3, we observe that autoignition occurs after a period of 'normal' combustion, where the rate of chemical reaction in the end-gas is negligible. In the context of autoignition, we call this period the 'compression stage', because we find that the leading-order temperature in the end-gas rises due to (approximately) adiabatic compression caused by the expansion of the gas burning at the flame. Understanding the behaviour of the flame and the gas surrounding it during normal combustion is an important step towards understanding autoignition, because acoustic waves generated by the flame during the compression period dictate where hot spots develop if autoignition occurs. In Chapter 3, we use perturbation methods to find an asymptotic solution to our model in the limit of large Péclet number, large activation energy and small Mach number in the case of normal combustion. The small Mach number limit, $M \to 0$, is a singular perturbation, so careful consideration is needed to find a solution that is (a) able to satisfy the initial conditions, and (b) valid for the time taken for the flame to cross the combustion chamber. Ultimately, we use ideas from the method of multiple scales in both time and space to describe the acoustic perturbations in the gas.

As the temperature rises, so do the rates of the chemical reactions in the end-gas. In Chapter 4, we find that the reaction in the end-gas starts to have a significant effect as the temperature approaches a critical temperature, which we determine algebraically in terms of the dimensionless parameters of the system. By comparing the critical temperature with the maximum possible temperature in the end-gas during normal combustion, we identify a parameter regime where autoignition does not occur. We are able to use this parameter regime to make predictions on whether autoignition occurs, based on the size of the combustion chamber as well as the physical and chemical properties of the fuel-air mixture.

We find that the behaviour of the gas as the critical temperature is approached depends on the relative sizes of the (dimensionless) activation energy and the typical Mach number of the flame. In Chapter 4, we derive a model for the evolution of the gas during the induction stage—the earliest stage of explosion where the temperature remains close to the critical temperature—for the distinguished case where the gas dynamics and chemistry are fully coupled. The induction stage is much shorter than the compression stage, as illustrated in Figure 1.8.

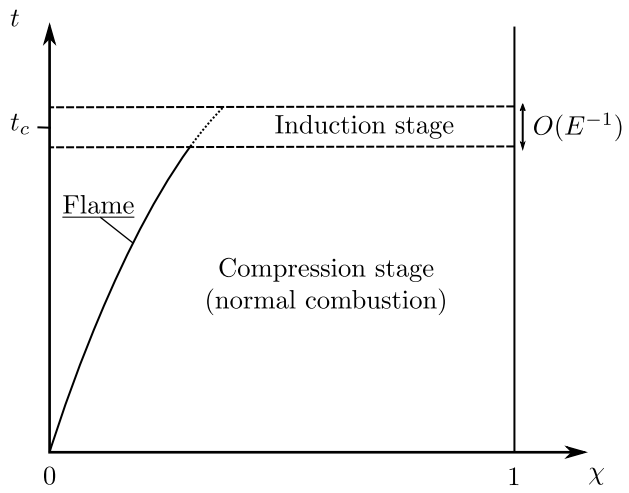


**Figure 1.8:** *Graphical depiction of the compression and induction stages of autoignition. During the compression stage, the effect of the chemistry in the end-gas is negligible and the temperature in the end-gas rises due to adiabatic compression by the burning gas expanding in the flame. The induction stage is a short boundary layer in time where the exothermic chemical reaction in the end-gas begins to have a significant effect. The dimensionless Lagrangian coordinate, $\chi$, the dimensionless time variable, $t$, and the dimensionless activation energy, $E$, are defined in Section 2.1, and the dimensionless critical time, $t_c$, is defined implicitly by* (4.23).

It is necessary to solve our model for the induction stage numerically. To determine suitable initial data, we use an intermediate variable method to match with the solution during the compression stage. The solution to our model for the induction stage becomes unbounded at a point within the end-gas in finite time, essentially indicating when and where a hot spot develops. To investigate how sensitive the position and timing of autoignition is to changes in the acoustic waves during the compression stage, we solve our model numerically for different initial conditions and different values of the typical Mach number of the flame, which we denote by $M$. We find that the variation in the time and position at which the hot spot appears decreases as $M$ decreases, with the hot spot preferentially occurring at the wall for small values of $M$.

Finally, in Chapter 5, we draw conclusions and indicate two possible avenues for further investigation.

# Chapter 2

# Modelling gaseous combustion

There are several ways in which mathematics can be used to provide insight into knock and autoignition. As we have already discussed, one approach would be to formulate a statistical model linking fuel composition and octane number. Another approach one could take is using computational fluid dynamics (CFD). In CFD, a computer is used to solve a model that accounts for all the known physics of a system. One could use CFD to provide a very detailed picture of what is going on within a knocking engine cylinder, or, indeed, in simpler systems as we discussed in Section 1.3.2. However, each CFD simulation requires substantial computational effort.

We provide an important middle ground between data-based models and large-scale CFD simulations. We study physics-based models for combustion in confinement, and, by taking physically relevant limits, we identify the important processes that result in autoignition. Using asymptotic analysis, we provide new models that are less computationally intensive than CFD, but precise enough to explore the relationship between the physical properties of a fuel-air mixture and whether autoignition occurs.

In this chapter, we begin by presenting two models for premixed gaseous combustion in 1D. Similar models are common throughout the literature [e.g. 16, 21, 30, 48, 58]. We adapt the usual equations governing the motion of an inert, viscous, compressible perfect gas to account for two different simple chemical reaction mechanisms that are both representative of premixed combustion.

There is a vast literature on mathematical modelling of combustion, and asymptotic analysis has played a part in many of the advances in theoretical understanding on the subject. In Section 2.2, we discuss results from the literature that are relevant for understanding autoignition in 1D. In particular, we review the theory of combustion waves—namely deflagrations and detonations—and the theory of ignition.

There are many other fascinating aspects of combustion beyond what we present in Section 2.2. In particular, we do not discuss inherently 3D aspects of combustion in any detail. For example, it has been shown that planar flames are unconditionally unstable in three dimensions, suffering from what is known as the Darrieus–Landau instability [14, 17], which may be a precursor to turbulence [13]. Such aspects of combustion may contribute to autoignition in 3D. However, we recognise that autoignition is an unexplained feature of 1D models of combustion, such as those studied by Yu and Chen [95]. We therefore make the judicious choice to only discuss results from the literature that are relevant to

understanding the mechanism that leads to autoignition in this simpler geometry. To ensure consistent notation, in Section 2.2 we present results from the literature in the notation introduced in Section 2.1.

While mathematical models for combustion are well studied in the literature, there is limited theoretical understanding of the particular scenario we study: premixed combustion in confinement. At the end of Section 2.2, we discuss previous studies of combustion in confinement, before highlighting what is novel about our research in Section 2.3.

## 2.1 Model

We take a continuum approach to modelling combustion. We formulate a system of partial differential equations describing conservation of mass, momentum and energy, as well as the production and transport of all but one of the chemical species involved in the chemical reactions. The final chemical species is determined algebraically from the conservation of mass.

When a fuel burns, it undergoes a complicated reaction comprising of many elementary reaction steps involving many intermediate species. For example, Li et al. [65] present a model for hydrogen reacting with oxygen comprising of some 11 species undergoing 19 elementary reactions. The situation is even more complicated for mixtures of fuels; Cai and Pitsch [18] present a model for combustion of mixtures of iso-octane, n-heptane and ethanol in air involving 339 chemical species and 2,791 elementary reactions.

We choose to study two simple chemical reactions that are representative of premixed combustion—that is, where the fuel and air are well-mixed—but which are substantially simpler than the detailed chemical reactions described in the previous paragraph. By using chemical reactions involving only a few reactive species, we formulate models whose behaviour can be more easily investigated using analytical tools. While we sacrifice accuracy by considering simplified chemical reaction schemes, we recognise that by studying paradigm models for combustion we provide valuable theoretical understanding of the stages a combusting gas goes through, and identify simple models that can be used to investigate how autoignition depends on the initial conditions and the properties of the fuel-air mixture.

In this section, we first outline the two specific chemical reactions we study, before incorporating them into a system of partial differential equations governing the evolution of the gaseous mixture. We then nondimensionalise the two models, and discuss typical values of the dimensionless parameters.

We make a number of simplifying assumptions in the derivation of our model, which we will discuss at the appropriate moments. To formulate a model for combustion with greater generality one would follow the procedure described by Buckmaster and Ludford [16, §1].

### 2.1.1 Specific chemical reactions

The first chemical reaction we consider is a one-step, irreversible, exothermic reaction,

$$\mathcal{F} \xrightarrow{\bar{r}} \mathcal{P}, \tag{2.1}$$

where $\mathcal{P}$ is formed from $\mathcal{F}$ at a rate $\bar{r}$, which we have to specify. We will refer to $\mathcal{F}$ as the 'fuel', and $\mathcal{P}$ as the 'product'. We assume that the reaction releases $\bar{Q}$ units of energy per unit mass of the fuel consumed. For simplicity, we assume that $\mathcal{F}$ and $\mathcal{P}$ are the only species present and that they have the same molar mass. This simplification means we may model the mixture of $\mathcal{F}$ and $\mathcal{P}$ as a single gas, and specify the transport of $\mathcal{F}$ relative to this gas.

This paradigm model can be thought of as representative of premixed combustion in air. It is reasonable to approximate the charge as a single gas with constant molar mass where nitrogen is the dominant component of the gas, as is the case for premixed combustion in air [16, §1.4]. Moreover, the simple chemical reaction (2.1) can be thought to be representative of the overall premixed combustion reaction,

$$\text{fuel} + \text{oxygen} \rightarrow \text{products}, \tag{2.2}$$

where $\mathcal{F}$ represents the 'active portion' of the fuel-oxygen mixture, that is, the portion of the excess reactant which balances with the limiting reactant. The inert gases, products and rest of the excess reactant are represented by $\mathcal{P}$ [16, §2.1].

We assume the reaction rate, $\bar{r}$, depends on the absolute temperature, $\bar{T}$, measured in Kelvin, and the *mass fraction*[1] of $\mathcal{F}$, denoted by $\bar{Y}_{\mathcal{F}}$. Specifically, we assume a first order reaction, so

$$\bar{r} = \bar{A}\bar{Y}_{\mathcal{F}} \exp\left(\frac{-\bar{E}}{\bar{\mathfrak{R}}\bar{T}}\right), \tag{2.3}$$

where $\bar{\mathfrak{R}} \approx 8.31\ \text{J mol}^{-1}\,\text{K}^{-1}$ is the universal gas constant [36], $\bar{E}$ is the constant activation energy, and $\bar{A}$ is the constant reaction rate coefficient.

The form of (2.3) is based on the law of mass action [93, §B.1] and the Arrhenius law [93, §B.3]. The law of mass action states that the rate of reaction is proportional to the product of the concentrations of the reactants. Meanwhile, the Arrhenius law is based on the assumption that reaction can only occur if the thermal energy of the reactants exceeds some constant minimum threshold, $\bar{E}$, known as the activation energy. The proportion of molecules that are sufficiently energetic to react can be approximated using Boltzmann's energy distribution law [93, §B.3],

$$\exp\left(-\frac{\bar{E}}{\bar{\mathfrak{R}}\bar{T}}\right). \tag{2.4}$$

The law of mass action and the Arrhenius law are derived from the theory of molecular collisions, and are therefore only valid for elementary reactions which actually occur on a molecular level [93, §B.1]. It is commonplace to use empirical formulae similar to (2.3) to approximate the overall rate of reaction [15, §2.1]. However, the overall reaction rate does not necessarily need to be proportional to the product of the concentrations of the reactants. Instead, the dependence of the reaction rate on the density of the gaseous

[1] Note that, in general, we use a bar to indicate a dimensional quantity. Mass fraction, however, is dimensionless. We denote the mass fractions, $\bar{Y}_{\mathcal{F}}$ and $\bar{Y}_{\mathcal{R}}$, in the same way as dimensional quantities because when we come to nondimensionalise our model in Section 2.1.3, we will also rescale the mass fractions.

mixture and the mass fractions of the reactants is determined empirically [16, §1.3]. For simplicity, we assume the reaction rate is proportional to the mass fraction, $\bar{Y}_{\mathcal{F}}$, of $\mathcal{F}$, and is independent of density, $\bar{\rho}$, of the gas. Note that, for the combustion processes we consider, the change in density, $\bar{\rho}$, is moderate compared to the change in the Arrhenius factor, $\exp\bigl(-\bar{E}/\bar{\mathfrak{R}}\bar{T}\bigr)$, so the effect of using mass fraction, $\bar{Y}_{\mathcal{F}}$, instead of concentration, $\bar{\rho}\bar{Y}_{\mathcal{F}}$, is minor.

The one-step reaction (2.1) with Arrhenius reaction rate (2.3) is ubiquitous in the mathematical literature on combustion. We include it in our discussion because it is critical to understanding the literature. However, it has been noted that the one-step reaction (2.1) is unsuitable for modelling unsteady processes, particularly ignition [67]. Ultimately, in Section 4.1.2.1, we dismiss the one-step reaction as unsuitable for modelling autoignition, because of unrealistic acceleration of the flame.

The second reaction we study is a three-step chain branching reaction. As we have already discussed, when hydrogen reacts with oxygen it undergoes a series of elementary reaction steps. As part of this reaction mechanism, highly reactive, transient chemical species are produced known as chain carriers. The chain carriers react with the hydrogen and oxygen molecules to produce more chain carriers in what are known as *branching* reactions. An example of a branching reaction involved in the combustion of hydrogen is

$$\mathrm{H} + \mathrm{O}_2 \rightarrow \mathrm{OH} + \mathrm{O}, \tag{2.5}$$

where the hydrogen, oxygen and hydroxyl radicals (H, O and OH) are the chain carriers. Note that two chain carriers are produced for each chain carrier used in the branching reaction. Therefore, provided that the branching reactions create chain carriers faster than the chain carriers combine to form stable products, the amount of chain carriers increases exponentially in a self-accelerating process known as a chain branching explosion [93, §B.2]. Chain branching not only plays a role in hydrogen combustion, but is also a feature of hydrocarbon combustion [93, §B.2].

We study a simple three-step chain branching reaction that captures the essence of the combustion mechanism for hydrogen, but without the detail of all the possible elementary reactions. The first step of the reaction is *initiation*,

$$\mathcal{F} \xrightarrow{\bar{r}_1} \mathcal{R}, \tag{2.6a}$$

where a radical, $\mathcal{R}$, is formed from the fuel, $\mathcal{F}$, at a rate $\bar{r}_1$ which we specify shortly. Some authors omit the initiation reaction (2.6a) when studying chain branching reactions, and instead assume that there is a small amount of radical present initially [e.g. 29, 50]. However, we find it is necessary to retain the initiation reaction because initiation plays an important role during autoignition. The second step in our chain branching reaction model is *branching*,

$$\mathcal{F} + \mathcal{R} \xrightarrow{\bar{r}_2} 2\mathcal{R}, \tag{2.6b}$$

where the fuel and radical react to form two radicals, at rate $\bar{r}_2$. The final step is *termination*,

$$\mathcal{R} \xrightarrow{\bar{r}_3} \mathcal{P}, \tag{2.6c}$$

where the radical, $\mathcal{R}$, reacts to become the product, $\mathcal{P}$, at rate $\bar{r}_3$. As with the one-step reaction (2.1), we assume that $\mathcal{F}$, $\mathcal{R}$ and $\mathcal{P}$ have the same molar mass and are the only

species present. This simplification allows us to model the mixture of $\mathcal{F}$, $\mathcal{R}$ and $\mathcal{P}$ as a single gas, and specify the transport of $\mathcal{F}$ and $\mathcal{R}$ relative to that gas.

The three-step chemical reaction (2.6) is well studied in the literature [9, 29, 30, 78, 81, 82]. We adopt two key simplifications present in this literature. Firstly, we assume that the termination reaction (2.6c) is exothermic, releasing $\bar{Q}$ units of energy per unit of mass of radical, and that the other two reactions, (2.6a) and (2.6b), are thermally neutral. Secondly, we assume that the rate, $\bar{r}_3$, of the termination reaction is independent of temperature, with

$$\bar{r}_1 = \bar{A}_1 \bar{Y}_{\mathcal{F}} \exp\left(-\frac{\bar{E}_1}{\hat{\mathfrak{R}}\bar{T}}\right), \tag{2.7a}$$

$$\bar{r}_2 = \bar{A}_2 \bar{Y}_{\mathcal{F}} \bar{Y}_{\mathcal{R}} \exp\left(-\frac{\bar{E}_2}{\hat{\mathfrak{R}}\bar{T}}\right), \tag{2.7b}$$

$$\bar{r} = \bar{r}_3 = \bar{A}_3 \bar{Y}_{\mathcal{R}}, \tag{2.7c}$$

where $\bar{Y}_{\mathcal{R}}$ is the mass fraction of the radical, and $\hat{\mathfrak{R}}$, $\bar{A}_1$, $\bar{A}_2$, $\bar{A}_3$, $\bar{E}_1$ and $\bar{E}_2$ are constants. Note that in (2.7c), we define $\bar{r} := \bar{r}_3$ for convenience later. These simplifications are justified in the literature by noting that, for the hydrogen-oxygen reaction, the amount of heat liberated during the initiation and branching reactions is small compared to the heat released during the termination reactions, and that, in reality, rates of the termination reactions in the hydrogen-oxygen reaction are only weakly dependent on temperature [82].

### 2.1.2 Dimensional model

We now turn our attention to modelling the dynamics of the gas using conservation of mass, momentum and energy, taking care to account for the energy released from the fuel during the chemical reaction. In general, it would be necessary to consider a mixture of gases, by, for example, taking into account the changing composition of the mixture and the partial pressure of each component [16, §1]. However, we treat the mixture of gases (reactants, products, intermediate species and inert components) to be a single gas with constant molar mass.

We take the velocity, $\bar{u}$, pressure, $\bar{p}$, density, $\bar{\rho}$, absolute temperature, $\bar{T}$, and mass fractions, $\bar{Y}_{\mathcal{F}}$ and $\bar{Y}_{\mathcal{R}}$, to be continuous functions of position, $\bar{x}$, and time, $\bar{t}$. Position is measured in an inertial, Eulerian (lab-based) reference frame. The parameters of the model are summarised in Table 2.1.

We now introduce a system of partial differential equations to model the motion of the gas. We use the familiar conservation of mass and momentum equations for a compressible Newtonian fluid,

$$\frac{\partial \bar{\rho}}{\partial \bar{t}} + \frac{\partial (\bar{\rho}\bar{u})}{\partial \bar{x}} = 0, \tag{2.8a}$$

$$\frac{\partial (\bar{\rho}\bar{u})}{\partial \bar{t}} + \frac{\partial}{\partial \bar{x}}\left(\bar{\rho}\bar{u}^2 + \bar{p} - \left(\frac{4\bar{\mu}}{3} + \bar{\kappa}\right)\frac{\partial \bar{u}}{\partial \bar{x}}\right) = 0, \tag{2.8b}$$

where $\bar{\mu}$ is the dynamic viscosity and $\bar{\kappa}$ is the bulk viscosity [7, §1]. We ignore the effect of gravity on the gas.

| Symbol | Units | Description |
|---|---|---|
| $\bar{E}$ | $\mathrm{J\,mol^{-1}}$ | Activation energy (one-step) |
| $\bar{E}_1$ | $\mathrm{J\,mol^{-1}}$ | Activation energy (initiation) |
| $\bar{E}_2$ | $\mathrm{J\,mol^{-1}}$ | Activation energy (branching) |
| $\bar{A}$ | $\mathrm{kg\,m^{-3}\,s^{-1}}$ | Reaction rate coefficient (one-step) |
| $\bar{A}_1$ | $\mathrm{kg\,m^{-3}\,s^{-1}}$ | Reaction rate coefficient (initiation) |
| $\bar{A}_2$ | $\mathrm{kg\,m^{-3}\,s^{-1}}$ | Reaction rate coefficient (branching) |
| $\bar{A}_3$ | $\mathrm{kg\,m^{-3}\,s^{-1}}$ | Reaction rate coefficient (termination) |
| $\bar{Q}$ | $\mathrm{J\,kg^{-1}}$ | Heat of combustion |
| $\bar{c}_v$ | $\mathrm{J\,kg^{-1}\,K^{-1}}$ | Specific heat capacity (constant volume) |
| $\bar{c}_p$ | $\mathrm{J\,kg^{-1}\,K^{-1}}$ | Specific heat capacity (constant pressure) |
| $\bar{R}$ | $\mathrm{J\,kg^{-1}\,K^{-1}}$ | Specific gas constant |
| $\bar{\mathfrak{R}}$ | $\mathrm{J\,mol^{-1}\,K^{-1}}$ | Universal gas constant |
| $\bar{M}$ | $\mathrm{kg\,mol^{-1}}$ | Average molar mass |
| $\bar{D}_{\mathcal{F}}$ | $\mathrm{kg\,m^{-1}\,s^{-1}}$ | Diffusion coefficient (fuel) |
| $\bar{D}_{\mathcal{R}}$ | $\mathrm{kg\,m^{-1}\,s^{-1}}$ | Diffusion coefficient (radical) |
| $\bar{\lambda}$ | $\mathrm{J\,m^{-1}\,K^{-1}\,s^{-1}}$ | Thermal conductivity |
| $\bar{\mu}$ | $\mathrm{kg\,m^{-1}\,s^{-1}}$ | Dynamic viscosity |
| $\bar{\kappa}$ | $\mathrm{kg\,m^{-1}\,s^{-1}}$ | Bulk viscosity |
| $\bar{L}$ | m | Length |
| $\bar{T}_{\mathsf{init}}$ | K | Initial temperature |
| $\bar{p}_{\mathsf{init}}$ | $\mathrm{kg\,m^{-1}\,s^{-2}}$ | Initial pressure |
| $\bar{Y}_{\mathsf{init}}$ | (dimensionless) | Initial mass fraction (fuel) |

**Table 2.1:** *Dimensional parameters and their units.*

To satisfy the First Law of Thermodynamics, the energy—that is, the thermal, kinetic *and chemical* energy—must be conserved. For both reaction mechanisms, (2.1) and (2.6), we assume that $\bar{Q}$ units of chemical energy are liberated per unit mass of product, $\mathcal{P}$, formed. We account for the chemical energy by incorporating a source term in the energy equation,

$$\frac{\partial}{\partial \bar{t}}\left(\bar{\rho}\left(\bar{c}_v\bar{T}+\frac{\bar{u}^2}{2}\right)\right)+\frac{\partial}{\partial \bar{x}}\left(\bar{\rho}\bar{u}\left(\bar{c}_v\bar{T}+\frac{\bar{u}^2}{2}\right)+\bar{p}\bar{u}-\bar{\lambda}\frac{\partial \bar{T}}{\partial \bar{x}}-\left(\frac{4\bar{\mu}}{3}+\bar{\kappa}\right)\bar{u}\frac{\partial \bar{u}}{\partial \bar{x}}\right)=\bar{Q}\bar{r}, \tag{2.8c}$$

where $\bar{r}$ is defined by (2.3) for the one-step reaction (2.1), and by (2.7c) for the three-step reaction (2.6). In deriving (2.8c), we have assumed that heat is conducted according to Fourier's law [7, §9], with thermal conductivity $\bar{\lambda}$, and that the internal energy per unit mass is given by $\bar{c}_v\bar{T}$, where $\bar{c}_v$ is the specific heat at constant volume. For simplicity, we assume that $\bar{\mu}$, $\bar{\kappa}$, $\bar{c}_v$ and $\bar{\lambda}$ are constant.

To relate the pressure, density and temperature, we use the constitutive law for a perfect gas,

$$\bar{p}=\bar{\rho}\bar{R}\bar{T}, \tag{2.8d}$$

where $\bar{R}$ is the specific gas constant. For a gaseous mixture, the specific gas constant is given by $\bar{R}=\bar{\mathfrak{R}}/\bar{M}$, where $\bar{\mathfrak{R}}$ is the universal gas constant and $\bar{M}$ is the average molar mass of the mixture. We have assumed that $\mathcal{F}$, $\mathcal{R}$ and $\mathcal{P}$ have the same molar mass, meaning $\bar{R}$ is indeed constant[2]. It is convenient, for when the problem is nondimensionalised, to introduce the specific heat at constant pressure, $\bar{c}_p$, which is given for a perfect gas by

$$\bar{c}_p=\bar{c}_v+\bar{R}. \tag{2.9}$$

We complement the gas dynamical equations (2.8) with equations governing the motion and consumption of the chemical species. For the one-step reaction, we only need to prescribe an equation governing the mass fraction, $\bar{Y}_{\mathcal{F}}$ of the fuel, $\mathcal{F}$; the conservation of mass dictates that mass fraction, $\bar{Y}_{\mathcal{P}}$, of the product, $\mathcal{P}$, is given by $\bar{Y}_{\mathcal{P}}=1-\bar{Y}_{\mathcal{F}}$. The equation we use to describe the advection, diffusion and reaction of the fuel is

$$\frac{\partial(\bar{\rho}\bar{Y}_{\mathcal{F}})}{\partial \bar{t}}+\frac{\partial}{\partial \bar{x}}\left(\bar{\rho}\bar{u}\bar{Y}_{\mathcal{F}}-\bar{D}_{\mathcal{F}}\frac{\partial \bar{Y}_{\mathcal{F}}}{\partial \bar{x}}\right)=-\bar{r}, \tag{2.10}$$

where $\bar{r}$ is the reaction rate (2.3). Note that, because $\bar{Y}_{\mathcal{F}}$ is the mass fraction of the fuel, the mass flux due to diffusion according to Fick's law is $-\bar{\rho}\bar{D}\,\partial\bar{Y}_{\mathcal{F}}/\partial\bar{x}$, where $\bar{D}$ is the diffusivity of the fuel in the gas [7, §17]. We take the diffusion coefficient, $\bar{D}_{\mathcal{F}}=\bar{\rho}\bar{D}$, to be constant. By using a linear constitutive law, $-\bar{D}_{\mathcal{F}}\,\partial\bar{Y}_{\mathcal{F}}/\partial\bar{x}$, for the mass flux due to diffusion, we are able to easily solve for the structure of flames in Section 2.2.1.

We similarly prescribe equations governing the motion and consumption of $\mathcal{F}$ and $\mathcal{R}$ for the three-step reaction,

$$\frac{\partial(\bar{\rho}\bar{Y}_{\mathcal{F}})}{\partial \bar{t}}+\frac{\partial}{\partial \bar{x}}\left(\bar{\rho}\bar{u}\bar{Y}_{\mathcal{F}}-\bar{D}_{\mathcal{F}}\frac{\partial \bar{Y}_{\mathcal{F}}}{\partial \bar{x}}\right)=-\bar{r}_1-\bar{r}_2, \tag{2.11a}$$

[2]Even if we had allowed the molar mass of the species to differ, taking $\bar{R}$ to be constant is a reasonable approximation for combustion in air, where nitrogen is the dominant component of the gas, both before and after combustion.

$$\frac{\partial(\bar{\rho}\bar{Y}_{\mathcal{R}})}{\partial\bar{t}} + \frac{\partial}{\partial\bar{x}}\left(\bar{\rho}\bar{u}\bar{Y}_{\mathcal{R}} - \bar{D}_{\mathcal{R}}\frac{\partial\bar{Y}_{\mathcal{R}}}{\partial\bar{x}}\right) = \bar{r}_1 + \bar{r}_2 - \bar{r}_3, \tag{2.11b}$$

where $\bar{r}_1$, $\bar{r}_2$ and $\bar{r}_3$ are defined by (2.7). As with the one-step reaction, we assume that the diffusion coefficients, $\bar{D}_{\mathcal{F}}$ and $\bar{D}_{\mathcal{R}}$, are constant.

#### 2.1.2.1 Physical problem

With {(2.3), (2.8), and (2.10)} and {(2.7), (2.8), and (2.11)}, we have derived two paradigm models for gaseous combustion in 1D. We now need to identify appropriate boundary and initial conditions to specify a solution. The physical problem we choose to study is the combustion of a gas following ignition at one end of a rigid, impermeable, insulated channel of finite length, $\bar{L}$, with closed ends. This paradigm model is chosen to be representative of combustion within an internal combustion engine, but with a simple 1D geometry. To represent the rigid, impermeable, insulated ends of the channel, we impose

$$\bar{u}(0,\bar{t}) = \bar{u}(\bar{L},\bar{t}) = 0, \tag{2.12a}$$

$$\frac{\partial\bar{T}}{\partial\bar{x}}(0,\bar{t}) = \frac{\partial\bar{T}}{\partial\bar{x}}(\bar{L},\bar{t}) = 0, \tag{2.12b}$$

$$\frac{\partial\bar{Y}_{\mathcal{F}}}{\partial\bar{x}}(0,\bar{t}) = \frac{\partial\bar{Y}_{\mathcal{F}}}{\partial\bar{x}}(\bar{L},\bar{t}) = \frac{\partial\bar{Y}_{\mathcal{R}}}{\partial\bar{x}}(0,\bar{t}) = \frac{\partial\bar{Y}_{\mathcal{R}}}{\partial\bar{x}}(\bar{L},\bar{t}) = 0, \tag{2.12c}$$

for $\bar{t} > 0$.

There are a number of different approaches we could take to representing the ignition of the flame. One reasonable approach would be to start with uniform initial conditions and to modify the energy equation (2.8c) to incorporate a transient source of energy [60], to represent ignition by a spark plug. Similarly, we could modify the boundary conditions (2.12) to prescribe a non-zero heat flux through one of the walls [22]. While representative of the physical source of ignition within an internal combustion engine, these approaches to modelling ignition of the flame add additional complexity to the model. For instance, one has to choose the rate of heat flux and, for the former, the dimensions of the heated region.

For simplicity, therefore, we do not model the ignition of the flame per se, but rather prescribe initial conditions representative of a flame 'already in existence' at $\bar{x} = 0$. We take the initial velocity to be zero throughout the channel, and take the initial pressure to be spatially uniform, with $\bar{p}(\bar{x},0) = \bar{p}_{\text{init}}$ for $\bar{x} \in (0,\bar{L})$. We prescribe initial profiles for the temperature and mass fractions, such that the initial temperature and mass fractions are approximately constant for most of the domain, $\bar{x} \in (0,\bar{L})$, with $\bar{T} \approx \bar{T}_{\text{init}}$, $\bar{Y}_{\mathcal{F}} \approx \bar{Y}_{\text{init}}$ and $\bar{Y}_{\mathcal{R}} \approx 0$ apart from close to the left-hand wall, $\bar{x} = 0$. We give suitable initial profiles for the temperature and mass fractions in dimensionless form in Section 2.1.3. Liberman et al. [66] and Yu and Chen [95] use similar initial conditions for their numerical simulations.

Note that we choose initial conditions that are approximately uniform away from the flame. We do not, for example, artificially bring about a hot spot in the end-gas by introducing significant variation in temperature close to the right-hand wall, $\bar{x} = \bar{L}$, as has been done in some numerical studies [91, 94]. The initial conditions that we use are

therefore appropriate for studying the mechanism that leads to autoignition in the absence of any sources of spontaneous ignition.

### 2.1.3 Dimensionless model

We now nondimensionalise the models presented in Section 2.1.2. The benefits to nondimensionalising are (at least) two-fold. Firstly, we identify dimensionless groups of the dimensional parameters presented in Table 2.1 that dictate the fundamental behaviour of each model. By expressing the model in terms of these dimensionless groups, which we call dimensionless parameters, we significantly simplify the parameter space without compromising any of the physics. Secondly, we are able to compare the size of the dimensionless parameters to identify which processes are important, and consequently derive simplified models that capture the most important aspects of combustion. For instance, it does not make sense to say the thermal conductivity, $\bar{\lambda}$, is large compared to the dynamic viscosity, $\bar{\mu}$, because these quantities have different dimensions. However, by identifying a suitable dimensionless parameter (in this case the Prandtl number, $\mathrm{Pr}$, see Table 2.2) we are able to quantify the relative importance of thermal diffusion and viscosity.

We have derived two similar models for combustion, $\{$(2.3), (2.8) and (2.10)$\}$ and $\{$(2.7), (2.8) and (2.11)$\}$. Both models share the gas dynamical equations (2.8), so it makes sense to nondimensionalise in such a way that the dimensionless version of (2.8) is the same for both reaction mechanisms. To this end, we will shortly define a length, $\bar{L}^*$, for each of the two reaction mechanisms (2.1) and (2.6), which is characteristic of the width of the flame.

For each variable, $\bar{\psi} \in \{\bar{T}, \bar{p}, \bar{\rho}, \bar{u}, \bar{Y}_{\mathcal{F}}, \bar{Y}_{\mathcal{R}}, \bar{x}, \bar{t}, \bar{r}, \bar{r}_1, \bar{r}_2, \bar{r}_3\}$, we define a typical scaling, $[\psi]$, and use it to define the corresponding normalised variable, $\psi$, given by

$$\psi := \frac{\bar{\psi}}{[\psi]}. \tag{2.13a}$$

The typical scalings we use are

$$[T] = \bar{T}_{\mathsf{init}}, \quad [p] = \bar{p}_{\mathsf{init}}, \quad [\rho] = \frac{\bar{p}_{\mathsf{init}}}{\bar{R}\bar{T}_{\mathsf{init}}} =: \bar{\rho}_{\mathsf{init}}, \quad [u] = \frac{\bar{\lambda}}{\bar{c}_p \bar{\rho}_{\mathsf{init}} \bar{L}^*}, \quad [Y_{\mathcal{F}}] = [Y_{\mathcal{R}}] = \bar{Y}_{\mathsf{init}}, \tag{2.13b}$$

$$[x] = \bar{L}, \quad [t] = \frac{\bar{L}}{[u]}, \quad [r] = [r_1] = [r_2] = [r_3] = \frac{\bar{\rho}_{\mathsf{init}}[u]\bar{Y}_{\mathsf{init}}}{\bar{L}^*}. \tag{2.13c}$$

Our choices for $[T]$, $[p]$, $[\rho]$ and $[x]$ are straightforward to understand; each represents the (approximate) initial values or the length of the channel, as discussed in Section 2.1.2.1. Likewise, $\bar{Y}_{\mathsf{init}}$ is the representative initial mass fraction of the fuel. Although mass fraction is dimensionless, we choose to rescale $\bar{Y}_{\mathcal{F}}$ and $\bar{Y}_{\mathcal{R}}$ so that $\bar{Y}_{\mathsf{init}}$ naturally appears in the definition of the dimensionless heat of combustion, $Q$, given in Table 2.2. We choose to rescale $\bar{u}$ by $[u]$, which is representative of the initial speed of the flame. The time scale, $[t]$, is therefore representative of the time taken for the flame to cross from $\bar{x} = 0$ to $\bar{x} = \bar{L}$. Our choice of scaling for the reaction rates, $[r]$, is natural to represent the typical rate at which the fuel is burned within a flame of width $\bar{L}^*$.

In terms of the dimensionless variables, the gas dynamical equations (2.8) become

$$\frac{\partial \rho}{\partial t} + \frac{\partial (\rho u)}{\partial x} = 0, \tag{2.14a}$$

$$\frac{\partial}{\partial t}(\rho u) + \frac{\partial}{\partial x}\left(\rho u^2 + \frac{1}{\gamma M^2} p - \epsilon \mathrm{Pr} \frac{\partial u}{\partial x}\right) = 0, \tag{2.14b}$$

$$\frac{1}{\gamma}\frac{\partial (\rho T)}{\partial t} + (\gamma - 1)M^2 \frac{\partial}{\partial t}\left(\frac{\rho u^2}{2}\right) + \frac{\partial (\rho u T)}{\partial x} + (\gamma - 1)M^2 \frac{\partial}{\partial x}\left(\frac{\rho u^3}{2}\right) - \epsilon \frac{\partial^2 T}{\partial x^2} - \epsilon\, \mathrm{Pr}(\gamma - 1)M^2 \frac{\partial}{\partial x}\left(u \frac{\partial u}{\partial x}\right) = \epsilon^{-1} Q r, \tag{2.14c}$$

$$p = \rho T, \tag{2.14d}$$

where the dimensionless parameters are defined in Table 2.2. We will derive the dimensionless reaction rate, $r$, for both reaction mechanisms shortly.

Each of the dimensionless parameters in Table 2.2 can be interpreted physically. The ratio of specific heats, $\gamma$, is the ratio of the specific heat at constant pressure and the specific heat at constant volume. As we have already discussed, the Prandtl number, $\mathrm{Pr}$, quantifies the relative importance of viscosity and thermal diffusion. The typical initial Mach number of the flame, $M$, is the ratio of the typical initial speed of the flame, $[u]$, and the initial speed of sound in the unburnt gas, given by $\sqrt{\gamma \bar{R} \bar{T}_{\mathsf{init}}}$. For the three-step reaction, we do not define $\bar{L}^*$ such that $[u]$ is actually the initial speed of the flame, because, as we will see in Section 2.2.2.2, the leading-order mass flux through a flame with three-step chemistry is given implicitly as the solution of an algebraic equation. Therefore, we emphasise that $M$ is the 'typical' Mach number. For simplicity, though, we will drop the word 'typical' during our discussion. The dimensionless heat of combustion, $Q$, is the ratio between the initial heat of combustion per unit mass of the fuel-air mixture and the initial enthalpy per unit mass of the fuel-air mixture. Burning the gas at constant pressure would raise the temperature from $\bar{T}_{\mathsf{init}}$ to $(1 + Q)\bar{T}_{\mathsf{init}}$. The reciprocal Péclet number, $\epsilon$, can be interpreted in two ways; $\epsilon$ represents both the ratio between the typical flame width and the length of the container, and also the ratio of the rate of thermal diffusion and the rate of thermal advection.

The dimensional scalings (2.13) are not unique. We could have, for example, chosen to nondimensionalise by scaling the velocity, $\bar{u}$, by the initial speed of sound in the unburnt gas, given by $\sqrt{\gamma \bar{R} \bar{T}_{\mathsf{init}}}$, or by scaling the spatial coordinate, $\bar{x}$, by the typical flame width, $\bar{L}^*$. While all dimensionless formulations of a model are equivalent, using different formulations to study different parameter regimes or distinguished stages of the solution allows one to more easily identify the structure of the solution. The dimensionless form (2.14) of model (2.8) is particularly convenient for studying the gas either side of the flame (on the length scale of the channel) over the time it takes for the flame to cross from one end of the channel to the other; having the typical Mach number as a parameter in the governing equations allows us to easily identify approximate governing equations in the physically relevant limit of small Mach number. We will frequently rescale the variables

| **Dimensionless parameters common to both reaction models** | | |
|---|---|---|
| **Definition** | **Name** | **Size** |
| $\gamma := \dfrac{\bar{c}_p}{\bar{c}_v}$ | Ratio of specific heats | $\gamma - 1 = \mathrm{ord}(1)$ |
| $\mathrm{Pr} := \dfrac{(4\bar{\mu} + 3\bar{\kappa})\bar{c}_p}{3\bar{\lambda}}$ | Prandtl number | $\mathrm{Pr} = \mathrm{ord}(1)$ |
| $M := \dfrac{[u]}{\sqrt{\gamma \bar{R} \bar{T}_{\mathsf{init}}}}$ | Typical Mach number of flame | See (2.39) & (2.40) |
| $Q := \dfrac{\bar{Q}\bar{Y}_{\mathsf{init}}}{\bar{c}_p \bar{T}_{\mathsf{init}}}$ | Heat of combustion | $Q = \mathrm{ord}(1)$ |
| $\epsilon := \dfrac{1}{\mathrm{Pe}} = \dfrac{\bar{L}^*}{\bar{L}}$ | Reciprocal Péclet number | See (2.39) & (2.42) |
| **Parameters specific to the one-step reaction model** | | |
| **Definition** | **Name** | **Size** |
| $E := \dfrac{\bar{E}}{\bar{\mathfrak{R}} \bar{T}_{\mathsf{init}}}$ | Activation energy (one-step) | $E \to \infty$ |
| $\mathrm{Le}_{\mathcal{F}} := \dfrac{\bar{\lambda}}{\bar{c}_p \bar{D}_{\mathcal{F}}}$ | Lewis number (fuel) | $\mathrm{Le}_{\mathcal{F}} = \mathrm{ord}(1)$ |
| **Parameters specific to the three-step reaction model** | | |
| **Definition** | **Name** | **Size** |
| $m := \dfrac{\bar{E}_1}{\bar{E}_2}$ | Activation energy ratio | $m = \mathrm{ord}(1)$ |
| $E := \dfrac{\bar{E}_2}{\bar{\mathfrak{R}} \bar{T}_{\mathsf{init}}}$ | Activation energy (branching) | $E \to \infty$ |
| $\mathrm{Le}_{\mathcal{F}} := \dfrac{\bar{\lambda}}{\bar{c}_p \bar{D}_{\mathcal{F}}}$ | Lewis number (fuel) | $\mathrm{Le}_{\mathcal{F}} = \mathrm{ord}(1)$ |
| $\mathrm{Le}_{\mathcal{R}} := \dfrac{\bar{\lambda}}{\bar{c}_p \bar{D}_{\mathcal{R}}}$ | Lewis number (radical) | $\mathrm{Le}_{\mathcal{R}} = \mathrm{ord}(1)$ |
| $T_{\times 1} := \dfrac{\bar{E}_1}{\bar{\mathfrak{R}} \bar{T}_{\mathsf{init}} \log\big(\bar{A}_1 \bar{\mathfrak{R}}^2 \bar{T}_{\mathsf{init}}^2 / (\bar{A}_3 \bar{E}_2^2)\big)}$ | Cross-over temperature (initiation) | See (2.41b) |
| $T_{\times 2} := \dfrac{\bar{E}_2}{\bar{\mathfrak{R}} \bar{T}_{\mathsf{init}} \log\big(\bar{A}_2 \bar{\mathfrak{R}}^2 \bar{T}_{\mathsf{init}}^2 \bar{Y}_{\mathsf{init}} / (\bar{A}_3 \bar{E}_2^2)\big)}$ | Cross-over temperature (branching) | See (2.41a) |

**Table 2.2:** *Dimensionless parameters.*

in the model (2.14) to present the most appropriate form of the governing equations for the structure or process we are studying.

We now consider each of the two reaction mechanisms in turn, to define a suitable typical flame width, $\bar{L}^*$, and nondimensionalise the species conservation equations, (2.10) and (2.11), and reaction rates, (2.3) and (2.7).

#### 2.1.3.1 One-step reaction

For the one-step reaction (2.1), a suitable choice for $\bar{L}^*$ is

$$\bar{L}^* := \sqrt{\frac{\bar{D}_{\mathcal{F}}}{2\bar{A}}}\,\frac{EQ}{(1+Q)^2}\exp\left(\frac{E}{2(1+Q)}\right). \tag{2.15}$$

This choice of $\bar{L}^*$ ensures that the dimensionless leading order mass flux through a flame is equal to 1.0 when the temperature, $T^{R*}$, and mass fraction, $Y_{\mathcal{F}}^{R*}$, of the fuel immediately ahead of the flame are both equal to 1.0, as demonstrated in Section 2.2.2.1.

Using the scalings (2.13) to normalise the variables in (2.3) and (2.10) and rearranging, we find that $Y_{\mathcal{F}}$ satisfies

$$\frac{\partial(\rho Y_{\mathcal{F}})}{\partial t} + \frac{\partial}{\partial x}\left(\rho u Y_{\mathcal{F}} - \frac{\epsilon}{\mathrm{Le}_{\mathcal{F}}}\frac{\partial Y_{\mathcal{F}}}{\partial x}\right) = -\epsilon^{-1} r, \tag{2.16}$$

where

$$r = Z Y_{\mathcal{F}} \exp\left(-\frac{E}{T}\right). \tag{2.17}$$

The reaction rate coefficient, $Z$, can be written in terms of the other dimensionless parameters listed in Table 2.2,

$$Z = \frac{Q^2}{2\mathrm{Le}_{\mathcal{F}}(1+Q)^4} E^2 \exp\left(\frac{E}{1+Q}\right). \tag{2.18}$$

Nondimensionalising (2.12), we find that suitable boundary conditions for $t > 0$ to represent the closed ends of the channel are given by

$$u(0,t) = u(1,t) = \frac{\partial T}{\partial x}(0,t) = \frac{\partial T}{\partial x}(1,t) = \frac{\partial Y_{\mathcal{F}}}{\partial x}(0,t) = \frac{\partial Y_{\mathcal{F}}}{\partial x}(1,t) = 0. \tag{2.19}$$

In Section 2.1.2.1, we suggested that suitable initial conditions could be provided that are approximately uniform, apart from close to the left-hand wall at $x = 0$ to represent the effect of the spark. Based on the structure of a flame that we present in Section 2.2.2.1, we impose initial conditions on $x \in (0,1)$ of the form

$$p(x,0) = 1, \quad u(x,0) = 0, \tag{2.20a}$$

$$T(x,0) = 1 + Q\exp(-x/\epsilon), \qquad Y_{\mathcal{F}}(x,0) = 1 - \exp(-\mathrm{Le}_{\mathcal{F}} x/\epsilon). \tag{2.20b}$$

In gaseous combustion problems, the Péclet number, $\mathrm{Pe} = 1/\epsilon$, is typically very large, as we shall discuss in Section 2.1.5. The initial temperature, $T(x,0)$, and mass fraction, $Y_{\mathcal{F}}(x,0)$, given by (2.20b) are therefore approximately equal to one, except close to $x = 0$.

#### 2.1.3.2 Three-step reaction

For the three-step reaction (2.6), we take the typical flame width, $\bar{L}^*$, to be

$$\bar{L}^* = \sqrt{\frac{\bar{\lambda}}{\bar{c}_p \bar{A}_3}}. \tag{2.21}$$

As with the one-step flame width (2.15), the choice of (2.21) is motivated by considering the leading order mass flux through a flame with the three-step reaction (2.6), which, in Section 2.2.2.2, we show is given implicitly as a solution of (2.88). Taking $\bar{L}^*$ to be given by (2.21) ensures there is a leading order balance between the termination reaction and diffusion within the flame, except in a very thin boundary layer. For simplicity, we do not choose $\bar{L}^*$ to normalise the initial mass flux through the flame like we did for the one-step reaction.

Nondimensionalising (2.7) and (2.11) using (2.13), we find that

$$\frac{\partial(\rho Y_F)}{\partial t} + \frac{\partial(\rho u Y_F)}{\partial x} - \frac{\epsilon}{\mathrm{Le}_{\mathcal{F}}}\frac{\partial^2 Y_F}{\partial x^2} = -\epsilon^{-1} r_1 - \epsilon^{-1} r_2 \tag{2.22a}$$

$$\frac{\partial(\rho Y_R)}{\partial t} + \frac{\partial(\rho u Y_R)}{\partial x} - \frac{\epsilon}{\mathrm{Le}_{\mathcal{R}}}\frac{\partial^2 Y_R}{\partial x^2} = \epsilon^{-1} r_1 + \epsilon^{-1} r_2 - \epsilon^{-1} r_3, \tag{2.22b}$$

where the dimensionless parameters are defined in Table 2.2, and the reaction rates, $r_1$, $r_2$ and $r_3$, are given by

$$r_1 = E^2 Y_F \exp\left(m\left(\frac{E}{T_{\times 1}} - \frac{E}{T}\right)\right), \tag{2.23a}$$

$$r_2 = E^2 Y_F Y_R \exp\left(\frac{E}{T_{\times 2}} - \frac{E}{T}\right), \tag{2.23b}$$

$$r_3 = r = Y_R. \tag{2.23c}$$

We solve (2.14), (2.22) and (2.23), subject to the dimensionless boundary conditions,

$$\begin{aligned} u(0,t) = u(1,t) = \frac{\partial T}{\partial x}(0,t) = \frac{\partial T}{\partial x}(1,t) \\ = \frac{\partial Y_{\mathcal{F}}}{\partial x}(0,t) = \frac{\partial Y_{\mathcal{F}}}{\partial x}(1,t) = \frac{\partial Y_{\mathcal{R}}}{\partial x}(0,t) = \frac{\partial Y_{\mathcal{R}}}{\partial x}(1,t) = 0, \end{aligned} \tag{2.24}$$

for $t > 0$, and the initial conditions,

$$p(x,0) = 1, \quad u(x,0) = 0, \tag{2.25a}$$

$$\begin{aligned} T(x,0) = 1 + (T_{\times 2} - 1)\exp\left(-q^{(0)} x/\epsilon\right) \\ + \frac{Q\mathrm{Le}_{\mathcal{R}} q^{(0)}}{(m_+ - m_-)(m_-^2 + m_- q^{(0)})}\left(\exp\left(-q^{(0)} x/\epsilon\right) - \exp(m_- x/\epsilon)\right), \end{aligned} \tag{2.25b}$$

$$Y_{\mathcal{F}}(x,0) = 1 - \exp\bigl(-\mathrm{Le}_{\mathcal{F}} q^{(0)} x/\epsilon\bigr), \quad Y_{\mathcal{R}}(x,0) = \frac{\mathrm{Le}_{\mathcal{R}} q^{(0)}}{m_+ - m_-} \exp(m_- x/\epsilon), \tag{2.25c}$$

for $x \in (0,1)$, where $q^{(0)}$ is the solution to (2.88) with $T^{R*} = Y_{\mathcal{F}}^{R*} = 1$, and $m_-$ is given by (2.78). As with the one-step reaction, the initial conditions (2.25) are based on the interior structure of a freely-propagating flame, which we determine in Section 2.2.2.2. In the limit of large Péclet number, $\epsilon \to 0$, the initial conditions (2.25) are approximately uniform, except for in a thin layer close to $x = 0$.

### 2.1.4 Lagrangian coordinate

Up until this point, we have used an Eulerian coordinate, $x$, to describe the spatial dependence of $p$, $T$, $\rho$, $u$, $Y_{\mathcal{F}}$ and $Y_{\mathcal{R}}$. However, when describing the motion of a flame, it is particularly convenient to use a Lagrangian coordinate system. Intuitively, each fluid particle is burned once. Therefore, if we ignore the effect of diffusion, we conclude that the flame position changes monotonically in time in a Lagrangian coordinate system. In this section, we rewrite (2.14), (2.16) and (2.22) in terms of $(\chi, t)$, where the Lagrangian coordinate, $\chi$, is defined by

$$\chi = \int_0^x \rho(s,t)\,\mathrm{d}s. \tag{2.26}$$

The Lagrangian coordinate (2.26) is commonly used in the combustion literature [e.g. 31]. In addition to introducing the Lagrangian coordinate, $\chi$, we also define the specific volume, $V$, as

$$V := \frac{1}{\rho}. \tag{2.27}$$

Using $V$ as a dependent variable instead of $\rho$ leads to a particularly simple equation describing the conservation of mass in the Lagrangian coordinate [31].

The motivation behind using the Lagrangian coordinate (2.26) to describe space is further demonstrated by considering the entropy, $S$, which, for the ideal gas we are considering, is given by

$$S = \gamma^{-1} \log(pV^\gamma). \tag{2.28}$$

Using the conservation of mass (2.14a) and momentum (2.14b), we find that (2.14c) can be written as

$$\rho\left(\frac{\partial T}{\partial t} + u\frac{\partial T}{\partial x}\right) - \frac{\gamma - 1}{\gamma}\left(\frac{\partial p}{\partial t} + u\frac{\partial p}{\partial x}\right) - \epsilon\frac{\partial^2 T}{\partial x^2} - \epsilon \mathrm{Pr} M^2(\gamma - 1)\left(\frac{\partial u}{\partial x}\right)^2 = \epsilon^{-1} Qr. \tag{2.29}$$

In terms of entropy, the energy equation (2.29) reads

$$p\left(\frac{\partial S}{\partial t} + u\frac{\partial S}{\partial x}\right) - \epsilon\frac{\partial^2 T}{\partial x^2} - \epsilon \mathrm{Pr} M^2(\gamma - 1)\left(\frac{\partial u}{\partial x}\right)^2 = \epsilon^{-1} Qr. \tag{2.30}$$

As we will discuss in more detail in Section 2.1.5, the reciprocal Péclet number, $\epsilon$, is often very small. In the physically relevant limit of $\epsilon \to 0$, we find that entropy, $S$, approximately satisfies an ordinary differential equation,

$$p\frac{\mathrm{d}S}{\mathrm{d}t} = \epsilon^{-1} Qr, \tag{2.31}$$

along characteristics following the flow, i.e. along lines of constant $\chi$.

In terms of $(\chi, t)$, the $x$- and $t$-derivatives in (2.14), (2.16) and (2.22) become

$$\left(\frac{\partial}{\partial t}\right)_x = \left(\frac{\partial}{\partial t}\right)_\chi - \rho u \left(\frac{\partial}{\partial \chi}\right)_t, \quad \left(\frac{\partial}{\partial x}\right)_t = \rho \left(\frac{\partial}{\partial \chi}\right)_t. \tag{2.32}$$

Therefore, written in terms of $(\chi, t)$, the gas dynamic equations (2.14) become

$$\frac{\partial V}{\partial t} - \frac{\partial u}{\partial \chi} = 0, \tag{2.33a}$$

$$\frac{\partial u}{\partial t} + \frac{1}{\gamma M^2}\frac{\partial p}{\partial \chi} - \epsilon \Pr \left(\frac{1}{V}\frac{\partial^2 u}{\partial \chi^2} - \frac{1}{V^2}\frac{\partial V}{\partial \chi}\frac{\partial u}{\partial \chi}\right) = 0, \tag{2.33b}$$

$$p\frac{\partial S}{\partial t} - \epsilon \left(\frac{1}{V^2}\frac{\partial^2 T}{\partial \chi^2} - \frac{1}{V^3}\frac{\partial V}{\partial \chi}\frac{\partial T}{\partial \chi}\right) - \epsilon \Pr M^2(\gamma - 1)\left(\frac{1}{V}\frac{\partial u}{\partial \chi}\right)^2 = \epsilon^{-1} Q r, \tag{2.33c}$$

$$T = pV, \tag{2.33d}$$

where, as before, $r$ is defined by (2.17) for the one-step reaction (2.1), and by (2.23c) for the three-step reaction (2.6). For the one-step reaction, $Y_{\mathcal{F}}$ satisfies

$$\frac{\partial Y_{\mathcal{F}}}{\partial t} - \frac{\epsilon}{\mathrm{Le}_{\mathcal{F}}}\left(\frac{1}{V}\frac{\partial^2 Y_{\mathcal{F}}}{\partial \chi^2} - \frac{1}{V^2}\frac{\partial V}{\partial \chi}\frac{\partial Y_{\mathcal{F}}}{\partial \chi}\right) = -\epsilon^{-1} V r, \tag{2.34}$$

whereas, for the three-step reaction, the evolution of $Y_{\mathcal{F}}$ and $Y_{\mathcal{R}}$ is governed by

$$\frac{\partial Y_{\mathcal{F}}}{\partial t} - \frac{\epsilon}{\mathrm{Le}_{\mathcal{F}}}\left(\frac{1}{V}\frac{\partial^2 Y_{\mathcal{F}}}{\partial \chi^2} - \frac{1}{V^2}\frac{\partial V}{\partial \chi}\frac{\partial Y_{\mathcal{F}}}{\partial \chi}\right) = -\epsilon^{-1} V r_1 - \epsilon^{-1} V r_2, \tag{2.35a}$$

$$\frac{\partial Y_{\mathcal{R}}}{\partial t} - \frac{\epsilon}{\mathrm{Le}_{\mathcal{R}}}\left(\frac{1}{V}\frac{\partial^2 Y_{\mathcal{R}}}{\partial \chi^2} - \frac{1}{V^2}\frac{\partial V}{\partial \chi}\frac{\partial Y_{\mathcal{R}}}{\partial \chi}\right) = \epsilon^{-1} V r_1 + \epsilon^{-1} V r_2 - \epsilon^{-1} V r_3, \tag{2.35b}$$

where $r_1$, $r_2$ and $r_3$ are defined by (2.23).

### 2.1.5 Asymptotic notation and distinguished limit

We have derived two paradigm models, {(2.14), (2.16)–(2.20)} and {(2.14), (2.22)–(2.25)}, for combustion in confinement. Since the chemical mechanisms, (2.1) and (2.6), are not specific to any particular combustion reaction, identifying appropriate values of the dimensionless parameters to accurately represent a real combustion reaction is not straightforward, and, indeed, may not be possible for certain fuel-air mixtures. Our goal, therefore, is not to provide quantitative predictions for a specific fuel-air mixture, but rather to provide a description of the general behaviour of the models for a range of realistic parameter values and identify trends in the relationship between autoignition and the general properties of a fuel-air mixture.

The typical size of some of the dimensionless parameters in Table 2.2 can be exploited to simplify the models. Asymptotic analysis is central to much of the theoretical understanding of combustion [14]. Before we define the physically relevant limits we study, we first define the notation we use to compare the relative size of functions in limiting processes. Suppose $f$ and $g$ are functions of some parameter $\epsilon$ (not necessarily $1/\mathrm{Pe}$), with $g > 0$.

- We use $f = O(g)$ as $\epsilon \to 0$ to mean that there exists a constant, $A > 0$, such that

$$\left|\frac{f}{g}\right| < A, \quad \text{as} \quad \epsilon \to 0. \tag{2.36}$$

- We use $f = \mathrm{ord}(g)$ as $\epsilon \to 0$ to mean that there exist constants, $A > 0$ and $B > 0$, such that

$$A < \frac{f}{g} < B, \quad \text{as} \quad \epsilon \to 0. \tag{2.37}$$

- We use $f = o(g)$ as $\epsilon \to 0$ to mean that

$$\frac{f}{g} \to 0, \quad \text{as} \quad \epsilon \to 0. \tag{2.38}$$

- We also use $f \ll g$ as $\epsilon \to 0$ and $g \gg f$ as $\epsilon \to 0$ to mean $f = o(g)$ as $\epsilon \to 0$.

Although we have used $\epsilon \to 0$ to define big-$O$, $\mathrm{ord}$ and little-$o$, we use the same notation for other limiting processes. For example, we use $f = o(1)$ as $E \to \infty$ to mean $f \to 0$ as $E \to \infty$. More informally, we will drop the 'as $\epsilon \to 0$' or 'as $E \to \infty$' where the limiting process is clear.

We will only briefly outline the limit we study for the one-step reaction. In the literature, it is often assumed that the dimensionless activation energy, $E$, is large, the Mach number, $M$, of the flame is small, and the Péclet number, $\mathrm{Pe}$, is large. The Péclet number, $\mathrm{Pe}$, is the ratio of the rate of advection to the rate of thermal diffusion. In the context of flames, the reciprocal Péclet number, $\epsilon = \mathrm{Pe}^{-1}$, gives an estimate of the ratio of the width of the flame to the length of the channel. We study the one-step reaction in the limit

$$M = O(E^{-1}), \quad \epsilon = O(E^{-1}), \quad \text{as} \quad E \to \infty. \tag{2.39}$$

We assume the other dimensionless parameters have the limiting behaviour described in Table 2.2 as $E \to \infty$.

The (dimensionless) activation energy, $E$, is the ratio of the dimensional activation energy to the typical initial internal energy of the gas. With $E$ large, the reaction rate is acutely sensitive to changes in temperature; an $O(E^{-1})$ change in temperature leads to an $O(1)$ change in the reaction rate. As we will discuss in Section 2.2, this sensitivity in the reaction rate is central to finding asymptotic solutions to (2.14), (2.16) and (2.17) in the limit (2.39).

For the three-step reaction, we also assume $\epsilon \ll 1$, $M \ll 1$ and $E \gg 1$. Typically, the activation energy, $\bar{E}_1$, of the initiation reaction is larger than the activation energy, $\bar{E}_2$, of the branching reaction. For example, the activation energy of the dissociation of hydrogen (the initiation reaction) in [65] is approximately six times larger than the activation energy of the chain branching reaction (2.5). When modelling ignition due to the three-step reaction (2.6), Blythe et al. [9] assume $m = \bar{E}_1/\bar{E}_2 > 1$ and $m = O(1)$, whereas Sharpe and Maflahi [78] take $m = 3$. We assume $m = \mathrm{ord}(1)$ as $E \to \infty$, and, for simplicity, we take $m = 1$ in the numerical simulations presented in Section 4.3.

The asymptotic limit of large dimensionless activation energy, $E \to \infty$, for the branching reaction (2.6b) is often studied in the literature [e.g. 9, 29, 78]. We also take this approach, studying the three-step reaction (2.6) in the limit $E \to \infty$. For the numerical simulations presented in Sections 3.4 and 4.3 we take larger values of $E$ than are perhaps justified by the literature; Sharpe and Maflahi [78] take $E = 5$, and, based on the activation energy for (2.5) given in [65] and the typical temperature $\bar{T}_{\text{init}} = 1000\,\text{K}$, we estimate that $E \approx 8$. However, by taking $E$ to be very large in our numerical simulations, we are able to fully investigate the asymptotic behaviour of our model with small errors.

Most freely-propagating flames observed in experiments are much slower than the speed of sound, with typical Mach numbers, $M$, between $10^{-2}$ and $10^{-3}$ [15, §2.1]. We estimate that the Mach number of the flames in the numerical simulations by Yu and Chen [95] is approximately $1/40$. We study the distinguished limit where $M$ satisfies

$$EM = O(1), \quad E^2 M \gg 1, \quad \text{as} \quad E \to \infty. \tag{2.40}$$

In Section 4.2, we find that, in the limit (2.40), the gas dynamics and the chemical reaction are coupled during the induction stage of autoignition.

We take the dimensionless heat of combustion, $Q$, to be $\mathrm{ord}(1)$, and the ratio of specific heats, $\gamma$, to satisfy $\gamma - 1 = \mathrm{ord}(1)$. This choice ensures there is an $\mathrm{ord}(1)$ jump in temperature across the flame, and that the temperature in the end-gas rises by an $\mathrm{ord}(1)$ amount during normal combustion. In numerical simulations, we exclusively use $\gamma = 1.4$, which is the ratio of specific heats of air [35], and $Q = 1.4$, which ensures our model approximately captures the rise in pressure exhibited by the numerical simulation presented in Figure 1.6a.

We choose the dimensionless cross-over temperatures, $T_{\times 1}$ and $T_{\times 2}$, such that the flame has the structure described by Dold [29]. In particular, we assume that

$$T_{\times 2} - 1 = \mathrm{ord}(1), \quad 1 + Q - T_{\times 2} = \mathrm{ord}(1), \quad \text{as} \quad E \to \infty, \tag{2.41a}$$

so that the branching cross-over temperature, $T_{\times 2}$, is within the temperature range of a flame initially, and bounded away from the extreme temperatures of $1$ and $1 + Q$. Furthermore, we assume that

$$T_{\times 1} - T_{\times 2} = \mathrm{ord}(1), \quad \text{as} \quad E \to \infty, \tag{2.41b}$$

which ensures that the initiation reaction has a negligible effect within the flame.

We define the distinguished limit of $\epsilon$ that we study in terms of the dimensionless critical temperature, $T_c$. In Section 4.1.1.2, we find that autoignition does not occur if the temperature of the end-gas remains less than this critical temperature, $T_c$, which we define in terms of the dimensionless parameters listed in Table 2.2. The plausible range of critical temperatures we study is

$$T_c - 1 = \mathrm{ord}(1), \quad T_{\times 2} - T_c = \mathrm{ord}(1), \quad \text{as} \quad E \to \infty. \tag{2.42a}$$

The assumption that $T_c - 1 = \mathrm{ord}(1)$ ensures that autoignition, if it occurs, follows a period of normal combustion. The assumption that $T_{\times 2} - T_c = \mathrm{ord}(1)$ ensures the flame

structure by Dold [29] is valid up until autoignition occurs, if autoignition occurs. In terms of $T_c$, the distinguished limit of $\epsilon$ we study is

$$\epsilon = E^2 \exp\left( m \left( \frac{E}{T_{\times 1}} - \frac{E}{T_c} \right) \right), \quad \text{as} \quad E \to \infty. \tag{2.42b}$$

Note that, $\epsilon$ is *exponentially small* in $E$. That is, for all $n \in \mathbb{N}$, $\epsilon = o(E^{-n})$.

Finally, we assume that the Prandtl number, $\mathrm{Pr}$, and the Lewis numbers, $\mathrm{Le}_{\mathcal{F}}$ and $\mathrm{Le}_{\mathcal{R}}$, are $\mathrm{ord}(1)$ as $E \to \infty$. Although our model is valid for a range of Lewis numbers, we take $\mathrm{Le}_{\mathcal{F}} = \mathrm{Le}_{\mathcal{R}} = 1$ for all of our numerical simulations.

In Chapters 3 and 4, we find asymptotic approximations to (2.14), (2.22)–(2.25) as $E \to \infty$ in the distinguished limit (2.40)–(2.42). First though, we review the relevant literature on modelling flames and ignition in 1D.

## 2.2 Literature review

There is a vast body of mathematical literature on combustion. The majority of the mathematical literature specifically on autoignition is based on CFD simulations, including those studies described in Section 1.3. Analytical studies have, for the most part, concentrated on particular aspects of combustion where simplifications can be made. This is not to say that the theoretical literature on combustion has no relevance to autoignition. On the contrary, by rewriting the models presented in Section 2.1.3 in equivalent parameter regimes to those studied already in the literature, we introduce important concepts that are crucial to understanding the behaviour of flames in confinement and autoignition. In Section 2.2.1, we discuss the Chapman–Jouguet theory of combustion waves, before showing how the mass flux through a slow, thin flame can be determined using asymptotic analysis in the limit of large activation energy in Section 2.2.2. We then review the theory of ignition in Sections 2.2.3 and 2.2.4, starting with the simple case of homogeneous ignition from uniform initial conditions. Finally, in Section 2.2.5, we discuss analytical approaches that have been taken to study combustion in confinement and autoignition specifically.

### 2.2.1 The Chapman–Jouguet conditions

For the physical problems of interest, the Péclet number, $\mathrm{Pe} = 1/\epsilon$, is typically large, so away from the flame we are justified in assuming that the transport processes—viscosity, heat diffusion and species diffusion—are negligible. The simplest approach to modelling a flame is to treat it as a discontinuity, at $x = x^*(t)$, in an inviscid gas, similar to a shock, across which heat is released. In the combustion literature, the limit $\epsilon \to 0$ is often called the *hydrodynamic limit* [23, §2.2]. In the limit $\epsilon \to 0$, the governing equations (2.14) and (2.16) may be written in conservation form as

$$\frac{\partial \rho}{\partial t} + \frac{\partial (\rho u)}{\partial x} = 0, \tag{2.43a}$$

$$\frac{\partial (\rho u)}{\partial t} + \frac{\partial}{\partial x}\left( \rho u^2 + \frac{1}{\gamma M^2} p \right) = 0, \tag{2.43b}$$

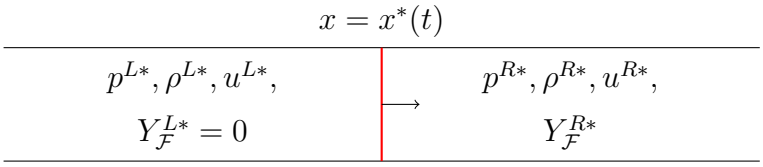


**Figure 2.1:** *Schematic of a deflagration or detonation in 1D.*

$$\frac{\partial}{\partial t}\left(\frac{p}{\gamma} + (\gamma-1)M^2\left(\frac{\rho u^2}{2}\right) + Q\rho Y_{\mathcal{F}}\right) + \frac{\partial}{\partial x}\left(pu + (\gamma-1)M^2\left(\frac{\rho u^3}{2}\right) + Q\rho u Y_{\mathcal{F}}\right) = 0. \quad (2.43c)$$

We have used the equation of state (2.14d) to eliminate $T$, and combined (2.14c) and (2.16) to write (2.43c) in conservation form[3]. We have therefore lost information about the reaction rate. Nevertheless, by considering the possible weak solutions to (2.43) allowing for discontinuities, we gain important insights into the behaviour of combustion waves.

We use the superscript $R*$ to denote the conditions in the gas immediately to the right of the discontinuity, and $L*$ to denote the conditions in the gas immediately to the left of the discontinuity, as illustrated in Figure 2.1. We assume the wave is travelling from left to right, and that in the gas behind the wave (that is, to the left of $x = x^*$), the fuel has been completely burned, so $Y_{\mathcal{F}}^{L*} = 0$.

For a hyperbolic system of partial differential equations written in conservation form, such as (2.43), *Rankine–Hugoniot conditions* can be identified which must hold across any discontinuities in weak solutions [72, §2.5]. For (2.43), the Rankine–Hugoniot conditions that apply at $x = x^*(t)$ are

$$\rho^{R*}(u^{R*} - \mathrm{d}x^*/\mathrm{d}t) = \rho^{L*}(u^{L*} - \mathrm{d}x^*/\mathrm{d}t), \quad (2.44a)$$

$$p^{R*} + \gamma M^2 \rho^{R*}(u^{R*} - \mathrm{d}x^*/\mathrm{d}t)^2 = p^{L*} + \gamma M^2 \rho^{L*}(u^{L*} - \mathrm{d}x^*/\mathrm{d}t)^2, \quad (2.44b)$$

$$\frac{p^{R*}}{\rho^{R*}} + (\gamma-1)M^2\frac{(u^{R*} - \mathrm{d}x^*/\mathrm{d}t)^2}{2} + QY_{\mathcal{F}}^{R*} = \frac{p^{L*}}{\rho^{L*}} + (\gamma-1)M^2\frac{(u^{L*} - \mathrm{d}x^*/\mathrm{d}t)^2}{2}. \quad (2.44c)$$

In the combustion literature, the Rankine–Hugoniot conditions (2.44) are known as the *Chapman–Jouguet conditions*. The presence of the typical Mach number, $M$, in (2.44) is a result of our nondimensionalisation, and could be removed by rescaling $u$ and $t$.

For future reference, it is helpful at this point to also write the Chapman–Jouguet conditions in terms of the Lagrangian spatial coordinate (2.26). In the Lagrangian coordinate, the position of the flame is given by

$$\chi^* = \int_0^{x^*} \rho(s,t)\,\mathrm{d}s. \quad (2.45)$$

[3]Although we have used the species conservation equation (2.16) for the one-step reaction (2.1) to formally express conservation of energy as (2.43c), we could equally have used a different reaction scheme. In the subsequent analysis, $QY_{\mathcal{F}}^{R*}$ should be interpreted as the energy released per unit mass passing through the discontinuity.

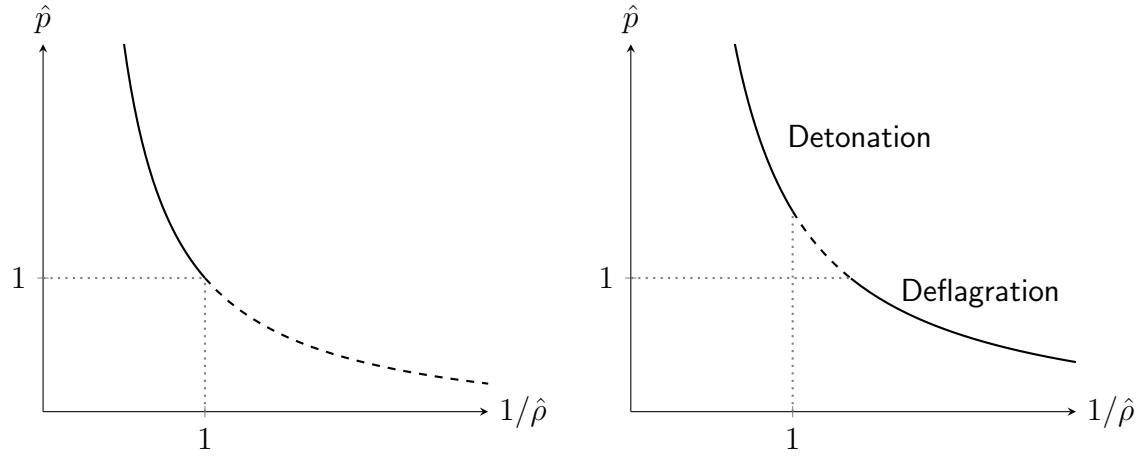


**(a)** *No energy release,* $QY_{\mathcal{F}}^{R*} = 0$.

**(b)** *Constant energy release,* $QY_{\mathcal{F}}^{R*} > 0$.

**Figure 2.2:** *The Chapman–Jouguet curve.*

Using Leibniz's integral rule and the conservation of mass (2.43a), we recognise that the $t$-derivative of $\chi^*$ is the mass flux though the flame, which, for convenience, we denote by $q$,

$$q := \frac{\mathrm{d}\chi^*}{\mathrm{d}t} = -\rho^{L*}(u^{L*} - \mathrm{d}x^*/\mathrm{d}t). \tag{2.46}$$

Substituting (2.27), (2.45) and (2.46) into (2.44) and rearranging, we find that, across $\chi = \chi^*(t)$,

$$[u + qV]_-^+ = 0, \tag{2.47a}$$

$$\left[p + \gamma M^2 V q^2\right]_-^+ = 0, \tag{2.47b}$$

$$\left[pV + \frac{\gamma - 1}{2} M^2 V^2 q^2 + QY_{\mathcal{F}}\right]_-^+ = 0, \tag{2.47c}$$

where here we use $[\psi]_-^+ = \lim_{\chi \searrow \chi^*} \psi(\chi, t) - \lim_{\chi \nearrow \chi^*} \psi(\chi, t)$ to indicate the jump in $\psi$ across $\chi = \chi^*$.

We now explore the possible behaviour of solutions to (2.44), and equivalently (2.47). Firstly, by eliminating $(u^{R*} - \mathrm{d}x^*/\mathrm{d}t)$ and $(u^{L*} - \mathrm{d}x^*/\mathrm{d}t)$ from (2.44), we find the pressure ratio, $\hat{p} = p^{L*}/p^{R*}$, and the density ratio, $\hat{\rho} = \rho^{L*}/\rho^{R*}$, satisfy

$$\hat{p} = \frac{(\gamma + 1) - (\gamma - 1)/\hat{\rho} + 2\gamma Q \rho^{R*} Y_{\mathcal{F}}^{R*}/p^{R*}}{(\gamma + 1)/\hat{\rho} - (\gamma - 1)}. \tag{2.48}$$

The hyperbola defined by (2.48) is known as the Chapman–Jouguet curve [71, §6.2.4] or the Hugoniot curve [25, §86], and is plotted in Figure 2.2, for the special case $QY_{\mathcal{F}}^{R*} = 0$ (no reaction) and the more general case $QY_{\mathcal{F}}^{R*} > 0$, along with the lines $\hat{p} = 1$ and $\hat{\rho} = 1$.

If $QY_{\mathcal{F}}^{R*} = 0$, then there is no energy release across the discontinuity, and the Chapman–Jouguet conditions (2.44) are simply the Rankine–Hugoniot conditions for a gas-dynamical shock [71, §6.1.2]. In this case, we are able to discount solutions based

on the additional physical consideration that entropy must increase across the shock. Imposing that entropy increases across the shock implies that the pressure ratio, $\hat{p}$, must be greater than one. Therefore, solutions to the Rankine–Hugoniot conditions lying on the dashed part of the Chapman–Jouguet curve in Figure 2.2a are unphysical and can be discounted [71, §6.2.4].

By contrast, when $QY_{\mathcal{F}}^{R*} > 0$ we can no longer discount solutions due to this entropy condition [71, §6.2.4]. By eliminating $(u^{L*} - \mathrm{d}x^*/\mathrm{d}t)$ from (2.44a) and (2.44b), we see that $\hat{p}$ and $1/\hat{\rho}$ satisfy

$$\hat{p} - 1 = \frac{\gamma M^2 \rho^{R*}(u^{R*} - \mathrm{d}x^*/\mathrm{d}t)^2}{p^{R*}} \left(1 - \frac{1}{\hat{\rho}}\right). \tag{2.49}$$

The equation (2.49) describes what is known as the Rayleigh line [40, §5.3]. From (2.49), it is clear to see that solutions to (2.44) with both $\hat{p} > 1$ and $\hat{\rho} < 1$ are impossible, as this would require $(u^{R*} - \mathrm{d}x^*/\mathrm{d}t)^2$ to be negative. This excludes solutions lying on the dashed part of the Chapman–Jouguet curve in Figure 2.2b, leaving two branches of the Chapman–Jouguet curve where physical solutions may lie. On each branch, the discontinuity exhibits different behaviour:

- Solutions on the upper branch ($\hat{\rho} > 1$) are known as *detonations*. Detonations are defined as supersonic waves sustained by chemical reaction [40, §5.1].
- Solutions on the lower branch ($\hat{p} < 1$) are known as *deflagrations*. Deflagrations are defined as subsonic waves sustained by chemical reaction [40, §5.1]. The terms flame and deflagration can be used interchangeably.

The Mach number, $M^R$, of the discontinuity relative to the unburnt gas to the right of it is given by

$$M^R = \sqrt{\frac{M^2 \rho^{R*}(u^{R*} - \mathrm{d}x^*/\mathrm{d}t)^2}{p^{R*}}}. \tag{2.50}$$

Using (2.48) and (2.49), we find

$$\gamma (M^R)^2 = \frac{\hat{p} - 1}{1 - 1/\hat{\rho}} = \frac{2\gamma(1 - 1/\hat{\rho}) + 2\gamma Q \rho^{R*} Y_{\mathcal{F}}^{R*}/p^{R*}}{(1 - 1/\hat{\rho})((\gamma + 1)/\hat{\rho} - (\gamma - 1))}. \tag{2.51}$$

From this expression, we conclude that $M^R > 1$ when $\hat{\rho} > 1$, and $M^R < 1$ when $\hat{p} < 1$, demonstrating that detonations are supersonic and deflagrations are subsonic as claimed.

Assuming we know the value of $QY_{\mathcal{F}}^{R*}$, we require four pieces of information in addition to the three Chapman–Jouguet conditions (2.44) to solve for the seven unknown variables: $\rho^{R*}$, $\rho^{L*}$, $u^{R*}$, $u^{L*}$, $p^{R*}$, $p^{L*}$ and $\mathrm{d}x^*/\mathrm{d}t$. For example, for a conventional gas-dynamical shock ($QY_{\mathcal{F}}^{R*} = 0$) caused by a piston being pushed into a column of gas, we know the conditions ahead of the shock, $p^{R*}, \rho^{R*}, u^{R*}$, and the speed of the gas adjacent to the piston, $u^{L*}$, allowing us to solve (2.44) for $\mathrm{d}x^*/\mathrm{d}t$, $p^{L*}$, and $\rho^{L*}$. However, in the combustion problems we are interested in, deflagrations and detonations are self-sustained by the release of chemical energy. Effectively, we only have three pieces of information about the flow either side of the combustion wave. Hence, an extra piece of information is

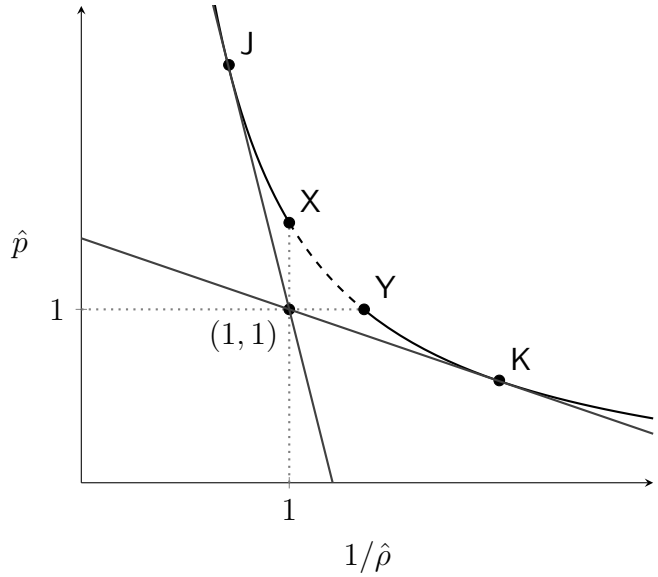


**Figure 2.3:** *The tangents of the Chapman–Jouguet curve through* $(1,1)$ *define the upper and lower Chapman–Jouguet points,* J *and* K*.*

needed to determine a unique solution to (2.44). In general, this extra piece of information comes from analysing the interior structure of the wave [40, §5.3].

Before discussing this additional piece of information, and without considering the specific chemical reaction mechanism, we can further narrow down the range of physically possible solutions by considering how the Mach number of the gas changes through the wave. In Figure 2.3, we plot the tangents to the Chapman–Jouguet curve that pass through $(\hat{p},\hat{\rho}) = (1,1)$. The two tangent points, J and K, are known as the upper and lower Chapman–Jouguet points, respectively. The solutions to (2.44) corresponding to these points are where the combustion wave is sonic relative to the burnt gas [25, §87]. That is, the Mach number,

$$M^L = \sqrt{\frac{M^2\rho^{L*}(u^{L*} - \mathrm{d}x^*/\mathrm{d}t)^2}{p^{L*}}}\,, \tag{2.52}$$

of the wave relative to the burnt gas is one. The Chapman–Jouguet points can be used to further distinguish between possible solutions to (2.44):

- Solutions lying to the left of point J on Figure 2.3 are called *strong detonations*, and have $M^L < 1$;
- Solutions lying between points J and X are *weak detonations*, with $M^L > 1$;
- Solutions lying between points Y and K are *weak deflagrations*, with $M^L < 1$; and
- Solutions lying to the right of point K are *strong deflagrations*, with $M^L > 1$.

We now briefly summarise why strong deflagrations are unphysical. In the combustion literature, frictionless steady flow with heat addition is known as Rayleigh flow, and is

an important consideration when designing jet engines [34, §8]. It is a result of Rayleigh flow theory that it is impossible to accelerate a subsonic gas in a duct with slip walls and a constant cross-section to a speed faster than the speed of sound using heat addition alone [40, §5.3]. We deduce, therefore, that strong deflagrations with $M^R < 1$ and $M^L > 1$ are impossible in 1D, and only weak deflagrations, lying between points Y and K in Figure 2.3, are physical. Indeed, often deflagrations are much slower than the speed of sound [40, §4.1], and lie close to the point Y on the Chapman–Jouguet curve in Figure 2.3.

Interestingly, most detonations observed in experiments correspond to the upper Chapman–Jouguet point, J. These detonations are known as *Chapman–Jouguet detonations*, and their speed relative to the gas ahead of them is known as the *Chapman–Jouguet speed*. It is possible to have strong detonations that are faster than the Chapman–Jouguet speed which are the result of continued compression by a piston [25, §90]. Such a detonation is called an overdriven detonation. However, self-sustained strong detonations are unstable, since any rarefaction waves produced in the burnt gas behind the detonation would catch up with the detonation (since strong detonations are subsonic relative to the gas behind them). Any rarefaction wave would reduce the pressure jump and cause the detonation to approach the Chapman–Jouguet speed [40, §5.3]. The entropy of burnt gas is minimised amongst detonations by the Chapman–Jouguet detonation, which is also the slowest of all possible detonations [25, §87].

We can also dismiss weak detonations *with a certain structure* as unphysical. The prototypical model for the structure of a detonation in one-dimensional space consists of a leading shock that preconditions the gas before it passes through a reaction zone [93, §6.1.5]. This model is known as the ZND model, after Zel'dovich, von Neumann and Döring who independently proposed it [32, 70, 96]. As the gas passes through the shock, the speed of the gas relative to the shock changes from supersonic to subsonic. For a weak detonation with the ZND structure to exist, the reaction zone would need to be a strong deflagration to bring the gas back to a supersonic speed. As we have already discussed, strong deflagrations are impossible in 1D, and, thus, so are weak detonations *with the ZND structure* [25, §94].

The autoignition front observed in the numerical simulations by Yu and Chen [95] travels through the end-gas faster than the Chapman–Jouguet speed. Furthermore, Yu and Chen [95] show that the density of each fluid particle changes very little during autoignition. We now recognise that the autoignition front observed in the numerical simulations by Yu and Chen [95], presented in Figure 1.7a, is a weak detonation. The weak detonation formed during autoignition does not have the ZND structure, so the observation of a weak detonation is not inconsistent with the previous paragraph.

Combustion in reality is inherently three-dimensional; deflagrations and detonations are seldom planar [13]. By considering the conservation of mass, momentum and energy in 3D, one can identify the Chapman–Jouguet conditions that apply across thin flames in 3D. It has been shown that planar hydrodynamic flames are unstable to small transverse perturbations of all wave lengths [23, §2.2]. Furthermore, the ZND model is known to be unstable in 3D [93, §6.1.5]. Understanding the behaviour of combustion waves in 1D is an important first step towards understanding the behaviour of deflagrations and detonations more generally in 3D [23, §2.1.3]. Therefore, we focus exclusively on combustion in confinement in 1D, and will not discuss the 3D structure of deflagrations

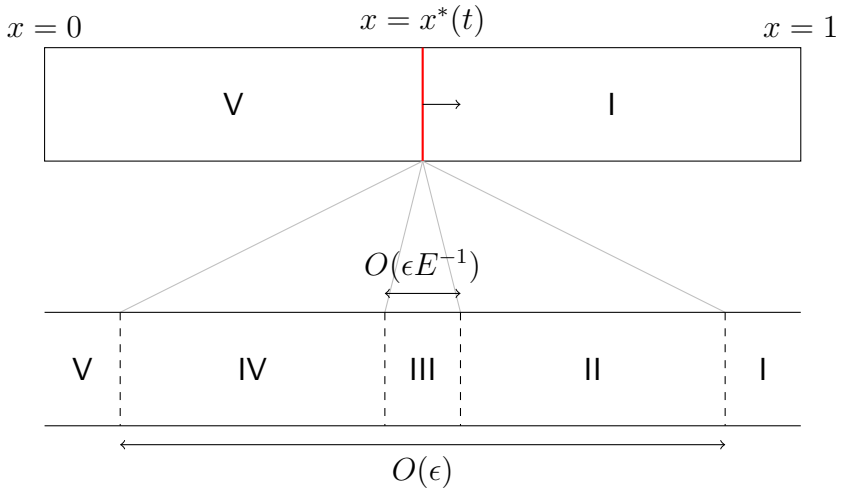


**Figure 2.4:** *Schematic of the structure of a flame in a channel with closed ends. On the length-scale of the channel, the flame appears as a free boundary between two regions of inviscid gas (I and V). The internal structure of the flame (II–IV) is resolved to find the jump conditions across the flame.*

or detonations in any further detail.

### 2.2.2 Flame structure

We now return to the question of the missing piece of information needed to solve the Chapman–Jouguet conditions (2.44). We find the mass flux through the flame by solving for the flame structure on the length-scale where the transport phenomena that we neglected in writing (2.43) are important. Specifically, we define the flame position, $x = x^*(t)$, to be the point where the rate of heat release is maximal, and seek approximate solutions to $\{$(2.14), (2.16) and (2.17)$\}$ and $\{$(2.14), (2.22) and (2.23)$\}$ for $x - x^*(t) = O(\epsilon)$ as $\epsilon \to 0$.

For a steady premixed, anchored flame—such as a Bunsen burner flame—where the fuel and oxidiser mixture is supplied at some finite point, the problem of finding the structure of the flame is a well-posed one [20]. However, when deriving simplified models for the structure of a freely-propagating premixed flame, we need to carefully avoid what is known as the *cold-boundary difficulty*.

By taking the limit $\epsilon \to 0$, we assume the width of the flame is much shorter than the length of the channel. It is tempting, therefore, to assume the flame is steady and seek a travelling wave solution for the structure of the flame, approximating channel as infinitely long. Unfortunately, such a travelling wave solution does not exist. The issue stems from supplying the reactant at infinity. In the reference frame of the flame, the reactant has to travel infinitely far to get to the flame without being completely used up [93, §5.3.2]. As the reaction rate at infinity is non-zero, this is simply not possible.

The approach we take here to avoid the cold-boundary difficulty is to use perturbation methods to identify a well-posed problem for the quasi-steady flame structure, and properly

match this into a time-dependent outer problem. In addition to the hydrodynamic limit, $\epsilon \to 0$, we take the distinguished limits summarised in Table 2.2, with small Mach number, $M \to 0$, and large activation energy, $E \to \infty$. In the literature, freely-propagating flames are described as steady if, *over the time-scale of interest*, the changes in the conditions in the outer region ahead of the flame are small enough to not affect the mass flux through the flame to the order of approximation of interest.

For both the one-step reaction (2.1) and three-step reaction (2.6), the leading-order flame structure in the distinguished limit of interest is available in the literature. In both cases, the flame has a three-layer structure, as illustrated in Figure 2.4, with a thin central boundary layer where the fuel is completely burned.

#### 2.2.2.1 One-step reaction

The problem of finding the structure of a slow, premixed flame with one-step Arrhenius chemistry is well-studied in the literature [e.g. 16, §2]. Here we find the leading-order flame structure and the leading-order mass flux through the flame in the distinguished limit (2.39), with $\epsilon = O(E^{-1})$ and $M = O(E^{-1})$ as $E \to \infty$.

The first step in the analysis of the flame structure is changing coordinates to a frame moving with the flame, $x - x^*(t) = \epsilon\xi$, where $\xi = O(1)$. By rescaling the spatial coordinate in this way, we effectively zoom in on the region—labelled II–IV in Figure 2.4—in which the transport terms we ignored in writing (2.43) are important. In terms of rescaled spatial coordinate, $\xi$, the governing equations (2.14) and (2.16) become

$$\epsilon\frac{\partial\rho}{\partial t} + \frac{\partial}{\partial\xi}\left(\rho\left(u - \frac{\mathrm{d}x^*}{\mathrm{d}t}\right)\right) = 0, \tag{2.53a}$$

$$\epsilon\frac{\partial}{\partial t}(\rho u) + \frac{\partial}{\partial\xi}\left(\rho u\left(u - \frac{\mathrm{d}x^*}{\mathrm{d}t}\right) + \frac{1}{\gamma M^2}p - \mathrm{Pr}\frac{\partial u}{\partial\xi}\right) = 0, \tag{2.53b}$$

$$\begin{aligned}\frac{\epsilon}{\gamma}\frac{\partial(\rho T)}{\partial t} + \epsilon(\gamma-1)M^2\frac{\partial}{\partial t}\left(\frac{\rho u^2}{2}\right) + \frac{\partial}{\partial\xi}\left(\rho\left(u - \frac{1}{\gamma}\frac{\mathrm{d}x^*}{\mathrm{d}t}\right)T\right)\\ + (\gamma-1)M^2\frac{\partial}{\partial\xi}\left(\frac{\rho u^2}{2}\left(u - \frac{\mathrm{d}x^*}{\mathrm{d}t}\right)\right) - \frac{\partial^2 T}{\partial\xi^2} - \mathrm{Pr}(\gamma-1)M^2\frac{\partial}{\partial\xi}\left(u\frac{\partial u}{\partial\xi}\right) = Qr,\end{aligned} \tag{2.53c}$$

$$p = \rho T, \tag{2.53d}$$

$$\epsilon\frac{\partial(\rho Y_{\mathcal{F}})}{\partial t} + \frac{\partial}{\partial\xi}\left(\rho\left(u - \frac{\mathrm{d}x^*}{\mathrm{d}t}\right)Y_{\mathcal{F}} - \frac{1}{\mathrm{Le}_{\mathcal{F}}}\frac{\partial Y_{\mathcal{F}}}{\partial\xi}\right) = -r, \tag{2.53e}$$

where $r$ is given by (2.17). We seek a bounded approximate solution to (2.53) for $\xi = O(1)$, which matches with the outer solution ahead of the flame—in the region labelled I in Figure 2.4—as $\xi \to \infty$. The appropriate matching conditions are

$$p \to p^{R*}(t), \quad T \to T^{R*}(t), \quad u \to u^{R*}(t), \quad Y_{\mathcal{F}} \to Y_{\mathcal{F}}^{R*}(t), \tag{2.54}$$

as $\xi \to \infty$, where, as in Section 2.2.1, we use the superscript $R*$ to denote the limiting value of the outer solution as $x \searrow x^*(t)$.

We pose that the solution to (2.53) takes the form of asymptotic series, for example $T \sim T_0 + E^{-1}T_1 + \cdots$, where $T_0, T_1 = O(1)$ as $E \to \infty$. In this section, for ease of notation, we drop the subscript on the leading-order approximation to the solution where doing so is not ambiguous. Statements such as '$Y_{\mathcal{F}} = 0$ to leading order', should therefore be taken to mean '$Y_{\mathcal{F}} = o(1)$ as $E \to \infty$'.

The partial $t$-derivatives in (2.53) are all premultiplied by $\epsilon$. We assume the leading-order flame structure is quasi-steady in the limit $\epsilon \to 0$, meaning that for $\xi = O(1)$ the solution to (2.53) only depends on time through the boundary conditions (2.54). Note, however, that if (2.54) vary too rapidly, because, for example, the outer solution in regions I and V exhibits disturbances with an $O(\epsilon)$ characteristic wave length, then the structure of the flame will change dynamically and the Chapman–Jouguet conditions will not accurately describe the relationship between the values of the dependant variables on either side of the flame [3, 68].

Taking the hydrodynamic and small Mach number limit, $\epsilon \to 0$ and $M \to 0$, and integrating (2.53a) and (2.53b), we find that the mass flux and pressure are spatially uniform to leading order, so

$$\rho\left(u - \frac{\mathrm{d}x^*}{\mathrm{d}t}\right) = -q(t), \quad p = p(t), \tag{2.55}$$

where the leading-order mass flux, $q(t)$, is to be found as part of the solution. Furthermore, combining (2.53c) and (2.53e) and taking the limit $M \to 0$ and $\epsilon \to 0$, we find upon integrating that the leading-order temperature and mass fraction satisfy

$$q(T + QY_{\mathcal{F}}) + \frac{\partial T}{\partial \xi} + \frac{Q}{\mathrm{Le}_{\mathcal{F}}}\frac{\partial Y_{\mathcal{F}}}{\partial \xi} = q(T^{R*}(t) + QY_{\mathcal{F}}^{R*}(t)). \tag{2.56}$$

The $qT$ term in (2.56) is justified from (2.53c) by noting that $\rho T\,\mathrm{d}x^*/\mathrm{d}t$ is independent of $\xi$ to leading order.

Consistent with the assumption that the temperature remains finite within the flame, the reaction must approach equilibrium as $\xi \to -\infty$, meaning $Y_{\mathcal{F}} \to 0$. We deduce from (2.56) that

$$\lim_{\xi \to -\infty} T(\xi, t) = T^{R*}(t) + QY_{\mathcal{F}}^{R*}(t) = T^{L*}(t) = \lim_{x \nearrow x^*(t)} T(x, t). \tag{2.57}$$

Note that (2.55) and (2.57) are consistent with the Chapman–Jouguet conditions (2.44) in the limit $M \to 0$, as expected.

To find an expression for the leading-order mass flux, $q(t)$, we need to solve for the leading-order temperature within the flame. Taking the limits $M \to 0$ and $\epsilon \to 0$ in (2.53c) and (2.53e), we deduce that the temperature profile is quasi-steady and that viscous dissipation has a negligible effect within the flame. Naïvely, before taking the limit $E \to \infty$, we might write down the problem of finding the structure inside the flame as

$$-q\frac{\partial T}{\partial \xi} - \frac{\partial^2 T}{\partial \xi^2} = QZY_{\mathcal{F}} \exp\left(-\frac{E}{T}\right), \tag{2.58a}$$

$$-q\frac{\partial Y_{\mathcal{F}}}{\partial \xi} - \frac{1}{\mathrm{Le}_{\mathcal{F}}}\frac{\partial^2 Y_{\mathcal{F}}}{\partial \xi^2} = -ZY_{\mathcal{F}} \exp\left(-\frac{E}{T}\right), \tag{2.58b}$$

subject to

$$\lim_{\xi\to\infty} T(\xi,t) = T^{R*}(t), \quad \lim_{\xi\to\infty} Y_{\mathcal{F}}(\xi,t) = Y_{\mathcal{F}}^{R*}(t), \quad |T| < \infty, \quad |Y_{\mathcal{F}}| < \infty, \tag{2.59}$$

where $q$ is the, as yet unknown, mass flux (2.55). However, the left-hand sides of both equations (2.58) tend to zero as $\xi \to \infty$, but the Arrhenius source terms on the right do not, meaning there is no solution to (2.58) and (2.59). We resolve this manifestation of the cold-boundary difficulty by taking the limit $E \to \infty$.

We assume, as in [15, §2.4], that in the limit $E \to \infty$ the reaction rate is only significant in a thin layer, region III, where the dominant balance is between reaction and diffusion, and the temperature is close to the highest temperature in the flame. Elsewhere, the reaction rate is exponentially small[4] as $E \to \infty$, so the dominant balance in regions II and IV is between advection and diffusion. Since the rate of reaction is negligible in region II, the solutions to the leading-order governing equations in region II are able to satisfy the boundary conditions (2.59) as $\xi \to \infty$, and hence match with the unsteady leading-order solution in region I.

**2.2.2.1.1 Region II — Preheat region** Since the activation energy is large, $E \gg 1$, we assume that the reaction only plays a role in a thin region (region III of Figure 2.4) where the gas is close to the maximum temperature, i.e. $T^{L*} - T = O(E^{-1})$. By comparison, in the cooler gas of region II, the reaction rate, $r$, is negligible and therefore the leading-order approximation to (2.53c) and (2.53e) as $M \to 0$, $\epsilon \to 0$ and $E \to \infty$ is

$$-q\frac{\partial T}{\partial \xi} - \frac{\partial^2 T}{\partial \xi^2} = 0, \tag{2.60a}$$

$$-q\frac{\partial Y_{\mathcal{F}}}{\partial \xi} - \frac{1}{\mathrm{Le}_{\mathcal{F}}}\frac{\partial^2 Y_{\mathcal{F}}}{\partial \xi^2} = 0. \tag{2.60b}$$

The model (2.60) represents a balance between advection and diffusion. Region II is often called the *preheat region* because the heat released in region III diffuses through region II, preheating the cold gas. The general solution to (2.60) is

$$T = a + b\exp(-q\xi), \quad Y_{\mathcal{F}} = c + d\exp(-q\mathrm{Le}_{\mathcal{F}}\xi), \tag{2.61}$$

where $a, b, c, d$ are functions of $t$ to be determined. It is clear that a non-spatially-uniform solution of the form (2.61) cannot remain finite as $\xi \to -\infty$, reinforcing the need for an interior layer where the reaction plays a significant role. We assume that this layer, region III, is located at $\xi = \xi_0$.

Matching the solution (2.61) in region II with the outer solution in region I comes through the boundary conditions

$$T \to T^{R*}(t), \quad Y_{\mathcal{F}} \to Y_{\mathcal{F}}^{R*}(t), \quad \text{as} \quad \xi \to \infty. \tag{2.62a}$$

[4] It is a consequence of the first-order reaction that the reaction rate is exponentially small in region IV behind the reaction zone. For higher orders of reaction, where the reaction rate is proportional to $Y_{\mathcal{F}}^n$ for $n > 1$, the mass fraction in region IV would be algebraically small in $E$.

Furthermore, the leading-order solution (2.61) must match with the leading-order solution in region III where $Y_{\mathcal{F}} = O(E^{-1})$ and $T - T^{L*} = O(E^{-1})$, meaning, in region II,

$$T \to T^{L*}(t), \quad Y_{\mathcal{F}} \to 0, \quad \text{as} \quad \xi \searrow \xi_0. \tag{2.62b}$$

We find that the solution in the preheat region, where $\xi - \xi_0 = \mathrm{ord}(1)$, is

$$T = T^{R*} + (T^{L*} - T^{R*}) \exp(-q(\xi - \xi_0)), \quad Y_{\mathcal{F}} = Y_{\mathcal{F}}^{R*}(1 - \exp(-q\mathrm{Le}_{\mathcal{F}}(\xi - \xi_0))). \tag{2.63}$$

**2.2.2.1.2 Region IV** The reaction also plays a negligible role in region IV, behind the reaction zone. However, rather than the reaction being *frozen* due to the temperature, as is the case in region II, the reaction is negligible in region IV because the mass fraction of the remaining fuel is exponentially small in $E$ as $E \to \infty$. For $\xi_0 - \xi = \mathrm{ord}(1)$, the leading-order temperature and mass fraction are governed by (2.60). Exponential growth is impossible as $\xi \to -\infty$ if the solution in region IV is to match with the outer solution in region V. Therefore, the only acceptable leading-order solution in region IV is

$$T = T^{L*}(t), \quad Y_{\mathcal{F}} = 0, \tag{2.64}$$

where $T^{L*}$ is given by (2.57).

**2.2.2.1.3 Region III — Reaction zone** With (2.63) and (2.64) we have found the leading-order structure of the flame. However, we are still to determine the leading-order mass flux, $q$, through the flame. We find $q$ by solving for the temperature in the reaction zone and matching it with (2.63) and (2.64).

We examine the reaction zone by rescaling the spatial variable $\xi - \xi_0 = E^{-1}\hat{\xi}$, and seeking a solution to (2.53) of the form $T \sim T^{L*} + E^{-1}\hat{T} + \cdots$, $Y_{\mathcal{F}} \sim E^{-1}\hat{Y} + \cdots$ in terms of $\hat{\xi} = O(1)$ as $E \to \infty$. We find that $\hat{T}$ and $\hat{Y}$ satisfy

$$\frac{\partial^2 \hat{T}}{\partial \hat{\xi}^2} = -\frac{QZ}{E^2}\hat{Y} \exp\left(-\frac{E}{T^{L*}} + \frac{\hat{T}}{(T^{L*})^2}\right), \tag{2.65a}$$

$$\frac{1}{\mathrm{Le}_{\mathcal{F}}}\frac{\partial^2 \hat{Y}}{\partial \hat{\xi}^2} = \frac{Z}{E^2}\hat{Y} \exp\left(-\frac{E}{T^{L*}} + \frac{\hat{T}}{(T^{L*})^2}\right), \tag{2.65b}$$

to leading order as $M \to 0$, $\epsilon \to 0$ and $E \to \infty$.

The corrections to (2.64) in region IV are exponentially small as $E \to \infty$. Therefore, to match the solution in region III with the solution in region IV, we require $\hat{T}, \hat{Y} \to 0$ as $\hat{\xi} \to -\infty$. Combining (2.65) and integrating, we deduce

$$\hat{T} + \frac{Q}{\mathrm{Le}_{\mathcal{F}}}\hat{Y} = 0. \tag{2.66}$$

We are therefore able to eliminate $\hat{Y}$ from (2.65) to find that $\hat{T}$ satisfies

$$\frac{\partial^2 \hat{T}}{\partial \hat{\xi}^2} = \frac{Z\mathrm{Le}_{\mathcal{F}}}{E^2}\hat{T} \exp\left(-\frac{E}{T^{L*}} + \frac{\hat{T}}{(T^{L*})^2}\right). \tag{2.67}$$

After multiplying (2.67) by $\partial\hat{T}\Big/\partial\hat{\xi}$, we may integrate once to find

$$\frac{1}{2}\left(\frac{\partial\hat{T}}{\partial\hat{\xi}}\right)^2 = \frac{Z\mathrm{Le}_{\mathcal{F}}}{E^2}\exp\left(-\frac{E}{T^{L*}}\right)\left(\int_0^{\hat{T}} s\exp\left(\frac{s}{(T^{L*})^2}\right)\mathrm{d}s\right), \tag{2.68}$$

where we have used the matching conditions as $\hat{\xi}\to-\infty$ to set the lower limit of the integral to zero.

We are now in a position to find $q$, by matching the temperature gradient as $\hat{\xi}\to\infty$ (or, equivalently, $\hat{T}\to-\infty$) with the temperature gradient in the preheat region, so that

$$-\sqrt{\frac{2Z\mathrm{Le}_{\mathcal{F}}(T^{L*})^4}{E^2}\exp\left(-\frac{E}{T^{L*}}\right)} = \lim_{\hat{T}\to-\infty}\frac{\partial\hat{T}}{\partial\hat{\xi}} = \lim_{\xi\searrow\xi_0}\frac{\partial T}{\partial\xi} = -q(T^{L*}-T^{R*}). \tag{2.69}$$

In Section 2.1.3, we chose the typical flame width, $\bar{L}^*$, such that the reaction coefficient, $Z$, is given by (2.18). With that choice of $\bar{L}^*$, we find

$$q = \sqrt{\frac{(T^{R*}+QY_{\mathcal{F}}^{R*})^4}{(Y_{\mathcal{F}}^{R*})^2(1+Q)^4}\exp\left(\frac{E}{1+Q}-\frac{E}{T^{R*}+QY_{\mathcal{F}}^{R*}}\right)}, \tag{2.70}$$

where we have used $T^{L*}=T^{R*}+QY_{\mathcal{F}}^{R*}$ to eliminate $T^{L*}$. Note that the scalings we have adopted imply that when $T^{R*}=1$ and $Y_{\mathcal{F}}^{R*}=1$, the leading-order mass flux through the flame is equal to 1.0.

We have found the leading-order mass flux, $q$, through the flame without resolving the translational invariance; that is, we have not determined $\xi_0$. If we wanted to find an approximation to $\xi_0$, we would find the $O(E^{-1})$ perturbation to the solution (2.63) in the preheat region. Then, by integrating (2.68) once more and matching with the solution in the preheat region, we could find $\xi_0$ so that the centre of the flame, $\xi=0$, corresponds to the point where the heat release rate is maximised.

The mass flux (2.70) through a flame with one-step chemistry is acutely sensitive to changes in the temperature, $T^{R*}$, ahead of the flame. Holding $Y_{\mathcal{F}}^{R*}$ constant, an $\mathrm{ord}(1)$ increase in $T^{R*}$ results in an exponentially large increase in $q$. As we will discuss in more detail in Section 4.1.2.1, our simplified models, based on the assumption the flame is slow, become invalid if the mass flux through the flame becomes too large. The one-step reaction is therefore unsuitable for modelling combustion in confinement because the temperature ahead of the flame increases by an $\mathrm{ord}(1)$ amount as the flame crosses from $x=0$ to $x=1$.

#### 2.2.2.2 Three-step reaction

Activation energy asymptotics can also be used to find an approximation to the mass flux through a thin, slow flame where the fuel is burning with the three-step reaction mechanism (2.6). In this section, we present the leading-order flame structure and mass flux for the three-step reaction—as determined by Dold [29]—for the distinguished limit summarised in Table 2.2, with $M\to0$ and $\epsilon\to0$ as $E\to\infty$. In addition, in Appendix A,

we extend the analysis in [29] to calculate the $O(E^{-1})$ correction to the mass flux through the flame, which, as we will discuss in more detail in Section 3.3.1, is necessary to give an asymptotically consistent description of normal combustion.

Dold [29] assumes that the branching cross-over temperature, $T_{\times 2}$, is within the temperature range of the flame. That is, if $T^{R*}$ is the temperature immediately ahead of the flame and $T^{L*}$ is the temperature immediately behind the flame, then $T_{\times 2} \in (T^{R*}, T^{L*})$. We choose to study the parameter regime (2.41a) so that the branching cross-over temperature is within the temperature range of the flame when $T^{R*} = 1$ and $T^{L*} = 1+Q$. Dold [29] finds that the flame has a three-layer structure with a thin central layer where the fuel is rapidly consumed by the branching reaction (2.6b), as illustrated in Figure 2.4. We call this boundary layer the *branching zone* because the dominant balance in this layer is between diffusion and the branching reaction (2.6b). Either side of the branching zone, the rate of the branching reaction is negligibly small and the behaviour of the gas is dominated by advection, diffusion, and the termination reaction.

Despite the similar three-layer flame structure for both the one-step (2.1) and three-step (2.6) reactions, there are two key differences in the flame structure to bear in mind. Firstly, for the three-step reaction, heat is released throughout the flame, including in regions II and IV, because the rate of the termination reaction (2.6c) is proportional to the mass fraction of radical. Secondly, the temperature in the branching zone is close to the cross-over temperature, $T_{\times 2}$, for the three-step reaction, rather than being close to the highest temperature within the flame as is the case for the one-step reaction.

The chemical model Dold [29] uses does not include the initiation reaction (2.6a). We include the initiation reaction in our model (2.6) because it plays an important role in increasing the amount of radical in the early stages of autoignition. However, we choose to study a parameter regime (2.41b) where the initiation reaction has a negligible effect on the flame structure and, hence, the mass flux through the flame. We assume that the initiation cross-over temperature, $T_{\times 1}$, is greater than the branching cross-over temperature, $T_{\times 2}$, with $T_{\times 1} - T_{\times 2} = \mathrm{ord}(1)$ as $E \to \infty$. In regions II and III, the rate of the initiation reaction is negligible because the Arrhenius factor, $\exp(E/T_{\times 1} - E/T)$, is exponentially small as $E \to \infty$. The initiation reaction also has a negligible effect on the leading-order temperature profile in region IV, even if the temperature approaches or exceeds $T_{\times 1}$, because the mass fraction of the fuel is exponentially small.

As with the one-step reaction, the first step in analysing the flame structure is changing variables to a coordinate frame moving with the flame. In terms of the rescaled spatial variable, $\xi = (x - x^*)/\epsilon$, the equations (2.14) and (2.22) governing the behaviour of the gas become

$$\epsilon \frac{\partial \rho}{\partial t} + \frac{\partial}{\partial \xi}\left(\rho\left(u - \frac{\mathrm{d}x^*}{\mathrm{d}t}\right)\right) = 0, \tag{2.71a}$$

$$\epsilon \frac{\partial}{\partial t}(\rho u) + \frac{\partial}{\partial \xi}\left(\rho u\left(u - \frac{\mathrm{d}x^*}{\mathrm{d}t}\right) + \frac{1}{\gamma M^2}p - \mathrm{Pr}\frac{\partial u}{\partial \xi}\right) = 0, \tag{2.71b}$$

$$\frac{\epsilon}{\gamma}\frac{\partial(\rho T)}{\partial t} + \epsilon(\gamma-1)M^2\frac{\partial}{\partial t}\left(\frac{\rho u^2}{2}\right) + \frac{\partial}{\partial \xi}\left(\rho\left(u - \frac{1}{\gamma}\frac{\mathrm{d}x^*}{\mathrm{d}t}\right)T\right) + (\gamma-1)M^2\frac{\partial}{\partial \xi}\left(\frac{\rho u^2}{2}\left(u - \frac{\mathrm{d}x^*}{\mathrm{d}t}\right)\right) - \frac{\partial^2 T}{\partial \xi^2} - \mathrm{Pr}(\gamma-1)M^2\frac{\partial}{\partial \xi}\left(u\frac{\partial u}{\partial \xi}\right) = Qr, \tag{2.71c}$$

$$p = \rho T, \tag{2.71d}$$

$$\epsilon\frac{\partial(\rho Y_{\mathcal{F}})}{\partial t} + \frac{\partial}{\partial \xi}\left(\rho\left(u - \frac{\mathrm{d}x^*}{\mathrm{d}t}\right)Y_{\mathcal{F}} - \frac{1}{\mathrm{Le}_{\mathcal{F}}}\frac{\partial Y_{\mathcal{F}}}{\partial \xi}\right) = -r_1 - r_2, \tag{2.71e}$$

$$\epsilon\frac{\partial(\rho Y_{\mathcal{R}})}{\partial t} + \frac{\partial}{\partial \xi}\left(\rho\left(u - \frac{\mathrm{d}x^*}{\mathrm{d}t}\right)Y_{\mathcal{R}} - \frac{1}{\mathrm{Le}_{\mathcal{R}}}\frac{\partial Y_{\mathcal{R}}}{\partial \xi}\right) = r_1 + r_2 - r_3, \tag{2.71f}$$

where $r$, $r_1$, $r_2$ and $r_3$ are given by (2.23). As before, we seek a bounded approximate solution to (2.71) for $\xi = O(1)$, which matches with the outer solution ahead of the flame as $\xi \to \infty$. The appropriate matching conditions[5] are

$$p \to p^{R*}(t), \quad T \to T^{R*}(t), \quad u \to u^{R*}(t), \quad Y_{\mathcal{F}} \to Y_{\mathcal{F}}^{R*}(t), \quad Y_{\mathcal{R}} \to 0, \tag{2.72}$$

as $\xi \to \infty$. As with the one-step reaction, we assume that the flame structure is quasi-steady in the limit $\epsilon \to 0$. Furthermore, it is straightforward to show that the Chapman–Jouguet conditions (2.44) follow from integrating the quasi-steady conservation equations (2.71), using the same argument as in Section 2.2.2.1.

We now present the leading-order governing equations for the temperature and mass fractions in each of the regions II–IV. By solving these equations subject to appropriate matching conditions, we find the leading-order approximation, $q^{(0)}$, to the mass flux,

$$q = -\rho\left(u - \frac{\mathrm{d}x^*}{\mathrm{d}t}\right) \sim q^{(0)}(t) + E^{-1}q^{(1)}(t) + \cdots. \tag{2.73}$$

**2.2.2.2.1 Regions II and IV** There is only a small range of temperatures, $T - T_{\times 2} = O(E^{-1})$, where the effect of the branching reaction (2.6b) is significant. For much of the flame temperature range, $(T^{R*}, T^{L*})$, the branching reaction plays a negligible role, either because $T_{\times 2} - T = \mathrm{ord}(1)$, and therefore the Arrhenius reaction rate (2.23b) is exponentially small as $E \to \infty$, or because the fuel has all but run out. The latter is the case when $T - T_{\times 2} = \mathrm{ord}(1)$, because the Arrhenius factor, $\exp(E/T_{\times 2} - E/T)$, is exponentially large as $E \to \infty$ and therefore the mass fraction of the fuel must be correspondingly small. For simplicity, we only consider the flame structure when $T_{\times 2} - T^{R*} = \mathrm{ord}(1)$.

We first consider regions II and IV of Figure 2.4, where the branching reaction plays a negligible role. In both of these regions, we seek a solution to (2.71) in the form of

[5] In Chapters 3 and 4, we find that the mass fraction, $Y_{\mathcal{R}}^L$, of the radical ahead of the flame is exponentially small as $E \to \infty$ during the stages of autoignition that we consider. The matching condition $Y_{\mathcal{R}} \to 0$ as $\xi \to \infty$ is therefore correct to the order of approximation necessary to determine the mass flux correct to $O(E^{-1})$.

Poincaré series,

$$p \sim p_0 + E^{-1}p_1 + \cdots, \tag{2.74a}$$
$$\rho \sim \rho_0 + E^{-1}\rho_1 + \cdots, \tag{2.74b}$$
$$u \sim u_0 + E^{-1}u_1 + \cdots, \tag{2.74c}$$
$$T \sim T_0 + E^{-1}T_1 + \cdots, \tag{2.74d}$$
$$Y_{\mathcal{F}} \sim Y_{\mathcal{F}0} + E^{-1}Y_{\mathcal{F}1} + \cdots, \tag{2.74e}$$
$$Y_{\mathcal{R}} \sim Y_{\mathcal{R}0} + E^{-1}Y_{\mathcal{R}1} + \cdots, \tag{2.74f}$$

as $E \to \infty$. Substituting (2.73) and (2.74) into (2.71) and comparing coefficients of $E^{-1}$, we deduce that, in the distinguished limit summarised in Table 2.2,

$$\frac{\partial p_0}{\partial \xi} = 0, \tag{2.75}$$

meaning $p_0 = p^{R*}(t)$. Furthermore, we find that $T_0$, $Y_{\mathcal{F}0}$ and $Y_{\mathcal{R}0}$ are governed by

$$-q^{(0)}\frac{\partial T_0}{\partial \xi} - \frac{\partial^2 T_0}{\partial \xi^2} = QY_{\mathcal{R}0}, \tag{2.76a}$$

$$-q^{(0)}\frac{\partial Y_{\mathcal{F}0}}{\partial \xi} - \frac{1}{\mathrm{Le}_{\mathcal{F}}}\frac{\partial^2 Y_{\mathcal{F}0}}{\partial \xi^2} = 0, \tag{2.76b}$$

$$-q^{(0)}\frac{\partial Y_{\mathcal{R}0}}{\partial \xi} - \frac{1}{\mathrm{Le}_{\mathcal{R}}}\frac{\partial^2 Y_{\mathcal{R}0}}{\partial \xi^2} = -Y_{\mathcal{R}0}. \tag{2.76c}$$

Note that the factor of $q^{(0)}$ in (2.76a) is justified from (2.71c) by noting that $x^*$ is independent of $\xi$, and $\partial(\rho_0 T_0)/\partial\xi = 0$ follows from (2.71d) and (2.75).

The general solution to (2.76) is

$$T_0 = C_1 + C_2\exp\bigl(-q^{(0)}\xi\bigr) - \frac{C_5 Q}{m_+^2 + q^{(0)}m_+}\exp(m_+\xi) - \frac{C_6 Q}{m_-^2 + q^{(0)}m_-}\exp(m_-\xi), \tag{2.77a}$$

$$Y_{\mathcal{F}0} = C_3 + C_4\exp\bigl(-\mathrm{Le}_{\mathcal{F}}q^{(0)}\xi\bigr), \tag{2.77b}$$

$$Y_{\mathcal{R}0} = C_5\exp(m_+\xi) + C_6\exp(m_-\xi), \tag{2.77c}$$

where $\{C_k \mid k \in \{1,\ldots,6\}\}$ are functions of time to be determined, and

$$m_\pm = \frac{-\mathrm{Le}_{\mathcal{R}}q^{(0)} \pm \sqrt{(\mathrm{Le}_{\mathcal{R}}q^{(0)})^2 + 4\mathrm{Le}_{\mathcal{R}}}}{2} \gtrless 0. \tag{2.78}$$

To arrive at the expression (2.77a) for $T_0$, we have assumed that $m_- \neq -q^{(0)}$. If equality were to hold, then $T_0$ would include a term proportional to $\xi\exp(m_-\xi)$, but the solution would still be a limit of solutions of the form (2.77a). We simply accept that limiting forms are included in special cases.

The appropriate boundary conditions to match (2.77) with the solution in region I are

$$\lim_{\xi\to\infty} T_0(\xi,t) = T^{R*}(t), \quad \lim_{\xi\to\infty} Y_{\mathcal{F}0}(\xi,t) = Y_{\mathcal{F}}^{R*}(t), \quad \lim_{\xi\to\infty} Y_{\mathcal{R}0}(\xi,t) = 0. \tag{2.79a}$$

Furthermore, for the solution in region IV to match with with region V, we must have

$$|T_0(\xi,t)|<\infty, \quad |Y_{\mathcal{F}0}(\xi,t)|<\infty, \quad |Y_{\mathcal{R}0}(\xi,t)|<\infty, \tag{2.79b}$$

as $\xi \to -\infty$. The remaining boundary conditions necessary to solve (2.76) in regions II and IV come from matching with the branching zone, a thin boundary layer where the branching reaction is significant. With (2.77) and (2.79), we have sufficient information from regions II and IV to find the leading-order approximation, $q^{(0)}$, to the mass flux once we have the matching conditions from analysing the branching zone. However, in Chapter 3, we additionally require an expression for $q^{(1)}$ to give an asymptotic description of combustion in confinement correct to $O(M)$ as $M \to 0$, with $EM = O(1)$ and $E^2M \gg 1$. To this end, in Appendix A, we extend the analysis in [29] to find $T_1$, $Y_{\mathcal{F}1}$ and $Y_{\mathcal{R}1}$ in regions II and IV.

**2.2.2.2.2 Region III — Branching zone** When the temperature, $T$, is close to the cross-over temperature, $T_{\times 2}$, the branching reaction can no longer be neglected. The branching zone is a thin boundary layer, labelled as region III in Figure 2.4, where the temperature satisfies $T - T_{\times 2} = O(E^{-1})$. We find $q^{(0)}$ by matching the asymptotic solution to (2.71) in the branching zone with (2.77) in regions II and IV.

We let $\xi = \xi_0(t)$ lie in the branching zone, and rescale the spatial variable so that

$$\xi - \xi_0 = E^{-1}\hat{\xi}, \quad \hat{\xi} = O(1). \tag{2.80}$$

The boundary layer position, $\xi_0$, is to be determined as part of the solution to ensure that $\xi = 0$ is the position of maximum heat release. We seek a solution to (2.71) of the form

$$T \sim T_{\times 2} + E^{-1}\hat{T}_1 + E^{-2}\hat{T}_2 + \cdots, \tag{2.81a}$$

$$Y_{\mathcal{F}} \sim E^{-1}\hat{Y}_{\mathcal{F}1} + E^{-2}\hat{Y}_{\mathcal{F}2} + \cdots, \tag{2.81b}$$

$$Y_{\mathcal{R}} \sim \hat{Y}_{\mathcal{R}0} + E^{-1}\hat{Y}_{\mathcal{R}1} + E^{-2}\hat{Y}_{\mathcal{R}2} + \cdots, \tag{2.81c}$$

as $E \to \infty$. We have introduced hats to the dependent variables to distinguish the solution in the branching zone from (2.74) in regions II and IV. Substituting (2.73), (2.80) and (2.81) into (2.71) and comparing coefficients of powers of $E^{-1}$, we find that $\hat{Y}_{\mathcal{R}0}$ is simply a function of time, and

$$\frac{\partial^2 \hat{T}_1}{\partial \hat{\xi}^2} = 0, \tag{2.82a}$$

$$-\frac{1}{\mathrm{Le}_{\mathcal{F}}}\frac{\partial^2 \hat{Y}_{\mathcal{F}1}}{\partial \hat{\xi}^2} = -\hat{Y}_{\mathcal{F}1}\hat{Y}_{\mathcal{R}0}\exp\left(\frac{\hat{T}_1}{T_{\times 2}^2}\right), \tag{2.82b}$$

$$-\frac{1}{\mathrm{Le}_{\mathcal{R}}}\frac{\partial^2 \hat{Y}_{\mathcal{R}1}}{\partial \hat{\xi}^2} = \hat{Y}_{\mathcal{F}1}\hat{Y}_{\mathcal{R}0}\exp\left(\frac{\hat{T}_1}{T_{\times 2}^2}\right). \tag{2.82c}$$

Integrating (2.82), we find

$$\hat{T}_1 = \hat{C}_1 + \hat{C}_2\hat{\xi}, \tag{2.83a}$$

$$\frac{1}{\mathrm{Le}_{\mathcal{F}}}\hat{Y}_{\mathcal{F}1}+\frac{1}{\mathrm{Le}_{\mathcal{R}}}\hat{Y}_{\mathcal{R}1}=\hat{C}_3+\hat{C}_4\hat{\xi}, \tag{2.83b}$$

where $\{\hat{C}_k \mid k \in \{1,\dots,4\}\}$ are functions of time to be determined. Through an appropriate choice of $\hat{Y}_{\mathcal{R}0}$, we can set $\hat{C}_3 = 0$ without loss of generality.

With (2.83), we have sufficient information from the branching zone to determine the leading-order approximation, $q^{(0)}$, to the mass flux, $q$. To find $q^{(0)}$, we match the three term inner expansions (2.81) with the two term outer expansions (2.74) using Van Dyke's matching rule [46, §5.1.5]; we rewrite (2.74) in terms of $\hat{\xi} = O(1)$ and expand in powers of $E^{-1}$. By comparing the form of the first two terms of the outer solutions, expressed in terms of the inner variable, with the form of the first two terms of the inner expansions (2.81), we find that the conditions we must apply at $\xi = \xi_0$ to solve for $q^{(0)}$, and $T_0$, $Y_{\mathcal{F}0}$ and $Y_{\mathcal{R}0}$ in regions II and IV are

$$\left[\frac{\partial T_0}{\partial \xi}\right]_-^+ = \left[\frac{1}{\mathrm{Le}_{\mathcal{R}}}\frac{\partial Y_{\mathcal{R}0}}{\partial \xi}+\frac{1}{\mathrm{Le}_{\mathcal{F}}}\frac{\partial Y_{\mathcal{F}0}}{\partial \xi}\right]_-^+ = [Y_{\mathcal{R}0}]_-^+ = Y_{\mathcal{F}0} = T_0 - T_{\times 2} = 0, \tag{2.84}$$

where here $[\psi]_-^+ = \lim_{\xi \searrow \xi_0}\psi(\xi,t) - \lim_{\xi \nearrow \xi_0}\psi(\xi,t)$. Using (2.79) and (2.84) with the general outer solution (2.77), we find that the leading-order solution in region II is

$$\begin{aligned} T_0 = T^{R*} &+ (T_{\times 2} - T^{R*})\exp\bigl(-q^{(0)}(\xi-\xi_0)\bigr) \\ &+ \frac{Q\mathrm{Le}_{\mathcal{R}}q^{(0)}Y_{\mathcal{F}}^{R*}}{(m_+-m_-)(m_-^2+m_-q^{(0)})}\bigl(\exp\bigl(-q^{(0)}(\xi-\xi_0)\bigr)-\exp(m_-(\xi-\xi_0))\bigr), \end{aligned} \tag{2.85a}$$

$$Y_{\mathcal{F}0} = Y_{\mathcal{F}}^{R*}\bigl(1-\exp\bigl(-\mathrm{Le}_{\mathcal{F}}q^{(0)}(\xi-\xi_0)\bigr)\bigr), \tag{2.85b}$$

$$Y_{\mathcal{R}0} = \frac{\mathrm{Le}_{\mathcal{R}}q^{(0)}Y_{\mathcal{F}}^{R*}}{m_+-m_-}\exp(m_-(\xi-\xi_0)). \tag{2.85c}$$

In region IV, the leading-order solution is given by

$$T_0 = T_{\times 2} + \frac{Q\mathrm{Le}_{\mathcal{R}}q^{(0)}Y_{\mathcal{F}}^{R*}}{(m_+-m_-)(m_+^2+m_+q^{(0)})}\bigl(1-\exp(m_+(\xi-\xi_0))\bigr), \tag{2.86a}$$

$$Y_{\mathcal{F}0} = 0, \tag{2.86b}$$

$$Y_{\mathcal{R}0} = \frac{\mathrm{Le}_{\mathcal{R}}q^{(0)}Y_{\mathcal{F}}^{R*}}{m_+-m_-}\exp(m_+(\xi-\xi_0)). \tag{2.86c}$$

From (2.85c) and (2.86c), we deduce that

$$\hat{Y}_{\mathcal{R}0} = \frac{\mathrm{Le}_{\mathcal{R}}q^{(0)}Y_{\mathcal{F}}^{R*}}{m_+-m_-}. \tag{2.87}$$

In deriving (2.85) and (2.86), we have yet to enforce one of the matching conditions (2.84), namely the continuity of temperature gradient, $[\partial T_0/\partial\xi]_-^+ = 0$ at $\xi = \xi_0$.

For the gradients of (2.85a) and (2.86a) to be equal at $\xi = \xi_0$, we find that the mass flux, $q^{(0)} > 0$, must satisfy

$$\frac{2Q\mathrm{Le}_{\mathcal{R}} Y_{\mathcal{F}}^{R*}}{T_{\times 2} - T^{R*}} \left( q^{(0)} + \sqrt{(\mathrm{Le}_{\mathcal{R}} q^{(0)})^2 + 4\mathrm{Le}_{\mathcal{R}}} \right) = \sqrt{(\mathrm{Le}_{\mathcal{R}} q^{(0)})^2 + 4\mathrm{Le}_{\mathcal{R}}} \left( 2\mathrm{Le}_{\mathcal{R}} + \mathrm{Le}_{\mathcal{R}} (q^{(0)})^2 + q^{(0)} \sqrt{(\mathrm{Le}_{\mathcal{R}} q^{(0)})^2 + 4\mathrm{Le}_{\mathcal{R}}} \right), \quad (2.88)$$

where recall that $T^{R*} + QY_{\mathcal{F}}^{R*} > T_{\times 2}$ by assumption. Using (2.88) we are able to simplify (2.86a),

$$T_0 = T^{R*} + QY_{\mathcal{F}}^{R*} + (T_{\times 2} - T^{R*} - QY_{\mathcal{F}}^{R*}) \exp(m_+(\xi - \xi_0)). \quad (2.89)$$

Taking the limit $\xi \to -\infty$ of (2.89), we observe that

$$\lim_{\xi \to -\infty} T_0 = T^{R*} + QY_{\mathcal{F}}^{R*}, \quad (2.90)$$

as expected from the leading-order approximation to the Chapman–Jouguet condition (2.44c) as $M \to 0$. In addition, we deduce from the matching that the gradient, $\hat{C}_2$, of the temperature perturbation, $\hat{T}_1$, in the branching zone satisfies

$$\hat{C}_2 = \lim_{\xi \searrow \xi_0} \frac{\partial T_0}{\partial \chi} = \lim_{\xi \nearrow \xi_0} \frac{\partial T_0}{\partial \chi} = \left( T_{\times 2} - T^{R*} - QY_{\mathcal{F}}^{R*} \right) m_+ < 0. \quad (2.91)$$

There is a unique solution to (2.88), as we would hope. We can see this by changing variables to $\beta$, where $\beta$ lies in $(0, 1)$ and is such that

$$q^{(0)} = \frac{4\beta}{\sqrt{\mathrm{Le}_{\mathcal{R}}}(1 - \beta^2)}. \quad (2.92)$$

Then $q^{(0)} \in (0, \infty)$ solves (2.88) if and only if $\beta$ solves

$$\frac{4}{(1-\beta)^2} = \frac{\mathrm{Le}_{\mathcal{R}} \left( QY_{\mathcal{F}}^{R*} - \left( T_{\times 2} - T^{R*} \right) \right)}{\left( T_{\times 2} - T^{R*} \right) \beta} + \frac{2QY_{\mathcal{F}}^{R*}}{\left( T_{\times 2} - T^{R*} \right) (1 + \beta^2)}. \quad (2.93)$$

As $\beta$ increases from 0 to 1, the left-hand side of (2.93) increases monotonically from 4 to $\infty$, while the right-hand side decreases monotonically from $\infty$ to $QY_{\mathcal{F}}^{R*}(\mathrm{Le}_{\mathcal{R}} + 1)/(T_{\times 2} - T^{R*}) - \mathrm{Le}_{\mathcal{R}} > 1$. Hence, we deduce that there is a unique solution to (2.93).

In his analysis, Dold [29] further shows that it is possible to find the profile of $\hat{Y}_{\mathcal{F}1}$ in terms of modified Bessel's functions. We outline his argument in Appendix A, and use well-known results on the asymptotic behaviour of solutions of modified Bessel's equation to find that $q^{(1)}$ is the solution to

$$\frac{1}{q^{(1)}} \left( \gamma_c - \frac{1}{2} \log \left( \frac{m_+^2 (m_+ - m_-)(T_{\times 2} - T^{R*} - QY_{\mathcal{F}}^{R*})^2}{\mathrm{Le}_{\mathcal{R}} \mathrm{Le}_{\mathcal{F}} q^{(0)} Y_{\mathcal{F}}^{R*} T_{\times 2}^4} \right) \right) = \frac{Q\mathrm{Le}_{\mathcal{R}} (1 - \mathrm{Le}_{\mathcal{R}}) q^{(0)} m_+^2 Y_{\mathcal{F}}^{R*}}{(m_+ - m_-)(\mathrm{Le}_{\mathcal{R}} q^{(0)} + 2m_+)(m_+^2 + q^{(0)} m_+)^2 T_{\times 2}^2} + \frac{T_{\times 2} - T^{R*} - QY_{\mathcal{F}}^{R*}}{2q^{(0)} T_{\times 2}^2} \left( 1 - \frac{(\mathrm{Le}_{\mathcal{R}} q^{(0)})^2}{(m_+ - m_-)^2} \right), \quad (2.94)$$

which is reprinted in Appendix A as (A.25). Note that, as with the one-step model, we did not need to find $\xi_0$ to find $q^{(0)}$ and $q^{(1)}$.

Note that the three-step reaction model for the mass flux does not suffer from the same acute sensitivity to the temperature, $T^{R*}$, ahead of the flame as the one-step reaction mass flux model, provided that $T^{R*}$ is not close to the crossover temperature, $T_{\times 2}$. If $T_{\times 2} - T^{R*} = \mathrm{ord}(1)$, then an $O(E^{-1})$ change in $T^{R*}$ leads to only an $O(E^{-1})$ change in $q$, rather than the $O(1)$ change we would see for the one-step reaction. This difference in behaviour can be explained by considering the temperature of region III for both reaction mechanisms. For the one-step reaction, the temperature of the reaction zone (region III) is close to the maximum temperature of the flame, $T^{L*} = T^{R*} + QY_{\mathcal{F}}^{R*}$. If the temperature ahead of the flame increases by an $O(E^{-1})$ amount, the reaction rate in the reaction zone increases by an $O(1)$ amount. By contrast, the temperature of the branching zone (region III for the three-step flame) is close to the fixed crossover temperature, $T_{\times 2}$, meaning the rate of reaction, and hence the mass flux through the flame, only changes by an $O(E^{-1})$ amount if the temperature ahead of the flame changes by an $O(E^{-1})$ amount.

As we will discuss in Section 4.1.2.2, care must be taken to determine whether the asymptotic approximations based on the limit $M \to 0$ remain valid as the temperature ahead of the flame increases. Both $q^{(0)}$ and $q^{(1)}$ become unbounded as $T^{R*} \to T_{\times 2}$. Our assumption that (2.73) is an asymptotic series holds if $T_{\times 2} - T^{R*} = \mathrm{ord}(1)$ and $T^{R*} + QY_{\mathcal{F}}^{R*} - T_{\times 2} = \mathrm{ord}(1)$.

#### 2.2.2.3 Summary

The Chapman–Jouguet conditions (2.44) describe the conservation of mass, momentum and energy across thin flames. However, in deriving the Chapman–Jouguet conditions in Section 2.2.1, we did not take into account the rate of reaction within the flame, and therefore were unable to solve for the flame speed without prescribing an additional piece of information—namely, the mass flux, $q$.

In Section 2.2.2, we have derived two models for the mass flux through a slow flame: one for the one-step reaction (2.1) and one for the three-step reaction (2.6). For both reaction mechanisms, we used asymptotic analysis in the limit of large activation energy, $E \to \infty$, small Mach number, $M \to 0$, and small reciprocal Péclet number, $\epsilon \to 0$, to identify the three-layer, interior structure of the flame and simplify the mathematical description of the behaviour of the gas in each layer. By solving for the temperature in each layer, and matching between neighbouring layers, we have derived an expression for the mass flux through the flame in terms of the temperature and mass fraction of fuel ahead of the flame. For the one-step reaction, the leading-order approximation to the mass flux is given explicitly by (2.70). For the three-step reaction, we sought an approximation to the mass flux in the form of an asymptotic series (2.73). We found the first two terms of this asymptotic series, with $q^{(0)}$ given by (2.88) and $q^{(1)}$ given by (2.94).

The two models for the mass flux presented here are by no means the only models we could use for $q$. For example, in Chapter 3, we will occasionally use $q = 1$ as a simple motivating example. Furthermore, activation energy asymptotics, and the similar concept of reaction rate asymptotics, can sometimes be used more generally to determine the structure of flames with more complex chemical reaction schemes. The analysis,

in principle, is similar to the analysis for the one- and three-step reaction mechanisms presented here; regions within the flame are identified where at most two elementary reactions in the reaction scheme are dominant. Solving simplified models for the behaviour of the gas in each of these regions and matching the solutions together gives the structure of the flame and the mass flux through the flame [13].

In Sections 2.2.2.1 and 2.2.2.2, we implicitly assumed that the flame was far from the walls at $x = 0$ and $x = 1$. Our analysis is not valid if $x^* = O(\epsilon)$ or $1 - x^* = O(\epsilon)$, because the boundary conditions at the wall change the interior structure of the flame. In order to accurately model the ignition of a flame from initial conditions such as (2.20) or (2.25), one would need to account for unsteady changes in the flame structure as the flame moves away from the wall [51, 77]. However, going forward, instead of modelling the nuances of flame ignition, we pragmatically choose to use the Chapman–Jouguet conditions (2.44), together with one of the mass flux models we have discussed, to describe the motion of the flame for all $x^* \in [0, 1]$.

## 2.2.3 Homogeneous ignition

Autoignition is a particular example of ignition; the fuel-oxidiser mixture ahead of the flame transitions from a weakly-reactive low-temperature state to a high-temperature state due to a rapid increase in reaction rate [51]. It is prudent, therefore, to study ignition models from the literature to understand the behaviour we should expect during autoignition. We start by studying homogeneous ignition before considering ignition with spatial variations.

### 2.2.3.1 One-step reaction

We start our discussion of ignition by discussing the simple case of homogeneous ignition due to the one-step reaction (2.1). That is, we solve (2.14), (2.16) and (2.17) subject to the spatially uniform initial conditions,

$$p(x, 0) = T(x, 0) = Y_{\mathcal{F}}(x, 0) = 1, \quad u(x, 0) = 0, \tag{2.95}$$

for all $x \in \mathbb{R}$. Homogeneous ignition would never be observed in reality; the slightest spatial variation, either in the initial conditions or from the boundary conditions, would induce gas motion [57], leading to inhomogeneous ignition as we shall discuss in Section 2.2.4. However, homogeneous ignition is an important problem to consider from a theoretical standpoint due to similarities with the case where the gas varies in space.

With no spatial variation in the initial conditions (2.95), the solution to (2.14), (2.16) and (2.17) is independent of $x$. From conservation of mass (2.14a) and momentum (2.14b), and the equation of state (2.14d), we deduce that, for $t > 0$,

$$\rho = 1, \quad u = 0, \quad p = T. \tag{2.96a}$$

By combining and integrating (2.14c) and (2.16), we recover conservation of (thermal and chemical) energy,

$$T + \gamma Q Y_{\mathcal{F}} = 1 + \gamma Q, \tag{2.96b}$$

for $t > 0$. Thus, the evolution of the temperature, $T$, mass fraction, $Y_{\mathcal{F}}$, and pressure, $p$, is governed by a single ODE.

We choose to introduce a new dimensionless time variable, $\hat{t}$, which is more appropriate than $t$ for describing ignition. We define $\hat{t}$ such that

$$t = \frac{\epsilon \exp(E)}{EQZ}\hat{t}. \tag{2.97}$$

In terms of $\hat{t}$, the energy equation (2.14c) becomes

$$\frac{\mathrm{d}T}{\mathrm{d}\hat{t}} = E^{-1}Q^{-1}(1+\gamma Q - T)\exp\left(E\left(1-\frac{1}{T}\right)\right), \tag{2.98}$$

where we have used (2.17) and (2.96) to eliminate $r$, $\rho$, $u$ and $Y_{\mathcal{F}}$. We solve (2.98) subject to $T(0) = 1$. As we will see in Section 2.2.3.1.1, our choice to define $\hat{t}$ by (2.97) ensures that (2.98) has a particularly simple asymptotic form as $E \to \infty$ when $T - 1 = O(E^{-1})$.

As time progresses, the temperature increases towards the maximum temperature, $1 + \gamma Q$, which is reached when all the reactant is used up. The exact solution of (2.98) may be written implicitly in quadrature form,

$$\hat{t} = \int_1^T \frac{EQ}{1+\gamma Q - s}\exp\left(-E\left(1-\frac{1}{s}\right)\right)\mathrm{d}s, \tag{2.99}$$

and can be expressed in terms of the exponential integral, $\mathrm{Ei}(x) = \int_{-\infty}^{x} e^t/t\,\mathrm{d}t$ [75], as

$$\hat{t} = EQ\exp(-E)\left[\mathrm{Ei}\left(\frac{E}{s}\right) - \exp\left(\frac{E}{1+\gamma Q}\right)\mathrm{Ei}\left(\frac{E}{s} - \frac{E}{1+\gamma Q}\right)\right]_1^T. \tag{2.100}$$

While we are able to find the exact solution to (2.98), finding an exact solution to more complicated combustion problems is not always possible. The dimensionless activation energy, $E$, is often large for combustion problems, and perturbation methods based on the limit $E \to \infty$ can help us understand more subtle combustion problems. Kassoy [54] uses asymptotic analysis in the limit $E \to \infty$, with $\gamma Q = \mathrm{ord}(1)$, to provide a complete description of homogeneous ignition for the one-step reaction (2.1).

As time progresses, the solution to (2.98) goes through two distinguished stages—*thermal explosion* and *relaxation*—each associated with its own timescale. We discuss these two stages in turn. First though, it is beneficial to discuss the first part of the thermal explosion stage, known as the *induction* stage, when the temperature only changes by an $O(E^{-1})$ amount.

**2.2.3.1.1 Induction stage** We first consider the solution to (2.98) when $T = 1 + O(E^{-1})$ as $E \to \infty$. Substituting the asymptotic series $T = 1 + E^{-1}T_1(\hat{t}) + O(E^{-2})$ into (2.98), we find that $T_1$ satisfies

$$\frac{\mathrm{d}T_1}{\mathrm{d}\hat{t}} = \gamma\exp(T_1), \quad T_1(0) = 0. \tag{2.101}$$

Note that the timescale (2.97) is chosen so that the leading-order terms balance during the induction stage. Integrating (2.101), we deduce

$$T_1 = -\log\bigl(1-\gamma\hat{t}\bigr). \tag{2.102}$$

The form of (2.102) motivates the definition of the *constant volume induction time*,

$$\hat{t}_I = \frac{1}{\gamma}. \tag{2.103}$$

The temperature perturbation $T_1$ tends to infinity as $\hat{t} \to \hat{t}_I$, invalidating our assumption that $T = 1 + E^{-1}T_1(\hat{t}) + O(E^{-2})$ is an asymptotic series. To capture the behaviour of (2.98) when $T - 1 \gg E^{-1}$, we must rescale the time variable.

**2.2.3.1.2 Thermal explosion** The induction stage solution (2.102) is only valid when $T = 1 + O(E^{-1})$, whereas we seek a solution which is valid for $\mathrm{ord}(1)$ changes in temperature. Based on the form of the induction stage solution (2.102), Kassoy [54] introduces a new time variable, $\sigma$, defined by

$$\hat{t} - t_*(E) = -\exp\left(-\sigma E + \sum_{k=0}^{\infty} E^{-k} g_k(\sigma)\right), \quad \sigma = O(1), \tag{2.104}$$

where the functions $(g_k(\sigma))_{k\geq 0}$ are to be determined as part of the solution and

$$t_*(E) = \exp\left(\sum_{k=0}^{\infty} E^{-k} g_k(0)\right), \tag{2.105}$$

so that the initial condition at $\hat{t} = 0$ is satisfied when $\sigma = 0$. In terms of the new time variable, $\sigma$, equation (2.98) reads

$$\frac{\mathrm{d}T}{\mathrm{d}\sigma} = Q^{-1}(1+\gamma Q - T)\exp\left(E\left(1-\sigma-\frac{1}{T}\right)\right)\exp(g_0)\left[1+E^{-1}\left(g_1 - \frac{\mathrm{d}g_0}{\mathrm{d}\sigma}\right)+O(E^{-2})\right]. \tag{2.106}$$

The $(1-\sigma-T^{-1})$ term in the argument of the exponential is critical to the behaviour of (2.106). For an order $O(1)$ rise in temperature on the $\sigma = O(1)$ timescale, we require

$$T = \frac{1}{1-\sigma}, \tag{2.107}$$

otherwise, the exponential term is exponentially small or large as $E \to \infty$. Equating terms of the same order yields a system of algebraic equations for $(g_k(\sigma))_{k\geq 0}$, which we solve to find

$$g_0 = \log\left(\frac{QT^2}{1+\gamma Q - T}\right), \quad g_1 = 2T + \frac{T^2}{1+\gamma Q - T}. \tag{2.108}$$

Substituting the expression for $g_0$ into (2.105), we find that the integration constant, $t_*$, is equal to the induction time to leading order, $t_* = \hat{t}_I + O(E^{-1})$, meaning the

induction time is not just representative of the early stages of combustion. The functions $g_0(\sigma)$ and $g_1(\sigma)$ blow up as $T \to 1+\gamma Q$, indicating that the asymptotic solution (2.107) is only valid up until $1+\gamma Q - T = O(E^{-1})$. A different distinguished limit of (2.98) governs the relaxation stage, as the concentration of reactant approaches zero.

By using the ansatz (2.104), we have effectively sought a solution of the form $\hat{t}(T;E)$, rather than $T(\hat{t};E)$. An asymptotic expansion for $T(\hat{t};E)$ could be found if we had instead used

$$\hat{t} - \hat{t}_*(E) = -\hat{t}_*(E)e^{-\hat{\sigma}E}, \quad \hat{\sigma} = O(1), \tag{2.109}$$

where $\hat{t}_*(E) = \hat{t}_I + O(E^{-1})$ is to be determined as part of the solution. The nonlinear time scaling (2.109) has been used to tackle other ignition problems [48, 51, 77], as we will discuss in Section 2.2.4.

**2.2.3.1.3 Relaxation stage** The thermal explosion stage ends when almost all of the reactant has been used up and the temperature approaches $1+\gamma Q$. We seek a solution of the form $T = 1+\gamma Q - E^{-1}\hat{T} + O(E^{-2})$. We define a new time variable, $\hat{\tau}$, by

$$\hat{t} - \hat{t}_* = EQ\exp\left(E\left(\frac{1}{1+\gamma Q} - 1\right)\right)\hat{\tau}, \quad \hat{\tau} = O(1), \tag{2.110}$$

so that the leading-order terms in (2.98) balance. This natural time scale for the relaxation stage is exponentially short compared to the induction time. We find that $\hat{T}$ satisfies

$$\frac{\mathrm{d}\hat{T}}{\mathrm{d}\hat{\tau}} = -\hat{T}\exp\left(-\frac{\hat{T}}{(1+\gamma Q)^2}\right). \tag{2.111}$$

Integrating (2.111), and matching with the explosion stage solution (2.107) to determine the constant of integration, Kassoy [54] completes his description of the homogeneous one-step reaction (2.1).

As we will discuss in Section 2.2.4, ignition with spatial variations also exhibits stages analogous to the induction, thermal explosion and relaxation stages of homogeneous ignition. By analysing the ODE (2.98) using matched asymptotic expansions in the limit $E \to \infty$, rather than using, for example, the method of steepest descent on the solution (2.99), we have demonstrated techniques that will allow us to better understand the behaviour of combustion problems where it is not possible to find an analytic solution.

### 2.2.3.2 Three-step reaction

Although homogeneous ignition seldom occurs in reality, by analysing (2.98) we have gained valuable insights into the temporal structure of explosions which will help when we come to model explosions with spatial variations. However, before we consider ignition with spatial variations, we first turn our attention to the three-step reaction (2.6). The solutions to the three-step reaction model, (2.14), (2.22) and (2.23), with uniform initial conditions on $x \in \mathbb{R}$,

$$p(x,0) = T(x,0) = Y_{\mathcal{F}}(x,0) = 1, \quad u(x,0) = Y_{\mathcal{R}}(x,0) = 0, \tag{2.112}$$

also exhibits an interesting temporal structure, which we reveal using asymptotic analysis in the limit $E \to \infty$.

Using an analogous argument to in Section 2.2.3.1, we deduce that

$$\rho = 1, \quad u = 0, \quad p = T, \tag{2.113a}$$

$$T + \gamma Q(Y_{\mathcal{F}} + Y_{\mathcal{R}}) = 1 + \gamma Q, \tag{2.113b}$$

for $t > 0$. For the three-step reaction (2.6), the dynamics of homogeneous ignition are governed by

$$\epsilon \frac{\mathrm{d}T}{\mathrm{d}t} = \gamma Q Y_{\mathcal{R}}, \tag{2.114a}$$

$$\epsilon \frac{\mathrm{d}Y_{\mathcal{R}}}{\mathrm{d}t} = E^2 Y_{\mathcal{F}} \exp\left(m\left(\frac{E}{T_{\times 1}} - \frac{E}{T}\right)\right) + E^2 Y_F Y_R \exp\left(\frac{E}{T_{\times 2}} - \frac{E}{T}\right) - Y_{\mathcal{R}}, \tag{2.114b}$$

subject to the initial conditions $T(0) = 1$ and $Y_{\mathcal{R}} = 0$.

The behaviour of (2.114) depends on the relative sizes of the initial temperature, $T = 1$, the final temperature, $T = 1+\gamma Q$, and the cross-over temperatures, $T_{\times 1}$ and $T_{\times 2}$. For simplicity, Blythe et al. [9] and Sharpe and Maflahi [78] assume the initiation cross-over temperature is greater than the maximum temperature, i.e. $T_{\times 1} > 1 + \gamma Q$. We consider a slightly less restrictive parameter regime than in [9, 78], with $T_{\times 1} - T_{\times 2} = \mathrm{ord}(1)$, but note that the temperature will exhibit the same behaviour to leading order.

Blythe et al. [9] consider five distinguished limits on the size of the branching reaction cross-over temperature, $T_{\times 2}$: one limit where $T_{\times 2} > 1 + \gamma Q$, one limit where $1 - T_{\times 2} = \mathrm{ord}(1)$, and three different distinguished limits where $T_{\times 2}$ is close to the initial temperature, i.e. $T_{\times 2} - 1 = o(1)$ as $E \to \infty$. Studying ignition where the branching cross-over temperature is close to or below the initial temperature is motivated by ignition caused by a shock reflecting at a wall. In this scenario, the temperature close to the wall rises very quickly to become close to or above the cross-over temperature, and the branching reaction dominates the ignition process.

As we have established in Section 2.2.2.2, in order to have a flame with $T^{R*} = 1$ and the structure described by Dold [29], we require that $T_{\times 2}$ satisfies (2.41a), meaning the branching cross-over temperature exceeds the initial temperature by an $\mathrm{ord}(1)$ amount, but is less than the maximum temperature, $1 + \gamma Q$. Blythe et al. [9] do not consider this parameter regime. However, by considering their results for $T_{\times 2} > 1 + \gamma Q$, and other work on chain-branching explosions [50, 78], we give a brief description of the different stages the reaction goes through, albeit without all the quantitative details.

**2.2.3.2.1 Initiation and thermal explosion** In the case where $T_{\times 2} > 1 + \gamma Q$, Blythe et al. [9] show that there is an $O(\epsilon)$ boundary layer in time—which they call the *initiation* stage—during which the mass fraction of the radical, $Y_{\mathcal{R}}$, approaches $E^2 \exp(m(E/T_{\times 1} - E))$. For $t \gg \epsilon$, the gas undergoes a thermal explosion, analogous to the thermal explosion due to the one-step reaction described in Section 2.2.3.1. To leading order, the temperature satisfies

$$\frac{\mathrm{d}T}{\mathrm{d}\hat{t}} = E^{-1} Q^{-1} (1 + \gamma Q - T) \exp\left(m\left(E - \frac{E}{T}\right)\right), \tag{2.115}$$

as $E \to \infty$, where

$$t = \gamma\epsilon E^{-3} \exp\left(-m\left(\frac{E}{T_{\times 1}} - E\right)\right)\hat{t}. \tag{2.116}$$

With $T_{\times 2} > 1 + \gamma Q$, the mass fraction of the radical remains exponentially small, with

$$Y_{\mathcal{R}} = E^2 Y_{\mathcal{F}} \exp\left(m\left(\frac{E}{T_{\times 1}} - \frac{E}{T}\right)\right) \tag{2.117}$$

to leading order, throughout each of the induction, explosion and relaxation stages of the thermal explosion.

The description of the early stages of the reaction is the same for the parameter regime of interest, summarised in Table 2.2. After the $O(\epsilon)$ initiation stage, the gas undergoes the beginnings of a thermal explosion, with the rise in temperature governed by (2.115) to leading order. However, as $T$ approaches $T_{\times 2}$, the approximation (2.115) becomes invalid.

**2.2.3.2.2 Chain-branching explosion stage** As $T \to T_{\times 2}$, the branching reaction becomes significant [78] and the gas undergoes what is known as a *chain-branching explosion*. Based on analysis by Kapila [50] and Blythe et al. [9] with $T_{\times 2} - 1 = o(1)$, we expect that while $T_{\times 2} - T = o(1)$, the branching reaction will act to quickly consume the remaining fuel, and increase the mass fraction, $Y_{\mathcal{R}}$, of the radical to an $\mathrm{ord}(1)$ amount.

The temporal structure of the chain-branching explosion in [9] subtly changes depending on the size of $T_{\times 2} - 1$. We therefore anticipate that careful asymptotic analysis of (2.114) would be needed to find the subtle temporal structure of the chain-branching explosion and match it to the thermal explosion stage.

**2.2.3.2.3 Termination stage** The chain-branching explosion comes to an end when the mass fraction, $Y_{\mathcal{F}}$, of the fuel becomes exponentially small. The temperature continues to rise as the radical is consumed by the termination reaction (2.6c). We call this final stage of the reaction process the *termination stage*, in line with the terminology in [9]. During the termination stage, the evolution of the temperature is governed by

$$\frac{\mathrm{d}T}{\mathrm{d}t} = 1 + \gamma Q - T, \tag{2.118}$$

to leading order. Note that the final temperature is given by $1 + \gamma Q$.

**2.2.3.2.4 Comparison with one-step reaction** For both the one-step and three-step reactions, we are able to identify an induction period, where the temperature only changes by an $O(E^{-1})$ amount. While the temporal structure of the reaction following the induction period is different for the two models, in both cases the induction time is indicative of *when* explosion occurs; the temperature rises through an $\mathrm{ord}(1)$ amount in an exponentially short boundary layer in time, centred around the constant-volume induction time. As we will see in Chapter 4, the induction period is of most importance in determining when and where autoignition occurs.

### 2.2.4 Ignition with spatial variations

As we have seen, we are able to use matched asymptotic expansions to find asymptotic solutions to the models {(2.14), (2.16) and (2.17)} and {(2.14), (2.22) and (2.23)} with spatially uniform initial conditions. Asymptotic analysis in the limit $E \to \infty$ can also help us understand ignition with spatial variations. However, the analysis is more nuanced due to the interplay between the dynamics of the gas and the exothermic chemical reaction.

There are a number of different scenarios that lead to spatial variations during ignition. Examples of scenarios considered in the literature include: homogenous initial conditions with fixed temperature boundary conditions [59, 77]; homogenous initial conditions with an additional source of heat [60, 83]; spatially inhomogeneous initial conditions [53, 79]; and ignition due to a shock reflecting at a boundary [10, 30, 78]. For the three-step reaction (2.6), ignition following the reflection of a shock at a boundary is often considered in the literature [10, 30, 78]. However, as we have already discussed, the waves present in the end-gas prior to the onset of autoignition are much weaker than shocks. Therefore, it is most instructive to discuss ignition from spatially inhomogeneous initial conditions. We choose to focus our attention in this section on the one-step reaction (2.1), because, as we noted in Section 2.2.3.2.4, the early stages of ignition are similar for both the one- and three-step reactions.

Diffusion can play a role in the ignition of gases, provided that the reaction is sufficiently slow such that the characteristic time over which diffusion has a significant effect is of the same order as the induction time [58, 77]. However, in the context of autoignition, the time over which diffusion has a significant effect in the end-gas is asymptotically long compared to the time taken for the flame to travel from $x = 0$ to $x = 1$. Autoignition develops rapidly on a yet shorter time scale, therefore, we deduce that diffusion plays a negligible role during autoignition.

The difficulty in modelling the ignition of a gas is that the energy released by the chemical reaction induces motion in the gas [55, 56], which, in turn, affects the rate of reaction and the subsequent evolution of the gas [53, 57]. If the gas dynamics are ignored and it is assumed that each fluid particle undergoes a constant volume ignition analogous to that described in Section 2.2.3.1, then we can easily identify a constant volume induction time for each fluid particle directly from the initial temperature profile [97]. However, in reality, the motion of the gas complicates how the time at which each particle explodes depends on the initial conditions.

When energy is deposited in an inert gas, it is converted into thermal and kinetic energy. Assuming the effect of diffusion is negligible, the behaviour of the gas depends on the ratio of the energy deposition time scale and the characteristic time scale for acoustic propagation through the region being heated, and on the ratio of the amount of energy being deposited and the initial thermal energy of the gas. For example, Kassoy [55] finds that, when a moderate amount of heat is added on a time scale much shorter than the acoustic time scale of the region being heated, the behaviour of the gas is characterised by 'nearly inertial confinement', where the temperature rises and the density remains almost constant. By contrast, if the time taken for an acoustic wave to cross the heated region is much shorter than the characteristic time scale for the energy deposition, then the temperature rises and the pressure remains nearly constant [56]. Other distinguished

limits are discussed in [55, 56].

For gaseous combustion, the situation is even more complicated. The rate of energy deposition (i.e. the reaction rate) increases considerably as the temperature rises. It is therefore possible for the behaviour of the gas to change from nearly constant pressure to nearly constant volume as the reaction rate increases during the course of ignition [27].

Spatial variation in any of the initial conditions will lead to a localised explosion [79], at what we will call a hot spot. Then, starting from the hot spot, either a detonation or a deflagration will travel through the unburnt gas. We note that steep gradients in the initial conditions can result in the ignition of a deflagration [53, 58]. However, due to its significance when modelling autoignition, we focus here on the case where ignition results in a weak detonation directly. We gain insight into when and where the gas first explodes by considering the induction stage, where $T = 1 + O(E^{-1})$.

#### 2.2.4.1 Induction stage

The earliest stage of ignition is the induction stage, where $T = 1 + O(E^{-1})$. We seek an approximate solution to the model (2.17), (2.33) and (2.34) of the form

$$p \sim 1 + E^{-1}p_1 + \cdots, \tag{2.119a}$$
$$V \sim 1 + E^{-1}V_1 + \cdots, \tag{2.119b}$$
$$T \sim 1 + E^{-1}T_1 + \cdots, \tag{2.119c}$$
$$Y_{\mathcal{F}} \sim 1 + E^{-1}Y_1 + \cdots, \tag{2.119d}$$
$$u \sim E^{-1}M^{-1}u_1 + \cdots. \tag{2.119e}$$

For easy comparison with the literature [e.g. 31], we use the Lagrangian coordinate representation of the governing equations, and rescale both the time and space variables,

$$t = \frac{\epsilon \exp(E)}{EQZ}\hat{t}, \quad \chi = \frac{\epsilon \exp(E)}{EMQZ}\hat{\chi}. \tag{2.120}$$

The time variable, $\hat{t}$, is the same time variable that we used to study homogeneous ignition in Section 2.2.3.1.

Substituting (2.119) and (2.120) into (2.17), (2.33) and (2.34), we find that the leading-order behaviour of the gas is governed by

$$\frac{\partial V_1}{\partial \hat{t}} - \frac{\partial u_1}{\partial \hat{\chi}} = 0, \tag{2.121a}$$
$$\frac{\partial u_1}{\partial \hat{t}} + \frac{1}{\gamma}\frac{\partial p_1}{\partial \hat{\chi}} = 0, \tag{2.121b}$$
$$\frac{\partial T_1}{\partial \hat{t}} - \frac{\gamma - 1}{\gamma}\frac{\partial p_1}{\partial \hat{t}} = \exp(T_1), \tag{2.121c}$$
$$\frac{1}{\gamma}\frac{\partial T_1}{\partial \hat{t}} + \frac{\gamma - 1}{\gamma}\frac{\partial V_1}{\partial \hat{t}} = \exp(T_1), \tag{2.121d}$$
$$\frac{\partial Y_1}{\partial \hat{t}} = -\frac{\exp(T_1)}{Q}. \tag{2.121e}$$

In writing (2.121), we have assumed the effect of the transport processes—viscosity and diffusion—are negligible as $\epsilon \to 0$. Eliminating $p_1$, $V_1$ and $u_1$ from (2.121), we find a single partial differential equation for $T_1$,

$$\frac{\partial^2}{\partial \hat{t}^2}\left(\frac{\partial T_1}{\partial \hat{t}} - \gamma \exp(T_1)\right) = \frac{\partial^2}{\partial \hat{\chi}^2}\left(\frac{\partial T_1}{\partial \hat{t}} - \exp(T_1)\right). \tag{2.122}$$

In the literature, (2.122) is known as *Clarke's equation* [21, 31]. The system of PDEs (2.121) is often easier to work with than Clarke's equation, so, for convenience, we will refer to (2.121) as *Clarke's equations*. In general, Clarke's equations (2.121) need to be solved numerically, although asymptotic solutions can be found in the limits $\gamma \to 1$ [8, 76] and $Q \to 0$ [12]. Furthermore, exact solutions to Clarke's equations (2.121) can be found in the special cases of where either the specific volume or the pressure is constant.

A key observation from the literature is that Clarke's equations (2.121) are singular. That is, given finite initial and boundary conditions, the solution to (2.121) will first become unbounded at some point, $\hat{\chi} = \hat{\chi}_I$, at the finite time, $\hat{t} = \hat{t}_I$. A hot spot develops at $\hat{\chi}_I$ as $\hat{t} \to \hat{t}_I$.

#### 2.2.4.2 Thermal explosion

The assumption that (2.119c) is an asymptotic series becomes invalid as $T_1 \to \infty$. For the one-step reaction (2.1), the subsequent evolution of the hot spot is described by Jackson et al. [48]. They show that the gas undergoes a thermal explosion as $\hat{t} \to \hat{t}_I$, with the temperature rising rapidly in a shrinking region of space centred around $\hat{\chi}_I$. Jackson et al. [48] use the nonlinear time scaling (2.109) introduced by Kassoy [54] to describe the evolution of the hot spot, and show that the leading-order approximation to the density within the hot spot is constant. Despite the steep temperature gradients within the hot spot, Jackson et al. [48] show that diffusion does not play a role in the evolution of the hot spot, at least in the parameter regime they consider where the induction time is of the same order as the acoustic time.

#### 2.2.4.3 Singularity path

For the one-step reaction, the thermal explosion at the centre of the hot spot ends as the mass fraction of the fuel approaches zero. Jackson et al. [48] do not go as far as determining the structure of the gas witin the hot spot during the relaxation stage. However, insights into the behaviour of the detonation formed during ignition can be gained by further considering the solution to Clarke's equations (2.121). Despite the singularity at $(\hat{\chi}_I, \hat{t}_I)$, we can continue to solve Clarke's equations at $\hat{\chi} \neq \hat{\chi}_I$ for $\hat{t} > \hat{t}_I$. With bounded initial data, the solution to Clarke' equations becomes unbounded for every $\hat{\chi}$ at some finite time, which we denote by $\hat{t}_I(\hat{\chi})$ so that $\hat{t}_I = \min_{\hat{\chi}} \hat{t}_I(\hat{\chi})$. In the literature, the path defined by $(\hat{\chi}, \hat{t}_I(\hat{\chi}))$ is known as the singularity path [31]. The singularity path can be determined using the numerical procedure outlined by Short and Dold [80].

The singularity path is necessarily supersonic because the solution to Clarke's equations is finite at $(\hat{\chi}, \hat{t})$ only if the solution is finite along the characteristics entering $(\hat{\chi}, \hat{t})$ [28].

What is more, $\mathrm{d}\hat{t}_I/\mathrm{d}\hat{\chi} \to 0$ as $\hat{\chi} \to \hat{\chi}_I$, meaning that, initially, the apparent speed of the singularity path is infinite [31].

While the singularity path travels through the gas at speeds faster than the Chapman–Jouguet speed, the combustion wave that originates at the hot spot is best described as a weak detonation. The structure of the weak detonation is quasi-steady [52], and its position is accurately predicted by the singularity path [53]. If the singularity path slows down below the Chapman–Jouguet speed, then structure of the detonation becomes unsteady and the singularity path no longer accurately describes the position of the detonation. A shock is formed at the rear of the detonation wave, as the gas there transitions from supersonic to subsonic relative to the combustion wave. The shock propagates forward towards the unburnt gas, ultimately resulting in a Chapman–Jouguet detonation with the ZND structure [52, 53].

The autoignition front in Figure 1.7a is a weak detonation, suggesting that the mechanism that results in autoignition is similar to mechanism of ignition presented here. Of course, for different chemical reaction mechanisms, the specific structure of the hot spot and of the weak detonation will be slightly different. However, we recognise that the position of the hot spot and the path of the weak detonation during autoignition will be determined by the behaviour of the gas during the induction stage.

### 2.2.5 Combustion in confinement and autoignition

In Section 2.2.1, we discussed the theoretical literature on deflagrations and detonations, and, in Section 2.2.2, we identified the quasi-steady structure of premixed flames for the one-step (2.1) and three-step (2.6) reaction mechanisms. However, we have not yet discussed how the flame interacts with the gas either side of it. We now begin to introduce the work that will come in Chapters 3 and 4 and the context in which it sits.

We are concerned with finding the behaviour of gaseous premixed flames propagating through a 1D channel of finite length with closed ends. Despite the apparent simplicity (modelling in 1D rather than 3D), the theoretical understanding of gaseous combustion in confinement is limited.

The difficulty with modelling premixed combustion in confinement is that flames are subsonic, and therefore affect the gas either side of them through the production of acoustic waves or shocks. For unconfined flames this does not present too much of a problem; the wave produced when the flame is initiated will travel out into the unburnt gas and does not subsequently interact with the flame. As long as the chemical activity between the flame and the wave is negligible over the time-scale of interest, we are justified in modelling the mass flux through the flame as constant[6].

For flames in confinement, however, the production of acoustic waves or shocks presents a particular difficulty. Any wave emitted from the flame will reflect from the boundaries and subsequently interact with the flame again. The repeated reflection of these waves between the flame and the confinements of the burning gas considerably complicates modelling the behaviour of the flame.

[6] If, however, the flame produces a shock of sufficient strength that the chemical activity in the gas behind the shock cannot be ignored, then DDT will follow [83].

Flames are often much slower than the speed of sound, meaning the disturbances to the surrounding gas are weak, i.e. acoustic waves. Analytic progress can be made by taking the limit of small Mach number, i.e. $M \to 0$. We discuss how the limit $M \to 0$ has been used in the literature to understand, in part, the behaviour of flames in confinement.

#### 2.2.5.1 Zero Mach number approximation

The limit $M \to 0$ is a singular perturbation. Taking $M = 0$ in the conservation of momentum equation (2.14b), we find that we are unable to specify the initial velocity, and that the pressure is necessarily spatially uniform at all times. The approximation $M = 0$, however, does allow us to gain some insight into how the pressure changes as the flame moves. This is the approach Sivashinsky [84] uses to model a confined spherically-symmetric flame. Sivashinsky [84] finds the structure of the combusting gas for a one-step reaction mechanism (2.1), assuming the reaction is negligible away from the flame. They find that the dynamics of the flame are governed by a single ODE. We discuss the zero Mach number approximation in detail in Section 3.1, and show how the results in [84] are applicable for reaction mechanisms other than the one-step reaction (2.1).

Like Sivashinsky [84], Kagan and Sivashinsky [49] study the behaviour of a flame in confinement using the $M = 0$ approximation. However, they do not assume the reaction rate is zero ahead of the flame. Instead they retain the source terms on the right-hand side of (2.14c) and (2.16) when modelling the gas ahead of the flame. The model Kagan and Sivashinsky [49] develop can be thought of as a simple model of autoignition, albeit one which does not capture the highly localised nature of autoignition due to the $M = 0$ approximation.

As a result of taking $M = 0$, Kagan and Sivashinsky [49] find that, ahead of the flame, the temperature, $T^R$, and the mass fraction, $Y_{\mathcal{F}}^R$, of the fuel are spatially uniform, as is the pressure, $p$, throughout the channel. They find that the evolution of $T^R$, $Y_{\mathcal{F}}^R$ and $p$ is governed by a system of three coupled ODEs. The reaction rate (2.17) we use is slightly different to that used in [49], but, by using analogous analysis to in [49], we find that the corresponding system of ODEs for our model (2.14), (2.16) and (2.17) is

$$\frac{\mathrm{d}\chi^*}{\mathrm{d}t} = \frac{(T^R + QY_{\mathcal{F}}^R)^2}{Y_{\mathcal{F}}(1+Q)^2} \exp\left(\frac{E}{2(1+Q)} - \frac{E}{2(T^R + QY_{\mathcal{F}}^R)}\right), \quad \chi^*(0) = 0, \tag{2.123a}$$

$$\frac{p}{T^R}\frac{\mathrm{d}T^R}{\mathrm{d}t} - \frac{\gamma - 1}{\gamma}\frac{\mathrm{d}p}{\mathrm{d}t} = \epsilon^{-1} Q r, \quad T^R(0) = 1, \tag{2.123b}$$

$$\frac{\mathrm{d}Y_{\mathcal{F}}^R}{\mathrm{d}t} = -\epsilon^{-1} r, \quad Y_{\mathcal{F}}^R(0) = 1, \tag{2.123c}$$

where $r$ is given by (2.17) and $\chi^*$ is the position of the flame in the Lagrangian coordinate (2.26). It follows from the conservation of mass that the pressure, $p$, is given in terms of $\chi^*$ and $Y_{\mathcal{F}}^R$ by

$$p = 1 + \gamma Q - \gamma Q\,(1 - \chi^*)\, Y_{\mathcal{F}}^R. \tag{2.123d}$$

Kagan and Sivashinsky [49] solve their system of ODEs (analogous to (2.123)) numerically, and find that, for some parameter values, the temperature ahead of the flame rises

suddenly before the flame completely crosses the domain. This sudden temperature rise can be thought of as representative of autoignition. Kagan and Sivashinsky [49] observe that autoignition occurs earlier for smaller values of $\epsilon$, corresponding to increasing the length of the container. Such behaviour agrees with the numerical simulations by Yu and Chen [95] that we have discussed in Section 1.3.2.2.2.

Kagan and Sivashinsky [49] stop short of providing the parameter regime where autoignition occurs. However, we recognise that further analysis of (2.123) in the limit $E \to \infty$ is possible and would shine a light on the parametric dependence of autoignition. In Section 4.1.1.1, we determine a critical temperature, below which autoignition does not occur, by considering where the approximation that the chemistry in the end-gas is negligible is justified in the limit $E \to \infty$.

#### 2.2.5.2 Multiple scales approach

The models by Sivashinsky [84] and Kagan and Sivashinsky [49] are instructive, but they do not exhibit any spatial variation in the end-gas. The zero Mach number approximation is therefore unable to capture the localised nature of autoignition.

As we will show in Section 3.3, ideas from the method of multiple scales [46, §7] can be used to capture the acoustic waves in the gas either side of the flame. Previous studies taking this approach [5, 37] have focused on modelling a channel with one end open and one end closed, which is simpler than the case with both ends closed because the pressure remains constant to leading order. It is assumed in [5, 37] that the chemistry in the gas either side of the flame is negligible, and that the gas surrounding the flame is inviscid.

For a channel with one end open and one end closed, Bauwens et al. [5] find the pressure perturbation either side of the flame can be written in terms of a series of sinusoidal eigenmodes. The leading-order temperature takes a different constant value on either side of the flame, meaning the frequency of each mode changes slowly as the flame propagates through the channel. Therefore, Bauwens et al. [5] introduce an infinite family of fast time variables to describe the time dependence of each mode. Pragmatically, Bauwens et al. [5] consider the motion of a flame whose speed relative to the velocity of the gas ahead of it is constant.

Fachini and Bauwens [37] build upon [5] by considering a flame where the gas is reacting with a one-step Arrhenius reaction. The one-step reaction mass flux (2.70) can be used consistently in the case where one end of the channel is open, because the temperature ahead of the flame only changes by an $O(E^{-1})$ amount. However, as we will discuss in Section 4.1.2.1, the one-step reaction is not suitable for modelling flames in a channel with both ends closed because the mass flux through the flame becomes exponentially large as the temperature rises by an $\mathrm{ord}(1)$ amount ahead of the flame.

We find that there is an inconsistency in how the Chapman–Jouguet conditions are applied in [5]. Bauwens et al. [5] find that the leading-order temperature and the density perturbation are discontinuous across the flame, but the temperature perturbation, the leading-order pressure and the pressure perturbation are continuous, which is inconsistent with the equation of state (2.14d). To resolve this issue, we find it is necessary to use ideas from the method of multiple scales in both time and space, as we discuss in Section 3.3.4.3.

In Section 3.3, we extend the work of Bauwens et al. [5] to describe the interaction between a flame and the gas surrounding it in a channel with both ends closed. The description of the eigenmodes in this case is more nuanced because the leading-order temperature is not spatially uniform behind the flame.

## 2.3 Statement of originality

As discussed in Section 2.2, there is already a vast literature on mathematical modelling of combustion. In the remaining chapters of this thesis, we build upon the existing body of literature to provide novel insights into combustion in confinement and autoignition.

We use ideas from the method of multiple scales to understand the evolution of acoustic waves during normal combustion in confinement. We describe the acoustic waves in the gas either side of the flame as a series of modes, whose amplitude, frequency and spatial structure slowly change. In private correspondence [4], Luc Bauwens has shared incomplete, preliminary work on extending his work [5] to a channel with both ends closed. In this unpublished work, Bauwens finds the leading-order pressure and density, but does not find the form of the eigenmodes. We identify the eigenvalue problem to solve for the spatial structure of each mode, and find the ordinary differential equations governing the evolution of the amplitude of each mode. We find that the eigenmodes depend on time only through the flame position, and not, for example, on the mass flux through the flame. Additionally, we find that the solution behind the flame exhibits short-scale spatial variations that have not been previously reported on in the literature.

The multiple scales framework we develop in Chapter 3 can be used with any chemical reaction mechanism, provided that a suitable model for the mass flux through the flame can be identified and that the asymptotic assumptions we make remain valid. We choose to focus on the three-step reaction (2.6) rather than the simpler one-step Arrhenius reaction (2.1) because, based on the experimental and numerical studies discussed in Section 1.3, we do not expect the flame to accelerate excessively prior to autoignition; for the one-step reaction, the mass flux through the flame increases to a point where our analysis based on the limit $M \to 0$ becomes invalid. We present numerical solutions of our model for normal combustion for the three-step reaction (2.6). For asymptotic consistency, we find we require an approximation to the mass flux with at most $o(M)$ errors. Therefore, in Appendix A, we extend the perturbation analysis by Dold [29] to find additional terms in the asymptotic approximation to the mass flux through the flame for the three-step reaction mechanism.

We further demonstrate how asymptotic analysis can be used to predict when and how autoignition occurs. By considering the size of the reaction rate in the limit $E \to \infty$, we identify a critical temperature at which autoignition occurs for the simple, zero Mach number model of Kagan and Sivashinsky [49]. Similarly, by considering which of the three elementary reactions in the three-step reaction (2.6) dominate in the early stages of autoignition, we identify a critical temperature at which autoignition occurs and derive a model for the initial development of a hot spot for the three-step reaction. We find that the behaviour of the end-gas is governed by Clarke's equations (2.121) during the induction stage. Even though Clarke's equations are well-studied in the literature, the

situation we consider—with the rise in temperature partially driven by compression due to the flame—is unconventional. We show how to systematically match the induction stage solution with the multiple scales solution during the compression stage, resulting in initial conditions that allow for numerical solution of the induction stage model. We solve our induction stage model numerically for a range of initial conditions, and observe that hot spots can develop at the flame, at the wall or in the bulk of the end-gas. As the amplitude of the acoustic waves in the end gas decreases (i.e. as $M$ gets smaller), we demonstrate that the hot spot tends to develop at the wall.

# Chapter 3

# Normal combustion

As we saw in Chapter 1, knock is a result of a sudden, rapid explosion in the unburnt end-gas ahead of the spark-ignited flame. This explosion, known as autoignition, is first apparent at localised points in the interior of the gas, often away from the flame or cylinder walls. Predicting when and where these so-called hot spots occur requires an understanding of the events leading up to autoignition. Therefore, in this chapter, we model the propagation of a flame in confinement during the compression stage—the period of normal combustion where we are justified in ignoring the effect of the chemical reactions in the end-gas. We use asymptotic analysis in the limit of small Mach number, $M \to 0$, large Péclet number, $\epsilon \to 0$, and large activation energy, $E \to \infty$ to simplify the model (2.14) and identify the structure of the combusting gas. First, we outline the simplifying assumptions that come from taking $\epsilon \to 0$ and $E \to \infty$, and write down a model for normal combustion with $M$ as a parameter. We then, in Sections 3.1–3.3, derive three approximate solutions to this model with increasing fidelity, using the fact $M \ll 1$ to simplify the gas dynamics.

Throughout this chapter we use the Lagrangian coordinate, $\chi$, defined in (2.26) to describe spatial variations either side of the flame. The benefit of using a Lagrangian coordinate system over an Eulerian (or lab-based) coordinate system is that in a Lagrangian coordinate system the flame position is monotonic in time because each fluid particle passes through the flame only once.

Since $\epsilon \ll 1$, the transport processes (thermal and chemical diffusion, and viscosity) only have a significant effect in boundary layers, which are thin compared to the length of the container. One such boundary layer is the flame, across which the gas burns. In this chapter and the next, we treat the flame as a discontinuity between two regions of inviscid gas, labelled as regions I and V in Figure 2.4. The Chapman–Jouguet conditions (2.47) apply across the flame and relate the pressure, velocity and specific volume adjacent to either side of the flame.

As part of the solution, we need to find the flame position, $\chi = \chi^*(t)$. To solve the free-boundary problem for the flame position, we require knowledge of the mass flux, $q$, through the flame. By analysing the quasi-steady interior structure of the flame in Section 2.2.2, we have derived models for the mass flux, consistent with the one-step (2.1) and three-step (2.6) reaction mechanisms. As a simple and motivating example, we also consider the case of constant mass flux, $q = 1$.

Throughout this chapter we assume that the rate of heat release due to chemical activity ahead of the flame is negligible in the limit $E \to \infty$ and $\epsilon \to 0$. Clearly, chemistry has a significant effect during autoignition, and in Chapter 4 we will analyse when the assumption that chemistry is negligible breaks down. However, for now, we consider the case of 'normal combustion' where the rate of chemical reaction in end-gas, ahead of the flame, is sufficiently small that we can ignore the effect of chemical reaction there. Furthermore, we assume the rate of heat release behind the flame is also zero because we assume the gas leaving the flame is completely burnt. That is, we assume there is no fuel or radical behind the flame, so $Y_{\mathcal{F}} = Y_{\mathcal{R}} = 0$ for $\chi \in (0, \chi^*)$.

Occasionally, we will need to specify the mass fraction of the fuel and/or radical, for example when evaluating the mass flux through the flame. In Section 4.1.1.2, we will use quadrature to track the small amounts of radical produced in the end-gas. However, for this chapter, it will be sufficient to approximate $Y_{\mathcal{F}}$ and $Y_{\mathcal{R}}$ where needed by

$$Y_{\mathcal{F}} = \begin{cases} 0, & \text{for } \chi \in (0, \chi^*), \\ 1, & \text{for } \chi \in (\chi^*, 1), \end{cases} \qquad Y_{\mathcal{R}} = 0, \quad \text{for } \chi \in (0, \chi^*) \cup (\chi^*, 1). \tag{3.1}$$

By taking $\epsilon \to 0$ and $E \to \infty$, we find that the problem of modelling normal combustion in confinement simplifies to modelling two regions of inert, inviscid gas separated by a free boundary (the flame). In the limit $\epsilon \to 0$ and $E \to \infty$, on both sides of the flame—that is, for $\chi \in (0, \chi^*)$ and $\chi \in (\chi^*, 1)$—the equations (2.33) governing the conservation of mass, momentum and energy become

$$\frac{\partial V}{\partial t} - \frac{\partial u}{\partial \chi} = 0, \tag{3.2a}$$

$$\frac{\partial u}{\partial t} + \frac{1}{\gamma M^2} \frac{\partial p}{\partial \chi} = 0, \tag{3.2b}$$

$$\frac{\partial S}{\partial t} = 0, \tag{3.2c}$$

where $V$ is the specific volume, $u$ is the velocity and $p$ is the pressure. The entropy, $S$, is given by

$$S = \gamma^{-1} \log(pV^{\gamma}), \tag{3.2d}$$

and the temperature, $T$, is given by

$$T = pV. \tag{3.2e}$$

The flame position, $\chi = \chi^*(t)$, is found by solving

$$\frac{\mathrm{d}\chi^*}{\mathrm{d}t} = q, \tag{3.3}$$

where $q$ is the mass flux. The mass flux through the flame in general depends on the conditions in the gas immediately ahead of the flame. In this chapter, we mainly consider the mass flux model for the three-step reaction (2.6), that we determined in Section 2.2.2.2.

However, for comparison, we will occasionally mention the one-step reaction mass flux model (2.70), and the constant mass flux model, $q = 1$.

The Chapman–Jouguet conditions (2.47) across the flame, $\chi = \chi^*$, are

$$[u + qV]^+_- = 0, \tag{3.4a}$$

$$\left[p + \gamma M^2 V q^2\right]^+_- = 0, \tag{3.4b}$$

$$\left[pV + \frac{\gamma - 1}{2} M^2 V^2 q^2\right]^+_- = -Q, \tag{3.4c}$$

where, as in Chapter 2, we use $[\psi]^+_-$ to indicate the jump in $\psi$; in this case, $[\psi]^+_- = \lim_{\chi \searrow \chi^*} \psi - \lim_{\chi \nearrow \chi^*} \psi$.

Finally, to specify a solution of (3.2)–(3.4), we require some boundary and initial conditions. At the fixed boundaries, $\chi = 0$ and $\chi = 1$, we impose that

$$u(0, t) = u(1, t) = 0, \tag{3.5}$$

for $t > 0$. For $0 < \chi < 1$, we impose the initial conditions

$$p(\chi, 0) = V(\chi, 0) = 1, \quad u(\chi, 0) = \chi^*(0) = 0. \tag{3.6}$$

The boundary and initial conditions (3.5) and (3.6) have been chosen to be representative of the ignition of a quiescent reactive gas at one end of a rigid, insulated, impermeable container. We do not concern ourselves with the actual ignition of the flame itself.

As an aside, taking $\epsilon \to 0$ is a singular perturbation, meaning we only require a reduced set of boundary conditions (3.5) to solve (3.2) compared to the set of boundary conditions (2.24) required to solve the full model, $\{$(2.14), (2.22) and (2.23)$\}$. If we had specified general heat or species flux boundary conditions in (2.24), then we would need to consider boundary layers at $\chi = 0$ and $\chi = 1$ of size $O(\epsilon^{1/2})$. However, as it is, the solution to (3.1)–(3.6) satisfies the zero flux boundary conditions (2.24), so further consideration of boundary layers at $\chi = 0$ and $\chi = 1$ is not necessary.

In the following sections we analyse the model (3.2)–(3.6) in the limit $M \to 0$. Taking $M \to 0$ is a singular perturbation problem; when $M = 0$ we are unable to freely choose the initial velocity or pressure profiles, and the pressure throughout the combustion chamber remains spatially uniform at all times. However, the approximation $M = 0$ does allow us to gain some important insights into how the pressure changes as the flame moves. Therefore, in Section 3.1, we take the zero Mach number approximation and find a simple model for a flame in confinement where the dynamics of the flame and surrounding gas are governed by a single ODE. In Section 3.2, we consider the early interactions between the flame and acoustic waves for $t = O(M)$. The resulting model is able to satisfy the initial conditions (3.6), but is not valid for $t = \mathrm{ord}(1)$ as $M \to 0$. In Section 3.3, we use an adapted version of the method of multiple scales to find an approximate solution to (3.2)–(3.6), valid in the limit $M \to 0$, which is both able to satisfy the initial conditions and is valid for $t = O(1)$. Finally, in Section 3.4, we compare the solutions to all three models.

## 3.1 Zero Mach number approximation

In the limit $M \to 0$, the momentum equation (3.2b) becomes

$$\frac{\partial p}{\partial \chi} = O(M^2). \tag{3.7}$$

The limit $M \to 0$ is a singular perturbation; if we take $M = 0$, then we are unable to choose the initial condition for $u$ freely. More significantly, (3.7) implies that the pressure is spatially uniform when $M = 0$, meaning we are unable to predict *any* spatial variation in pressure, let alone the large local pressure rise produced during autoignition.

By taking $M = 0$ we essentially ignore the acoustic waves produced by the flame, or, rather, we assume that the acoustic waves act to instantaneously regulate the pressure. In Sections 3.2 and 3.3, we account for these acoustic waves in the limit $M \to 0$. However, taking $M = 0$ substantially simplifies the analysis of (3.2)–(3.6), and we gain important insights into how a flame interacts with its surroundings by solving the resulting reduced model. In particular, the pressure and the temperature profiles we find by solving the zero Mach number approximation are precisely the leading-order approximation to the pressure and temperature we find using the method of multiple scales in Section 3.3.

The analysis in this section is analogous to the analysis of Sivashinsky [84]. Sivashinsky uses the zero Mach number approximation to model a spherically-symmetric flame in confinement, assuming the gas burns with a one-step reaction mechanism (2.1). We emphasise here that some of Sivashinsky's results are independent of the flame chemistry, including the temperature profile behind the flame.

### 3.1.1 Approximate governing equations

In Sections 3.2 and 3.3, we will seek an asymptotic solution to (3.2)–(3.6) as $M \to 0$. For now, though, we take $M$ to be equal to zero. This should be seen as an illustrative way of identifying the structure of the combusting gas, rather than a formal way of conducting asymptotic analysis.

Taking $M = 0$, we find that, on both sides of the flame, the governing equations (3.2) are

$$\frac{\partial V}{\partial t} - \frac{\partial u}{\partial \chi} = 0, \tag{3.8a}$$

$$\frac{\partial p}{\partial \chi} = 0, \tag{3.8b}$$

$$\frac{\partial}{\partial t}\left(\gamma^{-1}\log(pV^{\gamma})\right) = 0. \tag{3.8c}$$

The flame position, $\chi = \chi^*$, is found by solving (3.3). At the flame, $\chi = \chi^*$, the zero Mach number approximations to the Chapman–Jouguet conditions are

$$[u + qV]^{+}_{-} = 0, \tag{3.9a}$$

$$[p]^{+}_{-} = 0, \tag{3.9b}$$

$$[pV]^+_- = -Q. \tag{3.9c}$$

We solve (3.3), (3.8) and (3.9), subject to the boundary conditions (3.5) and the initial conditions,

$$p(\chi, 0) = V(\chi, 0) = 1, \quad \chi^*(0) = 0. \tag{3.10}$$

An immediate consequence of (3.8b) and (3.9b) is that the pressure is spatially uniform throughout the domain, with

$$p = p(t), \tag{3.11}$$

for $\chi \in (0, 1)$.

### 3.1.2 Ahead of the flame

We now consider the regions ahead of and behind the flame in turn to reveal the ODE governing the evolution of $p(t)$. Since we start with uniform conditions ahead of the flame (3.10), we deduce from (3.8c) that, for $\chi \in (\chi^*, 1)$,

$$V = V^R(t) = p(t)^{-1/\gamma}. \tag{3.12}$$

We use the superscript '$R$' for 'right' to indicate the values of the dependent variables ahead of the flame. Integrating (3.8a) with respect to $\chi$, and applying the boundary condition $u = 0$ at $\chi = 1$, we find

$$u = u^R(\chi, t) := \frac{(1-\chi)V^R}{\gamma p}\frac{\mathrm{d}p}{\mathrm{d}t}, \tag{3.13}$$

for $\chi \in (\chi^*, 1)$. Note that in (3.12) and (3.13) we have been able to write $u^R$ and $V^R$ in terms of $p$ and $\mathrm{d}p/\mathrm{d}t$.

### 3.1.3 Behind the flame

Similarly to the situation ahead of the flame, from (3.8c) we deduce that the entropy, $S$, behind the flame is constant along lines of constant $\chi$. However, since the flame starts at $\chi = 0$, the gas behind the flame was initially ahead of the flame so we cannot use the initial conditions (3.10) directly to determine the entropy behind the flame. Instead, the entropy at $\chi \in (0, \chi^*(t))$ is determined by the entropy at the earlier time, $t^* < t$, when the flame was at $\chi$. We define $t^*(\chi)$ as the inverse of the flame position function, $\chi^*(t)$, so that

$$\chi^*(t^*(\chi)) = \chi. \tag{3.14}$$

Using the superscript, '$L$' for 'left' to denote the values of the dependent variables behind the flame, we find the entropy, $S^L(\chi)$, is given by

$$\begin{aligned}
S^L(\chi) &= \gamma^{-1}\log\big(p(t)V^L(\chi,t)^\gamma\big) && \text{(3.15a)}\\
&= \gamma^{-1}\log\big(p(t^*(\chi))V^L(\chi,t^*(\chi))^\gamma\big) && \text{(3.15b)}\\
&= \gamma^{-1}\log\left(p(t^*(\chi))\left(V^R(t^*(\chi)) + \frac{Q}{p(t^*(\chi))}\right)^\gamma\right) && \text{(3.15c)}\\
&= \gamma^{-1}\log\left(\left(1 + Qp(t^*(\chi))^{\frac{1-\gamma}{\gamma}}\right)^\gamma\right). && \text{(3.15d)}
\end{aligned}$$

Here the equality (3.15c) follows from the Chapman–Jouguet condition (3.9c), and (3.15d) follows from (3.12). We deduce that the specific volume, $V$, is given by

$$V = V^L(\chi, t) = p(t)^{-1/\gamma} \left(1 + Qp(t^*(\chi))^{\frac{1-\gamma}{\gamma}}\right), \tag{3.16}$$

for $\chi \in (0, \chi^*(t))$. Differentiating (3.16), we find upon integrating (3.8a), and applying the boundary condition $u = 0$ at $\chi = 0$, that

$$u = u^L(\chi, t) = -\frac{1}{\gamma p}\frac{\mathrm{d}p}{\mathrm{d}t}\int_0^\chi V^L(s, t)\,\mathrm{d}s\,. \tag{3.17}$$

### 3.1.4 Pressure in terms of flame position

In Sections 3.1.2 and 3.1.3 we found expressions for the specific volume, $V$, and velocity, $u$, either side of the flame in terms of the pressure, $p(t)$, and the flame position, through $t^*(\chi)$. In this section we use the conservation of mass to identify an ODE we can solve for $p(t)$.

Eliminating $V$ from the Chapman–Jouguet conditions (3.9a) and (3.9c), which represent the conservation of mass and energy across the flame, we find that the jump in velocity across the flame is

$$u^R(\chi^*(t), t) - u^L(\chi^*(t), t) = \frac{Qq}{p(t)}. \tag{3.18}$$

Substituting the expressions for the velocity, (3.13) and (3.17), into (3.18), we find

$$\frac{1}{\gamma p(t)}\frac{\mathrm{d}p}{\mathrm{d}t}\int_0^1 V\,\mathrm{d}\chi = \frac{Qq}{p(t)}. \tag{3.19}$$

It follows from the conservation of mass (3.8a) that

$$\int_0^1 V\,\mathrm{d}\chi = 1. \tag{3.20}$$

We therefore deduce that the pressure, $p(t)$, satisfies

$$\frac{\mathrm{d}p}{\mathrm{d}t} = \gamma Qq, \quad p(0) = 1. \tag{3.21}$$

By eliminating $q$ from (3.3) and (3.21) and integrating, we find that the pressure and flame position satisfy

$$p = 1 + \gamma Q\chi^*(t). \tag{3.22}$$

Note, in deriving (3.22) we have not used any information about $q$, so the relationship (3.22) between the flame position and pressure holds regardless of the underlying chemistry. Substituting (3.22) into the expression (3.16) for the specific volume behind the flame, we find

$$V^L(\chi, t) = (1 + \gamma Q\chi^*(t))^{-1/\gamma} \left(1 + Q\left(1 + \gamma Q\chi\right)^{\frac{1-\gamma}{\gamma}}\right). \tag{3.23}$$

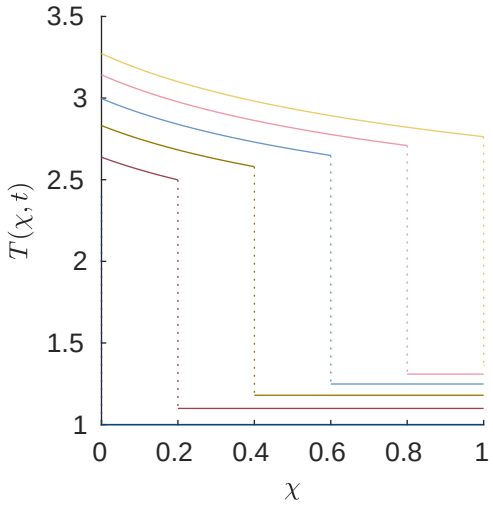


**(a)** *Temperature,* (3.24).

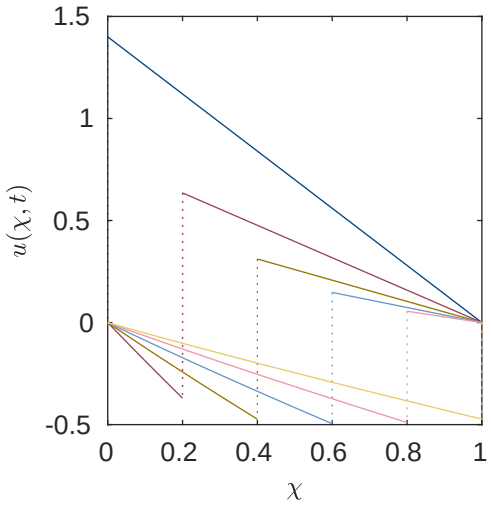


**(b)** *Velocity,* (3.13) *and* (3.17).

**Figure 3.1:** *Temperature and velocity profiles for six equally-spaced flame positions, including* $\chi^* = 0$ *and* $\chi^* = 1$*, found by taking* $M = 0$*. For this figure,* $\gamma = Q = 1.4$ *and* $q = 1$*.*

We recognise that the specific volume profile depends on time only through the position of the flame, and not, for instance, on the mass flux through the flame. The same is also true for temperature, since we have

$$T = pV = \begin{cases} T^L = (1 + \gamma Q \chi^*(t))^{\frac{\gamma-1}{\gamma}} \left(1 + Q\left(1 + \gamma Q \chi\right)^{\frac{1-\gamma}{\gamma}}\right) & \text{for } \chi \in (0, \chi^*), \\ T^R = (1 + \gamma Q \chi^*(t))^{\frac{\gamma-1}{\gamma}} & \text{for } \chi \in (\chi^*, 1). \end{cases} \tag{3.24}$$

The temperature profile (3.24) is plotted for six equally-spaced flame positions in Figure 3.1a.

By taking $M = 0$ we have reduced the dynamics of a flame in confinement to a single ordinary differential equation (3.21), which is a substantial simplification from the system of partial differential equations (3.2). The simple zero Mach number approximation captures some of the features of normal combustion, including the Mache effect—the non-uniform temperature profile behind the flame [49]. Unfortunately, however, by taking $M = 0$ we are unable to specify the initial velocity of the gas; the velocity profile is given by (3.13) and (3.17), and is plotted for $q = 1$ for six equally-spaced flame positions in Figure 3.1b.

## 3.2 Early-time behaviour: acoustic disturbances

In Section 3.1, we derived a simple model for a flame in confinement by taking $M = 0$ in (3.2)–(3.6). While the zero Mach number approximation provides us with useful insights into the structure of the combusting gas, it is not able to capture the initial velocity profile of the gas. From the numerical simulations discussed in Chapter 1, we expect that the

expansion of the burning gas produces an acoustic wave that propagates into the unburnt gas at a speed much higher than the flame speed. In this section, we investigate the behaviour of the acoustic waves produced at the flame, and derive an asymptotic solution to (3.2)–(3.6), valid for $t = O(M)$ as $M \to 0$.

### 3.2.1 Rescaled governing equations

In order to model the acoustic waves produced by the flame, we introduce a new time variable, $\tau$, defined by

$$t = M\tau. \tag{3.25}$$

The motivation behind rescaling the time variable in this way is so that $\tau = O(1)$ is representative of the time taken for an acoustic wave to cross the domain. As we will see, the time at which the first acoustic wave arrives at the right-hand wall, $\chi = 1$, is $\tau = 1$.

In terms of $\tau$, the governing equations (3.2) are

$$\frac{\partial V}{\partial \tau} - M\frac{\partial u}{\partial \chi} = 0, \tag{3.26a}$$

$$M\frac{\partial u}{\partial \tau} + \frac{1}{\gamma}\frac{\partial p}{\partial \chi} = 0, \tag{3.26b}$$

$$\frac{\partial S}{\partial \tau} = 0, \tag{3.26c}$$

where the entropy, $S$, is given in terms of $p$ and $V$ by

$$S = \gamma^{-1}\log(pV^{\gamma}). \tag{3.26d}$$

The flame position is found by solving

$$\frac{\mathrm{d}\chi^*}{\mathrm{d}\tau} = Mq. \tag{3.27}$$

We seek an asymptotic solution to (3.26) and (3.27) in the limit $M \to 0$, subject to the Chapman–Jouguet conditions (3.4), boundary conditions (3.5) and initial conditions (3.6).

Formally, we pose that the solution takes the form of Poincaré series [46, §2.5], with

$$\chi^* \sim M\chi_1^* + \cdots, \tag{3.28a}$$

$$p \sim p_0 + Mp_1 + \cdots, \tag{3.28b}$$

$$V \sim V_0 + MV_1 + \cdots, \tag{3.28c}$$

$$u \sim u_0 + \cdots, \tag{3.28d}$$

as $M \to 0$. By substituting (3.28b) and (3.28c) into (3.26d), we see that the entropy, $S$, can also be written as an asymptotic series,

$$S \sim S_0 + MS_1 + \cdots, \tag{3.28e}$$

as $M \to 0$, where

$$S_0 = \gamma^{-1}\log(p_0V_0^{\gamma}), \tag{3.29a}$$

$$S_1 = \frac{p_1}{\gamma p_0} + \frac{V_1}{V_0}. \tag{3.29b}$$

To proceed we substitute the expansions (3.28) into the governing equations (3.26) and compare coefficients of $M$. In Sections 3.2.2 and 3.2.3 we show that the leading-order pressure, $p_0$, and specific volume, $V_0$, are constant either side of the flame, and the perturbations, $p_1$ and $u_0$, to the pressure and velocity are linear acoustic waves.

### 3.2.2 Ahead of the flame

We first consider the behaviour of the gas ahead of the flame. Substituting the expansions (3.28) into the governing equations (3.26) and comparing $\mathrm{ord}(1)$ terms, we find

$$\frac{\partial V_0}{\partial \tau} = \frac{\partial p_0}{\partial \chi} = \frac{\partial S_0}{\partial \tau} = 0. \tag{3.30}$$

Applying the leading-order initial conditions, $V_0(\chi, 0) = p_0(\chi, 0) = 1$, we deduce that the leading-order specific volume and pressure ahead of the flame are constant,

$$V_0^R = p_0^R = 1. \tag{3.31}$$

Initially the specific volume and pressure perturbations are zero—that is, $V_1(\chi, 0) = p_1(\chi, 0) = 0$ for $\chi \in (0, 1)$. From the expression (3.29b) for the entropy perturbation, $S_1$, and the $\mathrm{ord}(M)$ approximation to the energy equation (3.26c),

$$\frac{\partial S_1}{\partial \tau} = 0, \tag{3.32}$$

we deduce that $S_1^R = 0$. Substituting $S_1^R = 0$ and (3.31) into (3.29b), we find

$$V_1^R = -\frac{p_1^R}{\gamma}. \tag{3.33}$$

Using (3.33), we are able to eliminate $V_1$ from the $\mathrm{ord}(M)$ approximation to (3.26a),

$$\frac{\partial V_1}{\partial \tau} - \frac{\partial u_0}{\partial \chi} = 0. \tag{3.34}$$

We find that the remaining equations to solve to determine $p_1^R$ and $u_0^R$ are

$$\frac{1}{\gamma}\frac{\partial p_1^R}{\partial \tau} + \frac{\partial u_0^R}{\partial \chi} = 0, \tag{3.35a}$$

$$\frac{\partial u_0^R}{\partial \tau} + \frac{1}{\gamma}\frac{\partial p_1^R}{\partial \chi} = 0. \tag{3.35b}$$

The hyperbolic system of partial differential equations (3.35) describes acoustic waves travelling through the unburnt gas with unit speed. We solve (3.35) using the method of characteristics in Section 3.2.4.

### 3.2.3 Behind the flame

We now show that the leading-order specific volume, $V_0$, and pressure, $p_0$, behind the flame are also constant. The leading-order approximations (3.30) to the governing equations (3.26) hold for $\chi \in (0, \chi^*(\tau))$. We infer that $p_0$ is spatially uniform behind the flame from (3.30). From the leading-order approximation to the Chapman–Jouguet condition (3.4b),

$$[p_0]^+_- = 0, \tag{3.36}$$

we deduce that $p_0$ is continuous across the flame, and therefore $p_0 = 1$ for $\chi \in (0, 1)$. From the leading-order approximation to the Chapman–Jouguet condition (3.4a) and the leading-order solution ahead of the flame (3.31), we deduce that the specific volume, $V_0^L$, immediately behind the flame is given by

$$V_0^L(\chi^*(\tau), \tau) = 1 + Q. \tag{3.37}$$

Since, by (3.30), $V_0^L$ is constant along lines of constant $\chi$, we conclude that behind the flame

$$p_0^L = 1, \quad V_0^L = 1 + Q. \tag{3.38}$$

Behind the flame, we eliminate $V_1$ from (3.34)—the $\mathrm{ord}(M)$ approximation to (3.26a)—using (3.29b) and (3.32). We find that $p_1^L$ and $u_0^L$ satisfy

$$\frac{1+Q}{\gamma}\frac{\partial p_1^L}{\partial \tau} + \frac{\partial u_0^L}{\partial \chi} = 0, \tag{3.39a}$$

$$\frac{\partial u_0^L}{\partial \tau} + \frac{1}{\gamma}\frac{\partial p_1^L}{\partial \chi} = 0. \tag{3.39b}$$

In deriving (3.39), we have used (3.38) to evaluate $V_0^L$ and $p_0^L$. We solve the hyperbolic system of partial differential equations (3.39), which describe acoustic waves travelling at speed $1/(1+Q)$, using the method of characteristics in Section 3.2.4.

For completeness, the specific volume perturbation, $V_1^L$, can be written as

$$V_1^L = -\frac{V_0^L}{\gamma p_0} p_1^L(\chi, \tau) + V_0^L S_1^L(\chi), \tag{3.40}$$

where $V_0^L = 1 + Q$, $p_0 = 1$, and $p_1^L$ is the solution to (3.39). One would need to consider the $\mathrm{ord}(M)$ approximation to the Chapman–Jouguet condition (3.4a),

$$[p_0 V_1 + p_1 V_0]^+_- = 0, \tag{3.41}$$

to find an expression for $S_1^L$. However, in the context of autoignition, there is very little benefit to finding an expression for $S_1^L$ explicitly; we are more interested in the behaviour of the gas ahead of the flame. From the solution to (3.39), we have sufficient information about the conditions behind the flame to solve for $p_1$, $V_1$, $u_0$ ahead of the flame.

### 3.2.4 Solution using the method of characteristics

In Sections 3.2.2 and 3.2.3 we found that the pressure and velocity perturbations, $p_1$ and $u_0$, are linear acoustic waves, described on either side of the flame by

$$\frac{V_0}{p_0}\frac{\partial}{\partial\tau}\left(\frac{p_1}{\gamma}\right)+\frac{\partial u_0}{\partial\chi}=0, \tag{3.42a}$$

$$\frac{\partial u_0}{\partial\tau}+\frac{\partial}{\partial\chi}\left(\frac{p_1}{\gamma}\right)=0, \tag{3.42b}$$

where $p_0$ and $V_0$ are given by (3.31) and (3.38) either side of the flame. After some algebraic manipulation, we see that (3.42) can be rewritten as,

$$\frac{\partial}{\partial\tau}\left(\pm\sqrt{\frac{V_0}{p_0}}\frac{p_1}{\gamma}+u_0\right)\pm\sqrt{\frac{p_0}{V_0}}\frac{\partial}{\partial\chi}\left(\pm\sqrt{\frac{V_0}{p_0}}\frac{p_1}{\gamma}+u_0\right)=0. \tag{3.43}$$

Using the method of characteristics [72, §2.2], we deduce that, on either side of the flame, the quantity $\pm\gamma^{-1}p_1\sqrt{V_0/p_0}+u_0$ is constant along lines with $\mathrm{d}\chi/\mathrm{d}\tau=\pm\sqrt{p_0/V_0}$. We solve (3.43) subject to the initial and boundary conditions

$$p_1(\chi,0)=u_0(\chi,0)=0,\quad u_0(0,\tau)=u_0(1,\tau)=0, \tag{3.44}$$

for $\tau>0$, $\chi\in(0,\chi^*(\tau))\cup(\chi^*(\tau),1)$.

We are yet to solve (3.27) for the flame position, $\chi=\chi^*(\tau)$. In general, the mass flux, $q$, through the flame will change in time as the conditions in the gas ahead of the flame change. If the $\mathrm{ord}(M)$ temperature perturbation, $T_1$, ahead of the flame affects the leading-order approximation to the mass flux, $q$, as is the case for the one-step reaction (2.70) when $(EM)^{-1}=O(1)$, then we would have to solve for $q$, $p_1$ and $u_0$ simultaneously. However, the leading-order approximation to the mass flux for the three-step reaction, given by (2.88), is constant for $\tau=O(1)$ because the leading-order chemical composition (3.1) and leading-order thermodynamic properties (3.31) ahead of the flame are constant. Hence, for simplicity, we choose to focus on the case where $q=q_0+O(M)$ and $q_0$ is constant. Substituting (3.28a) into (3.27) and integrating, we find that

$$\chi_1^*=q_0\tau, \tag{3.45}$$

where we have used the initial condition, $\chi_1^*(0)=0$, to set the constant of integration to zero. Across the flame, the Chapman–Jouguet conditions (3.4) imply the pressure perturbation, $p_1$, is continuous,

$$[p_1]_-^+=0, \tag{3.46a}$$

and there is a jump in $u_0$,

$$[u_0]_-^+=Qq_0. \tag{3.46b}$$

We are now in a position to model the interaction between the flame and acoustic waves. Initially, the flame is at the left-hand wall, $\chi^*=0$, and the gas ahead of it is still. Having $u_0=0$ on either side of the flame is inconsistent with (3.46b). A step-like acoustic wave is therefore produced from the flame and travels into the unburnt gas

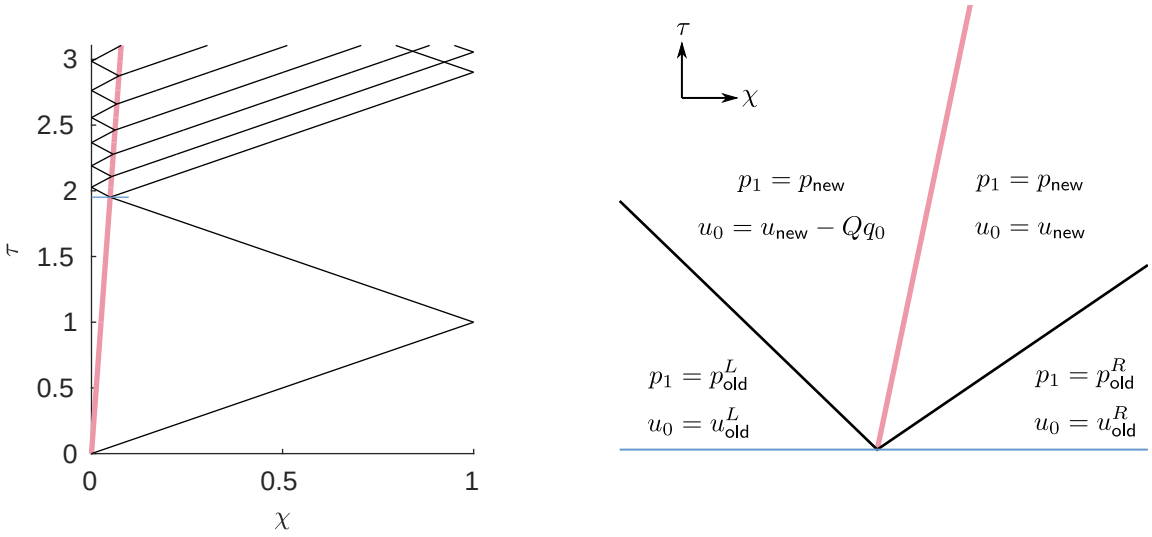


**Figure 3.2:** *Characteristic diagram: (a) Reflection and transmission of acoustic waves (black) at the flame (pink), and reflection of acoustic waves at the walls, $\chi = 0$ and $\chi = 1$; (b) Acoustic waves emanating from the flame. For this figure, $Q = 1.4$, $q_0 = 1$ and $M = 1/40$.*

along the characteristic $\chi = \tau$, as illustrated in Figure 3.2a. From (3.46b), we deduce that $u_0 = Qq_0$ immediately ahead of the flame, because the gas adjacent to the rigid wall $\chi = 0$ has zero velocity. Since $-\gamma^{-1}p_1 + u_0$ is constant along the $\mathrm{d}\chi/\mathrm{d}\tau = -1$ characteristics ahead of the flame, we deduce from the initial and boundary conditions (3.44) that the pressure perturbation, $p_1$, behind the first pressure wave is $p_1 = \gamma Q q_0$.

At $\tau = 1$, the acoustic wave hits the boundary, $\chi = 1$, and reflects back towards the flame. The magnitude of the pressure jump across the reflected wave is the same as the incident wave, meaning the pressure perturbation at the wall, $\chi = 1$, is $p_1 = 2\gamma Q q_0$. Behind the reflected wave, the velocity is zero. At the moment the reflected acoustic wave hits the flame there is an instantaneous imbalance of pressure across the flame. To restore the gas to a state where the Chapman–Jouguet conditions (3.46) hold across the flame, two acoustic waves are generated—one travelling into the unburnt gas and one travelling into the burnt gas. The characteristics emanating from the flame following a flame-acoustic interaction are depicted in Figure 3.2b. We denote the values of $p_1$ and $u_0$ adjacent to the flame at the moment the acoustic wave hits the flame by $p_1^R = p^R_{\text{old}}$, $u_0^R = u^R_{\text{old}}$, $p_1^L = p^L_{\text{old}}$ and $u_0^L = u^L_{\text{old}}$, and denote the values of $p_1$ and $u_0$ adjacent to and ahead of the flame following the collision by $p_1^R = p_{\text{new}}$ and $u_0^R = u_{\text{new}}$, as shown in Figure 3.2b. Using the method of characteristics on (3.43), and taking into account the Chapman–Jouguet conditions (3.46), we find that $p_{\text{new}}$ and $u_{\text{new}}$ satisfy

$$\sqrt{1+Q}\,\frac{p_{\text{new}}}{\gamma} + u_{\text{new}} - Qq_0 = \sqrt{1+Q}\,\frac{p^L_{\text{old}}}{\gamma} + u^L_{\text{old}}, \tag{3.47a}$$

$$\frac{p_{\text{new}}}{\gamma} - u_{\text{new}} = \frac{p^R_{\text{old}}}{\gamma} - u^R_{\text{old}}. \tag{3.47b}$$

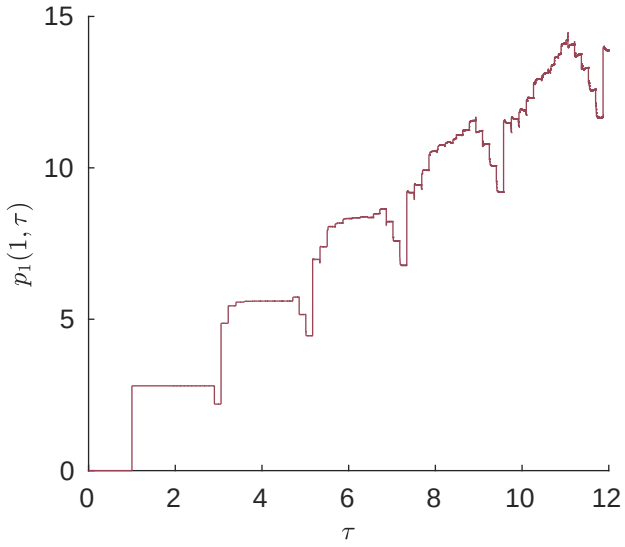


**Figure 3.3:** *Pressure perturbation, $p_1$, at the right-hand wall, $\chi = 1$, plotted against $\tau$. For this figure, $\gamma = Q = 1.4$, $q = 1$ and $M = 1/40$.*

Each acoustic wave produced at the flame travels away from the flame until it arrives at one of the boundaries, $\chi = 0$ or $\chi = 1$. The wave then reflects back towards the flame, before hitting the flame and generating more acoustic waves, as illustrated in the characteristic diagram in Figure 3.2a.

We use a numerical implementation of the method of characteristics that tracks each acoustic wave. At each step of our method, we note the position of the flame, and the position, amplitude and direction of travel of all the acoustic wave fronts. Using the speed of sound on either side of the flame and the speed of the flame, we calculate the time at which an acoustic wave next hits either the flame or one of the walls, and then update the position of the flame and all the acoustic waves. When an acoustic wave hits the flame, we delete that acoustic wave from our list, and add two new acoustic waves at the flame position—one travelling in each direction for the transmitted and reflected components of the incident wave. When an acoustic wave hits one of the walls, we delete that acoustic wave from our list, and add another wave travelling in the opposite direction. Despite the simplicity of the method of characteristics, it is infeasible to use this method for large times because the number of waves that need tracking increases exponentially.

In Figure 3.3, the pressure perturbation, $p_1$, at the right-hand wall, $\chi = 1$, is plotted against $\tau$. The cumulative effect of the repeated interactions between the flame and the acoustic waves is an overall increase in pressure, which is evident in Figure 3.3. As the pressure perturbation, $p_1$, increases, our assumption that (3.28b) is an asymptotic series becomes invalid. The model (3.42)–(3.46) is therefore only valid for $\tau = O(1)$ as $M \to 0$. In Section 3.3, we use the method of multiple scales to derive a model for normal combustion that is valid for $t = O(1)$.

## 3.3 Long-time behaviour: multiple scales analysis

So far in this chapter we have looked at the problem of flame propagation on two distinct time scales. In Section 3.1, we looked at the adiabatic compression of the unburnt gas on the $t$-time scale, with $t = O(1)$ representative of the time taken for the flame to cross the domain. In Section 3.2, we looked at acoustic variations in the unburnt gas on the $\tau$-time scale, with $\tau = O(1)$ representative of the time taken for an acoustic wave to cross the domain. Unfortunately, both of these models are unsatisfactory for understanding normal combustion; the former does not satisfy all of the initial conditions (3.6) and the latter does not remain asymptotic for $t = \mathrm{ord}(1)$.

To understand the long-time behaviour of the flame, we need to account for both the rapid acoustic variations in the gas and the slow adiabatic compression associated with the flame propagation, which, as we have seen, occur on disparate time scales. One might expect that we could use the method of multiple scales [46, §7], treating $t$ and $\tau = t/M$ as independent variables. However, due to the changing sound speed in the gas either side of the flame, we are unable to find an asymptotically consistent solution using only a single short time variable. Instead, we use a method similar to the WKBJ method for linear equations [46, §7.5] and similar to the method exploited by Bauwens et al. [5].

Ultimately, we find that the leading-order approximations to the pressure, temperature and specific volume vary slowly in time. The leading-order pressure, temperature and specific volume perturbations and the leading-order approximation to the velocity vary rapidly in time, and can be written in terms of a series of modes whose frequency, amplitude and spatial structure all vary slowly with time. Specifically, in Section 3.3.4, we find that the solution to (3.2) for the pressure, $p$, has the form

$$p \sim p_0(t) + M\left(\check{p}_1(t) + \tilde{p}_1(\chi, t)\right) + o(M), \tag{3.48}$$

as $M \to 0$, where

$$\tilde{p}_1(\chi, t) = \sum_{n=1}^{\infty} \left( A_n(t) e^{i\phi_n(t)/M} + \overline{A_n(t)} e^{-i\phi_n(t)/M} \right) G_n(\chi, t), \tag{3.49}$$

and $p_0(t)$, $\check{p}_1(t)$, $(A_n(t))_{n\geq 1}$, $(\phi_n(t))_{n\geq 1}$ and $(G_n(\chi, t))_{n\geq 1}$ are functions we define as part of the solution. In some sense, the phase, $\tau_n = \phi_n(t)/M$, can be thought of as a short time variable that describes the evolution of the mode indexed by $n$. It is tempting to press forward with the method of multiple scales by treating $t$ and $(\tau_n)_{n\geq 1}$ as independent variables [5]. However, we will need slightly more flexibility in our notation to deal with nonlinear terms, such as $\partial(p^2)/\partial t$. For all $n \geq 1$, $\tau_n$ is $\mathrm{ord}(1/M)$, so while developing the model we let $\tau$ be a representative short time variable, where

$$\tau = \phi(t)/M \tag{3.50}$$

and $\phi(t)$ is a function of $t$ with $\phi(t) = O(1)$ as $M \to 0$. As usual in multiple scales analysis [6, §11.2], we treat $\tau$ and $t$ as independent variables, so that the $t$-derivatives in (3.2) become

$$\frac{\partial}{\partial t} = \frac{\phi'(t)}{M} \left( \frac{\partial}{\partial \tau} \right)_t + \left( \frac{\partial}{\partial t} \right)_\tau. \tag{3.51}$$

At this stage, it is also necessary to introduce a representative short space variable, $\zeta$, because, in Section 3.3.4, we find that the entropy, $S$, exhibits fine spatial variations behind the flame. We define $\zeta$ by

$$\zeta = \psi(\chi)/M, \tag{3.52}$$

where $\psi(\chi)$ is a function of $\chi$ with $\psi(\chi) = O(1)$ as $M \to 0$. We treat $\zeta$ and $\chi$ as independent variables, so the $\chi$-derivatives in (3.2) become

$$\frac{\partial}{\partial \chi} = \frac{\psi'(\chi)}{M}\left(\frac{\partial}{\partial \zeta}\right)_{\chi} + \left(\frac{\partial}{\partial \chi}\right)_{\zeta}. \tag{3.53}$$

Written in terms of $t$, $\tau$, $\chi$ and $\zeta$, the governing equations (3.2a) and (3.2b) either side of the flame are

$$\phi'(t)\frac{\partial V}{\partial \tau} + M\frac{\partial V}{\partial t} - \psi'(\chi)\frac{\partial u}{\partial \zeta} - M\frac{\partial u}{\partial \chi} = 0, \tag{3.54a}$$

$$M^2\phi'(t)\frac{\partial u}{\partial \tau} + M^3\frac{\partial u}{\partial t} + \frac{\psi'(\chi)}{\gamma}\frac{\partial p}{\partial \zeta} + \frac{M}{\gamma}\frac{\partial p}{\partial \chi} = 0. \tag{3.54b}$$

From (3.2c), we conclude that the entropy, $S$, on both sides of the flame is independent of $t$. Therefore, in this multiple scales formulation, $S$ is a function of $\chi$ and $\zeta$,

$$S(\chi, \zeta) = \gamma^{-1}\log(pV^{\gamma}). \tag{3.54c}$$

In terms of $t$ and $\tau$, the equation (3.3) for the flame position, $\chi^*$, is

$$\phi'(t)\frac{\partial \chi^*}{\partial \tau} + M\frac{\partial \chi^*}{\partial t} = Mq. \tag{3.55}$$

We pose that the solution of (3.54) and (3.55) takes the form of Poincaré series [46, §2.5], with

$$\chi^* \sim \chi_0^* + M\chi_1^* + M^2\chi_2^* + \cdots, \tag{3.56a}$$
$$p \sim p_0 + Mp_1 + M^2p_2 + M^3p_3 + \cdots, \tag{3.56b}$$
$$V \sim V_0 + MV_1 + M^2V_2 + \cdots, \tag{3.56c}$$
$$u \sim u_0 + Mu_1 + M^2u_2 + \cdots, \tag{3.56d}$$

as $M \to 0$. Substituting (3.56b) and (3.56c) into (3.2e) and (3.54c) and Taylor expanding in powers of $M$, we deduce

$$T \sim T_0 + MT_1 + \cdots, \tag{3.56e}$$
$$S \sim S_0 + MS_1 + M^2S_2 + \cdots, \tag{3.56f}$$

as $M \to 0$, where

$$T_0 = p_0V_0, \tag{3.57a}$$
$$T_1 = p_1V_0 + p_0V_1. \tag{3.57b}$$

$$S_0(\chi,\zeta) = \gamma^{-1}\log(p_0 V_0^{\gamma}), \tag{3.58a}$$

$$S_1(\chi,\zeta) = \frac{p_1}{\gamma p_0} + \frac{V_1}{V_0}, \tag{3.58b}$$

$$S_2(\chi,\zeta) = \frac{p_2}{\gamma p_0} - \frac{p_1^2}{2\gamma p_0^2} + \frac{V_2}{V_0} - \frac{V_1^2}{2V_0^2}. \tag{3.58c}$$

To proceed, we substitute the expansions (3.56) into (3.4)–(3.6), (3.54) and (3.55), and compare coefficients of powers of $M$. By introducing additional variables to represent short time and length scales, we have introduced additional degrees of freedom to the model (3.2)–(3.6). In the following analysis, as with conventional multiple scales analysis, we exploit the extra degrees of freedom to ensure the solution (3.56) remains asymptotic for $t = O(1)$. Note that, in writing (3.48), we have separated the $\mathrm{ord}(M)$ term into an oscillatory component, $\tilde{p}_1$, with zero mean, and a slowly-varying component, $\check{p}_1$, where $\partial\check{p}_1/\partial\tau = 0$. Separating the pressure, and subsequently all other dependent variables, into two components in this way allows us to identify the solubility (or solvability[1]) conditions that are necessary for us to proceed with the method of multiple scales, and will form a central part of the analysis for the rest of this chapter.

### 3.3.1 Approximate flame position

Finding an approximation to the flame position, $\chi^*$, is an important first step in our analysis. We use the leading-order approximation, $\chi_0^*$, to the flame position to define the domain on which we solve (3.54).

To solve (3.55) for the flame position, we must specify a model for the mass flux, $q$. In this section we consider the mass flux model derived in Section 2.2.2.2 for the three-step reaction (2.6). We do not consider the one-step reaction mechanism in this section; the unsuitability of the one-step reaction mechanism for modelling normal combustion in confinement and autoignition will be discussed in Section 4.1.

In Section 2.2.2.2, we found the mass flux through a flame with three-step chemistry (2.6) has form

$$q \sim q^{(0)}(T^{R*}, Y^{R*}) + E^{-1}q^{(1)}(T^{R*}, Y^{R*}) + O(E^{-2}), \tag{3.59}$$

as $E \to \infty$, where $q^{(0)}$ and $q^{(1)}$ are given by (2.88) and (2.94) respectively, provided that $EM = O(1)$. Recall that, here, $T^{R*} = \lim_{\chi\searrow\chi^*} T^R$ and $Y^{R*} = \lim_{\chi\searrow\chi^*} Y_{\mathcal{F}}^R$ are the temperature and mass fraction of fuel immediately in front of the flame, respectively. To use (3.59) consistently with the asymptotic expansions (3.56) in (3.4) and (3.55), we need to specify the relative sizes of $E$ and $M$. In Section 4.2, we will reason that the distinguished limit defined by $EM = O(1)$ and $E^2M \gg 1$ is of most interest for studying autoignition. Hence, for the rest of this chapter, we will limit our discussion to the parameter regime where $EM = O(1)$ and $E^2M \gg 1$.

[1]We use the same terminology as Hinch [46].

In Section 3.3.4, we find that the temperature, $T^{R*}$, immediately ahead of the flame can be written as

$$T^{R*} \sim T_0^{R*} + M(\check{T}_1^{R*} + \tilde{T}_1^{R*}) + o(M), \tag{3.60}$$

where $\partial T_0^{R*}/\partial\tau = \partial\check{T}_1^{R*}/\partial\tau = \int_0^{2\pi} \tilde{T}_1^{R*}\,\mathrm{d}\tau = 0$. Substituting (3.1) and (3.60) into (3.59) and expanding in powers of $M$, we find that $q$ can be written as,

$$q \sim q_0 + Mq_1 + o(M), \tag{3.61}$$

where $q_1 = \check{q}_1 + \tilde{q}_1$, and

$$q_0 = q^{(0)}(T_0^{R*}, 1) + E^{-1}q^{(1)}(T_0^{R*}, 1), \tag{3.62a}$$

$$\check{q}_1 = \check{T}_1^{R*}\left.\frac{\partial q^{(0)}}{\partial T^{R*}}\right|_{(T^{R*},Y^{R*})=(T_0^{R*},1)}, \tag{3.62b}$$

$$\tilde{q}_1 = \tilde{T}_1^{R*}\left.\frac{\partial q^{(0)}}{\partial T^{R*}}\right|_{(T^{R*},Y^{R*})=(T_0^{R*},1)}. \tag{3.62c}$$

As with (3.48), we have split the $\mathrm{ord}(M)$ term in (3.61) into two parts, emphasising that $\partial\check{q}_1/\partial\tau = 0$ and $\int_0^{2\pi}\tilde{q}_1\,\mathrm{d}\tau = 0$. Before the end of this section, we will see that splitting $q_1$ in this way allows us to find an equation governing the evolution of $\chi_1^*$.

As a brief aside, note that the $O(E^{-1})$ term, $E^{-1}q^{(1)}(T_0^{R*}, 1)$, has been included in the $O(1)$ term (3.62a) because the parameter regime we are studying, defined by $EM = O(1)$ and $E^2M \gg 1$, includes the possibility that $E^{-1} \gg M$. Furthermore, the error in the approximate mass flux (3.61) is $o(M)$, not $O(M^2)$. We could include $O(E^{-2})$ and $O(E^{-1}M)$ terms in $q_1$, if we were so inclined. However, an $O(M)$ description of the mass flux with $o(M)$ errors is acceptable for our discussion.

We are now in a position to find the flame position, $\chi^*$. Substituting (3.56a) and (3.61) into (3.55) and comparing powers of $M$, we find the leading-order flame position, $\chi_0^*$, satisfies

$$\frac{\partial\chi_0^*}{\partial\tau} = 0. \tag{3.63}$$

We conclude that $\chi_0^*$ is a function of $t$ only. From the $\mathrm{ord}(M)$ approximation of (3.55), we find that

$$\phi'(t)\frac{\partial\chi_1^*}{\partial\tau} = -\frac{\mathrm{d}\chi_0^*}{\mathrm{d}t} + q_0. \tag{3.64}$$

For (3.56a) to remain asymptotic for $t = \mathrm{ord}(1)$, we cannot have $\chi_1^*$ growing faster than $\chi_0^*$. As we have established in (3.62a) and (3.63), $\chi_0^*$ and $q_0$ are independent of $\tau$. We therefore insist that

$$\frac{\mathrm{d}\chi_0^*}{\mathrm{d}t} = q_0, \tag{3.65}$$

to prevent $\chi_1^*$ growing linearly with $\tau$, which would otherwise invalidate our assumption that (3.56a) is asymptotic for $t = \mathrm{ord}(1)$. Similarly, from the $\mathrm{ord}(M^2)$ terms of (3.55), we find

$$\phi'(t)\frac{\partial\chi_2^*}{\partial\tau} - \tilde{q}_1 = -\frac{\mathrm{d}\chi_1^*}{\mathrm{d}t} + \check{q}_1. \tag{3.66}$$

Since $\chi_1^*$ and $\check{q}_1$ are independent of $\tau$, and $\int_0^{2\pi} \tilde{q}_1 \, \mathrm{d}\tau = 0$, we require

$$\frac{\mathrm{d}\chi_1^*}{\mathrm{d}t} = \check{q}_1, \tag{3.67}$$

to prevent $\chi_2^*$ growing linearly with $\tau$.

By solving (3.65) subject to the initial condition $\chi_0^*(0) = 0$, we find the leading-order approximation to the flame position, $\chi^* = \chi_0^*(t)$. Going forward, we use the leading-order flame position, $\chi_0^*$, as the divider between the burnt and unburnt gas. That is, we solve (3.54) for $\chi \in (0, \chi_0^*) \cup (\chi_0^*, 1)$, rather than for $\chi \in (0, \chi^*) \cup (\chi^*, 1)$. To find the appropriate boundary conditions to apply at $\chi = \chi_0^*$, we substitute (3.56a) into the Chapman–Jouguet conditions (3.4) and Taylor expand around $\chi_0^*$. We will state the approximate Chapman–Jouguet conditions at $\chi = \chi_0^*$ where needed without further comment. For the three-step mass flux model (3.62), we find that the solution to (3.67) with $\chi_1^*(0) = 0$ is $\chi_1^* = 0$. We will, however, continue to account for $\chi_1^*$ in our analysis below, so that our analysis is applicable for a generic mass flux model of the form (3.61) as far as possible.

### 3.3.2 Leading order in terms of $p_0(t)$

Having established the leading-order flame position, $\chi_0^*$, we are now in a position to solve (3.54) for $\chi \in (0, \chi_0^*) \cup (\chi_0^*, 1)$. By substituting (3.56) into (3.4)–(3.6) and (3.54) and comparing coefficients of $M$, we find that the zero Mach approximation from Section 3.1 yields the leading-order pressure, $p_0$ and specific volume, $V_0$.

The leading-order terms from (3.54b),

$$\frac{\partial p_0}{\partial \zeta} = 0, \tag{3.68}$$

imply that $p_0$ is independent of $\zeta$ on both sides of the flame. If (3.56b) is to remain asymptotic as $M \to 0$, we cannot have $p_1$ growing linearly with $\zeta$. The $\mathrm{ord}(M)$ terms from (3.54b) yield that, on both sides of the flame,

$$\psi'(\chi) \frac{\partial p_1}{\partial \zeta} = -\frac{\partial p_0}{\partial \chi}. \tag{3.69a}$$

To prevent $p_1$ having a linear dependence on $\zeta$, we conclude that $p_0$ must satisfy

$$\frac{\partial p_0}{\partial \chi} = 0, \tag{3.69b}$$

on both sides of the flame. In a moment, we will use a very similar argument to show that $\partial u_0 / \partial \zeta = 0$. To streamline the presentation, the equivalent of (3.69) will be combined into a single line where possible.

#### 3.3.2.1 Ahead of the flame

With (3.68) and (3.69) we have shown that $p_0$ is independent of $\chi$ and $\zeta$ on both sides of the flame. We now consider the leading-order entropy, $S_0^R$, ahead of the flame to show $p_0^R$ is a function of $t$ only.

Applying the initial conditions (3.6) to (3.58a), we find that $S_0^R = 0$, or equivalently,

$$p_0^R (V_0^R)^\gamma = 1. \tag{3.70}$$

Since $\partial p_0^R/\partial\chi = \partial p_0^R/\partial\zeta = 0$, we deduce from (3.70) that $V_0^R$ is also independent of $\chi$ and $\zeta$. Considering the $\mathrm{ord}(1)$ terms from (3.54a), we require

$$\psi'(\chi)\frac{\partial u_0^R}{\partial\zeta} = \phi'(t)\frac{\partial V_0^R}{\partial\tau} = 0, \tag{3.71}$$

to prevent $u_0^R$ growing linearly with $\zeta$ ahead of the flame.

From (3.70) and (3.71), we conclude that the leading-order pressure, $p_0^R$, ahead of the flame is some, as yet unknown, function of $t$ only,

$$p_0^R = p_0(t). \tag{3.72}$$

It follows from (3.57a) and (3.70), that the leading-order temperature, $T_0^R$, and specific volume, $V_0^R$, are also functions of $t$ only, with

$$T_0^R = p_0(t)^{1-1/\gamma}, \quad V_0^R = p_0(t)^{-1/\gamma}. \tag{3.73}$$

It follows from (3.62a) and (3.73) that the leading-order mass flux, $q_0$, is independent of $\tau$ as asserted in section 3.3.1. The leading-order flame position, $\chi_0^*(t)$, is therefore found by solving (3.65) subject to the initial condition $\chi_0^*(0) = 0$.

#### 3.3.2.2 Behind the flame

Since the flame starts at $\chi = 0$, any gas behind the flame at $t > 0$ has passed through the flame at some earlier time $t_0^* < t$. We are therefore unable to use the initial conditions (3.6) directly to determine the entropy, $S^L$, for $\chi \in (0, \chi_0^*(t))$. We now consider the Chapman–Jouguet conditions (3.4) at the approximate flame position, $\chi = \chi_0^*(t)$, to find the pressure and entropy behind the flame. Similarly to in Section 3.1.3, we define $t_0^*(\chi)$ as the inverse of the leading-order flame position function, $\chi_0^*(t)$, so that

$$\chi_0^*(t_0^*(\chi)) = \chi. \tag{3.74}$$

Balancing the $\mathrm{ord}(1)$ terms in the approximation to the Chapman–Jouguet condition (3.4b) at $\chi = \chi_0^*(t)$, we deduce that

$$[p_0]_-^+ = 0. \tag{3.75}$$

From (3.68) and (3.69) we have already established that $p_0^L$ is spatially uniform. We therefore infer from (3.75) that

$$p_0 = p_0(t) \tag{3.76}$$

for $\chi \in (0, \chi_0^*)$, as well as for $\chi \in (\chi_0^*, 1)$.

From (3.58a) we have that the leading-order entropy, $S_0^L$, behind the flame does not vary with time. However, due to the liberation of chemical energy as the fuel burns across the flame, the entropy does vary in space behind the flame. To find $S_0^L$ at $\chi \in (0, \chi_0^*(t))$, we use (3.58a), (3.75) and the $\mathrm{ord}(1)$ approximation to the Chapman–Jouguet condition (3.4c),

$$[p_0 V_0]_-^+ = -Q. \tag{3.77}$$

Following an identical argument to that used in Section 3.1.3, we find that

$$S_0^L = \log\left(1 + Q p_0^R (t_0^*(\chi))^{\frac{1-\gamma}{\gamma}}\right). \tag{3.78}$$

Substituting (3.76) and (3.78) into (3.58a), we deduce that

$$V_0^L = p_0(t)^{-1/\gamma}\left(1 + Q p_0 (t_0^*(\chi))^{\frac{1-\gamma}{\gamma}}\right). \tag{3.79}$$

As is the case ahead of the flame, we recognise that the leading-order specific volume, $V_0^L$, behind the flame is independent of $\zeta$. Therefore, by considering the $\mathrm{ord}(1)$ terms from (3.54a), we require

$$\psi'(\chi)\frac{\partial u_0^L}{\partial \zeta} = \phi'(t)\frac{\partial V_0^L}{\partial \tau} = 0, \tag{3.80}$$

to prevent $u_0^L$ growing linearly with $\zeta$.

#### 3.3.2.3 Summary

Before pressing ahead to find $u_0$, we reflect on what we have found so far. We have found that the pressure, $p$, is spatially uniform to leading order as $M \to 0$. That is,

$$p \sim p_0(t), \tag{3.81}$$

for $\chi \in (0, 1)$, $t > 0$, where $p_0(t)$ is some, as yet unknown, function of $t$. We have also found that the leading-order specific volume, $V_0$, can be written in terms of $p_0$, with

$$V_0(\chi, t) = \begin{cases} V_0^L(\chi, t) = p_0(t)^{-1/\gamma}\left(1 + Q p_0 (t_0^*(\chi))^{\frac{1-\gamma}{\gamma}}\right), & \text{for } \chi \in (0, \chi_0^*(t)), \\ V_0^R(t) = p_0(t)^{-1/\gamma}, & \text{for } \chi \in (\chi_0^*(t), 1). \end{cases} \tag{3.82}$$

### 3.3.3 Leading order pressure in terms of flame position

In Section 3.3.2, we found the leading-order approximations to the specific volume, $V$, and pressure, $p$, in terms of a function, $p_0(t)$, which we are still to determine. In this section, we use the conservation of mass to find an ordinary differential equation governing the evolution of $p_0(t)$ for $t > 0$.

Our first step towards finding an ODE for $p_0(t)$ is to show that $\partial u_1/\partial \zeta = 0$. From (3.71), (3.80) and (3.82), we have that $\partial u_0/\partial \zeta = \partial V_0/\partial \zeta = 0$ on both sides of the flame. Furthermore, by rearranging (3.58b), and making use of (3.69), we find

$$V_1 = V_0(\chi, t) S_1(\chi, \zeta) - \frac{V_0(\chi, t) p_1(\chi, t, \tau)}{\gamma p_0(t)}, \tag{3.83}$$

on both sides of the flame. Differentiating (3.83) with respect to $\tau$, we note that $\partial V_1/\partial\tau$ is independent of $\zeta$. Considering the $\mathrm{ord}(M)$ terms from (3.54a), we require

$$\psi'(\chi)\frac{\partial u_1}{\partial\zeta} = \phi'(t)\frac{\partial V_1}{\partial\tau} + \frac{\partial V_0}{\partial t} - \frac{\partial u_0}{\partial\chi} = 0, \tag{3.84}$$

to avoid $u_1$ with growing linearly in $\zeta$. The solubility condition (3.84) ensures (3.56d) remains asymptotic.

With (3.84), we have an equation relating $V_0$ and $u_0$ that we might hope to use to derive the ODE for $p_0$. From (3.82), we have that $V_0$ is independent of $\tau$, but currently we have no similar information about $u_0$, so a suitable solubility condition for $V_1$ in not immediately obvious. To proceed, we assume that $u_0$ can be written as

$$u_0 = \check{u}_0(\chi, t) + \tilde{u}_0(\chi, t, \tau), \tag{3.85}$$

where $\partial\check{u}_0/\partial\tau = 0$, $\int_0^{2\pi}\tilde{u}_0\,\mathrm{d}\tau = 0$, $\tilde{u}_0$ is continuous for $\chi \in (0,1)$, and

$$\check{u}_0(0,t) = \check{u}_0(1,t) = \tilde{u}_0(0,t,\tau) = \tilde{u}_0(1,t,\tau) = 0. \tag{3.86}$$

Now, to ensure (3.56c) remains asymptotic, we insist that

$$\frac{\partial V_0}{\partial t} - \frac{\partial\check{u}_0}{\partial\chi} = 0, \tag{3.87}$$

so that $V_1$ does not grow linearly with $\tau$ in (3.84).

Integrating (3.87) with respect to $\chi$ yields the ODE for $p_0(t)$ we require. To see this, first note that the $\mathrm{ord}(1)$ approximations to the Chapman–Jouguet conditions (3.4a) and (3.4c) indicate there is a discontinuity in $\check{u}_0$ across $\chi = \chi_0^*$,

$$[\check{u}_0]_-^+ = \frac{Q\check{q}_0}{p_0}. \tag{3.88}$$

Secondly, it follows from (3.82) that

$$\frac{\partial V_0}{\partial t} = -\frac{V_0(\chi,t)}{\gamma p_0(t)}\frac{\mathrm{d}p_0}{\mathrm{d}t}. \tag{3.89}$$

Making use of (3.86), (3.88) and (3.89), we find upon integrating (3.87) with respect to $\chi$ that

$$\frac{1}{\gamma p_0}\frac{\mathrm{d}p_0}{\mathrm{d}t}\int_0^1 V_0\,\mathrm{d}\chi = \frac{Qq_0}{p_0}. \tag{3.90}$$

It follows from (3.4a), (3.6), (3.65) and (3.87) that

$$\int_0^1 V_0(\chi,t)\,\mathrm{d}\chi = 1, \tag{3.91}$$

meaning that $p_0(t)$ satisfies

$$\frac{\mathrm{d}p_0}{\mathrm{d}t} = \gamma Q q_0, \quad p_0(0) = 1. \tag{3.92}$$

By eliminating $q_0$ from (3.66) and (3.92) and integrating, we find that

$$p_0 = 1 + \gamma Q \chi_0^*(t). \tag{3.93}$$

By substituting (3.93) into (3.82), we find

$$V_0(\chi, t) = \begin{cases} (1 + \gamma Q \chi_0^*(t)))^{-1/\gamma} \left(1 + Q(1 + \gamma Q \chi)^{\frac{1-\gamma}{\gamma}}\right), & \text{for } \chi \in (0, \chi_0^*(t)), \\ (1 + \gamma Q \chi_0^*(t))^{-1/\gamma}, & \text{for } \chi \in (\chi_0^*(t), 1). \end{cases} \tag{3.94}$$

As with the zero Mach number approximation from Section 3.1, we conclude from (3.94) that the leading-order specific volume, $V_0(\chi, t)$, only depends on time through the flame position, $\chi_0^*(t)$. In other words, the leading-order specific volume and temperature profiles for a fixed flame position do not depend on the chemistry of the flame. We also recognise that $\check{u}_0$ is precisely the velocity profile we found using the zero Mach number approximation in Section 3.1.

### 3.3.4 The form of $p_1$ and $\tilde{u}_0$

In Section 3.3.3, we found that the leading-order pressure, $p_0(t)$, and specific volume, $V_0(\chi, t)$, only depend on time through the flame position, $\chi_0^*(t)$. To find $p_0(t)$ in terms of the flame position, we split the leading-order velocity, $u_0$, into two parts: a discontinuous slowly-varying part, $\check{u}_0$, and a continuous rapidly-varying part, $\tilde{u}_0$. We now look to complete our leading-order description of normal combustion by finding an expression for $\tilde{u}_0$.

To arrive at a system of equations that can be solved for $\tilde{u}_0$ and $p_1$, we first substitute the asymptotic series (3.56) into (3.54b) and compare coefficients of $M^2$ to find

$$\psi'(\chi) \frac{\partial p_2}{\partial \zeta} = -\phi'(t) \frac{\partial \tilde{u}_0}{\partial \tau} - \frac{1}{\gamma} \frac{\partial p_1}{\partial \chi}, \tag{3.95}$$

where we have used $\partial \check{u}_0 / \partial \tau = 0$ to eliminate $\check{u}_0$. With (3.69), (3.71) and (3.80), we have already established that $u_0$ and $p_1$ are independent of $\zeta$. We therefore require

$$\phi'(t) \frac{\partial \tilde{u}_0}{\partial \tau} + \frac{1}{\gamma} \frac{\partial p_1}{\partial \chi} = 0, \tag{3.96}$$

because our assumption that (3.56b) is an asymptotic series for $\chi = \mathrm{ord}(1)$ would become invalid for if $p_2$ was allowed to grow linearly with $\zeta$.

By eliminating $V_1$ and $\check{u}_0$ from (3.84) using (3.83) and (3.87), we find a second equation relating $p_1$ and $\tilde{u}_0$,

$$\phi'(t) \frac{V_0}{\gamma p_0} \frac{\partial p_1}{\partial \tau} + \frac{\partial \tilde{u}_0}{\partial \chi} = 0. \tag{3.97}$$

We have assumed that $\tilde{u}_0$ is continuous across $\chi = \chi_0^*$, and it follows from the approximation to the Chapman–Jouguet condition (3.4b) at $\chi = \chi_0^*$ that $p_1$ is also continuous. By eliminating $\tilde{u}_0$ from (3.96) and (3.97), we are left to solve

$$\phi'(t)^2 \frac{V_0(\chi, t)}{p_0(t)} \frac{\partial^2 p_1}{\partial \tau^2} - \frac{\partial^2 p_1}{\partial \chi^2} = 0. \tag{3.98}$$

From (3.86) and (3.96), we deduce that $p_1$ is continuously differentiable and satisfies

$$\frac{\partial p_1}{\partial \chi} = 0, \tag{3.99}$$

at the rigid boundaries, $\chi = 0$ and $\chi = 1$.

Ignoring the $t$ dependence of the coefficient of $\partial^2 p_1/\partial \tau^2$ for the moment, we recognise (3.98) as the linear wave equation with an inhomogeneous wave speed. Experience with solving the wave equation on a finite domain would suggest that we seek a solution that is a superposition of eigenmodes [71, §4.2].

#### 3.3.4.1 Eigenvalue problem

We identify the eigenmodes using separation of variables, treating $t$ as a parameter. Suppose $p_1 = F(\tau, t)G(\chi, t)$ satisfies (3.98), then, separating variables, we find $F$ and $G$ satisfy

$$\frac{\phi'(t)^2}{F(\tau,t)}\frac{\partial^2 F}{\partial \tau^2} = \frac{p_0(t)}{V_0(\chi,t)G(\chi,t)}\frac{\partial^2 G}{\partial \chi^2} = -\omega(t)^2, \tag{3.100}$$

where $\omega(t)$ is to be determined.

The resulting eigenvalue problem for $G$ is

$$\frac{\partial^2 G}{\partial \chi^2} = -\frac{\omega(t)^2 V_0(\chi,t)}{p_0(t)}G, \tag{3.101a}$$

with boundary conditions

$$\frac{\partial G}{\partial \chi} = 0 \quad \text{at} \quad \chi = 0, 1. \tag{3.101b}$$

It follows from Sturm–Liouville theory [42, §11.4] that there are a countably infinite number of eigenvalues, $\omega(t)$, where the solution to (3.101) is non-trivial. We index the eigenvalues, which are real and distinct, by $n$ such that $\omega_0 = 0$ and $\omega_{n+1}(t) > \omega_n(t)$ for $n \in \mathbb{N}$. For the eigenvalue, $\omega_n(t)$, we denote the corresponding eigenfunction by $G_n(\chi, t)$.

It follows from (3.101a) that $(G_n(\chi,t))_{n\geq 0}$ are continuously differentiable, despite the discontinuity in $V_0(\chi, t)$. To specify each $G_n$ uniquely, we insist that

$$\int_0^1 \frac{V_0(\chi,t)G_n(\chi,t)^2}{p_0(t)}\,\mathrm{d}\chi = 1 \quad \text{and} \quad G_n(0,t) \geq 0. \tag{3.101c}$$

A consequence of the integral constraint (3.101c) is that $G_n$ is real for $n \geq 0$. Since $p_0$ and $V_0$ depend on time only through the flame position, we find that the eigenfunctions, $(G_n(\chi,t))_{n\geq 0}$, and eigenvalues, $(\omega_n(t))_{n\geq 0}$, are similarly independent of the underlying rate of chemical reaction. We solve (3.101) numerically, using the Chebfun `eigs` function [33, §7.5]. It is necessary to solve for $(G_n(\chi,t))_{n\geq 1}$ numerically, because $V_0/p_0$ is not spatially uniform behind the flame. In Figure 3.4a, we plot $G_n(\chi, t_0^*(0.4))$ for $n = 0, 1, \ldots, 5$, and, in Figure 3.4b, we plot $\omega_n(t)$ against $\chi_0^*(t)$ for $n = 0, 1, \ldots, 5$.

We now treat the special case, $n = 0$, separately. From (3.101), we deduce that $\partial G_0/\partial \chi = 0$. Furthermore, we require $\partial F_0/\partial \tau = 0$ in order to satisfy (3.100) when

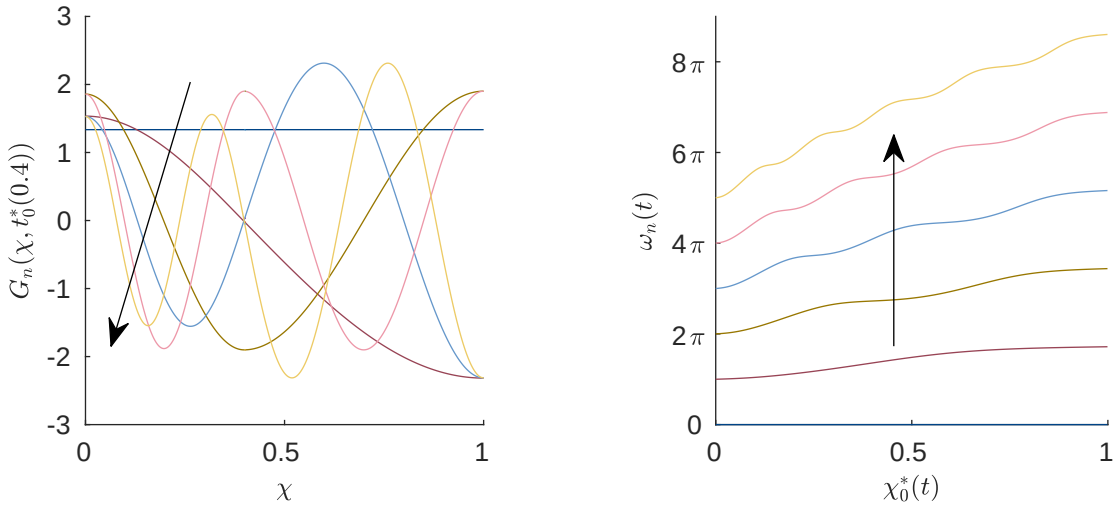


**(a)** *Eigenfunctions.* **(b)** *Eigenvalues.*

**Figure 3.4:** *Solutions to the eigenvalue problem* (3.101) *for* $n = 0, 1 \ldots, 5$*: (a) Spatial structure of the eigenfunctions,* $\{G_n(\chi, t)\}$*, with the flame position fixed at* $\chi_0^* = 0.4$*; (b) The eigenvalues,* $\{\omega_n(t)\}$*, plotted against flame position,* $\chi_0^*(t)$*. The arrows pass though the plotted functions in order of increasing* $n$*. For this figure,* $\gamma = Q = 1.4$*.*

$\omega = 0$, whilst also ensuring the series (3.56b) remains asymptotic for $t = \mathrm{ord}(1)$. The 'zeroth' eigenmode is therefore simply a function of $t$ that we will call $\check{p}_1(t)$.

Now, considering the general case, from (3.100) we have that, for $n \geq 1$,

$$\phi'(t)^2 \frac{\partial^2 F_n}{\partial \tau^2} + \omega_n(t)^2 F_n = 0. \tag{3.102}$$

At this stage, we must remember that we introduced $\tau = \phi(t)/M$ as a representative short time variable, where $\phi$ is to still be defined. For the $n$-th eigenmode, we require $F_n$ to be periodic in $\tau$, with a period independent of $t$. Without loss of generality, we choose the period to be $2\pi$, and hence define $\tau = \tau_n = \phi_n(t)/M$, where $\phi_n$ is the solution to

$$\frac{\mathrm{d}\phi_n}{\mathrm{d}t} = \omega_n(t), \quad \phi_n(0) = 0. \tag{3.103}$$

Then, the real solution to (3.102) is

$$F_n = A_n(t) e^{i\tau_n} + \overline{A_n(t)} e^{-i\tau_n}, \tag{3.104}$$

where $A_n(t)$ is some complex function of $t$ to be determined, and $\overline{A_n(t)}$ is the complex conjugate of $A_n(t)$.

Equation (3.102), representing a simple oscillator with slowly-varying frequency, highlights why we needed to introduce a representative short time variable, $\tau = \phi(t)/M$, rather than simply setting $\tau = t/M$. By introducing a representative short time variable, $\tau = \phi(t)/M$, and then specifying $\phi(t)$ in order to remove the $t$ dependence in (3.102), we are essentially using the WKBJ method [46, §7.5].

#### 3.3.4.2 Solution as a series of eigenmodes

We conclude that $p_1$ can be written as

$$p_1 = \check{p}_1(t) + \tilde{p}_1(\chi, t), \tag{3.105a}$$

where

$$\tilde{p}_1 = \sum_{n=1}^{\infty} \left( A_n(t) e^{i\phi_n(t)/M} + \overline{A_n(t)} e^{-i\phi_n(t)/M} \right) G_n(\chi, t), \tag{3.105b}$$

and $(G_n(\chi,t))_{n\geq 1}$ are the eigenfunctions satisfying (3.101), $(\phi_n(t))_{n\geq 1}$ satisfy (3.103), and $\check{p}_1(t)$ and $(A_n(t))_{n\geq 1}$ are still to be determined. To streamline notation slightly, we will write 'c.c.' to denote the complex conjugate. Substituting (3.105) into (3.96), we deduce that

$$\tilde{u}_0 = \frac{1}{\gamma} \sum_{n=1}^{\infty} \left( \frac{i A_n(t)}{\phi_n'(t)} e^{i\phi_n(t)/M} + \text{c.c.} \right) \frac{\partial G_n}{\partial \chi}. \tag{3.106}$$

To determine the unknown functions, $\check{p}_1(t)$ and $(A_n(t))_{n\geq 1}$, we must consider the problem for $p_2$ and $u_1$. We find that the solubility conditions necessary to avoid secularity in $p_2$ are ordinary differential equations governing the evolution of $\check{p}_1(t)$ and $(A_n(t))_{n\geq 1}$.

#### 3.3.4.3 The form of $V_1$

Before we consider the problem to solve for $p_2$ and $u_1$, we first identify $S_1$ on both sides of the flame, so we can use (3.57b) and (3.83) to find expressions for $V_1$ and $T_1$.

Ahead of the flame, the initial conditions (3.6) imply

$$S_1^R = 0, \tag{3.107}$$

meaning, for $\chi \in (\chi_0^*, 1)$,

$$V_1^R = -\frac{V_0^R}{\gamma p_0} p_1. \tag{3.108}$$

Substituting (3.81), (3.82), (3.105) and (3.108) into (3.57b), we confirm that the temperature, $T^{R*} = \lim_{\chi \searrow \chi_0^*} T^R$, immediately in front of the flame can indeed be written in the form (3.60)—that is, $T^{R*} \sim T_0^{R*} + M(\check{T}_1^{R*} + \tilde{T}_1^{R*})$, where $T_0^{R*} = p_0(t)^{1-1/\gamma}$,

$$\check{T}_1^{R*} = \frac{(\gamma-1) p_0(t)^{-1/\gamma}}{\gamma} \check{p}_1(t), \tag{3.109}$$

and

$$\tilde{T}_1^{R*} = \frac{(\gamma-1) p_0(t)^{-1/\gamma}}{\gamma} \tilde{p}_1(\chi_0^*(t), t, \tau). \tag{3.110}$$

Behind the flame, the entropy at $\chi$ is determined at the moment the gas crosses the flame, i.e. at $t = t_0^*(\chi)$. To find $S_1^L$, we utilise the $\mathrm{ord}(M)$ approximation to the Chapman–Jouguet condition (3.4c) at $\chi = \chi_0^*(t)$, which is given by

$$\left[ p_0 V_1 + p_0 \chi_1^* \frac{\partial V_0}{\partial \chi} + p_1 V_0 \right]_-^+ = 0, \tag{3.111}$$

where $\chi_1^*$ is the solution to (3.66) subject to the initial condition, $\chi_1^*(0) = 0$. The $\partial V_0/\partial\chi$ term in (3.111) comes from approximating the Chapman–Jouguet condition (3.4c) at $\chi = \chi_0^*$, rather than $\chi = \chi^*$. Using (3.58b), (3.82) and (3.111), we deduce that, for $\chi \in (0, \chi_0^*)$,

$$S_1^L = \left.\frac{(1-\gamma)Q(p_1 - \gamma Q\chi_1^*)}{\gamma p_0(p_0^{(\gamma-1)/\gamma} + Q)}\right|_{t=t_0^*(\chi)}. \tag{3.112}$$

The $\mathrm{ord}(M)$ specific volume, $V_1^L$, can then be found by substituting (3.112) into (3.83).

Substituting (3.105) into (3.112) justifies our assertion that a representative short space variable, $\zeta = \psi(\chi)/M$, is necessary. Evaluating (3.105b) at $t = t_0^*(\chi)$, we recognise that $S_1^L$ has short-scale spatial variations, described by $(\zeta_n)_{n\geq 1}$, where $\zeta_n = \phi_n(t_0^*(\chi))/M$. While the short space scale has not played a role up until this point, by including $\zeta$ in our analysis we are confident that the short spatial variations in $V_1^L$ do not drive short-scale spatial variations in $p_0$, $V_0$, $u_0$ or $p_1$.

It is helpful at this stage to separate the $\mathrm{ord}(M)$ entropy, $S_1$, into two components,

$$S_1 = \check{S}_1(\chi) + \tilde{S}_1(\chi, \zeta), \tag{3.113}$$

where $\tilde{S}_1$ has short-scale *spatial* variations and $\check{S}_1$ does not. Using (3.105) to evaluate (3.112), we find

$$\check{S}_1 = \begin{cases} \check{S}_1^L, & \text{for } \chi \in (0, \chi_0^*(t)), \\ 0, & \text{for } \chi \in (\chi_0^*(t), 1), \end{cases} \quad \tilde{S}_1 = \begin{cases} \tilde{S}_1^L, & \text{for } \chi \in (0, \chi_0^*(t)), \\ 0, & \text{for } \chi \in (\chi_0^*(t), 1), \end{cases} \tag{3.114a}$$

where

$$\check{S}_1^L = \frac{(1-\gamma)Q(\check{p}_1(t_0^*(\chi)) - \gamma Q\chi_1^*(t_0^*(\chi)))}{\gamma p_0(t_0^*(\chi))(p_0(t_0^*(\chi))^{(\gamma-1)/\gamma} + Q)}, \tag{3.114b}$$

$$\tilde{S}_1^L = \frac{(1-\gamma)Q}{\gamma p_0(t_0^*(\chi))(p_0(t_0^*(\chi))^{(\gamma-1)/\gamma} + Q)} \sum_{n=1}^{\infty} (A_n(t_0^*(\chi))e^{i\phi_n(t_0^*(\chi))/M} + \text{c.c.})G_n(\chi, t_0^*(\chi)). \tag{3.114c}$$

For completeness, it is necessary to include $\check{S}_1^L$ in our analysis. However, we will shortly show $\check{p}_1 = \gamma Q\chi_1^*$, meaning $\check{S}_1^L = 0$.

### 3.3.5 Identifying solubility conditions to find $\check{p}_1(t)$

In Section 3.3.4 we found $p_1$ and $\tilde{u}_0$ as a series of modes whose spatial structure, amplitude and frequency all vary slowly in time. To complete our leading-order description of normal combustion, we need to find equations governing the evolution of the unknown functions, $(A_n(t))_{n\geq 1}$ and $\check{p}_1(t)$. In this section, we use the conservation of mass to show that $\check{p}_1(t)$ is proportional to $\chi_1^*(t)$.

The $\mathrm{ord}(M^2)$ terms from (3.54a) are

$$\phi'(t)\frac{\partial V_2}{\partial \tau} + \frac{\partial V_1}{\partial t} - \psi'(\chi)\frac{\partial u_2}{\partial \zeta} - \frac{\partial u_1}{\partial \chi} = 0. \tag{3.115}$$

Rearranging (3.58) gives

$$V_1 = S_1 V_0 - \frac{p_1 V_0}{\gamma p_0}, \tag{3.116a}$$

$$V_2 = S_2 V_0 - \frac{p_2 V_0}{\gamma p_0} + \frac{p_1^2 V_0}{2\gamma p_0^2} + \frac{S_1^2 V_0}{2} - \frac{S_1 p_1 V_0}{\gamma p_0} + \frac{p_1^2 V_0}{2\gamma^2 p_0^2}, \tag{3.116b}$$

allowing us to then eliminate $V_1$ and $V_2$ from (3.115) to find

$$\phi'(t)\frac{\partial}{\partial \tau}\left(-\frac{p_2 V_0}{\gamma p_0} + \frac{p_1^2 V_0}{2\gamma p_0^2} - \frac{S_1 p_1 V_0}{\gamma p_0} + \frac{p_1^2 V_0}{2\gamma^2 p_0^2}\right) + \frac{\partial}{\partial t}\left(S_1 V_0 - \frac{p_1 V_0}{\gamma p_0}\right) = \psi'(\chi)\frac{\partial u_2}{\partial \zeta} + \frac{\partial u_1}{\partial \chi}, \tag{3.117}$$

on both sides of the flame. To derive (3.117) we have used that

$$\frac{\partial}{\partial \tau}\left(S_2 V_0 + \frac{S_1^2 V_0}{2}\right) = 0. \tag{3.118}$$

To ensure that the series (3.56c) remains asymptotic, we cannot have $u_2$ growing linearly with $\zeta$. The terms in (3.117) with no $\zeta$ dependence must therefore sum to zero. Using (3.113) in (3.117), we infer that, on both sides of the flame, the solubility condition for $u_2$ is

$$\frac{\phi'(t) V_0}{\gamma p_0}\frac{\partial p_2}{\partial \tau} + \frac{\partial u_1}{\partial \chi} = \phi'(t)\frac{\partial}{\partial \tau}\left(\frac{(\gamma+1)p_1^2 V_0}{2\gamma^2 p_0^2} - \frac{\check{S}_1 p_1 V_0}{\gamma p_0}\right) + \frac{\partial}{\partial t}\left(\check{S}_1 V_0 - \frac{p_1 V_0}{\gamma p_0}\right). \tag{3.119}$$

Similarly, we need to find a solubility condition to prevent $p_2$ growing linearly in $\tau$, so that our assumption that (3.56b) is asymptotic for $t = \mathrm{ord}(1)$ remains valid. We currently have no information about the $\tau$ dependence of $u_1$, so, to proceed, we separate $u_1$ into two components, so that

$$u_1 = \check{u}_1(\chi, t) + \tilde{u}_1(\chi, t, \tau), \tag{3.120}$$

where $\partial \check{u}_1/\partial \tau = 0$, $\int_0^{2\pi} \tilde{u}_1 \,\mathrm{d}\tau = 0$, and

$$\check{u}_1(0,t) = \check{u}_1(1,t) = \tilde{u}_1(0,t,\tau) = \tilde{u}_1(1,t,\tau) = 0. \tag{3.121}$$

The solubility condition to prevent $p_2$ growing linearly in $\tau$ due to (3.119) is therefore

$$\frac{\partial \check{u}_1}{\partial \chi} = \check{S}_1 \frac{\partial V_0}{\partial t} - \frac{V_0}{\gamma p_0}\frac{\mathrm{d}\check{p}_1}{\mathrm{d}t} + \frac{(\gamma+1)V_0}{\gamma^2 p_0^2}\frac{\mathrm{d}p_0}{\mathrm{d}t}\check{p}_1. \tag{3.122}$$

To find an ordinary differential equation describing the evolution of $\check{p}_1$, we integrate (3.122) with respect to $\chi$ and make use of the boundary conditions (3.121) and the Chapman–Jouguet conditions (3.4). Combining the $\mathrm{ord}(M)$ mass and energy Chapman–Jouguet conditions, (3.4a) and (3.4c), we find the jump in $u_1$ across the approximate flame position, $\chi = \chi_0^*(t)$, satisfies

$$\left[u_1 + \chi_1^* \frac{\partial u_0}{\partial \chi} - \frac{q_0 p_1 V_0}{p_0} + q_1 V_0\right]_-^+ = 0. \tag{3.123}$$

Separating the terms in (3.123) that are independent of $\tau$ and making use of (3.87) and (3.89), we take the jump in $\check{u}_1$ across $\chi_0^*$ to be

$$[\check{u}_1]_-^+ = -\frac{Q\chi_1^*}{\gamma p_0^2}\frac{\mathrm{d}p_0}{\mathrm{d}t} - \frac{Qq_0\check{p}_1}{p_0^2} + \frac{Q\check{q}_1}{p_0}. \tag{3.124a}$$

Correspondingly, the jump in $\tilde{u}_1$ is therefore

$$[\tilde{u}_1]_-^+ = -\frac{Q\chi_1^*}{\gamma p_0^2}\phi'(t)\left.\frac{\partial\tilde{p}_1}{\partial\tau}\right|_{\chi=\chi_0^*} - \left.\frac{Qq_0\tilde{p}_1}{p_0^2}\right|_{\chi=\chi_0^*} + \frac{Q\tilde{q}_1}{p_0}. \tag{3.124b}$$

Upon integrating (3.122), we find that

$$\int_0^1 \check{S}_1\frac{\partial V_0}{\partial t}\,\mathrm{d}\chi - \frac{1}{\gamma p_0}\frac{\partial\check{p}_1}{\partial t} + \frac{Q(\gamma+1)q_0}{\gamma p_0^2}\check{p}_1 = \frac{Q\chi_1^*}{\gamma p_0^2}\frac{\mathrm{d}p_0}{\mathrm{d}t} + \frac{Qq_0\check{p}_1}{p_0^2} - \frac{Q\check{q}_1}{p_0}, \tag{3.125}$$

where we have used (3.91), (3.121) and (3.124a). From (3.66), (3.114) and (3.125) we conclude that

$$\check{p}_1 = \gamma Q\chi_1^*, \tag{3.126}$$

where we have set the integrating constant so that $\check{p}_1 = \chi_1^* = 0$ at $t = 0$. Substituting (3.126) into (3.114b), we deduce that $\check{S}_1 = 0$. Furthermore, using (3.62b), (3.109) and (3.126), we recognise that the solution to (3.67) with $\chi_1^*(0) = 0$ is $\chi_1^* = 0$, and hence

$$\check{p}_1 = 0. \tag{3.127}$$

### 3.3.6 Identifying solubility conditions to find $(A_n(t))_{n\geq 1}$

In this section, we find the solubility conditions necessary to avoid secularity in the solution for $p_2$ and $\tilde{u}_1$. The solubility conditions provide a system of ordinary differential equations that we can solve to find $(A_n(t))_{n\geq 1}$, hence completing our leading-order description of normal combustion.

We start by considering the $\mathrm{ord}(M^3)$ approximation to (3.54b). From (3.71), (3.80), (3.84) and (3.95), we have that $u_0$, $u_1$ and $p_2$ are independent of $\zeta$. Therefore, to avoid $p_3$ growing linearly with $\zeta$, we require

$$-\frac{\psi'(\chi)}{\gamma}\frac{\partial p_3}{\partial\zeta} = \phi'(t)\frac{\partial\tilde{u}_1}{\partial\tau} + \frac{\partial u_0}{\partial t} + \frac{1}{\gamma}\frac{\partial p_2}{\partial\chi} = 0. \tag{3.128}$$

Here we have used that $\partial\check{u}_1/\partial\tau = 0$ to eliminate $\check{u}_1$.

Similarly, for (3.56d) to be asymptotic for $t = O(1)$, we cannot have $\tilde{u}_1$ growing linearly with $\tau$. We currently have no information to tell us if $p_2$ depends on $\tau$. We therefore assume $p_2$ can be written as

$$p_2 = \check{p}_2(\chi, t) + \tilde{p}_2(\chi, t, \tau), \tag{3.129}$$

where $\partial\check{p}_2/\partial\tau = 0$, $\int_0^{2\pi}\tilde{p}_2\,\mathrm{d}\tau = 0$, and

$$[\check{p}_2]_-^+ = \frac{\gamma Qq_0^2}{p_0}, \tag{3.130a}$$

$$[\tilde{p}_2]_-^+ = 0, \tag{3.130b}$$

across $\chi = \chi_0^*$. The jump (3.130a) in $\check{p}_2$ is necessary so that $p_2$ satisfies the Chapman–Jouguet condition (3.4b). Substituting (3.85) and (3.129) into (3.128), we find the solubility condition for $\tilde{u}_1$ is

$$\frac{1}{\gamma}\frac{\partial \check{p}_2}{\partial \chi} = -\frac{\partial \check{u}_0}{\partial t}. \tag{3.131}$$

We are now in a position to write down two equations governing the evolution of $\tilde{p}_2$ and $\tilde{u}_1$. Substituting (3.122) and (3.131) into (3.119) and (3.128), we find that

$$\frac{\phi'(t)V_0}{\gamma p_0}\frac{\partial \tilde{p}_2}{\partial \tau} + \frac{\partial \tilde{u}_1}{\partial \chi} = \phi'(t)\frac{\partial}{\partial \tau}\left(\frac{(\gamma+1)p_1^2 V_0}{2\gamma^2 p_0^2}\right) - \frac{\partial}{\partial t}\left(\frac{\tilde{p}_1 V_0}{\gamma p_0}\right), \tag{3.132a}$$

$$\phi'(t)\frac{\partial \tilde{u}_1}{\partial \tau} + \frac{1}{\gamma}\frac{\partial \tilde{p}_2}{\partial \chi} = -\frac{\partial \tilde{u}_0}{\partial t}. \tag{3.132b}$$

Eliminating $\tilde{u}_1$ from (3.132), we find that $\tilde{p}_2$ satisfies

$$\underbrace{\frac{\phi'(t)^2 V_0}{p_0}\frac{\partial^2 \tilde{p}_2}{\partial \tau^2}}_{①} - \underbrace{\frac{\partial^2 \tilde{p}_2}{\partial \chi^2}}_{②} = \underbrace{\phi'(t)^2\frac{\partial^2}{\partial \tau^2}\left(\frac{(\gamma+1)p_1^2 V_0}{2\gamma p_0^2}\right)}_{③} - \underbrace{\phi'(t)\frac{\partial^2}{\partial \tau \partial t}\left(\frac{\tilde{p}_1 V_0}{p_0}\right)}_{④} + \underbrace{\gamma\frac{\partial^2 \tilde{u}_0}{\partial t \partial \chi}}_{⑤}. \tag{3.133}$$

Labels have been added to (3.133) so we can refer to each term easily.

From the Chapman–Jouguet condition (3.130b), we know that $\tilde{p}_2$ is continuous. However, due to the jump (3.124b) in $\tilde{u}_1$ across $\chi = \chi_0^*$, we deduce from (3.132b) that there is a discontinuity in $\partial \tilde{p}_2/\partial \chi$ across $\chi = \chi_0^*$, given by

$$\frac{1}{\gamma}\left[\frac{\partial \tilde{p}_2}{\partial \chi}\right]_-^+ = \frac{Q(\gamma+1)\phi'(t)q_0}{\gamma p_0^2}\frac{\partial \tilde{p}_1}{\partial \tau}\bigg|_{\chi=\chi_0^*(t)} + \frac{Q\chi_1^*}{\gamma p_0^2}\phi'(t)^2\,\frac{\partial^2 \tilde{p}_1}{\partial \tau^2}\bigg|_{\chi=\chi_0^*} - \frac{Q\phi'(t)}{p_0}\frac{\partial \tilde{q}_1}{\partial \tau}. \tag{3.134}$$

We further conclude from (3.86), (3.121) and (3.132b) that, at the rigid boundaries, $\chi = 0$ and $\chi = 1$,

$$\frac{\partial \tilde{p}_2}{\partial \chi} = 0. \tag{3.135}$$

From (3.126) and (3.127), we conclude that $\chi_1^* = 0$. We retain $\chi_1^*$ in (3.134) to indicate where $\chi_1^*$ would appear if we had used a different model for $\check{q}_1$ that admits a non-zero solution to (3.67) with $\chi_1^*(0) = 0$.

Note that the differential operator acting on $\tilde{p}_2$ in (3.133) is the same as the differential operator in (3.98). We therefore seek a solution to (3.133) of the form

$$\tilde{p}_2 = \sum_{n=1}^{\infty} c_n(t,\tau)G_n(\chi,t), \tag{3.136}$$

where $(G_n(\chi,t))_{n\geq 1}$ is the basis of eigenfunctions satisfying (3.101) we found in Section 3.3.4. It follows from Sturm–Liouville theory [42, §11.4] and the integral (3.101c) that, for $m, n \in \mathbb{N}$,

$$\int_0^1 \frac{V_0(\chi,t)}{p_0(t)}G_m(\chi,t)G_n(\chi,t)\,\mathrm{d}\chi = \begin{cases} 1, & \text{if } m = n, \\ 0, & \text{otherwise.} \end{cases} \tag{3.137}$$

We use the orthonormality relation (3.137) to find equations governing the evolution of $(c_n)_{n\geq 1}$.

#### 3.3.6.1 The equation for $c_k$

We now multiply (3.133) by $G_k(\chi,t)$ and integrate from $\chi=0$ to $\chi=1$ to derive an equation for $c_k$, for $k=1,2,\ldots$. For clarity, we consider each term of (3.133) in turn. Substituting $\tilde{p}_2$ for the series of eigenmodes (3.136), we find, upon multiplying ① by $G_k$ and integrating, that

$$\int_0^1 \frac{\phi'(t)^2 V_0(\chi,t)}{\gamma p_0(t)} \frac{\partial^2 \tilde{p}_2}{\partial \tau^2} G_k(\chi,t)\,\mathrm{d}\chi = \phi'(t)^2 \frac{\partial^2 c_k}{\partial \tau^2}. \tag{3.138}$$

We must carefully account for the discontinuity (3.134) using integration by parts. Multiplying ② by $G_k(\chi,t)$ and integrating with respect to $\chi$, we find

$$\int_0^1 \frac{\partial^2 \tilde{p}_2}{\partial \chi^2} G_k\,\mathrm{d}\chi = -\left[\frac{\partial \tilde{p}_2}{\partial \chi} G_k - \tilde{p}_2 \frac{\partial G_k}{\partial \chi}\right]_-^+ + \int_0^1 \tilde{p}_2 \frac{\partial^2 G_k}{\partial \chi^2}\,\mathrm{d}\chi \tag{3.139a}$$

$$= -\gamma\left(\frac{Q(\gamma+1)\phi'(t)q_0}{\gamma p_0^2}\frac{\partial \tilde{p}_1}{\partial \tau}\bigg|_{\chi=\chi_0^*(t)} + \frac{Q\chi_1^*}{\gamma p_0^2}\phi'(t)^2\,\frac{\partial^2 \tilde{p}_1}{\partial \tau^2}\bigg|_{\chi=\chi_0^*} - \frac{Q\phi'(t)}{p_0}\frac{\partial \tilde{q}_1}{\partial \tau}\right) G_k(\chi_0^*(t),t) - \int_0^1 \frac{\omega_k(t)^2 V_0(\chi,t)}{p_0(t)} \tilde{p}_2 G_k\,\mathrm{d}\chi\,. \tag{3.139b}$$

In deriving (3.139) we have made use of the continuity of $\partial G_k/\partial\chi$, the definition of the eigenfunctions (3.101a), and the boundary conditions (3.101b), (3.130b), (3.134) and (3.135). Using (3.62c), (3.105b), (3.110), (3.126), (3.127) and (3.136) to evaluate $\chi_1^*$, $\tilde{q}_1$, $\tilde{p}_1$ and $\tilde{p}_2$ in (3.139), we find

$$\int_0^1 \frac{\partial^2 \tilde{p}_2}{\partial \chi^2} G_k\,\mathrm{d}\chi = -\sum_{n=1}^{\infty}\left[\frac{iQ\phi_n'(t)A_n}{p_0^2}\left((\gamma+1)q_0 - (\gamma-1)p_0^{\frac{\gamma-1}{\gamma}}\frac{\partial q^{(0)}}{\partial T^{R*}}\right)e^{i\phi_n(t)/M} + \text{c.c.}\right] G_n(\chi_0^*(t),t)G_k(\chi_0^*(t),t) - \omega_k^2 c_k. \tag{3.140}$$

Note that in going from (3.139) to (3.140), we have used the fact that $\chi_1^*(t)=0$. Our discussion, therefore, has changed from a general discussion of normal combustion with mass flux of the form (3.61), to the specific case where the mass flux is given by (3.62).

Squaring (3.105), we deduce that

$$p_1^2 = \sum_{m=1}^{\infty}\sum_{n=1}^{\infty}\left(A_m e^{i\phi_m/M} + \text{c.c.}\right)\left(A_n e^{i\phi_n/M} + \text{c.c.}\right) G_m G_n + 2\check{p}_1 \sum_{n=1}^{\infty}\left(A_n e^{i\phi_n/M} + \text{c.c.}\right) G_n + \check{p}_1^2. \tag{3.141}$$

Substituting (3.141) into ③, multiplying by $G_k$ and integrating, we find

$$\begin{aligned}\int_0^1 \phi'(t)^2 \frac{\partial^2}{\partial\tau^2}\left(\frac{(\gamma+1)p_1^2 V_0}{2\gamma p_0^2}\right) G_k \,\mathrm{d}\chi \\ = -\frac{(\gamma+1)\check{p}_1}{\gamma p_0}\left(\phi_k'(t)^2 A_k e^{i\phi_k/M} + \text{c.c.}\right) \\ - \frac{\gamma+1}{2\gamma p_0^2}\sum_m\sum_n \Bigg[\Big((\phi_m'(t)+\phi_n'(t))^2 A_m A_n e^{i(\phi_m+\phi_n)/M} \\ + (\phi_m'(t)-\phi_n'(t))^2 A_m \overline{A_n} e^{i(\phi_m-\phi_n)/M}\Big) + \text{c.c.}\Bigg] \int_0^1 V_0 G_m G_n G_k \,\mathrm{d}\chi\end{aligned} \tag{3.142}$$

Again, from (3.127), we have that $\check{p}_1 = 0$ for the specific mass flux model (3.62) we consider. We highlight the presence of $\check{p}_1$ in (3.142) to emphasise that, given a different model for the mass flux, the nonlinear term ③ could indeed contribute to the solubility conditions for $(A_n(t))_{n\geq 1}$.

We now consider the linear terms in $p_1$ and $u_0$ on the right-hand side of (3.133). Substituting (3.105b) and (3.106) into ④ and ⑤ we find

$$\phi'(t)\frac{\partial^2}{\partial\tau\partial t}\left(\frac{\tilde{p}_1 V_0}{p_0}\right) = \sum_n \left[i\phi_n'(t)\frac{\partial}{\partial t}\left(\frac{A_n(t)V_0(\chi,t)G_n(\chi,t)}{p_0(t)}\right) e^{i\phi_n(t)/M} + \text{c.c.}\right], \tag{3.143}$$

$$\frac{\partial^2 \tilde{u}_0}{\partial t\partial\chi} = -\frac{1}{\gamma}\sum_n \left[ie^{i\phi_n(t)/M}\frac{\partial}{\partial t}\left(\frac{A_n(t)\phi_n'(t)V_0(\chi,t)G_n(\chi,t)}{p_0(t)}\right) + \text{c.c.}\right]. \tag{3.144}$$

Multiplying (3.143) and (3.144) by $G_k$, using the product rule of differentiation and integrating with respect to $\chi$, we find

$$\begin{aligned}\int_0^1 \left(-\phi'(t)\frac{\partial^2}{\partial\tau\partial t}\left(\frac{\tilde{p}_1 V_0}{p_0}\right) + \gamma\frac{\partial^2\tilde{u}_0}{\partial t\partial\chi}\right) G_k \,\mathrm{d}\chi \\ = \left[-ie^{i\phi_k/M}\left(\phi_k'(t)\frac{\mathrm{d}A_k}{\mathrm{d}t} + \frac{\mathrm{d}}{\mathrm{d}t}\left(\phi_k'(t)A_k\right)\right) + \text{c.c.}\right] \\ + 2\sum_n \left[-ie^{i\phi_n/M}\phi_n'(t)A_n\int_0^1 \frac{\partial}{\partial t}\left(\frac{V_0 G_n}{p_0}\right) G_k \,\mathrm{d}\chi + \text{c.c.}\right].\end{aligned} \tag{3.145}$$

For $n = k$, we find, by differentiating (3.137) with respect to $t$, that the integral on the right-hand side of (3.145) is given by

$$\int_0^1 \frac{\partial}{\partial t}\left(\frac{V_0(\chi,t)G_k(\chi,t)}{p_0(t)}\right) G_k(\chi,t)\,\mathrm{d}\chi = -\frac{QG_k(\chi_0^*(t),t)^2 q_0(t)}{p_0(t)^2} - \frac{1}{\omega_k}\frac{\mathrm{d}\omega_k}{\mathrm{d}t}. \tag{3.146}$$

Combining (3.138), (3.140), (3.142), (3.145) and (3.146), and using (3.127), we find that $c_k$ satisfies

$$\begin{aligned}
&\phi'(t)^2\frac{\partial^2 c_k}{\partial \tau^2} + \omega_k(t)^2 c_k \\
&\quad = -\sum_{n=1}^{\infty}\left[\frac{iQ\omega_n A_n}{p_0^2}\left((\gamma+1)q_0 - (\gamma-1)p_0^{\frac{\gamma-1}{\gamma}}\frac{\partial q^{(0)}}{\partial T^{R*}}\right)e^{i\phi_n/M}\right. \\
&\qquad \left. + \text{c.c.}\right] G_n(\chi_0^*(t),t)G_k(\chi_0^*(t),t) \\
&\qquad - \frac{(\gamma+1)}{2\gamma p_0}\sum_{m=1}^{\infty}\sum_{n=1}^{\infty}\left[\left((\omega_m(t)+\omega_n(t))^2 A_m A_n e^{i(\phi_m+\phi_n)/M}\right.\right. \\
&\qquad \left.\left. + (\omega_m(t)-\omega_n(t))^2 A_m \overline{A_n} e^{i(\phi_m-\phi_n)/M}\right) + \text{c.c.}\right]\int_0^1 \frac{V_0}{p_0} G_m G_n G_k \,\mathrm{d}\chi \\
&\qquad + \left[-ie^{i\phi_k/M}\left(\omega_k\frac{\mathrm{d}A_k}{\mathrm{d}t} + \frac{\mathrm{d}}{\mathrm{d}t}\left(\omega_k A_k\right)\right) + \text{c.c.}\right] \\
&\qquad + 2\left(ie^{i\phi_k/M}\omega_k A_k + \text{c.c.}\right)\left(\frac{QG_k(\chi_0^*(t),t)^2 q_0(t)}{p_0(t)^2} + \frac{1}{\omega_k}\frac{\mathrm{d}\omega_k}{\mathrm{d}t}\right) \\
&\qquad + 2\sum_{n\geq 1, n\neq k}\left[-ie^{i\phi_n/M}\omega_n A_n \int_0^1 \frac{\partial}{\partial t}\left(\frac{V_0 G_n}{p_0}\right)G_k \,\mathrm{d}\chi + \text{c.c.}\right]. \qquad (3.147)
\end{aligned}$$

#### 3.3.6.2 The solubility conditions and transient resonance

The partial differential equation (3.147) governing the evolution of $c_k$ is linear in $c_k$ and inhomogeneous. The general solution to (3.147) can be therefore be written as the sum of a complementary function, $c_k^{\mathsf{CF}}$, and a particular integral, $c_k^{\mathsf{PI}}$. The complementary function satisfies the homogeneous equation (3.102), meaning

$$c_k^{\mathsf{CF}} = B_k(t)e^{i\phi_k(t)/M} + \text{c.c.}, \qquad (3.148)$$

where $B_k(t)$ is a complex function of time to be determined.

We cannot have secular terms, i.e. $\tau e^{i\tau}$, in the particular integral, $c_k^{\mathsf{PI}}$, if (3.56b) is to remain asymptotic for all $t = O(1)$. The solubility condition to prevent secular growth of $\tilde{p}_2$ comes from setting the sum of the coefficients of $e^{i\phi_k(t)/M}$ on the right-hand side of (3.147) to zero. That is, we require

$$A_k\frac{\mathrm{d}\omega_k}{\mathrm{d}t} - 2\omega_k\frac{\mathrm{d}A_k}{\mathrm{d}t} - \frac{(\gamma-1)Q\omega_k A_k}{p_0^2}\left(q_0 - p_0^{(\gamma-1)/\gamma}\frac{\partial q^{(0)}}{\partial T^{R*}}\right)G_k(\chi_0^*(t),t)^2 = 0. \quad (3.149)$$

With (3.149), we finally have an equation governing the evolution of $A_k(t)$, which, given some initial conditions, we are able to solve to complete our leading-order description of the velocity during normal combustion. The equation (3.149) is a linear, homogeneous

ordinary differential equation with time-varying coefficients. We also note, by considering the real and imaginary parts of $A_k$ separately, that the modulus of $A_k$ satisfies

$$\frac{\mathrm{d}}{\mathrm{d}t}\left(\frac{|A_k|^2}{\omega_k}\right) = -\frac{(\gamma-1)QG_k(\chi_0^*(t),t)^2}{p_0^2}\left(q_0 - p_0^{(\gamma-1)/\gamma}\frac{\partial q^{(0)}}{\partial T^{R*}}\right)\left(\frac{|A_k|^2}{\omega_k}\right), \tag{3.150}$$

and the argument of $A_k$ is constant.

Before we move on and state the initial conditions we use to solve (3.149), we should briefly reassure ourselves that the other terms on the right-hand side of (3.147) will not force $c_k$ to grow in such a way that invalidates our assumption that (3.56b) is asymptotic. From Sturm–Liouville theory [42, §11.4], we have that $\omega_n \neq \omega_k$ for $n \neq k$. Therefore, the terms on the right-hand side of (3.147) of the form $f(t)e^{\pm i\phi_n(t)/M}$, where $n \neq k$ and $f(t)$ is an arbitrary function of $t$, do not lead to secular solutions. The situation is more subtle for terms of the form $f(t)e^{\pm i(\phi_m(t)+\phi_n(t))/M}$ and $f(t)e^{\pm i(\phi_m(t)-\phi_n(t))/M}$, because there exist $k,m,n \in \mathbb{N}$ and $t_0 \geq 0$ such that $|\omega_m(t_0) \pm \omega_n(t_0)| = \omega_k(t_0)$. We assume that the resonance is transient. In other words, we assume that, for fixed $k,m,n \in \mathbb{N}$, the forcing frequency and the natural frequency are equal only at discrete times. Kevorkian [61] shows that $c_k$ becomes asymptotically large in a boundary layer around $t = t_0$. Crucially, though, $Mc_k$ remains $o(1)$ in the boundary layer as $M \to 0$, meaning (3.56b) remains asymptotic. We conclude that we are justified in ignoring the terms of the form $f(t)e^{\pm i(\phi_m(t)+\phi_n(t))/M}$ and $f(t)e^{\pm i(\phi_m(t)-\phi_n(t))/M}$ on the right-hand side of (3.147) when deriving the solubility condition (3.149).

#### 3.3.6.3 Initial conditions

To solve (3.149) for $A_k(t)$, we require initial conditions for the real and imaginary parts of $A_k$. Here we present the initial conditions which are representative of quiescent gas ahead of the flame at $t = 0$.

We are unable to choose an initial condition for $\breve{u}_0$; the profile of $\breve{u}_0$ is determined by (3.87), meaning for $t = 0$, $\chi \in (0,1)$, we have

$$\breve{u}_0^R = Q(1-\chi)q_0(0). \tag{3.151}$$

To ensure $u_0 = 0$ initially, we therefore require that

$$\tilde{u}_0^R = -Q(1-\chi)q_0(0), \tag{3.152}$$

for $t = 0$, $\chi \in (0,1)$. To find an initial condition for $A_k$ from (3.152) we rewrite $\tilde{u}_0$ using (3.106). Then, by multiplying (3.152) by $\partial G_k/\partial\chi$ and integrating with respect to $\chi$, we find

$$A_k(0) - \overline{A_k(0)} = \frac{i\gamma Q q_0(0)}{\omega_k(0)}\int_0^1 (1-\chi)\left.\frac{\partial G_k}{\partial\chi}\right|_{t=0}\mathrm{d}\chi\,. \tag{3.153}$$

In deriving (3.153) we have used the initial condition for $\phi_k$, (3.103), and

$$\int_0^1 \frac{\partial G_m}{\partial\chi}\frac{\partial G_n}{\partial\chi}\,\mathrm{d}\chi = \begin{cases}\omega_n(t)^2, & \text{if } m = n,\\ 0, & \text{otherwise,}\end{cases} \tag{3.154}$$

which follows from (3.101) and (3.137). From (3.101), we deduce that $\omega_k(0) = k\pi$ for $k = 1, 2, \ldots$ and $G_k(\chi, 0) = \sqrt{2}\cos(k\pi\chi)$. Evaluating the integral in (3.153), we find

$$A_k(0) - \overline{A_k(0)} = -\frac{i\sqrt{2}\gamma Q q_0(0)}{k\pi}. \tag{3.155a}$$

Note that, because $\lim_{\chi\searrow 0} \tilde{u}_0(\chi, 0) \neq 0$, partial sums of (3.106) will exhibit the Gibbs phenomenon around $\chi = 0$ at $t = 0$. We will not concern ourselves unduly over the presence of the Gibbs phenomenon in the solution, but flag its presence here so we know to look out for it later on.

The second initial condition we require to solve (3.149) for $A_k$ comes from the initial condition, $p_1 = 0$. We have already assumed that $\check{p}_1(0) = 0$, and therefore we require $\tilde{p}_1 = 0$ at $t = 0$. Using (3.103), (3.105b), and (3.137), we deduce that

$$A_k(0) + \overline{A_k(0)} = 0. \tag{3.155b}$$

The same procedure can be used to identify $(A_n(0))_{n\geq 1}$ when there are $O(M)$ perturbations in the initial conditions for $p$ or $O(1)$ perturbations in the initial conditions for $u$. As we will discuss further in Section 4.3.3, acoustic variations in the gas prior to ignition can change where and when the hot spot develops if autoignition occurs.

### 3.3.7 Summary

We have used an adaptation of the method of multiple scales to derive an asymptotic solution to (3.2)–(3.6) as $M \to 0$, valid for $t = O(1)$. Here we briefly summarise the form of the solution, before presenting realisations of the solution in Section 3.4.

To solve (3.3) we first specified a model for the mass flux, $q$, through the flame. For the three-step reaction, the mass flux, $q$, depends on the temperature, $T^{R*} \sim T_0^{R*} + MT_1^{R*}$, ahead of and immediately adjacent to the flame. In the distinguished limit $EM = O(1)$, $E^2M \gg 1$, we found that, for the three-step reaction (2.6), $q$ has the form

$$q = q_0(T_0^{R*}) + MT_1^{R*} \left.\frac{\partial q^{(0)}}{\partial T^{R*}}\right|_{(T^{R*}, Y_{\mathcal{F}}^{R*}) = (T_0^{R*}, 1)} + o(M), \tag{3.156}$$

where $q_0(T^{R*}) = q^{(0)}(T^{R*}, 1) + E^{-1}q^{(1)}(T^{R*}, 1)$, and $q^{(0)}$ and $q^{(1)}$ are the defined by (2.88) and (2.94) respectively.

We have found that the solution to (3.2)–(3.6), with $q$ given by (3.156), has the form

$$\chi^* = \chi_0^*(t) + o(M), \tag{3.157a}$$
$$p = p_0(t) + M\tilde{p}_1(\chi, t) + o(M), \tag{3.157b}$$
$$V = V_0(\chi, t) + M\tilde{V}_1(\chi, t) + o(M), \tag{3.157c}$$
$$u = \check{u}_0(\chi, t) + \tilde{u}_0(\chi, t) + o(1), \tag{3.157d}$$
$$T = p_0(t)V_0(\chi, t) + M(p_0(t)\tilde{V}_1(\chi, t) + \tilde{p}_1(\chi, t)V_0(\chi, t)) + o(M), \tag{3.157e}$$

as $M \to 0$. Note that (3.157) is expressed in terms of $\chi$ and $t$ only. We included $\zeta$ and $\tau$ as independent variables in expressions such as (3.85) while developing the model, but it would be inappropriate to include them here now that we know the $\chi$ and $t$ dependence of the then unknown rapid variations in the solution.

Combining (3.65), (3.73) and (3.93), we found that the leading-order flame position, $\chi_0^*$, is the solution to

$$\frac{\mathrm{d}\chi_0^*}{\mathrm{d}t} = q_0 \left( (1 + \gamma Q \chi_0^*)^{\frac{\gamma-1}{\gamma}} \right), \quad \chi_0^*(0) = 0. \tag{3.158}$$

In Section 3.3.3, we deduced that $p_0$ and $V_0$ depend on time only through the leading-order flame position, with

$$p_0(t) = 1 + \gamma Q \chi_0^*(t), \quad \text{for } \chi \in (0,1), \tag{3.159a}$$

$$V_0(\chi,t) = \begin{cases} p_0(t)^{-1/\gamma} \left( 1 + Q(1+\gamma Q \chi)^{\frac{1-\gamma}{\gamma}} \right), & \text{for } \chi \in (0, \chi_0^*(t)), \\ p_0(t)^{-1/\gamma}, & \text{for } \chi \in (\chi_0^*(t), 1). \end{cases} \tag{3.159b}$$

Additionally, we noted that $\check{u}_0$ is the solution to (3.87), subject to the boundary conditions (3.86), meaning

$$\check{u}_0(\chi,t) = \begin{cases} -Q q_0 \left( p_0(t)^{\frac{\gamma-1}{\gamma}} \right) \int_0^\chi V_0(s,t)\,\mathrm{d}s \,/ p_0(t), & \text{for } \chi \in (0, \chi_0^*(t)), \\ Q q_0 \left( p_0(t)^{\frac{\gamma-1}{\gamma}} \right) \int_\chi^1 V_0(s,t)\,\mathrm{d}s \,/ p_0(t), & \text{for } \chi \in (\chi_0^*(t), 1). \end{cases} \tag{3.159c}$$

In Section 3.3.4, we wrote $\tilde{p}_1$, $\tilde{V}_1$ and $\tilde{u}_0$ in terms of the solutions of the eigenvalue problem (3.101), with

$$\tilde{p}_1(\chi,t) = \sum_{n=1}^{\infty} \left( A_n(t) e^{i\phi_n(t)/M} + \overline{A_n(t)} e^{-i\phi_n(t)/M} \right) G_n(\chi,t), \tag{3.160a}$$

$$\tilde{V}_1(\chi,t) = V_0(\chi,t)\tilde{S}_1(\chi) - \frac{\tilde{p}_1(\chi,t) V_0(\chi,t)}{\gamma p_0(t)}, \tag{3.160b}$$

$$\tilde{u}_0(\chi,t) = \frac{1}{\gamma} \sum_{n=1}^{\infty} \left( \frac{i A_n(t)}{\omega_n(t)} e^{i\phi_n(t)/M} - \frac{i\overline{A_n(t)}}{\omega_n(t)} e^{-i\phi_n(t)/M} \right) \frac{\partial G_n}{\partial \chi}. \tag{3.160c}$$

where $\tilde{S}_1(\chi)$ is defined by (3.114). For $k = 0, 1, \ldots$, recall that the solution to (3.101) corresponding to the eigenvalue, $\omega_k(t)$, is denoted by $G_k(\chi,t)$, and that the eigenvalues are indexed such that $\omega_0 = 0$ and $\omega_{k+1}(t) > \omega_k(t)$. Furthermore, $\phi_k(t)$ is defined as the solution to (3.103) for $k = 1, 2, \ldots$, i.e.

$$\phi_k(t) = \int_0^t \omega_k(s)\,\mathrm{d}s\,. \tag{3.161}$$

Finally, in Section 3.3.6, we found that $A_k(t)$ is the solution to

$$A_k \frac{\mathrm{d}\omega_k}{\mathrm{d}t} - 2\omega_k \frac{\mathrm{d}A_k}{\mathrm{d}t} - \frac{(\gamma-1) Q \omega_k A_k}{p_0^2} \left( q_0 - p_0^{(\gamma-1)/\gamma} \frac{\partial q^{(0)}}{\partial T^{R*}} \right) G_k(\chi_0^*(t), t)^2 = 0, \tag{3.162}$$

subject to the initial condition

$$A_k(0) = -\frac{i\sqrt{2}\gamma Q q_0(0)}{2k\pi}. \tag{3.163}$$

#### 3.3.7.1 Numerical solution

To use (3.157) practically, it is necessary to truncate the series (3.114c) and (3.160), and solve (3.101), (3.158), (3.161) and (3.162) numerically. Partial sums of (3.114c) and (3.160) with $K = 9$ terms are used to create Figures 3.5–3.7. We briefly outline the numerical procedure we use to solve (3.101), (3.158), (3.161) and (3.162) here.

Firstly, we use the MATLAB `ode45` function to solve (3.158) for $\chi_0^*(t)$. Then, for 1000 equally-spaced times between $t = 0$ to $t = t_0^*(1)$, we solve the eigenvalue problem (3.101) using the Chebfun `eigs` function [33, §7.5]. For each time, we record the $K$ smallest non-zero eigenvalues, $\{\omega_k(t) \mid k = 1, 2, \ldots, K\}$, and the corresponding values of the eigenfunction at the flame, $\{G_k(\chi_0^*(t), t)\}$. We also calculate the value of $\mathrm{d}\omega_k/\mathrm{d}t$ for $k = 1, 2, \ldots, K$, using

$$\frac{\mathrm{d}\omega_k}{\mathrm{d}t} = \frac{Qq_0(T_0^{R*}(t))\omega_k(t)}{2p_0(t)^2}\left((\gamma+1)p_0(t) - G_k(\chi_0^*(t), t)^2\right), \tag{3.164}$$

which follows from (3.146) and (3.154). We use linear interpolation of this data to specify the time-dependent coefficients in (3.162). We then solve (3.162) using the MATLAB `ode45` function. Finally, we calculate $\phi_k(t)$, which is given by (3.161), for $k = 1, 2, \ldots, K$ using the samples of $\omega_k(t)$ and the MATLAB `cumtrapz` function.

## 3.4 Discussion

In this chapter, we have formulated and solved a model for normal gaseous combustion in confinement. By 'normal' we mean that the gas burns in a slow, thin premixed flame, and that the rate of the chemical reactions is negligibly small in the gas away from the flame. In the limit of large Péclet number, $\epsilon \ll 1$, we are justified in treating the flame as a discontinuity across which the Chapman–Jouguet conditions (3.4) hold. With $\epsilon \ll 1$ and the chemistry either side of the flame negligible, we found that the model, (2.14), (2.22), and (2.23), reduces to the free-boundary problem (3.2)–(3.6) for two regions of inviscid, inert gas.

Flames are subsonic, often with Mach numbers significantly less than unity [15, §2.1]. Consequentially, flames produce acoustic waves in the surrounding gas. These acoustic waves present a particular difficulty when modelling combustion in confinement; the acoustic waves produced at the flame reflect at the boundaries and subsequently interact with the flame. We need to be able to account for flame-acoustic interactions to satisfactorily model combustion in confinement.

In Section 3.3, we used ideas from the method of multiple scales [46, §7] to derive an asymptotic solution to (3.2)–(3.6) in the limit of small Mach number, $M \to 0$, which is summarised in Section 3.3.7. We use (3.157) to refer to the solution hereafter and trust that the details are adequately signposted from Section 3.3.7.

In essence, the solution (3.157) describes acoustic perturbations, $\tilde{p}_1$, $\tilde{V}_1$ and $\tilde{u}_0$, to the slowly-varying zero Mach number approximation, $p_0$, $V_0$ and $\breve{u}_0$, derived in Section 3.1. Unlike the early-time acoustic solution (3.28) derived in Section 3.2, the multiple scales solution (3.157) is valid for all $t = O(1)$ provided $q_0 = O(1)$; we will discuss the restriction on the size of $q_0$ in more detail in Section 4.1.2.

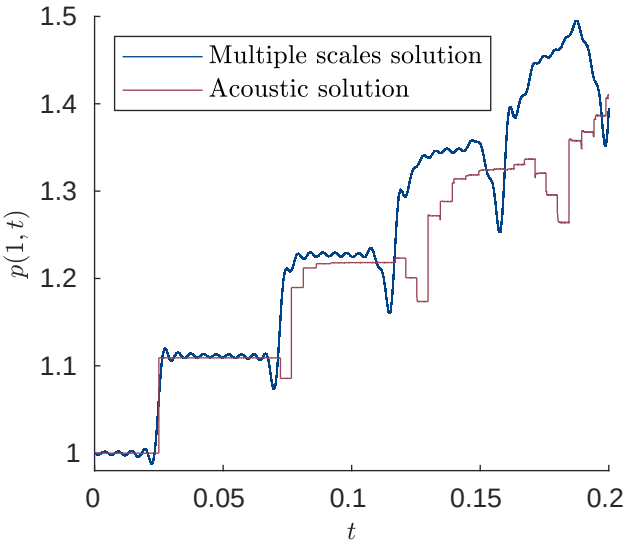


**Figure 3.5:** *Pressure trace at the right-hand wall,* $\chi = 1$*, predicted by the acoustic solution* (3.28b) *and the (truncated) multiple scales solution* (3.157b)*, plotted against time,* $t$*. For this figure, the mass flux through the flame is given by the three-step mass flux model* (3.62)*, and* $E = 100$*,* $K = 9$*,* $T_{\times 2} = 1.6$*,* $\gamma = Q = 1.4$*,* $\mathrm{Le}_{\mathcal{F}} = \mathrm{Le}_{\mathcal{R}} = 1$ *and* $M = 1/40$*.*

The divergence of the two solutions (3.28) and (3.157) for later times, $t = \mathrm{ord}(1)$, is clear to see when they are compared directly; in Figure 3.5, the pressure trace at the right-hand wall, $\chi = 1$, is plotted against time for both acoustic and multiple scales solutions. Notwithstanding the Gibbs phenomenon, which is an artefact of truncating the series (3.160), the two solutions predict the same magnitude for the first acoustic wave, and agree on its arrival time at the right-hand wall. The linear wave equation (3.42), however, does not account for the overall rise in temperature in the gas either side of the flame, meaning the acoustic solution (3.28b) predicts that subsequent waves arrive at the wall later than the multiple scales solution (3.157b) does. The increase in the leading-order mass flux, $q_0$, with temperature also plays a role in the difference between the two solutions plotted in Figure 3.5; we use the initial value of the mass flux, $q_0(1)$, in (3.45) to determine the flame position in the acoustic model. However, we would still see the acoustic solution predicting a slower rise in pressure than the multiple scales solution even if there was a constant mass flux, $q = 1$, through the flame.

In Figure 3.6, the pressure (3.157b) at the right-hand wall, $\chi = 1$, is plotted against time for the full time it takes the flame to cross from $\chi = 0$ to $\chi = 1$. For comparison, we plot both $p_0(t)$ and $p_0(t) + M\tilde{p}_1(1,t)$. The parameters used to create Figures 3.5 and 3.6 have been chosen such that the initial jump in pressure, $2M\gamma Q q_0(1)$, at the right-hand wall and the final leading-order pressure, $1+\gamma Q$, correspond to the dimensional changes in pressure exhibited in Figure 1.6a. Recall that a numerical simulation for the combustion of hydrogen from [95] is depicted in Figure 1.6a. We have not conducted a formal procedure to find the parameters that best fit our solution (3.157) with the numerical simulation in used to create Figures 1.5–1.6, however, qualitatively, our solution (3.157) to (3.2)–

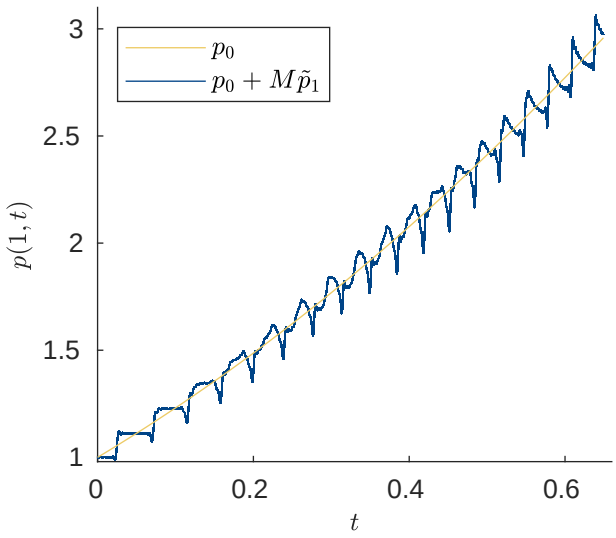


**Figure 3.6:** *Pressure trace at the right-hand wall,* $\chi = 1$*, predicted by the multiple scales solution* (3.157b)*. Both* $p_0(t)$ *and* $p_0(t) + M\tilde{p}_1(1,t)$ *are plotted. For this figure, the mass flux through the flame is given by the three-step mass flux model* (3.62)*, and* $E = 100$*,* $K = 9$*,* $T_{\times 2} = 1.6$*,* $\gamma = Q = 1.4$*,* $\mathrm{Le}_{\mathcal{F}} = \mathrm{Le}_{\mathcal{R}} = 1$ *and* $M = 1/40$*.*

(3.6) does exhibit much of the same behaviour as the solution to the comparatively more complicated model Yu and Chen [95] use. For instance, we find that the pressure at the right-hand wall, plotted in blue in Figure 3.6, rises with rapid variations around the slowly-varying leading-order solution, plotted in yellow. By using the three-step reaction mass flux model (3.62), we also find that the rate of change of the leading-order pressure increases with time, which is similar to the trend exhibited by the pressure trace in Figure 1.6a.

For normal combustion, the gain from conducting the multiple scales analysis in Section 3.3 appears to be small; the much simpler zero Mach number approximation correctly predicts the leading-order pressure, specific volume and temperature profiles. Using the method of multiple scales, we found the leading-order velocity and the $O(M)$ perturbations to the leading-order pressure, specific volume and temperature. The temperature (3.157e) profile at $t = t_0^*(0.4)$ is plotted in Figure 3.7. The $O(M)$ perturbations introduce spatial variations in pressure, specific volume and temperature ahead of the flame. Our model also predicts short-scale spatial variations in specific volume and temperature behind the flame, which are necessary to satisfy the Chapman–Jouguet conditions across the flame.

With a view to modelling autoignition, spatial variations in temperature ahead of the flame are significant. For our three-step reaction model, the rates, (2.23a) and (2.23b) of the initiation and branching reactions are temperature dependent. Therefore, a local increase in temperature leads to a local increase in reaction rate, which, in turn, will further increase the temperature locally. The resulting positive feedback cycle is responsible for autoignition. In the next chapter, we model the early stages of autoignition development by matching the multiple scales combustion solution (3.157) with a boundary layer in time where the exothermic chemical reaction in the gas ahead of the flame is significant.

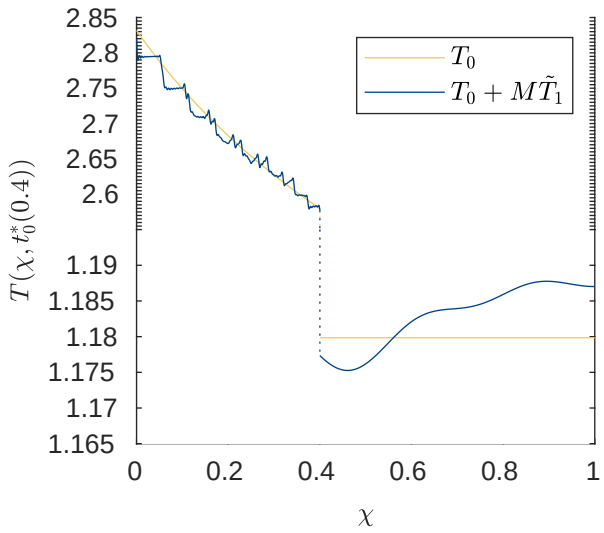


**Figure 3.7:** *Temperature predicted by the multiple scales solution* (3.157e)*, plotted against* $\chi$ *at the moment* $\chi_0^*(t) = 0.4$*. Both* $T_0(\chi, t_0^*(0.4))$ *and* $T_0(\chi, t_0^*(0.4)) + M\tilde{T}_1(\chi, t_0^*(0.4))$ *are plotted. Note that the vertical axis has been split, omitting* $T \in (1.195, 2.55)$*, and different scales have been used for either side of the discontinuity. For this figure, the mass flux through the flame is given by the three-step mass flux model* (3.62)*, and* $E = 100$*,* $K = 9$*,* $T_{\times 2} = 1.6$*,* $\gamma = Q = 1.4$*,* $\mathrm{Le}_{\mathcal{F}} = \mathrm{Le}_{\mathcal{R}} = 1$ *and* $M = 1/40$*.*

# Chapter 4

# Autoignition

In Chapter 3, we assumed that the flame is slow, and that the chemical activity in the unburnt gas ahead of the flame has a negligible effect on the gas dynamics. These are reasonable assumptions during normal combustion. However, the reactions in the end-gas play a significant role and the flame speeds up considerably during autoignition and DDT, respectively. In this chapter, we first uncover boundaries of regions in parameter space where autoignition or DDT may occur by assessing where the asymptotic approximations made in Chapter 3 become invalid. Then, in Section 4.2, we consider parameter regimes where the three-step chemical reaction becomes significant in the end-gas before the flame arrives at $\chi = 1$, and identify a model for the interplay between chemical reaction and gas dynamics during autoignition. We use asymptotic analysis in the limit $M \to 0$ to investigate the behaviour of the model during the early stages of autoignition. We choose to focus our attention on the parameter regime where $EM = O(1)$ and $E^2M \gg 1$ as $M \to 0$, because, in this distinguished case, the gas dynamics are fully coupled to the chemical reaction during the induction stage of autoignition.

## 4.1 Validity of normal combustion model

In the work presented in Chapter 3, we found that, during normal combustion, the leading-order temperature in the end-gas rises as the flame propagates across the domain. As a consequence of the rising temperature, the rate of reaction in the end-gas increases, as does the mass flux, $q$, through the flame. In this section, we consider the validity of the inert gas approximation, $\epsilon^{-1}Qr = o(1)$, and the validity of the slow flame approximation, $Mq = o(1)$, in turn to identify parameter regimes in which autoignition or DDT may occur, respectively.

### 4.1.1 Inert gas approximation

Firstly, we consider the validity of the assumption that the chemical activity is negligible in front of the flame. Specifically, in Chapter 3, we assumed that

$$\epsilon^{-1}Qr = o(1), \tag{4.1}$$

as $\epsilon \to 0$, $E \to \infty$, so that (3.2c) is the leading-order approximation to (2.33c). Clearly, the assumption (4.1) does not hold during autoignition. By identifying where the assumption (4.1) breaks down, we reveal the parameter regime in which the normal combustion model (3.2) is a valid approximation to (2.14). For both chemical reaction mechanisms, (2.1) and (2.6), we identify a critical temperature, $T_c$, such that the assumption (4.1) holds when the temperature, $T^R$, ahead of the flame satisfies $T_c - T^R \gg E^{-1}$. For the one-step chemical reaction, we identify the critical temperature from the reaction rate, whereas determining the critical temperature for the three-step reaction requires tracking the small amount of radical ahead of the flame.

#### 4.1.1.1 One-step reaction

Substituting the reaction rate (2.17) for the one-step reaction into (4.1), we find that the normal combustion model (3.2) is valid when

$$\epsilon^{-1}Qr = \epsilon^{-1}QZY_{\mathcal{F}} \exp\left(-\frac{E}{T}\right) = o(1), \tag{4.2}$$

where we recall that $Z$ is given by (2.18). If $\epsilon^{-1}QZ > 1$, which we assume to be true given the form of $Z$ in terms of $E$, $Q$, and $\mathrm{Le}_{\mathcal{F}}$, then we are able to identify a critical temperature, $T_c$,

$$T_c = \frac{E}{\log(\epsilon^{-1}QZ)}, \tag{4.3}$$

such that $T_c < 1 + Q$ and

$$\epsilon^{-1}Qr = Y_{\mathcal{F}} \exp\left(\frac{E}{T_c} - \frac{E}{T}\right). \tag{4.4}$$

Ahead of the flame, the assumption (4.2) is valid only when $T_c - T^R \gg E^{-1}$. Of course, if $\epsilon$ is sufficiently small then we could have a situation where $T_c - 1 = O(E^{-1})$ or indeed $T_c < 1$, in which case the assumption $\epsilon^{-1}Qr = o(1)$ never holds, not even initially. Assuming $T_c - 1 = \mathrm{ord}(1)$, there is a period, at least initially, where the chemistry ahead of the flame is negligible and (3.2c) is a valid approximation to (2.33c). Any spark-ignited internal combustion engine is, of course, designed to operate in this regime. However, if the temperature ahead of the flame rises to a point where $T_c - T^R = O(E^{-1})$, then the effect of the chemical reaction in the end-gas can no longer be ignored.

To illustrate numerically that (4.2) is valid when $T_c - T^R \gg E^{-1}$, we compare the critical temperature (4.3) with numerical simulations of (2.123). Recall that (2.123) is a simple model for autoignition—analogous to that of Kagan and Sivashinsky [49]. To derive their model, Kagan and Sivashinsky use the same zero Mach number approximation as Sivashinsky [84] that we use in Section 3.1, but they retain the reaction term, $\epsilon^{-1}r$, from (2.14c) and (2.16) when modelling the gas ahead of the flame.

In Figure 4.1, we plot the numerical solution to (2.123) for three different values of $T_c$, together with the solution to

$$\frac{\mathrm{d}\chi^*}{\mathrm{d}t} = \frac{(T^R + QY_{\mathcal{F}}^R)^2}{Y_{\mathcal{F}}^R(1+Q)^2} \exp\left(\frac{E}{2(1+Q)} - \frac{E}{2(T^R + QY_{\mathcal{F}}^R)}\right), \quad \chi^*(0) = 0, \tag{4.5a}$$

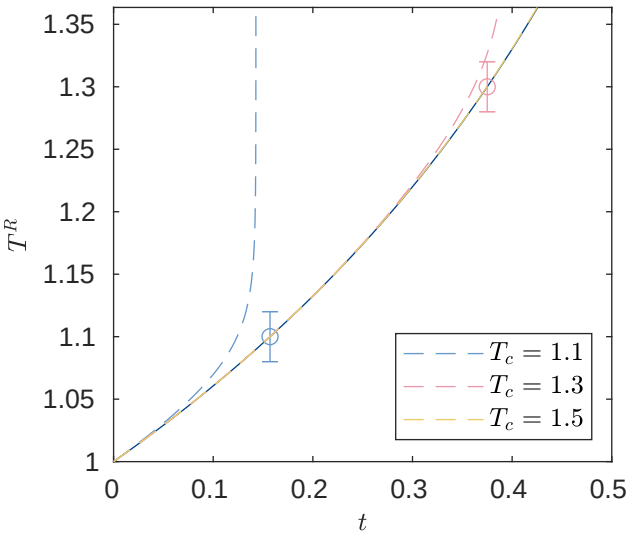


**Figure 4.1:** *Temperature, $T^R$, ahead of the flame, plotted against time, $t$. The dashed curves are numerical solutions of* (2.123)*, and the solid blue curve is the numerical solution of* (4.5)*. The critical temperatures, $T_c$, given by* (4.3) *are indicated by circles, with error bars showing $T_c \pm E^{-1}$. For this figure, $E = 50$ and $\gamma = Q = 1.4$.*

$$p = 1 + \gamma Q \chi^*, \quad T^R = p^{1-1/\gamma}, \quad Y_{\mathcal{F}}^R = 1. \tag{4.5b}$$

The model (4.5) is found by combining (2.70), (3.1) and (3.21)–(3.24), and is analogous to the zero Mach number model by Sivashinsky [84] for our 1D geometry and specific reaction rate (2.17).

For $T_c = 1.1$ and $T_c = 1.3$, the critical temperature, $T_c$, is indicated in Figure 4.1 by a circle, and the error bars show $T_c \pm E^{-1}$, where $E = 50$. Note that $T_c = 1.5$ is greater than the maximum temperature, $\max T^R = (1 + \gamma Q)^{1-1/\gamma}$, predicted by (4.5), and therefore the circle and error bar corresponding to $T_c = 1.5$ are not displayed in Figure 4.1.

The solution to (4.5), shown as a solid blue curve in Figure 4.1, is virtually indistinguishable from the solution to (2.123) with $T_c = 1.5$, shown by the dashed yellow curve. For $T_c = 1.1$ and $T_c = 1.3$, the solutions to (4.5) and (2.123) coincide initially, but then start to deviate appreciably when the temperature is within $O(E^{-1})$ of $T_c$. For $T_c = 1.1$, this is not so clear to see. However, the temperature predicted by (2.123) with $T_c = 1.1$ first differs from the temperature predicted by (4.5) by $E^{-1}$, when $t = 0.12$, or, equivalently, when the temperature given by (4.5) is $T^R = T_c - 1.3E^{-1}$.

We conclude that (4.5) is a valid asymptotic approximation to the more complicated model (2.123) for $T_c - T^R \gg E^{-1}$. For the simple zero Mach number model (2.123), autoignition does not occur if $T_c - \max T^R \gg E^{-1}$, or equivalently,

$$\frac{1+Q}{1 + E^{-1}(1+Q)(\log(E^2Q^3) - \log(2\epsilon \mathrm{Le}_{\mathcal{F}}(1+Q)^4))} - (1+\gamma Q)^{1-1/\gamma} \gg E^{-1}, \tag{4.6}$$

where we have used (2.18) and (4.3) to evaluate $T_c$.

Our analysis here has yielded an algebraic expression for the critical temperature (4.3), a quantitative prediction of the temperature at which autoignition occurs in the sense of [49], without having to solve (2.123). If we were so inclined, we could use matched asymptotic expansions to explain the behaviour of (2.123) for $T_c - T^R = O(E^{-1})$. However, because the zero Mach number approximation precludes any spatial variation in the temperature ahead of the flame, we do not analyse the model by Kagan and Sivashinsky [49] any further.

#### 4.1.1.2 Three-step reaction

Substituting (2.23c) into (4.1), we find that (3.2c) is a valid approximation to (2.33c) in the limit $\epsilon \to 0$ when

$$\epsilon^{-1} Q r = \epsilon^{-1} Q Y_{\mathcal{R}} = o(1). \tag{4.7}$$

To identify when (4.7) breaks down, we must track the small amount of radical produced in the end-gas during normal combustion. Assuming, as we did in Chapter 3, that diffusion has a negligible effect away from the flame in the limit $\epsilon \to 0$, we find that the mass fractions of the fuel and radical satisfy

$$\epsilon \frac{\partial Y_{\mathcal{F}}}{\partial t} = -V\left(r_1 + r_2\right), \tag{4.8a}$$

$$\epsilon \frac{\partial Y_{\mathcal{R}}}{\partial t} = V\left(r_1 + r_2 - r_3\right), \tag{4.8b}$$

where $r_1$, $r_2$ and $r_3$ are given by (2.23). At $t = 0$, we assume that there is no radical ahead of the flame, meaning (4.7) holds initially. Provided that (4.7) continues to hold, $p$, $V$ and $u$ satisfy (3.2)–(3.6), and $Y_{\mathcal{F}}$ and $Y_{\mathcal{R}}$ are then found through quadrature of (4.8).

To identify the parameter regime where (4.7) holds, we use asymptotic analysis to approximate (4.8) in the limit $E \to \infty$, $\epsilon \to 0$. We define the critical temperature, $T_c$, as

$$T_c = \frac{mET_{\times 1}}{mE + 2\log(E) - \log(\epsilon)}, \tag{4.9}$$

such that

$$\epsilon = E^2 \exp\left(m\left(\frac{E}{T_{\times 1}} - \frac{E}{T_c}\right)\right). \tag{4.10}$$

We choose to study the parameter regime where the critical temperature, $T_c$, satisfies

$$T_c - 1 = \mathrm{ord}(1), \quad T_{\times 2} - T_c = \mathrm{ord}(1), \quad T_{\times 1} - T_{\times 2} = \mathrm{ord}(1). \tag{4.11}$$

As we will see in Section 4.1.2.2, the restriction $T_{\times 2} - T_c = \mathrm{ord}(1)$ ensures that if autoignition occurs then it occurs before there is significant acceleration of the flame, and the restriction $T_c - 1 = \mathrm{ord}(1)$ ensures there is an $\mathrm{ord}(1)$ period of $t$-time before the temperature $T_c$ is reached. As discussed in Section 2.2.2.2, the restriction $T_{\times 1} - T_{\times 2} = \mathrm{ord}(1)$ ensures that the initiation reaction (2.6a) is subdominant in the interior of the flame, and the flame has the three-layer structure described by Dold [29].

We will now show that, in the parameter regime (4.11), the assumption (4.7) breaks down as $T^R \to T_c$. Consider the size of the terms in the equation (4.8b) in the limit

$E \to \infty$ and $\epsilon \to 0$. For $T_{\times 2} - T \gg E^{-1}$, the rate, $r_2$, of the branching reaction is asymptotically small compared to the rate, $r_3$, of the termination reaction as $E \to \infty$. Furthermore, since $Y_{\mathcal{R}} = 0$ at $t = 0$, the initiation reaction (2.6a) dominates over the branching reaction (2.6b), at least initially. There is an $O(\epsilon)$ boundary layer in $t$-time as the amount of radical increases from $Y_{\mathcal{R}} = 0$, but then the dominant balance in (4.8b) as $E \to \infty$ is

$$Y_{\mathcal{R}} = E^2 Y_{\mathcal{F}} \exp\left(m\left(\frac{E}{T_{\times 1}} - \frac{E}{T}\right)\right). \tag{4.12}$$

Substituting (4.9) and (4.12) into (4.7), we find

$$\epsilon^{-1} Q r = Q Y_{\mathcal{F}} \exp\left(m\left(\frac{E}{T_c} - \frac{E}{T}\right)\right). \tag{4.13}$$

As with the one-step reaction, we deduce that $\epsilon^{-1} Q r = o(1)$ as $E \to \infty$ while $T_c - T^R \gg E^{-1}$. In Section 3.3, we found that the perturbations to the leading-order temperature during normal combustion are $O(M)$. Comparing the critical temperature, $T_c$, with the maximum leading-order temperature, $\max T_0^R = (1 + \gamma Q)^{(\gamma-1)/\gamma}$, of the end-gas during normal combustion, we conclude that if $EM = O(1)$ and

$$T_c - (1 + \gamma Q)^{\frac{\gamma-1}{\gamma}} \gg E^{-1}, \tag{4.14}$$

where $T_c$ is given by (4.9), then the normal combustion model (3.2) is valid up until the time the flame reaches $\chi = 1$, and therefore autoignition does not occur. For $EM \gg 1$, it is necessary to consider the higher order corrections to $T^R$, not just $T_0^R$, to determine whether (4.7) holds.

### 4.1.2 Slow flame approximation

With (4.14), we have identified a boundary of the region in parameter space where autoignition does not occur. Before we turn our attention to analysing what happens when autoignition does occur, we first investigate the validity of the assumption that the flame is slow. In Chapter 3, we were able to significantly simplify the model (3.2) by taking the limit $M \to 0$ with $Q = O(1)$ and $\gamma - 1 = O(1)$. Particularly, in Sections 3.2 and 3.3 we found that if $Mq = o(1)$ then the perturbations to the leading-order solution satisfied linear partial differential equations. If the mass flux, $q$, becomes large enough that $q$ no longer satisfies $Mq = o(1)$, then the mass flux appears in the leading-order approximation to the Chapman–Jouguet conditions (3.4), and we expect nonlinear gas dynamics to play a role in the subsequent behaviour of the solution to (3.2). We do not analyse the solution further in this case, but postulate that the acceleration of the flame would lead to the formation of shocks in the gas ahead of the flame, indicating the beginnings of DDT [83].

In the analysis below, we identify a critical temperature, $T_C$, such that the assumption that $Mq^{(0)} = o(1)$ becomes invalid as $T^{R*} \to T_C$, for both the one-step and three-step reaction mass flux models, (2.70) and (2.88). We conclude that the asymptotic solution (3.157) to the normal combustion model (3.2)–(3.6) is valid provided that $T_C - T^{R*} = \mathrm{ord}(1)$.

#### 4.1.2.1 One-step reaction

For the one-step reaction, the leading-order approximation, $q^{(0)}$, to the mass flux through the flame is given by (2.70), and is acutely sensitive to the temperature ahead of the flame; an $O(E^{-1})$ rise in temperature causes an $O(1)$ rise in $q^{(0)}$. We find that $M$ must be exponentially small in $E$ if $Mq^{(0)} = o(1)$ is to hold for $T^{R*} - 1 = \mathrm{ord}(1)$.

If $M\exp(E/(2(1+Q))) \leq 1$, then $Mq^{(0)} = o(1)$ as $E \to \infty$ for all fixed $T^{R*} > 0$, $Y_{\mathcal{F}}^{R*} > 0$. However, when $M\exp(E/(2(1+Q))) > 1$, we identify the critical temperature, $T_C$, as

$$T_C = \frac{1+Q}{1+2E^{-1}(1+Q)\log M} - Q. \tag{4.15}$$

The critical temperature (4.15) is chosen so that

$$Mq^{(0)} = \frac{(T^{R*}+QY_{\mathcal{F}}^{R*})^2}{Y_{\mathcal{F}}^{R*}(1+Q)^2}\exp\left(\frac{E}{2(T_C+Q)} - \frac{E}{2(T^{R*}+QY_{\mathcal{F}}^{R*})}\right). \tag{4.16}$$

Initially, $T^{R*} = 1 < T_C$ and $Y_{\mathcal{F}}^{R*} = 1$, meaning $Mq^{(0)} = o(1)$ as $E \to \infty$. However, with $Y_{\mathcal{F}}^{R*} = 1$, we recognise from (4.16) that the assumption $Mq^{(0)} = o(1)$ becomes invalid as $T^{R*}$ approaches $T_C$ from below.

In the experimental results and numerical simulations discussed in Chapter 1, flame acceleration does not play a significant role before or during autoignition. Therefore, for the parameter regimes of interest, we would expect that $Mq^{(0)} = o(1)$ would hold for an $\mathrm{ord}(1)$ time on the $t$-time scale, or, equivalently, until $T^{R*} - 1 = \mathrm{ord}(1)$. From (4.16), we deduce that, unless $M$ is exponentially small in $E$, the slow flame approximation breaks down when $T^{R*} - 1 = o(1)$. We conclude that the one-step reaction is not suitable for studying the interplay between chemistry and gas dynamics during autoignition because the acceleration of the flame is unrealistic. We therefore do not consider the one-step reaction mechanism (2.1) in any further detail.

#### 4.1.2.2 Three-step reaction

For the three-step reaction model, we require $Mq = o(1)$ for the asymptotic approximations we made in Section 3.3 to be valid. The leading-order approximation, $q^{(0)}$, to the mass flux through the flame is given by the solution to (2.88). Since $M \to 0$, the mass flux needs to be correspondingly large for $Mq^{(0)} \neq o(1)$. As $q^{(0)} \to \infty$, the solution to (2.88) behaves like

$$(q^{(0)})^2 \sim \frac{QY_{\mathcal{F}}^{R*}(1+\mathrm{Le}_{\mathcal{R}})}{\mathrm{Le}_{\mathcal{R}}(T_{\times 2} - T^{R*})}. \tag{4.17}$$

We know that $Y_{\mathcal{F}}^{R*} \leq 1$, and we assume that $Q = \mathrm{ord}(1)$ and $\mathrm{Le}_{\mathcal{R}} = \mathrm{ord}(1)$. We therefore deduce that our asymptotic approximations to (3.4) in the limit $M \to 0$ become invalid as $T^{R*}$ approaches the critical temperature, $T_C = T_{\times 2}$. Given that flame acceleration does not play a significant part in normal combustion or autoignition, we restrict our attention to the parameter regime (4.11), where $T_{\times 2} - T^{R*} = \mathrm{ord}(1)$.

## 4.2 Hot spot development

The value of the critical temperature, $T_c$, defined by (4.9), should be seen to provide an indication of whether autoignition occurs or not, rather than a prediction of how autoignition occurs; if the temperature, $T^R$, of the end-gas rises to a point where $T_c - T^R = O(E^{-1})$, then the effect of the chemical reaction in the end-gas becomes significant and autoignition follows. We are yet to address how a hot spot develops at localised points within the end-gas, as observed in the experiments and numerical simulations from the literature discussed in Chapter 1. To understand the early stages of hot spot development, in this section we analyse a model which accounts for spatial variations in pressure as the chemical activity in the end-gas first becomes significant. We choose to focus on the more realistic three-step chemical reaction scheme (2.6), since we are able to identify a parameter regime where autoignition occurs without significant flame acceleration.

We find that, in the parameter regime defined by (4.11), there is an initial period of time where $\epsilon^{-1}Qr = o(1)$, meaning it is appropriate to model the dynamics of the gas using the normal combustion model (3.2). We call this period of time the 'compression stage' because the compression due to expansion of the burning gas at the flame is the dominant cause of the increase in temperature and pressure in the end-gas. If, eventually, the end-gas reaches a temperature where $T_c - T^R = O(E^{-1})$, then the effect of the chemical reaction in the end-gas can no longer be ignored. To analyse the behaviour of the end-gas when $T_c - T^R = O(E^{-1})$, it is necessary to consider an $O(E^{-1})$ boundary layer in $t$-time, analogous to the induction stage in homogeneous explosion theory [54]. We therefore refer to this boundary layer in time as the 'induction stage'. By matching the solution in the compression stage with the solution in the induction stage, we reveal how the acoustic waves generated during the compression stage affect where autoignition occurs.

As before, we treat the flame as a free boundary between two regions of inviscid gas. However, unlike in Chapter 3, we now retain the reaction terms in the governing equations. We make use of (4.9) to eliminate $\epsilon$, and assume that $T_c$ satisfies (4.11) so the mass fraction of the radical, $Y_{\mathcal{R}}$, satisfies (4.12). We further assume that the fuel and radical are completely consumed as the gas passes through the flame, meaning $Y_{\mathcal{F}} = Y_{\mathcal{R}} = 0$ for $\chi \in (0, \chi^*)$. With this in mind, we have that, for $\chi \in (0, \chi^*) \cup (\chi^*, 1)$,

$$\frac{\partial V}{\partial t} - \frac{\partial u}{\partial \chi} = 0, \tag{4.18a}$$

$$\frac{\partial u}{\partial t} + \frac{1}{\gamma M^2}\frac{\partial p}{\partial \chi} = 0, \tag{4.18b}$$

$$p\frac{\partial S}{\partial t} = QY \exp\left(m\left(\frac{E}{T_c} - \frac{E}{T}\right)\right), \tag{4.18c}$$

$$\frac{\partial Y}{\partial t} = -VY \exp\left(m\left(\frac{E}{T_c} - \frac{E}{T}\right)\right), \tag{4.18d}$$

$$Y_{\mathcal{R}} = E^2 Y \exp\left(m\left(\frac{E}{T_{\times 1}} - \frac{E}{T}\right)\right), \tag{4.18e}$$

$$T = pV, \tag{4.18f}$$

$$S = \gamma^{-1}\log(pV^{\gamma}), \tag{4.18g}$$

where we have written $Y = Y_{\mathcal{F}}$ to simplify our notation. We have not included the branching reaction in (4.18d) because $r_2 = 0$ behind the flame, and, ahead of the flame, the rate, $r_2$, of the branching reaction is exponentially small compared to the rate, $r_1$, of the initiation reaction. The flame position, $\chi^*$, is found by solving

$$\frac{\mathrm{d}\chi^*}{\mathrm{d}t} = q, \tag{4.19}$$

where $q \sim q^{(0)} + E^{-1}q^{(1)}$ is the mass flux through the flame, where $q^{(0)}$ and $q^{(1)}$ are defined by (2.88) and (2.94) respectively. At $\chi = \chi^*(t)$, the relationships between the dependent variables on either side of the flame are given by the Chapman–Jouguet conditions (2.47),

$$[u + qV]^+_- = 0, \tag{4.20a}$$

$$\left[p + \gamma M^2 q^2 V\right]^+_- = 0, \tag{4.20b}$$

$$\left[pV + \frac{\gamma - 1}{2}M^2 q^2 V^2 + QY\right]^+_- = 0. \tag{4.20c}$$

Note, we have not included $Y_{\mathcal{R}}$ in (4.20c), because from (4.18e) we have that $Y_{\mathcal{R}}$ is exponentially small away from the flame during the compression and induction stages. To reiterate, we assume the fuel is completely burned in the flame, so

$$Y^{L*} = \lim_{\chi \nearrow \chi^*} Y = 0. \tag{4.20d}$$

We seek an approximate solution to (4.18)–(4.20) in the limit $E \to \infty$, $M \to 0$ for $t > 0$ and $\chi \in (0, 1)$, subject to the boundary and initial conditions,

$$u(0, t) = u(1, t) = 0, \tag{4.21}$$

$$p(\chi, 0) = V(\chi, 0) = Y(\chi, 0) = 1, \quad u(\chi, 0) = \chi^*(0) = 0. \tag{4.22}$$

The approximate solution to (4.18)–(4.22) during the compression stage is simply the solution (3.157) we found in Section 3.3. If the temperature, $T^R$, in the end-gas reaches a point where $T_c - T^R = O(E^{-1})$, then the source term on the right-hand side of (4.18c) can no longer be ignored and we enter the induction stage. Matching back to the compression stage, we have that the acoustic perturbations to the leading-order temperature are $O(M)$. Due to the form of the source term on the right-hand side of (4.18c), the role acoustics play during the induction stage depends on the relative sizes of $E$ and $M$. Consider the following cases with increasing $M$:

1. If $E^2 M = O(1)$, then the $O(M)$ perturbations to the leading-order temperature generated during the compression stage are too small to affect the reaction rate at leading order, resulting in spatially uniform blow up of the leading-order perturbation to the temperature during the induction stage. Preliminary work has shown that, in order to determine the spatial variations, an additional time scale is needed to resolve the acoustic waves—which appear as a higher order correction—using the method of multiple scales, but we do not present that work here.

2. If $EM = O(1)$ with $E^2M \gg 1$, then the $O(M)$ perturbations to the leading-order temperature are sufficiently large to appear in the source term on the right-hand side of (4.18c) at leading order. In this case, chemical reaction and gas dynamics are fully coupled.

3. If $EM \gg 1$, then the $O(E^{-1})$ induction stage is much shorter than the $O(M)$ time taken for an acoustic wave to cross the domain. We anticipate that autoignition will develop rapidly close to the time and location where the temperature, $T^R$, ahead of the flame first reaches $T_c$.

We find that the induction stage is an $O(E^{-1})$ boundary layer in $t$-time, centred around a critical time, $t_c$. For the first two cases described above, since $EM = O(1)$, we define the critical time as the time the leading-order temperature, $T_0^R$, in the compression stage reaches the critical temperature, $T_c$. That is,

$$T_0^R(t_c) = T_c. \tag{4.23}$$

For the third case, since $M \gg E^{-1}$, the higher order corrections to $T^R$, not just $T_0^R$, will be important in determining the critical time.

Of the three cases above, the second, with

$$EM = O(1), \quad E^2M \gg 1, \tag{4.24}$$

exhibits the richest variety of behaviour during the induction stage. In the subsequent parts of this chapter, we develop an asymptotic model for the induction stage in the limit $M \to 0$ with $EM = O(1)$ and $E^2M \gg 1$, match it with the compression stage solution, and solve it numerically to investigate how a hot spot develops following a period of normal combustion.

### 4.2.1 Asymptotic description of the induction stage

We now analyse the model (4.18)–(4.22) as $M \to 0$, in the distinguished limit summarised in Table 2.2. During the compression stage, the asymptotic solution to (4.18)–(4.22) is simply (3.157)—the solution we found in Section 3.3 to the normal combustion model (3.2)–(3.6). We assume that the parameters do not satisfy (4.14), so the chemistry in the end-gas becomes significant before the flame reaches the right-hand boundary, $\chi = 1$, and, hence, autoignition occurs. To understand the early stages of autoignition, we consider the induction stage, an $O(E^{-1})$ boundary layer in $t$-time where the temperature in the end-gas satisfies $T_c - T^R = O(E^{-1})$.

To describe the induction stage, we define a new time variable, $\tau$, by

$$t = t_c + M\tau, \quad \tau = O(1). \tag{4.25}$$

We will justify shortly that $t_c$ is the critical time defined implicitly by (4.23). Additionally, we use hats on the dependent variables, for example $\hat{p}$, to distinguish the solution during the induction stage from the solution (3.157) during the compression stage. In the

induction stage, we seek approximate solutions to (4.18)–(4.21) of the form

$$p \sim \hat{p}_0 + M\hat{p}_1 + \cdots, \tag{4.26a}$$
$$V \sim \hat{V}_0 + M\hat{V}_1 \cdots, \tag{4.26b}$$
$$u \sim \hat{u}_0 + M\hat{u}_1 + \cdots, \tag{4.26c}$$
$$\chi^* \sim \hat{\chi}_0^* + M\hat{\chi}_1^* + \cdots, \tag{4.26d}$$
$$Y \sim \hat{Y}_0 + M\hat{Y}_1 + \cdots, \tag{4.26e}$$
$$S \sim \hat{S}_0 + M\hat{S}_1 + \cdots, \tag{4.26f}$$
$$T \sim \hat{T}_0 + M\hat{T}_1 + \cdots. \tag{4.26g}$$

We proceed by substituting (4.25) and (4.26) into (4.18)–(4.21) and comparing coefficients of $M$. To satisfy the initial condition (4.22), we insist the solution for $\tau = O(1)$ matches with the solution (3.157) in the compression stage as $\tau \to -\infty$. Results from matching with the normal combustion model will be stated where required. In Section 4.2.6, we will look closer at how the matching works in practice.

### 4.2.2 The leading-order pressure ahead of the flame

Assuming the source term on the right-hand side of (4.18c) is $\mathrm{ord}(1)$ during the induction stage, upon substituting (4.25) and (4.26) into (4.18), we find that, on both sides of the flame,

$$\frac{\partial \hat{V}_0}{\partial \tau} = \frac{\partial \hat{p}_0}{\partial \chi} = \frac{\partial \hat{S}_0}{\partial \tau} = \frac{\partial \hat{Y}_0}{\partial \tau} = 0. \tag{4.27}$$

From (4.27) and $\hat{S}_0 = \gamma^{-1}\log\left(\hat{p}_0\hat{V}_0^{\gamma}\right)$, we deduce that $\hat{p}_0$ is constant ahead of the flame. Furthermore, to match with the compression stage solution, we require that, ahead of the flame, $\hat{S}_0^R \to 0$ as $\tau \to -\infty$. We deduce that $\hat{S}_0^R = 0$ for $\chi \in (\chi^*, 1)$, and hence that $\hat{V}_0^R$ and $\hat{T}_0^R$ are constant ahead of the flame. Matching with the leading-order compression stage solution, we find

$$\hat{p}_0^R = p_0(t_c) =: p_c, \quad \hat{V}_0^R = p_0(t_c)^{-1/\gamma} =: V_c, \quad \hat{T}_0^R = p_0(t_c)^{(\gamma-1)/\gamma}, \quad \hat{Y}_0^R = 1, \tag{4.28}$$

for $\chi \in (\chi^*, 1)$, where $p_0(t)$ is the solution to (3.92).

Substituting the asymptotic series, (4.26e) and (4.26g), into the source term on the right-hand side of (4.18c), we find that, ahead of the flame

$$QY\exp\left(m\left(\frac{E}{T_c} - \frac{E}{T^R}\right)\right) \sim Q\exp\left(m\left(\frac{E}{T_c} - \frac{E}{\hat{T}_0^R} + \frac{EM\hat{T}_1^R}{\left(\hat{T}_0^R\right)^2}\right)\right)(1 + o(1)), \tag{4.29}$$

as $M \to 0$ with $EM = O(1)$. From (4.29), it is clear that we require $\hat{T}_0^R = T_c$ for the source term in the right-hand side of (4.18c) to be $\mathrm{ord}(1)$ during the induction stage. We are therefore justified in our assertion that $t_c$ is defined implicitly by (4.23).

### 4.2.3 The flame position and the entropy behind the flame

In order to solve (4.19) for the flame position, $\chi^*$, we need to specify a model for the mass flux, $q$. In Section 3.3.1, we found that, for the three-step reaction, the mass flux is given by (3.62). Since the leading-order temperature, $\hat{T}_0^R$, and mass fraction of fuel, $\hat{Y}_0^R$, ahead of the flame are constant during the induction stage, we deduce that the mass flux, $q$, is also constant to leading order. Substituting (4.26e) and (4.26g) into (3.62), we find

$$q \sim \hat{q}_0 + O(M), \tag{4.30}$$

where

$$\hat{q}_0 = q^{(0)}(T_c, 1) + E^{-1}q^{(1)}(T_c, 1) =: q_c. \tag{4.31}$$

As before, we include the $O(E^{-1})$ term with the $O(1)$ term because $E^{-1}$ could be asymptotically large compared to $M$ in the parameter regime $EM = O(1)$, $E^2M \gg 1$.

Substituting (4.25), (4.26d) and (4.30) into (4.19) and comparing coefficients of powers of $M$, we find

$$\frac{\mathrm{d}\hat{\chi}_0^*}{\mathrm{d}\tau} = 0, \tag{4.32}$$

$$\frac{\mathrm{d}\hat{\chi}_1^*}{\mathrm{d}\tau} = q_c. \tag{4.33}$$

Matching with the first two terms of the asymptotic expansion (3.157a) for flame position during the compression stage, we deduce

$$\hat{\chi}_0^* = \chi_0^*(t_c) =: \chi_c^*, \quad \hat{\chi}_1^* = q_c\tau, \tag{4.34}$$

where $\chi_0^*(t)$ satisfies (3.158).

We assume that the fuel is completely burned in the flame, meaning $Y = 0$ behind the flame. Hence, from (4.18c), we deduce that the entropy of the gas behind the flame is constant along lines of constant $\chi$. Far behind the flame—that is, for $\chi_c^* - \chi = \mathrm{ord}(1)$—the gas will have passed through the flame before there was any significant chemistry in the end-gas. Hence we can match to the entropy behind the flame during the compression stage, given by (3.78), and deduce that

$$\hat{S}_0^L = \log\Big(1 + Q(1 + \gamma Q\chi)^{\frac{1-\gamma}{\gamma}}\Big), \tag{4.35a}$$

for $\chi_c^* - \chi = \mathrm{ord}(1)$. By comparison, the gas in a narrow layer behind the flame will have passed through the flame during the induction stage. From the Chapman–Jouguet conditions (4.20) we deduce that the leading-order entropy, $\hat{S}_0^L$, behind the flame is constant for $\chi < \chi^*$ with $\chi^* - \chi = O(M)$, with

$$\hat{S}_0^L = \log\Big(1 + Q(1 + \gamma Q\chi_c)^{\frac{1-\gamma}{\gamma}}\Big). \tag{4.35b}$$

Noting that the two expressions (4.35a) and (4.35b) differ by only an $O(M)$ amount when $\chi - \chi_c = O(M)$, we recognise that (4.35a) is the leading-order entropy throughout the gas behind the flame.

It simplifies our analysis to seek an approximate solution to (4.18) for $\chi \in (0, \chi_c^*) \cup (\chi_c^*, 1)$. However, if we fix the flame position at $\chi_c^*$ then we are unable to specify the higher order corrections to the entropy immediately behind the flame in a way that is consistent with the Chapman–Jouguet condition (4.20c), because the entropy behind the flame is constant along characteristics parallel to the boundary, $\chi = \chi_c^*$. Fortunately, the $O(M)$ corrections to entropy behind the flame do not affect the solution for $\hat{p}_1$ and $\hat{T}_1^R$, which are of most interest during autoignition. We are therefore justified in solving (4.18) with the flame position fixed at $\chi = \chi_c^*$, and approximating the Chapman–Jouguet conditions (4.20) by Taylor expanding around $\chi^* = \chi_c^*$.

Behind the flame, from (4.18b), we have that $\partial \hat{p}_0 / \partial \chi = 0$ for $\chi \in (0, \chi_c^*)$. From (4.20b), we deduce that the leading-order pressure, $\hat{p}_0$, is continuous across the flame, meaning

$$\hat{p}_0 = p_c, \tag{4.36}$$

for $\chi \in (0, 1)$. From (4.35), we deduce that

$$\hat{V}_0^L = p_c^{-1/\gamma} \left(1 + Q(1 + \gamma Q \chi)^{\frac{1-\gamma}{\gamma}}\right), \tag{4.37}$$

for $\chi \in (0, \chi_c^*)$. Since $\hat{V}_0 = V_0(\chi, t_c)$, we deduce from (3.91) that

$$\int_0^1 \hat{V}_0 \, \mathrm{d}\chi = 1. \tag{4.38}$$

### 4.2.4 Induction stage model

We now turn our attention to finding the partial differential equations describing ignition in the gas ahead of the flame. Substituting (4.25) and (4.26) into (4.18) and comparing coefficients of powers of $M$, we find that, on both sides of the flame,

$$\frac{\partial \hat{V}_1}{\partial \tau} - \frac{\partial \hat{u}_0}{\partial \chi} = 0, \tag{4.39a}$$

$$\frac{\partial \hat{u}_0}{\partial \tau} + \frac{1}{\gamma} \frac{\partial \hat{p}_1}{\partial \chi} = 0, \tag{4.39b}$$

$$\hat{S}_1 = \frac{\hat{p}_1}{\gamma \hat{p}_0} + \frac{\hat{V}_1}{\hat{V}_0}, \tag{4.39c}$$

$$\hat{T}_1 = \hat{p}_0 \hat{V}_1 + \hat{p}_1 \hat{V}_0. \tag{4.39d}$$

Behind the flame—that is, for $\chi \in (0, \chi_c^*)$—we have that

$$\hat{Y}_0^L = 0, \tag{4.40a}$$

meaning the entropy behind the flame is constant along lines of constant $\chi$,

$$\frac{\partial \hat{S}_1^L}{\partial \tau} = 0. \tag{4.40b}$$

By comparison, ahead of the flame, the $\mathrm{ord}(1)$ approximations to (4.18c) and (4.18d) give that, for $\chi \in (\chi_c^*, 1)$,

$$p_c \frac{\partial \hat{S}_1^R}{\partial \tau} = Q \exp\left(\frac{mEM\hat{T}_1^R}{T_c^2}\right), \tag{4.41a}$$

$$\frac{\partial \hat{Y}_1^R}{\partial \tau} = -V_c \exp\left(\frac{mEM\hat{T}_1^R}{T_c^2}\right). \tag{4.41b}$$

Eliminating $\hat{T}_1^R$ from (4.41a) and (4.41b) and integrating, we find that the perturbation, $\hat{Y}_1^R$, to the mass fraction of fuel ahead of the flame is given by

$$\hat{Y}_1^R = -\frac{p_c V_c}{Q} \hat{S}_1^R. \tag{4.42}$$

Here we have used the fact that we require $\hat{Y}_1^R \to 0$ and $\hat{S}_1^R \to 0$ ahead of the flame as $\tau \to -\infty$ to match with the compression stage solution. Therefore $\hat{Y}_1^R$, $\hat{S}_1^R$ and $\hat{T}_1^R$ ahead of the flame are given algebraically in terms of $\hat{p}_1^R$ and $\hat{V}_1^R$.

To determine $\hat{p}_1^R$ and $\hat{V}_1^R$ ahead of the flame, we solve (4.39)–(4.41), subject to the boundary conditions

$$\hat{u}_0(0, \tau) = \hat{u}_0(1, \tau) = 0, \tag{4.43}$$

and the approximate Chapman–Jouguet conditions (4.20) at $\chi = \chi_c^*$,

$$\left[\hat{u}_0 + q_c \hat{V}_0\right]_-^+ = 0, \tag{4.44a}$$

$$[\hat{p}_1]_-^+ = 0, \tag{4.44b}$$

$$\left[\hat{p}_0 \hat{V}_0 + Q\hat{Y}_0\right]_-^+ = 0. \tag{4.44c}$$

Since we already have that $[\hat{p}_0]_-^+ = 0$ and $[\hat{Y}_0]_-^+ = -1$, we simplify (4.44a) and (4.44c) to

$$[\hat{u}_0]_-^+ = -\frac{Qq_c}{p_c}. \tag{4.45}$$

### 4.2.5 The compressive effect of the flame

Before we set about solving (4.39)–(4.41) numerically, we first isolate the bulk effect of compression due to combustion at the flame. As in our previous analysis, on both sides of the flame, we pose that the solution takes the separated form

$$\hat{u}_0 = \check{\hat{u}}_0(\chi) + \tilde{\hat{u}}_0(\chi, \tau), \tag{4.46a}$$

$$\hat{p}_1 = \check{\hat{p}}_1(\tau) + \tilde{\hat{p}}_1(\chi, \tau), \tag{4.46b}$$

$$\hat{V}_1 = \check{\hat{V}}_1(\chi, \tau) + \tilde{\hat{V}}_1(\chi, \tau), \tag{4.46c}$$

where $\tilde{\hat{u}}_0$ and $\tilde{\hat{p}}_1$ are continuous, including across $\chi = \chi_c^*$. Separating the dependent variables into components in this way is convenient because it allows us to solve for continuous quantities, $\tilde{\hat{p}}_1$ and $\tilde{\hat{u}}_0$, numerically.

We define $\check{\hat{V}}_1$ by

$$\check{\hat{V}}_1 = -\frac{\hat{V}_0(\chi)\check{\hat{p}}_1(\tau)}{\gamma \hat{p}_0}. \tag{4.47}$$

By defining $\check{\hat{V}}_1$ by (4.47) we avoid $\check{\hat{p}}_1$ appearing in the expression for $\hat{S}_1$,

$$\hat{S}_1 = \frac{\tilde{\hat{p}}_1}{\gamma \hat{p}_0} + \frac{\tilde{\hat{V}}_1}{\hat{V}_0}. \tag{4.48}$$

We suppose that $\check{\hat{u}}_0$ satisfies

$$\frac{\mathrm{d}\check{\hat{u}}_0}{\mathrm{d}\chi} = \frac{\partial \check{\hat{V}}_1}{\partial \tau}, \tag{4.49}$$

subject to the boundary conditions $\check{\hat{u}}_0(0) = \check{\hat{u}}_0(1) = 0$. From (4.45) we have that $\check{\hat{u}}_0$ is discontinuous at $\chi = \chi_c^*$, with

$$\left[\check{\hat{u}}_0\right]_-^+ = -\frac{Qq_c}{p_c}. \tag{4.50}$$

To find an equation for $\check{\hat{p}}_1$, we now multiply $\partial \check{\hat{p}}_1/\partial \tau$ by $\hat{V}_0$ and integrate from $\chi = 0$ to $\chi = 1$. Using (4.38), (4.49) and (4.50), we find

$$\frac{\mathrm{d}\check{\hat{p}}_1}{\mathrm{d}\tau} = \gamma q_c Q. \tag{4.51}$$

Matching with the first two terms of the compression stage solution (3.157b), we find that

$$\check{\hat{p}}_1 = \gamma Q q_c \tau. \tag{4.52}$$

We are yet to find $\tilde{\hat{p}}_1$ and $\tilde{\hat{u}}_0$ on both sides of the flame, and $\tilde{\hat{V}}_1^R$ ahead of the flame. Substituting (4.46) into (4.39)–(4.41), we see that the appropriate equations to solve for $\tilde{\hat{p}}_1$, $\tilde{\hat{u}}_0$ and $\tilde{\hat{V}}_1^R$ during the induction stage are

$$\frac{\partial \tilde{\hat{p}}_1}{\partial \tau} = -\frac{\gamma p_c}{\hat{V}_0^L}\frac{\partial \tilde{\hat{u}}_0}{\partial \chi}, \tag{4.53a}$$

$$\frac{\partial \tilde{\hat{u}}_0}{\partial \tau} = -\frac{1}{\gamma}\frac{\partial \tilde{\hat{p}}_1}{\partial \chi}, \tag{4.53b}$$

for $\chi \in (0, \chi_c^*)$, and

$$\frac{\partial \tilde{\hat{V}}_1^R}{\partial \tau} = \frac{\partial \tilde{\hat{u}}_0}{\partial \chi}, \tag{4.53c}$$

$$\frac{\partial \tilde{\hat{u}}_0}{\partial \tau} = -\frac{1}{\gamma}\frac{\partial \tilde{\hat{p}}_1}{\partial \chi}, \tag{4.53d}$$

$$\frac{\partial \tilde{\hat{p}}_1}{\partial \tau} = -\frac{\gamma p_c}{V_c}\frac{\partial \tilde{\hat{u}}_0}{\partial \chi} + \gamma Q \exp\left(\frac{mEM}{T_c^2}\left((\gamma-1)Qq_cV_c\tau + p_c\tilde{\hat{V}}_1^R + \tilde{\hat{p}}_1V_c\right)\right), \qquad (4.53e)$$

for $\chi \in (\chi_c^*, 1)$, subject to the boundary conditions

$$\tilde{\hat{u}}_0(0,\tau) = \tilde{\hat{u}}_0(1,\tau) = 0. \qquad (4.54)$$

The form of (4.53) is particularly amenable to numerical solution via the method of lines. However, we first need to identify initial conditions by matching with the solution during the compression stage.

### 4.2.6 Matching with normal combustion

We now have two asymptotic approximations to (4.18)–(4.22) in the limit $M \to 0$ with $EM = O(1)$ and $E^2M \gg 1$, valid in two different time stages: the normal combustion model (3.2)–(3.6), which we solved in Section 3.3, is valid for $t = O(1)$ during the compression stage, and the induction stage model (4.53) is valid for $t = t_c + M\tau$ with $\tau = O(1)$. It is not obvious how to match the two solutions using Van Dyke's matching rule [46, §5.1.5], because we do not have a closed-form solution to (4.53). To find suitable initial data to solve (4.53) numerically, we adopt the method of intermediate variables [24, §2.7]. We seek some $\alpha \in (0,1)$ such that the solutions to the compression stage and induction stage models agree with only $o(M)$ errors at $t = t_c + M\tau_\star$, where

$$\tau_\star = -M^{-\alpha}. \qquad (4.55)$$

By comparing the asymptotic behaviour of the two models at $t = t_c + M\tau_\star$ as $M \to 0$, we identify appropriate initial conditions to apply at $\tau = \tau_\star$ to solve (4.53) numerically.

The first step in matching the two models is writing the solution (3.157) during the compression stage in terms of $\tau_\star$ and expanding to include $O(M)$ terms. We will only discuss the details of matching the pressure, $p$; the procedure for $u$ and $V$ is analogous. Provided that $M\tau_\star^2 \ll 1$, the asymptotic behaviour of the compression stage solution (3.157b) at $t = t_c + M\tau_*$ is

$$\begin{aligned} p \sim\ & p_0(t_c) + M\tau_* \left.\frac{\mathrm{d}p_0}{\mathrm{d}t}\right|_{t=t_c} \\ & + M\sum_{n=1}^{\infty}\left(A_n(t_c)\exp\left(i\left(\frac{\phi_n(t_c)}{M} + \phi_n'(t_c)\tau_\star\right)\right) + \text{c.c.}\right)G_n(\chi,t_c) + o(M), \end{aligned} \qquad (4.56)$$

as $M \to 0$. The additional restriction, $M\tau_\star^2 \ll 1$, on $\tau_\star$ is necessary so that the third term in the Taylor expansion of $\phi_n(t)/M$ around $t_c$ is $o(1)$ and therefore does not appear in the argument of the exponential.

We have already used (4.56) to derive (4.28) and (4.52). The form of (4.56), and analogous expansions for $u$ and $V$, suggests that the initial conditions we should use at $\tau = \tau_\star$ for (4.53) are

$$\tilde{\hat{p}}_1(\chi,\tau_\star) = \sum_{n=1}^{\infty}\left(A_n(t_c)\exp\left(i\left(\frac{\phi_n(t_c)}{M} + \phi_n'(t_c)\tau_\star\right)\right) + \text{c.c.}\right)G_n(\chi,t_c), \qquad (4.57a)$$

$$\tilde{\hat{u}}_0(\chi,\tau_\star)=\sum_{n=1}^{\infty}\left(\frac{iA_n(t_c)}{\gamma\omega_n(t_c)}\exp\left(i\left(\frac{\phi_n(t_c)}{M}+\phi_n'(t_c)\tau_\star\right)\right)+\text{c.c.}\right)\left.\frac{\partial G_n}{\partial\chi}\right|_{t=t_c}, \quad (4.57b)$$

for $\chi\in(0,1)$, and

$$\tilde{\hat{V}}_1^R(\chi,\tau_\star)=-\frac{V_c}{\gamma p_c}\tilde{\hat{p}}_1(\chi,\tau_\star), \quad (4.57c)$$

for $\chi\in(\chi_c^*,1)$.

The solution to (4.53) behaves like (4.57) to leading order when the source term in (4.53e) is asymptotically small. That is, when

$$\gamma Q\exp\left(\frac{mEM}{T_c^2}\left((\gamma-1)Qq_cV_c\tau_\star+p_c\tilde{V}_1+\tilde{p}_1V_c\right)\right)=o(1). \quad (4.58)$$

For (4.58) to hold, we require $-EM\tau_\star\gg 1$. We now have three requirements on $\tau_\star$ for the compression stage solution and the induction stage solution to match:

$$|\tau_\star|\gg 1,\quad M\tau_\star^2\ll 1,\quad -EM\tau_\star\gg 1. \quad (4.59)$$

For some $\alpha\in(0,0.5)$ to exist such that $\tau_\star=-M^{-\alpha}$ satisfies the conditions (4.59), we require

$$E^2M\gg 1. \quad (4.60)$$

### 4.2.7 Numerical solution

With the boundary conditions (4.54) and initial conditions (4.57), we are now in a position to solve (4.53) numerically using the method of lines. We use a staggered grid to discretise space [74, §6.3]—that is, we seek approximations to $\tilde{\hat{u}}_0$ and $\tilde{\hat{p}}_1$ at alternate points of a uniform grid on $[0,1]$. We use central differences to approximate the spatial derivatives in (4.53), and then solve the resulting system of ordinary differential equations numerically using MATLAB `ode15s`.

To describe the grid, we let $N=200$, and define $h=1/(2N)$ and $\chi=\chi_k=kh$ for $k\in\{0,1,\ldots,2N\}$. For simplicity, we ensure that the leading-order flame position, $\chi_c^*$, lies at one of the even-indexed grid points, say, $\chi_c^*=\chi_{2F}$ for some $F\in\{1,2,\ldots,N-1\}$. To approximate the solution to (4.53), we solve

$$\frac{\mathrm{d}p_{2k+1}}{\mathrm{d}\tau}=-\gamma p_c\frac{u_{2k+2}-u_{2k}}{2hV_0^L(\chi_{2k+1})}, \quad (4.61a)$$

for $k\in\{0,1,\ldots,F-1\}$,

$$\frac{\mathrm{d}V_{2k+1}}{\mathrm{d}\tau}=\frac{u_{2k+2}-u_{2k}}{2h}, \quad (4.61b)$$

$$\frac{\mathrm{d}p_{2k+1}}{\mathrm{d}\tau}=-\gamma p_c\frac{u_{2k+2}-u_{2k}}{2hV_c}+\gamma Q\exp\left(\frac{mEM}{T_c^2}\left((\gamma-1)Qq_cV_c\tau+p_cV_{2k+1}+p_{2k+1}V_c\right)\right), \quad (4.61c)$$

for $k\in\{F,F+1,\ldots,N-1\}$, and

$$\frac{\mathrm{d}u_{2k}}{\mathrm{d}\tau}=-\frac{p_{2k+1}-p_{2k-1}}{2\gamma h}, \quad (4.61d)$$

for $k \in \{1, 2, \ldots, N-1\}$, where

$$u_0 = u_{2N} = 0, \tag{4.61e}$$

and

$$p_k(\tau) \approx \tilde{\hat{p}}_1(\chi_k, \tau), \tag{4.62a}$$

$$V_k(\tau) \approx \tilde{\hat{V}}_1(\chi_k, \tau), \tag{4.62b}$$

$$u_k(\tau) \approx \tilde{\hat{u}}_0(\chi_k, \tau), \tag{4.62c}$$

for $k \in \{0, 1, \ldots, 2N\}$.

For the specific form of equations in (4.53) there are advantages to using a staggered grid, rather than solving for $u_k$ and $p_k$ at every grid point. For one, the central difference approximations to the $\chi$-derivatives naturally depend on values at alternate grid points. By using a staggered grid, we not only reduce the number of ordinary differential equations we need to solve, but also avoid inconsistencies whereby differences in, for example, pressure between neighbouring grid points can have no effect on the solution, because the central difference approximations only depend on the difference between alternate grid points [74, §6.3]. Another benefit of using a staggered grid is that we are able to apply the boundary conditions (4.61e) directly, without having to also calculate $p_0$, $p_{2N}$ and $V_{2N}$. Similarly, by enforcing that the leading-order flame position, $\chi_c^*$, lies at the grid point where we solve for $u_{2F}$, we avoid having to introduce additional variables to deal with the jump in derivative in $\tilde{\hat{u}}_0$ across the flame.

We solve (4.61) numerically using the MATLAB `ode15s` function. To prevent oscillations on the grid scale, we reduce the relative tolerance of `ode15s` to $10^{-6}$, but otherwise use the default settings. To use the matching conditions (4.57) practically, it is necessary to truncate the series (4.57a) and (4.57b). In the numerical simulations used to create Figures 4.2–4.5, we use partial sums of (4.57) with nine terms as initial conditions for (4.61) at $\tau = \tau_\star$. We further discuss appropriate choices of the overlap time, $\tau_\star = -M^{-\alpha}$, in Section 4.3.1.

## 4.3 Discussion and numerical studies

In this chapter, we have investigated when and how autoignition occurs for the three-step chemical reaction (2.6). Before presenting numerical solutions to (4.61), we briefly summarise our modelling approach.

In Section 4.1, we identified a critical temperature, $T_c$, given by (4.9). The critical temperature, $T_c$, can be used to give an indication of when autoignition occurs on the $t$-time scale. That is to say, if the temperature rises to a point where $T_c - T^R = O(E^{-1})$, then the effect of the chemical reactions in the end-gas becomes significant, resulting in autoignition.

The critical temperature, $T_c$, is given in terms of the dimensionless parameters $E$, $T_{\times 1}$, $m$ and $\epsilon$. By comparing $T_c$ with the maximum leading-order temperature, $\max T_0^R = (1 + \gamma Q)^{1-1/\gamma}$, ahead of the flame, we are able to relate the occurrence of autoignition

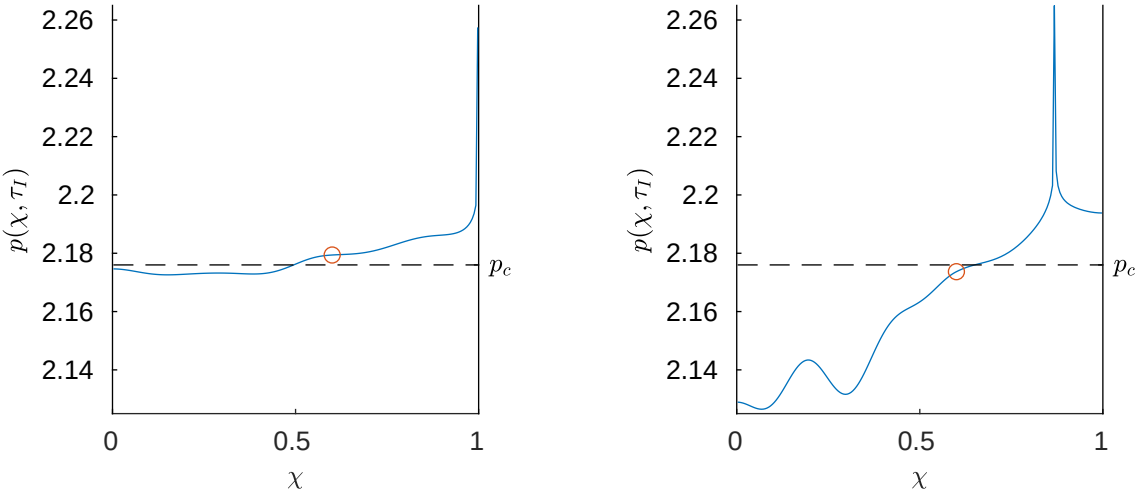


**(a)** $EM = 1$. **(b)** $EM = 10$.

**Figure 4.2:** *The pressure, $p = p_c + M\hat{p}_1$, at the ignition time, $\tau = \tau_I$, plotted against $\chi$ for two different values of $EM$. The flame position is indicated by the circle and the leading-order pressure, $p_c$, is indicted by the dashed line. For this figure, $E = 1000$, $T_{\times 2} = 1.6$, $\gamma = Q = 1.4$, $m = \mathrm{Le}_{\mathcal{F}} = \mathrm{Le}_{\mathcal{R}} = 1$, $\chi_c^* = 0.6$ and $\alpha = 0.45$.*

with the dimensionless parameters, and hence the dimensional properties of the system, summarised in Table 2.1. For example, an increase in the length, $\bar{L}$, of the domain corresponds to a decrease in the dimensionless parameter $\epsilon$, and hence a decrease in the critical temperature, $T_c$. We conclude that increasing the length, $\bar{L}$, of the container lowers the temperature the end-gas needs to reach for autoignition to occur. This observation fits with the numerical results of Yu and Chen [95].

In Section 4.2, we analysed the model (4.18)–(4.22) to describe how a hot spot develops as $T^R \to T_c$, during the early stages of autoignition. We chose to focus on the distinguished limit where $EM = O(1)$ and $E^2 M \gg 1$ as $M \to 0$, because, in this limit, the gas dynamics and chemical reactions are fully-coupled in the end-gas during the induction stage.

During the induction stage, we find that the perturbations to the spatially-uniform leading-order solution ahead of the flame satisfy (4.39) and (4.41). To isolate the compressive effects of combustion at the flame, we have separated the solution into components (4.46). We now solve the resulting system (4.53) for $\tilde{\hat{p}}_1$, $\tilde{\hat{V}}_1^R$ and $\tilde{\hat{u}}_0$ numerically, using the method of lines as described in Section 4.2.7.

After rescaling the variables, we recognise (4.39) and (4.41) as Clarke's reactive acoustic equations [21, 80], which allows us to gain useful insights into the solution behaviour. It is well known that solutions to Clarke's equations (2.121) with bounded initial data become unbounded in finite time [31]. It is therefore no surprise that solutions to (4.53), with (4.54) and (4.57), are singular. We find $\tilde{\hat{p}}_1 \to \infty$ at some location $\chi_I \in [\chi_c^*, 1]$ as $\tau \to \tau_I$ for some $\tau_I \in (\tau_\star, \infty)$. Depending on context, we call both $\tau_I$ and $t_I = t_c + M\tau_I$ the ignition time, and $\chi_I$ the position of the ignition centre. Numerically, the singularity

causes a failure in the ODE solver. The failure of `ode15s` is evident as it is unable to solve (4.61) accurately without reducing the step size to below the minimum step size. In order to quantify the time and place of the singularity, we record the time at which `ode15s` fails as the ignition time, $\tau_I$, and the position of the maximum pressure at $\tau = \tau_I$ as $\chi_I$.

Using the time at which the ODE solver fails gives a crude, but reasonable, approximation to the singularity. However, the approximation we obtain using this method depends on the particular ODE solver being used. A more reliable approximation for the singularity could be found if we fitted the asymptotic behaviour of Clarke's equations (2.121) as $\tau \to \tau_I$ to our numerical simulation. The simpler approach of using the time at which the ODE solver fails is sufficient for our purposes. For consistency, we use MATLAB `ode15s` with the same settings for all numerical simulations. We set the relative tolerance to $10^{-6}$, but otherwise use the default settings of the MATLAB `ode15s` function.

In this section, we present numerical simulations with the critical temperature fixed such that $\chi_c^* = 0.6$. The pressure profiles at $\tau_I$ for two different values of $M$ are plotted in Figure 4.2. Although we have not studied the details, we expect that the remainder of the end-gas will explode shortly after the ignition time, following a supersonic singularity path (or paths) starting at the ignition centre [28]. We anticipate that the singularity path for $EM = 1$ will move much faster than the singularity path for $EM = 10$, because the pressure gradient in Figure 4.2a is much shallower than in Figure 4.2b.

To understand and fully explore the range of behaviour exhibited by (4.53) for different values of $EM$ in the limit $E \to \infty$, we choose to use a larger value of the parameter $E$ here than the value we used in the numerical simulations presented in Section 3.4. We observe that the ignition centre is in a different location for the two different values of $EM$ presented in Figure 4.2. We will explore the sensitivity of $\chi_I$ and $\tau_I$ to changes in $EM$ and on changes to the initial conditions (4.22) shortly. First, though, it is necessary to discuss how we select $\tau_\star = -M^{-\alpha}$ to accurately match the solution of (4.53) with the solution (3.157) in the compression stage.

### 4.3.1 Choosing $\tau_\star$

Typically, Clarke's equations (2.121) are solved numerically from fixed initial conditions where the temperature is already close to the critical temperature, $T_c$. The situation with autoignition is therefore somewhat unusual, because the temperature of the end-gas starts at $T = 1$, far below the critical temperature. To solve (4.53) for the temperature during the induction stage, it is necessary to match with the solution (3.157) during the compression stage. We solve (4.53) by applying the matching conditions (4.57) at some

$$\tau_\star = -M^{-\alpha}, \tag{4.63}$$

where $\alpha \in (0, 0.5)$. The matching parameter, $\alpha$, does not appear in the full model (4.18)–(4.22), so the solution should not depend on $\alpha$.

The conditions (4.59) provide a theoretical range of acceptable $\tau_\star$ in the limit $M \to 0$, $E \to \infty$, such that the errors introduced to the solution (4.26) by matching are $o(M)$. As $EM$ decreases, the range of acceptable values for $\alpha$ reduces. To investigate how the

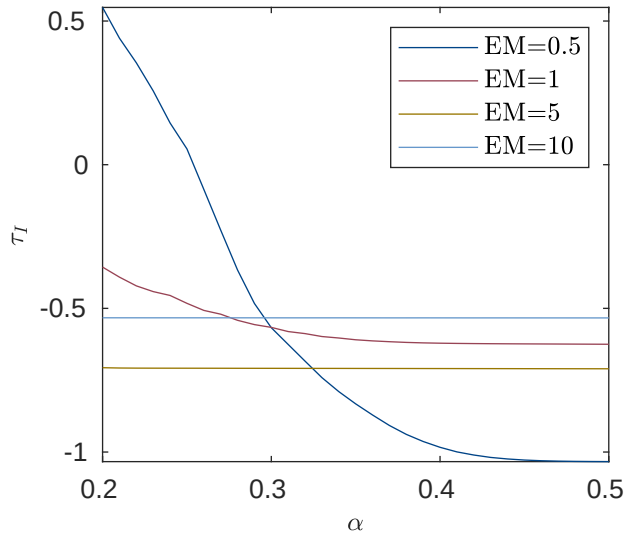


**Figure 4.3:** *The ignition time, $\tau_I$, plotted against the matching parameter, $\alpha$. For this figure, $E = 1000$, $T_{\times 2} = 1.6$, $\gamma = Q = 1.4$, $m = \mathrm{Le}_{\mathcal{F}} = \mathrm{Le}_{\mathcal{R}} = 1$ and $\chi_c^* = 0.6$.*

numerical solution to (4.53) depends on $\alpha$, we plot the ignition time, $\tau_I$, against $\alpha$, for a large, but fixed, value of $E$ in Figure 4.3. We observe that as $\alpha$ increases, the ignition time appears to approach a constant, albeit a different constant for each $EM$. We choose to use $\alpha = 0.45$ for our numerical simulations, because Figure 4.3 appears to show the behaviour of $\tau_I$ has become independent of $\alpha$ by this point for the range of values of $EM$ we consider.

### 4.3.2 Varying $M$

In Section 4.2, we recognised that the behaviour of (4.18)–(4.22) during the induction stage depends on the relative sizes of $E$ and $M$. We have derived a model (4.53) for the induction stage for the distinguished limit $M \to 0$ with $EM = O(1)$ and $E^2 M \gg 1$. In this section, we investigate how the behaviour of the solution to (4.53) depends on the size of the product $EM$, by varying $M$ with $E$ fixed. To ensure we are comparing the time at which the solution becomes unbounded consistently for different values of $M$, we use $t_I$ here, rather than $\tau_I$, to describe the ignition time.

We solve (4.61), subject to the initial conditions (4.57) at $\tau = -M^{-0.45}$, for 200 values of $EM$ drawn from the uniform random distribution on $(0.5, 15)$. The predicted ignition centre positions, $\chi_I$, and ignition times, $t_I$, are plotted against $EM$ in Figure 4.4. The data presented in Figure 4.4 looks discontinuous but does, in fact, have an underlying continuous structure, which we reveal in Figure 4.5 by considering a small range of $EM$ in detail.

It is clear to see from Figure 4.4a, that autoignition preferentially occurs at the wall for the parameter range under consideration; for 72% of the simulations presented in Figure 4.4, the highest pressure at $t = t_I$ is at $\chi_I = 0.9975$, which is the grid point closest to the wall where we solve for the pressure. We find that as $EM$ decreases,

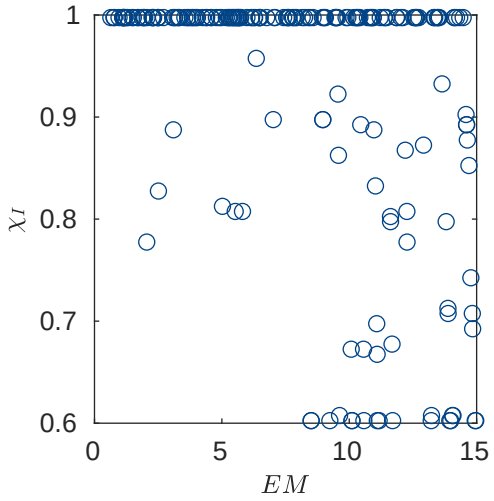


**(a)** *Position of ignition centre.*

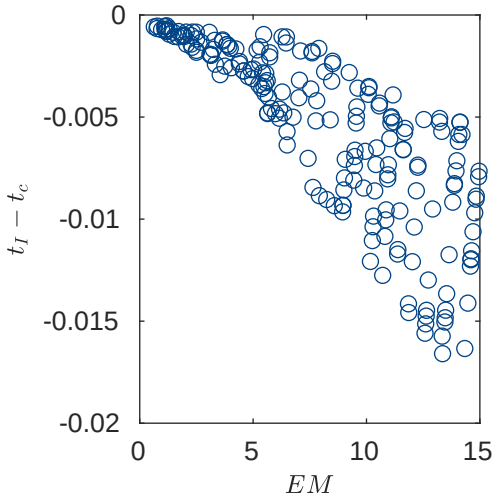


**(b)** *Ignition time.*

**Figure 4.4:** *Position, $\chi_I$, of ignition centre and ignition time, $t_I$, for 200 values of $EM$ drawn from the uniform random distribution on $(0.5, 15)$. For this figure, $E = 1000$, $T_{\times 2} = 1.6$, $\gamma = Q = 1.4$, $m = \mathrm{Le}_{\mathcal{F}} = \mathrm{Le}_{\mathcal{R}} = 1$, $\chi_c^* = 0.6$ and $\alpha = 0.45$.*

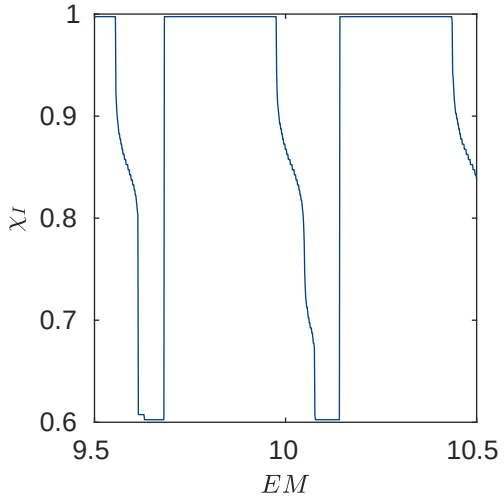


**(a)** *Position of ignition centre.*

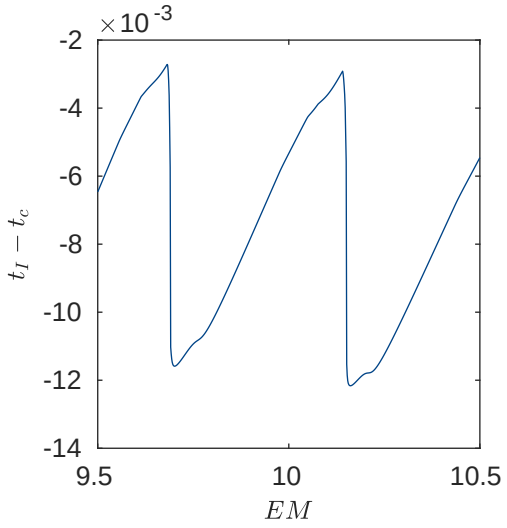


**(b)** *Ignition time.*

**Figure 4.5:** *Position, $\chi_I$, of ignition centre and ignition time, $t_I$, for 750 equally-spaced values of $EM$. For this figure, $E = 1000$, $T_{\times 2} = 1.6$, $\gamma = Q = 1.4$, $m = \mathrm{Le}_{\mathcal{F}} = \mathrm{Le}_{\mathcal{R}} = 1$, $\chi_c^* = 0.6$ and $\alpha = 0.45$.*

the proportion of simulations where the reaction centre is located adjacent to the wall increases. For instance, 80% of the simulations with $EM \in (5, 10)$ presented in Figure 4.4 result in autoignition at the wall, compared to 49% for $EM \in (10, 15)$.

To create Figure 4.5, we solve (4.61) for 750 equally-spaced values of $EM \in [9.5, 10.5]$. We observe that there are intervals of $EM$ where the ignition centre occurs at the wall, $\chi = 1$, and intervals of $EM$ where autoignition occurs at the flame, $\chi_c^* = 0.6$. At approximately $EM = 9.68$ and $EM = 10.14$, the ignition time, $t_I$, reaches a local maximum, and the ignition centre transitions sharply from being at the flame to being at the wall. By comparison, the ignition centre transitions from the wall to the flame over the intervals $EM \in (9.55, 9.61)$ and $EM \in (9.98, 10.08)$.

For the relatively large values of $EM$ considered in Figure 4.5, the chemistry in the end-gas is very sensitive to the acoustic changes in temperature. By varying $M$, we vary both the amplitude of the acoustic waves produced by the flame, and the relative speeds of the acoustic waves and the flame. Effectively, changing $M$ changes the shape of the initial conditions (4.57) we apply at $t = t_c + M\tau_\star$. It appears as if the position, $\chi_I$, of the ignition centre tracks the point of highest pressure, and hence temperature, of any of the wave fronts passing between the flame and the wall. The sudden transition from ignition at the flame to ignition at the wall can be thought of as the change in the position of maximum pressure following the reflection of a compressive acoustic wave at the wall.

By comparison, we do not see ignition anywhere other than at the wall in the numerical simulations presented in Figure 4.4 for $EM < 2$. From Figure 4.4b, we also note that the variability in ignition time, $t_I$, decreases as $EM$ decreases. By reducing $M$, we increase the speed of the acoustic waves relative to the flame, and decrease their amplitude. For lower values of $EM$, therefore, the rate of reaction in the end-gas is less sensitive to the acoustic perturbations to the temperature, which partially explains the reduced variation in $t_I$. Furthermore, the temperature adjacent to the wall rises higher than in the surrounding gas as compressive acoustic waves are reflected from the wall. We speculate that autoignition preferentially occurs at the wall for small values of $EM$, because the repeated reflection of acoustic waves, coupled with the heating due to the chemical reaction, causes a local increase in temperature at the wall that builds up during the induction stage.

### 4.3.3 Varying the initial conditions

For the numerical simulations presented in Figures 4.2–4.5, we solved (4.61) subject to the initial conditions (4.57) at $\tau = \tau_\star$. We derive (4.57) by matching with the solution (3.157) to (4.18)–(4.22) during the compression stage. By using the initial conditions (4.22), we assume the gas is quiescent at $t = 0$. In practical applications, such as within an internal combustion engine, the gas will not be stationary at the moment the flame is ignited. Hence, we briefly investigate the sensitivity of the solution to (4.61) to noise by introducing acoustic perturbations in the gas at $t = 0$.

To introduce perturbations to the gas at $t = 0$, of the same magnitude as the acoustic wave produced by the flame, we shift the phase of each mode in (3.160) at $t = 0$; that is, for $k = 1, 2, \ldots$, we replace $A_k(0)$ with $A_k(0)e^{i\eta_k}$ where $\eta_k \in (0, 2\pi)$ is the phase shift. In Section 3.3.6.2, we noted that the argument of the solution to (3.149) remains constant.

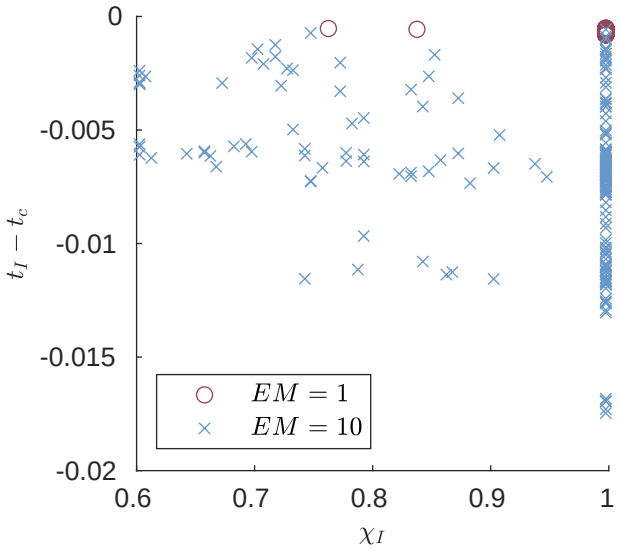


**Figure 4.6:** *Ignition time, $t_I$, plotted against ignition centre position, $\chi_I$, found by solving* (4.61) *subject to the initial conditions* (4.64)*. For this figure, $E = 1000$, $K = 9$, $T_{\times 2} = 1.6$, $\gamma = Q = 1.4$, $m = \mathrm{Le}_{\mathcal{F}} = \mathrm{Le}_{\mathcal{R}} = 1$, $\chi_c^* = 0.6$ and $\alpha = 0.45$.*

The introduced phase shift therefore persists up until $\tau = \tau_\star$, meaning the (truncated) matching conditions (4.57) become

$$\tilde{\hat{p}}_1(\chi, \tau_\star) = \sum_{n=1}^{K} \left( A_n(t_c) \exp\left( i \left( \eta_n + \frac{\phi_n(t_c)}{M} + \phi_n'(t_c)\tau_\star \right) \right) + \text{c.c.} \right) G_n(\chi, t_c), \quad \text{(4.64a)}$$

$$\tilde{\hat{u}}_0(\chi, \tau_\star) = \sum_{n=1}^{K} \left( \frac{iA_n(t_c)}{\gamma\omega_n(t_c)} \exp\left( i \left( \eta_n + \frac{\phi_n(t_c)}{M} + \phi_n'(t_c)\tau_\star \right) \right) + \text{c.c.} \right) \left. \frac{\partial G_n}{\partial \chi} \right|_{t=t_c}, \quad \text{(4.64b)}$$

for $\chi \in (0, 1)$, and

$$\tilde{\hat{V}}_1^R(\chi, \tau_\star) = -\frac{V_c}{\gamma p_c} \tilde{\hat{p}}_1(\chi, \tau_\star), \quad \text{(4.64c)}$$

for $\chi \in (\chi_c^*, 1)$. As before, $A_k$ satisfies (3.162) subject to the initial conditions (3.163) for $k = 1, 2, \ldots, K$. To create Figure 4.6, we solve (4.61) subject to the initial conditions (4.64) with $K = 9$, for 200 samples of $(\eta_1, \ldots, \eta_9)$ drawn from the uniform random distribution on $(0, 2\pi)^9$.

For $EM = 1$, there is very little variation in the ignition time, $t_I$; the difference between the minimum $t_I$ and the maximum $t_I$ is $3.0 \times 10^{-4}$. Furthermore, we find that the ignition centre is located at the wall for 99% of the simulations presented in Figure 4.6.

By comparison, the location, $\chi_I$, of the reaction centre is much more strongly dependent on the initial conditions for $EM = 10$, with autoignition occurring at the wall in only 67.5% of the simulations with $EM = 10$ presented in Figure 4.6. Additionally, the reaction centre was located at the grid point closest to the flame in 4% of the simulations we conducted with $EM = 10$. The variation in ignition time, $t_I$, for $EM = 10$ is also

much wider than for $EM = 1$; the difference between the maximum and minimum $t_I$ in Figure 4.6 is $1.7 \times 10^{-2}$ for $EM = 10$.

We conclude that the sensitivity of the ignition time, $t_I$, and location, $\chi_I$, on the initial conditions in the gas at $t = 0$ increases as $EM$ increases. As before, we postulate that the increase in sensitivity for larger values of $EM$ is due to the size of the acoustic waves and their ability to raise the temperature locally. For $EM = 1$, the effect of the acoustic waves on the rate of reaction in the end-gas is relatively weak. We see autoignition at the wall in almost all of the simulations presented in Figure 4.6 because the temperature perturbation builds up slowly close to the wall where the heating due to the acoustic waves is amplified. For $EM = 10$, the preferential heating at the wall is still important, as evidenced by the fact that autoignition occurs at the wall in the majority of simulations. However, the amplitude of the acoustic waves is sufficiently large that the local variations in temperature can, in some cases, initiate a positive feedback cycle that leads to the development of a hot spot within the interior of the end-gas.

### 4.3.4 Explosion stage

The induction stage is only the beginning of autoignition. As the temperature perturbation, $\hat{T}_1$ increases, the asymptotic approximations we made to derive (4.53) break down and the solution enters the explosion stage. We will not explore the explosion stage, but point out that the model (4.18) continues to be valid while the initiation reaction (2.6a) dominates over the branching reaction (2.6b)—that is, while $T_{\times 2} - T^R = \mathrm{ord}(1)$. The temperature at the ignition centre, $\chi_I$, will continue to rise to form a hot spot with the self-similar structure described by Jackson et al. [48]. When the temperature rises sufficiently, the branching reaction will become important, and the analysis in [48] will need modifying to account for the chain-branching explosion. After the explosion stage, there will be a depletion stage as the radical is consumed, but we have not considered the behaviour that will occur then.

# Chapter 5

# Conclusion

Knock in internal combustion engines is a result of an explosion, known as autoignition, in the unburnt gas ahead of the flame. Autoignition produces high pressures and temperatures in the gas within the cylinder, which can cause catastrophic damage to the engine. It is desirable therefore for knock to be controlled.

Knock and autoignition remain relevant areas of study, even as we as a society transition away from using fossil fuels to propel our vehicles. Many factors are known to affect whether knock occurs, including the geometry of the engine, the intake temperature of the air-fuel mixture and the fuel being used. To ensure compatibility with engines of vehicles on the road, a fuel's propensity to cause knock is determined through experimental procedures, and is quantified using octane numbers, before it is sold to the public. In order to lessen the environmental impact of our transportation needs, fuel manufacturers are starting to blend more sustainable fuel components, such as ethanol, into their products. Hydrogen is also being considered as an alternative fuel for use in internal combustion engines. Knock is not only a concern for traditional gasoline, but also for novel fuels including bio-fuels and hydrogen. Understanding how the physical and chemical properties of a fuel influences whether or not autoignition occurs would help the automotive industry expedite the development and adoption of more environmentally-friendly fuels.

Autoignition does not occur uniformly throughout the end-gas. Rather, autoignition is first apparent at localised points, known as hot spots, which appear in the end-gas after a period of seemingly normal combustion. It is not well understood how hot spots develop or why they are located away from the flame.

Autoignition is not unique to internal combustion engines. Experiments in rapid compression machines exhibit autoignition, as do one- and two-dimensional numerical simulations of combustion in an enclosed volume. The simplicity of these systems precludes many of the mechanisms proposed in the literature for how a hot spot develops in internal combustion engines. For example, a rapid compression machine operates for a single cycle, so spontaneous ignition due to hot combustion products left over from a previous cycle is not possible. Furthermore, one-dimensional simulations do not exhibit flame folding or turbulence, which are said to contribute to autoignition. We do not conclude that these mechanisms play no role in the development of hot spots in internal combustion engines. After all, an engine cylinder is a complex system with numerous chemical reactions taking place in a turbulent mixture of gases, confined within moving boundaries in

three-dimensions. It may be possible that more than one mechanism leads to autoignition in an internal combustion engine. However, the fact that autoignition is a feature of these simpler systems suggests that autoignition is a more fundamental aspect of combustion in confinement. We therefore recognise that the formation of a hot spot can be explained by considering the interplay between the gas dynamics and chemistry in the end-gas and concentrate on understanding that dynamic interplay.

In this thesis, we have used perturbation methods to analyse a one-dimensional model of gaseous combustion in confinement, to investigate the role acoustic waves play during normal combustion and autoignition. We have identified a parameter regime where autoignition does not occur, and, for a parameter regime where autoignition does occur, we have derived and solved a model to identify when and where hot spots develop.

We have studied two simple chemical reaction mechanisms that are representative of premixed combustion: a one-step Arrhenius reaction and a three-step chain-branching reaction. These reaction mechanisms are a significant simplification of the actual reaction mechanisms for hydrogen and hydrocarbon combustion. However, by using tractable chemical models with only a few reactive species, we are able to provide analytic insights into the interplay between gas dynamics and chemistry during autoignition. The one-step reaction is limited in accuracy, but is key to understanding the modelling literature on combustion. The three-step reaction we use is also well-studied in the literature, and is more representative of the initiation, branching and termination reactions that occur during the combustion of hydrogen and hydrocarbons than the one-step model.

In the limit of large Péclet number, $\mathrm{Pe}^{-1} = \epsilon \to 0$, we are justified in modelling the flame as an interface between two regions of inviscid gas. We use the well-known Chapman–Jouguet conditions to relate the density, pressure and velocity adjacent to both sides of the flame. However, in order to write down a well-defined free-boundary problem, an additional piece of information is required to supplement the Chapman–Jouguet conditions, namely the mass flux through the flame.

For both the one-step and three-step reactions, we follow established analysis in the literature to determine the leading-order mass flux through the flame by examining the quasi-steady structure of the flame. Additionally, we extend the analysis by Dold [29] to find the second order approximation to the mass flux for the three-step reaction, in the limit of large activation energy, $E \to \infty$, and small Mach number, $M \to 0$, with $EM = O(1)$.

In a cycle of an internal combustion engine where knock occurs, a period of normal combustion precedes autoignition. We call this period—where the rate of chemical reaction in the end-gas is negligible—the compression stage. Modelling the compression stage is important to understand the conditions in the gas prior to the development of a hot spot.

Acoustic waves are an intrinsic feature of combustion. Flames are subsonic combustion waves, so affect the gas either side of them through the production of acoustic waves. Although we do not study the details of ignition of the flame, acoustic waves are generated by the ignition of the flame and the expansion of the burning gas through the flame. In confinement, the acoustic waves generated by the flame reflect from the boundaries and subsequently interact with the flame again. Despite their small amplitude, acoustic waves provide the spatial variation necessary for a localised hot spot to develop in the end-gas.

We use an adaptation of the method of multiple scales to account for the interactions between the flame and acoustic waves during the compression stage, in the limit $M \to 0$. A similar method is used by Bauwens et al. [5] and Fachini and Bauwens [37] to study 1D premixed flames propagating through a tube with one end closed and the other end open. As in [5, 37], we find that the solution during the compression stage can be expressed as a series of modes, whose spatial structure, frequency and amplitude all slowly vary. However, with both ends of the tube closed, the leading-order temperature rises slowly on either side of the flame, and the leading-order temperature behind the flame is not spatially uniform. As a result, we are unable to express the spatial structure of the modes in terms of sine and cosine. Instead, we find the spatial structure and frequency of the modes numerically, using Chebfun [33].

We use Lagrangian spatial coordinates throughout our analysis. The benefit of using Lagrangian coordinates is that the path of the flame is monotonic in time because each fluid particle passes through the flame once. Using Lagrangian coordinates allows us to apply the Chapman–Jouguet conditions at the leading-order flame position without having to worry about characteristics following the flow incorrectly crossing the leading-order flame position more than once. The Chapman–Jouguet conditions dictate that the entropy immediately behind the flame changes rapidly as the acoustic waves interact with the flame. Because the entropy behind the flame is constant following the flow, we find that the entropy (and hence temperature and specific volume) behind the flame exhibits fine-scale spatial variations. A novelty of our analysis is that we employ ideas from the method of multiple scales in both time and space to ensure that the Chapman–Jouguet conditions can be applied consistently.

In physical experiments, significant acceleration of the flame is not observed prior to autoignition. For the one-step reaction, the mass flux through the flame is acutely sensitive to the temperature ahead of the flame, with an $O(E^{-1})$ increase in temperature leading to an $O(1)$ increase in mass flux. We find that there is an $\mathrm{ord}(1)$ rise in temperature ahead of the flame prior to the onset of autoignition. Therefore, we conclude that the one-step reaction is unsuitable for modelling autoignition, because the acceleration of the flame is unrealistic.

Furthermore, for the three-step reaction, the mass flux through the flame tends to infinity as $T^{R*} \to T_{\times 2}$. To ensure that the flame speed remains $\mathrm{ord}(1)$, we assume that the leading-order temperature, $T_0^R$, in the end-gas remains sufficiently below the branching reaction cross-over temperature, $T_{\times 2}$, so that $T_{\times 2} - T_0^R = \mathrm{ord}(1)$. For temperatures in this range, the rate of the branching reaction in the end-gas is negligibly small compared to the rates of the initiation and termination reactions as $E \to \infty$.

Generally, when ignition due to the three-step reaction is discussed in the literature [10, 30, 78], the initial temperature is assumed to be close to the cross-over temperature, $T_{\times 2}$. Often the assumption is that a shock has reflected from a wall causing the temperature to jump to above $T_{\times 2}$. In this case, the branching reaction plays a role during the early stages of ignition. The situation with autoignition is a little different. The acoustic waves in the unburnt gas are much weaker than shocks, and the temperature is far below the cross-over temperature, $T_{\times 2}$. Therefore, for autoignition to occur prior to any significant acceleration of the flame, we conclude that the initiation and termination reactions must be the driving force behind the formation of a hot spot.

We identify a critical temperature, $T_c$, given by (4.9). Provided that the temperature, $T^R$, satisfies $T_c - T^R \gg E^{-1}$, the rate of heat release in the end-gas is sufficiently small that it has a negligible effect on the gas dynamics and autoignition does not occur. However, if the temperature, $T^R$, in the end-gas rises to a point where $T_c - T^R = O(E^{-1})$, then reaction in the end-gas starts to have a significant effect.

We use the critical temperature, $T_c$, and the maximum possible leading-order temperature of the end-gas during normal combustion, $(1 + \gamma Q)^{1-1/\gamma}$, to find an algebraic expression (4.14) for a boundary of the region of parameter space where autoignition does not occur. By rewriting (4.14) in terms of the dimensional parameters in Table 2.1, we are able to predict whether autoignition occurs or not, based on the length of the combustion chamber, the physical and chemical properties of the fuel-air mixture, and the initial conditions within the combustion chamber. The same boundary in parameter space could be found numerically by solving (2.14), (2.22) and (2.23) for different parameter values. However, such a parameter sweep would require substantial computational effort.

Comparing the critical temperature with the maximum temperature gives an indication of *if* autoignition occurs. In order to describe *how* autoignition occurs, we formulate a model for the induction stage when $T_c - T^R = O(E^{-1})$. For simplicity, we only consider the distinguished limit where $EM = O(1)$ and $E^2 M \gg 1$ as $M \to 0$ in detail. In this distinguished limit, the chemical reaction and gas dynamics of the end-gas are fully coupled during the induction stage. The perturbation to the leading-order temperature is governed by Clarke's equations (2.121), and blows up at a point in finite time, indicating the onset of autoignition.

For our model of the induction stage, the initial conditions come from matching with the multiple scales solution during the compression stage. This is unconventional; Clarke's equations are well-studied in the literature, but are usually solved from fixed initial data where the initial temperature is close to the critical temperature. By comparison, the temperature in the end-gas during the compression stage is far below the critical temperature, and rises due to compression by the gas burning in the flame, rather than because of the reaction in the end-gas. To solve for the pressure in the gas during the induction stage numerically, we use matching with an intermediate variable, $\tau_\star$, to identify suitable initial conditions to impose at $\tau = \tau_\star$. We consider how the choice of the intermediate variable affects the accuracy of the solution.

By solving our model for the induction stage numerically, we show that autoignition can occur at the wall, at the flame and in the bulk of the end-gas for different values the typical flame Mach number, $M$, with all other parameters fixed. For large values of the product $EM$, we find that the time and position at which autoignition occurs are very sensitive to changes in $EM$. As $EM$ decreases, we observe that the variation in the time and position at which autoignition occurs decreases, with the hot spot preferentially occurring at the wall for small values of $EM$.

Using asymptotic analysis, we provide a framework that can be used to identify if, when and where autoignition occurs in cases where the chemistry of the fuel-air mixture is well described using the three-step reaction (2.6). Understanding the relationship between knock and fuel composition is key to the adoption of environmentally fuels for internal combustion engines. Our work provides quantitative insight into the relationship between the physical and chemical properties of a fuel-air mixture and whether knock occurs.

## 5.1 Future work

We have analysed a 1D model for combustion in confinement with a simple three-step chemical reaction mechanism, and presented a plausible description of the early stages of autoignition. We now outline possible avenues for future research.

It would be worthwhile studying the subsequent evolution of the gas in the later stages of autoignition to better understand how knock intensity depends on the dimensionless parameters. The induction stage ends as the temperature perturbation blows up at some ignition centre in finite time. The natural question to ask is 'What happens next?' From our analysis, we identify when and where autoignition first occurs. However, if we wanted to describe the large amplitude pressure waves characteristic of knock, then we would need to consider the behaviour of the gas after the singularity develops in the induction stage solution.

While $T_{\times 2} - T^R = \mathrm{ord}(1)$, the three-step chemical reaction mechanism (2.6) is well-approximated by the one-step Arrhenius reaction (2.1). We therefore expect that the hot spot will continue to develop from the ignition centre in a self-focusing thermal explosion, as described by Jackson et al. [48]. However, at some point when $T_{\times 2} - T^R = o(1)$, the rate of the branching reaction will exceed the rate of the initiation reaction, and we anticipate that the fuel will be rapidly converted to radical in a chain-branching explosion in the core of the hot spot. The analysis in [48] would need to be modified to reveal the structure of the hot spot during the chain-branching explosion and the subsequent depletion of radicals.

The autoignition of the gas does not end with the formation of the hot spot. We anticipate that the remainder of the end-gas will explode sequentially in an autoignition front, starting from the hot spot. Based on solutions to Clarke's equations (2.121) in the literature [31, 80], we expect that, at first, the autoignition front will take the form of a quasi-steady weak detonation, following a supersonic singularity path that we can determine numerically from the induction stage model. As with the one-step reaction [52], we expect that if the singularity path drops below the Chapman–Jouguet speed, then a shock will form, causing the weak detonation to transition to a Chapman–Jouguet detonation with the ZND structure. This description of the later stages of autoignition appears to agree with the numerical simulations of autoignition of a hydrogen-air mixture by Yu and Chen [95], depicted in Figure 1.7a.

A further study, incorporating both numerical and asymptotic methods, is needed to fill in the details. However, a desirable outcome of such a study would be a description of the pressure waves following autoignition, and how their amplitude, in particular, depends on the dimensionless parameters listed in Table 2.2. The behaviour of the gas following autoignition is of interest to the fuel industry because the amplitude of the pressure waves corresponds to knock intensity.

Octane numbers remain the primary measure used by fuel and engine manufacturers to quantify a fuel's propensity to cause knock. Another potential avenue of investigation is using our model to provide insights into the relationship between fuel composition and octane number. While the geometry and chemistry of our model is a significant simplification of the reality inside a cylinder of an internal combustion engine, our model could be used to investigate the propensity of different fuel blends to cause knock, provided

that the chemistry of the fuel-air mixture is well approximated by the three-step reaction (2.6), and suitable values of the dimensionless parameters can be identified. Careful consideration would be needed to test whether the three-step chemical reaction (2.6) can accurately capture the competing chemical mechanisms acting during the combustion of a fuel blend with multiple components.

One particular challenge to overcome would be how to determine $\bar{T}_{\text{init}}$ to represent the conditions within the test engine used to determine MON and RON [1, 2]. For RON especially, it would be necessary to consider the enthalpy of vaporisation of the fuel, because, in the RON test procedure, the fuel-air mixture is not heated again after the fuel is introduced to the air in the carburettor [2].

Another useful direction for further research is to investigate how autoignition is affected by the physical aspects of internal combustion engines that we have not captured in our simple 1D model. For example, the gas in an internal combustion engine is slowly compressed by the piston. In addition, the walls of an internal combustion engine are generally not flat as we have assumed, and are not perfectly thermally insulating. Natural questions to ask are 'How does the additional compression by the piston affect whether autoignition occurs or not?', 'Does focusing of acoustic waves in 3D lead to the development of hot spots in particular locations within an engine?' and 'Does the thermal conductivity of the walls affect the development of hot spots at the walls?'

One might also consider how to model autoignition in different types of internal combustion engines. We have chosen to focus on spark-ignited internal combustion engines where the fuel-air mixture is well mixed, because in the MON and RON tests the fuel and air are mixed in the carburettor prior to entering the cylinder of a spark-ignited engine. Further work would be needed to adapt our methodology to combustion of imperfectly-mixed reactants, which are a feature of direct injection internal combustion engines. It would also be interesting to explore how our approach to modelling combustion and autoignition could be applied to diesel engines, where the fuel-air mixture is ignited by a glow plug, rather than a spark plug.

It is clear that there is still a great deal more to understand about autoignition. However, we have been able to shed light on the role acoustic waves play in normal combustion in confinement, and in the development of a hot spot during the early stages of autoignition.

# Appendix A

# Three-step flame structure

In Section 2.2.2.2, we derive the leading-order flame structure for the three-step chain branching reaction (2.6). Here, we extend the analysis by Dold [29] in order to find the next term, $q^{(1)}$, in the asymptotic expansion for the mass flux through the flame.

## A.1 Regions II and IV

To find $q^{(1)}$, it is necessary to solve for $T_1$, $Y_{\mathcal{F}1}$ and $Y_{\mathcal{R}1}$ in regions II and IV. Substituting (2.73) and (2.74) into (2.71) and comparing coefficients of $E^{-1}$, we deduce that

$$-q^{(0)}\frac{\partial T_1}{\partial \xi} - \frac{\partial^2 T_1}{\partial \xi^2} = QY_{\mathcal{R}1} + q^{(1)}\frac{\partial T_0}{\partial \xi}, \tag{A.1a}$$

$$-q^{(0)}\frac{\partial Y_{\mathcal{F}1}}{\partial \xi} - \frac{1}{\mathrm{Le}_{\mathcal{F}}}\frac{\partial^2 Y_{\mathcal{F}1}}{\partial \xi^2} = q^{(1)}\frac{\partial Y_{\mathcal{F}0}}{\partial \xi}, \tag{A.1b}$$

$$-q^{(0)}\frac{\partial Y_{\mathcal{R}1}}{\partial \xi} - \frac{1}{\mathrm{Le}_{\mathcal{R}}}\frac{\partial^2 Y_{\mathcal{R}1}}{\partial \xi^2} + Y_{\mathcal{R}1} = q^{(1)}\frac{\partial Y_{\mathcal{R}0}}{\partial \xi}. \tag{A.1c}$$

Using (2.77) to evaluate $T_0$, $Y_{\mathcal{F}0}$ and $Y_{\mathcal{R}0}$, we find that the general solution to (A.1) is

$$\begin{aligned} T_1 = {} & C_7 + (C_8 - C_2 q^{(1)}\xi)\exp\bigl(-q^{(0)}\xi\bigr) + \frac{QC_5 m_+ q^{(1)}\mathrm{Le}_{\mathcal{R}}}{(\mathrm{Le}_{\mathcal{R}}q^{(0)} + 2m_+)(m_+^2 + q^{(0)}m_+)}\xi\exp(m_+\xi) \\ & + \frac{QC_6 m_- q^{(1)}\mathrm{Le}_{\mathcal{R}}}{(\mathrm{Le}_{\mathcal{R}}q^{(0)} + 2m_-)(m_-^2 + q^{(0)}m_-)}\xi\exp(m_-\xi) \\ & + \exp(m_+\xi)\left(\frac{2(1-\mathrm{Le}_{\mathcal{R}})QC_5 m_+^2 q^{(1)} - QC_{11}(\mathrm{Le}_{\mathcal{R}}q^{(0)} + 2m_+)(m_+^2 + q^{(0)}m_+)}{(\mathrm{Le}_{\mathcal{R}}q^{(0)} + 2m_+)(m_+^2 + q^{(0)}m_+)^2}\right) \\ & + \exp(m_-\xi)\left(\frac{2(1-\mathrm{Le}_{\mathcal{R}})QC_6 m_-^2 q^{(1)} - QC_{12}(\mathrm{Le}_{\mathcal{R}}q^{(0)} + 2m_-)(m_-^2 + q^{(0)}m_-)}{(\mathrm{Le}_{\mathcal{R}}q^{(0)} + 2m_-)(m_-^2 + q^{(0)}m_-)^2}\right), \end{aligned} \tag{A.2a}$$

$$Y_{\mathcal{F}1} = C_9 + C_{10}\exp\bigl(-\mathrm{Le}_{\mathcal{F}}q^{(0)}\xi\bigr) - C_4 q^{(1)}\mathrm{Le}_{\mathcal{F}}\xi\exp\bigl(-\mathrm{Le}_{\mathcal{F}}q^{(0)}\xi\bigr), \tag{A.2b}$$

$$Y_{\mathcal{R}1} = \left(C_{11} - \frac{C_5 \mathrm{Le}_{\mathcal{R}} m_+ q^{(1)} \xi}{\mathrm{Le}_{\mathcal{R}} q^{(0)} + 2m_+}\right) \exp(m_+ \xi) + \left(C_{12} - \frac{C_6 \mathrm{Le}_{\mathcal{R}} m_- q^{(1)} \xi}{\mathrm{Le}_{\mathcal{R}} q^{(0)} + 2m_-}\right) \exp(m_- \xi), \tag{A.2c}$$

where $\{C_k \mid k \in \{7, \ldots, 12\}\}$ are functions of time to be determined by matching.

To match the solution in region II with the solution in region I, we require

$$\lim_{\xi \to \infty} T_1(\xi, t) = 0, \quad \lim_{\xi \to \infty} Y_{\mathcal{F}1}(\xi, t) = 0, \quad \lim_{\xi \to \infty} Y_{\mathcal{R}1}(\xi, t) = 0. \tag{A.3a}$$

Furthermore, we require that the solution within the flame remains finite. In particular,

$$|T_1(\xi, t)| < \infty, \quad |Y_{\mathcal{F}1}(\xi, t)| < \infty, \quad |Y_{\mathcal{R}}(\xi, t)| < \infty, \tag{A.3b}$$

as $\xi \to -\infty$.

## A.2 Region III — Branching zone

The next step in solving for $q^{(1)}$ is identifying boundary conditions to apply at $\xi = \xi_0$. We do this by solving the next order problem in the branching zone.

### A.2.1 Solution to (2.82) in terms of modified Bessel's functions

A key insight from [29] is that the leading-order solution within the branching zone can be expressed in terms of modified Bessel's functions. We demonstrate this by following the argument Dold [29] uses.

Using (2.83a), we eliminate $\hat{\xi}$ from (2.82b) in favour of $\hat{T}_1$, so that

$$\frac{\hat{C}_2^2}{\mathrm{Le}_{\mathcal{F}}} \frac{\partial^2 \hat{Y}_{\mathcal{F}1}}{\partial \hat{T}_1^2} = \hat{Y}_{\mathcal{F}1} \hat{Y}_{\mathcal{R}0} \exp\left(\frac{\hat{T}_1}{T_{\times 2}^2}\right). \tag{A.4}$$

Then, by changing variables, $\zeta = 2e^{\hat{T}_1/(2T_{\times 2}^2)} \hat{Y}_{\mathcal{R}0}^{1/2} \mathrm{Le}_{\mathcal{F}}^{1/2} T_{\times 2}^2 / |\hat{C}_2|$, we find

$$\zeta \frac{\partial^2 \hat{Y}_{\mathcal{F}1}}{\partial \zeta^2} + \frac{\partial \hat{Y}_{\mathcal{F}1}}{\partial \zeta} - \zeta \hat{Y}_{\mathcal{F}1} = 0, \tag{A.5}$$

which is modified Bessel's equation. The solutions to modified Bessel's equation are discussed in [73]. Since $\hat{Y}_{\mathcal{F}1}$ cannot tend to infinity as $\zeta \to \infty$, which corresponds to $\hat{T}_1 \to \infty$, the only possible solution is

$$\hat{Y}_{\mathcal{F}1} = A K_0(\zeta), \tag{A.6}$$

where $A$ is a function of $t$ to be determined via matching.

The asymptotic behaviour of $K_0$ is

$$K_0(\zeta) \sim \begin{cases} -\log(\zeta/2) - \gamma_c + O(\zeta^2 \log(\zeta)), & \text{as } \zeta \to 0, \\ O(\zeta^{-1/2} \exp(-\zeta)), & \text{as } \zeta \to \infty, \end{cases} \tag{A.7}$$

where $\gamma_c \approx 0.5772\ldots$ is Euler's constant[1] [73]. Rewriting (A.6) in terms of $\hat{\xi}$, we infer that

$$\hat{Y}_{\mathcal{F}1} = AK_0 \sim A \begin{cases} \frac{\hat{C}_1+\hat{C}_2\hat{\xi}}{2T_{\times 2}^2} + \frac{1}{2}\log\left(\frac{\hat{C}_2^2}{\hat{Y}_{\mathcal{R}0}\mathrm{Le}_{\mathcal{F}}T_{\times 2}^4}\right) - \gamma_c, & \text{as } \hat{C}_2\hat{\xi} \to -\infty, \\ o\left(\exp\left(-\hat{C}_2\hat{\xi}\right)\right), & \text{as } \hat{C}_2\hat{\xi} \to \infty, \end{cases} \tag{A.8}$$

where we recall from (2.91) that $\hat{C}_2 < 0$. Using (A.8) to match (2.81b) with the leading-order outer solution (2.85b) in region II, we find $\lim_{\xi \searrow \xi_0} \partial Y_{\mathcal{F}0}/\partial\xi = \lim_{\hat{\xi}\to\infty} \partial\hat{Y}_{\mathcal{F}1}\Big/\partial\hat{\xi}$, meaning

$$A = \frac{2q^{(0)}\mathrm{Le}_{\mathcal{F}}Y_{\mathcal{F}}^{R*}T_{\times 2}^2}{\hat{C}_2}. \tag{A.9}$$

### A.2.2 Matching

To proceed, we extend the analysis by Dold [29] to identify the seven boundary conditions at $\xi = \xi_0$ needed in addition to (A.3) to solve (A.1) for $q^{(1)}$, and $T_1$, $Y_{\mathcal{F}1}$ and $Y_{\mathcal{R}1}$ in regions II and IV. Throughout this section, we will frequently need to refer to the constant part of the limiting form of $\hat{Y}_{\mathcal{F}1}$ as $\hat{\xi} \to \infty$. For convenience, we define

$$B := A\left(\frac{\hat{C}_1}{2T_{\times 2}^2} + \frac{1}{2}\log\left(\frac{\hat{C}_2^2}{\hat{Y}_{\mathcal{R}0}\mathrm{Le}_{\mathcal{F}}T_{\times 2}^4}\right) - \gamma_c\right). \tag{A.10}$$

Substituting (2.73), (2.80) and (2.81) into (2.71), we find that $\hat{T}_2$, $\hat{Y}_{\mathcal{F}2}$ and $\hat{Y}_{\mathcal{R}2}$ satisfy[2]

$$\frac{\partial^2\hat{T}_2}{\partial\hat{\xi}^2} = -q^{(0)}\frac{\partial\hat{T}_1}{\partial\hat{\xi}} - Q\hat{Y}_{\mathcal{R}0}, \tag{A.11a}$$

$$\frac{1}{\mathrm{Le}_{\mathcal{F}}}\frac{\partial^2\hat{Y}_{F2}}{\partial\hat{\xi}^2} + \frac{1}{\mathrm{Le}_{\mathcal{R}}}\frac{\partial^2\hat{Y}_{R2}}{\partial\hat{\xi}^2} = -q^{(0)}\frac{\partial\hat{Y}_{\mathcal{F}1}}{\partial\hat{\xi}} - q^{(0)}\frac{\partial\hat{Y}_{\mathcal{R}1}}{\partial\hat{\xi}} + \hat{Y}_{\mathcal{R}0}. \tag{A.11b}$$

Integrating (A.11a), we find that $\hat{T}_2$ satisfies

$$\hat{T}_2 = -\frac{\hat{C}_2q^{(0)} + Q\hat{Y}_{\mathcal{R}0}}{2}\hat{\xi}^2 + \hat{C}_5\xi + \hat{C}_6, \tag{A.12}$$

where $\hat{C}_5$ and $\hat{C}_6$ are functions of $t$ to be determined. Using Van Dyke's rule to match the first two terms of (2.74d) in regions II and IV with the first three terms of (2.81a), we deduce from (2.83a) that

$$\hat{C}_1 = \lim_{\xi\searrow\xi_0} T_1 = \lim_{\xi\nearrow\xi_0} T_1, \tag{A.13}$$

[1] Euler's constant is usually denoted by $\gamma$. We use $\gamma_c$ here to differentiate Euler's constant from the ratio of specific heats.

[2] Note, in writing (A.11a), we use that the $\hat{\xi}$-derivative of the leading-order velocity within the branching zone is $O(E^{-1})$ in the distinguished limit $EM = O(1)$.

and from (A.12) that

$$\hat{C}_5 = \lim_{\xi \searrow \xi_0} \frac{\partial T_1}{\partial \xi} = \lim_{\xi \nearrow \xi_0} \frac{\partial T_1}{\partial \xi}. \tag{A.14}$$

In other words, at $\xi = \xi_0$,

$$[T_1]^+_- = \left[\frac{\partial T_1}{\partial \xi}\right]^+_- = 0. \tag{A.15}$$

To match the mass fractions of fuel and radical in regions II and IV with the branching zone, we require the limiting behaviour of $\hat{Y}_{\mathcal{F}1}$ and $\hat{Y}_{\mathcal{F}1}$ as $\hat{\xi} \to \pm\infty$. From (2.83b), (A.8) and (A.10), we deduce that

$$\hat{Y}_{\mathcal{R}1} \sim \begin{cases} \hat{C}_4 \mathrm{Le}_{\mathcal{R}} \hat{\xi}, & \text{as } \hat{\xi} \to -\infty, \\ \left(\hat{C}_4 \mathrm{Le}_{\mathcal{R}} - \frac{A\hat{C}_2 \mathrm{Le}_{\mathcal{R}}}{2\mathrm{Le}_{\mathcal{F}} T_{\times 2}^2}\right) \hat{\xi} - \frac{\mathrm{Le}_{\mathcal{R}}}{\mathrm{Le}_{\mathcal{F}}} B, & \text{as } \hat{\xi} \to \infty. \end{cases} \tag{A.16}$$

Using (A.8) and (A.16), we find that the solution (A.2) in region II must satisfy

$$Y_{\mathcal{F}1} \to B, \quad Y_{\mathcal{R}1} \to -\frac{\mathrm{Le}_{\mathcal{R}}}{\mathrm{Le}_{\mathcal{F}}} B, \tag{A.17a}$$

as $\xi \searrow \xi_0$ to match with the inner solution in the branching zone. Similarly, for the solutions in regions III and IV to match, we require

$$Y_{\mathcal{F}1} \to 0, \quad Y_{\mathcal{R}1} \to 0, \tag{A.17b}$$

as $\xi \nearrow \xi_0$.

With (A.3), (A.15) and (A.17) we have 12 boundary conditions we can use to solve (A.1) in regions II and IV for $T_1$, $Y_{\mathcal{F}1}$ and $Y_{\mathcal{R}1}$. However, $q^{(1)}$ is also unknown, so we require one more condition across $\xi = \xi_0$ to find $q^{(1)}$. Integrating (A.11b) we find

$$\frac{1}{\mathrm{Le}_{\mathcal{F}}} \frac{\partial \hat{Y}_{F2}}{\partial \hat{\xi}} + \frac{1}{\mathrm{Le}_{\mathcal{R}}} \frac{\partial \hat{Y}_{R2}}{\partial \hat{\xi}} = -q^{(0)} \hat{Y}_{\mathcal{F}1} - q^{(0)} \hat{Y}_{\mathcal{R}1} + \hat{Y}_{\mathcal{R}0} \hat{\xi} + \hat{C}_7, \tag{A.18}$$

where $\hat{C}_7$ is a function of $t$ to be determined. To conduct the matching with regions II and IV, we only require the asymptotic behaviour of the solution of (A.18) as $\xi \to \pm\infty$. As such, we use (A.8) and (A.16) to give the asymptotic behaviour of $Y_{\mathcal{F}1}$ and $Y_{\mathcal{R}1}$ in (A.18), and integrate once more to deduce

$$\frac{\hat{Y}_{F2}}{\mathrm{Le}_{\mathcal{F}}} + \frac{\hat{Y}_{R2}}{\mathrm{Le}_{\mathcal{R}}} \sim \left(\frac{A\hat{C}_2(\mathrm{Le}_{\mathcal{R}} - \mathrm{Le}_{\mathcal{F}}) q^{(0)}}{2T_{\times 2}^2 \mathrm{Le}_{\mathcal{F}}} + \hat{Y}_{\mathcal{R}0} - \hat{C}_4 \mathrm{Le}_{\mathcal{R}} q^{(0)}\right) \frac{\hat{\xi}^2}{2} + \left(\frac{q^{(0)} B(\mathrm{Le}_{\mathcal{R}} - \mathrm{Le}_{\mathcal{F}})}{\mathrm{Le}_{\mathcal{F}}} + \hat{C}_7\right) \hat{\xi} \quad \text{as } \hat{\xi} \to \infty, \tag{A.19a}$$

$$\frac{\hat{Y}_{F2}}{\mathrm{Le}_{\mathcal{F}}} + \frac{\hat{Y}_{R2}}{\mathrm{Le}_{\mathcal{R}}} \sim \frac{\left(\hat{Y}_{\mathcal{R}0} - \hat{C}_4 \mathrm{Le}_{\mathcal{R}} q^{(0)}\right) \hat{\xi}^2}{2} + \hat{C}_7 \hat{\xi}, \quad \text{as } \hat{\xi} \to -\infty. \tag{A.19b}$$

By using Van Dyke's matching rule on $Y_{\mathcal{F}}/\mathrm{Le}_{\mathcal{F}}+Y_{\mathcal{R}}/\mathrm{Le}_{\mathcal{R}}$, we deduce from the coefficients of $\hat{\xi}$ in (A.19) that, across $\xi=\xi_0$,

$$\left[\frac{1}{\mathrm{Le}_{\mathcal{F}}}\frac{\partial Y_{\mathcal{F}1}}{\partial\xi}+\frac{1}{\mathrm{Le}_{\mathcal{R}}}\frac{\partial Y_{\mathcal{R}1}}{\partial\xi}\right]_{-}^{+}=\frac{q^{(0)}B(\mathrm{Le}_{\mathcal{R}}-\mathrm{Le}_{\mathcal{F}})}{\mathrm{Le}_{\mathcal{F}}}. \tag{A.20}$$

Having now found thirteen boundary conditions—(A.3), (A.15), (A.17) and (A.20)—we are in a position to solve (A.1) for $T_1$, $Y_{\mathcal{F}1}$ and $Y_{\mathcal{R}1}$ in regions II and IV, and $q^{(1)}$. In region II the solution to (A.1) is

$$\begin{aligned}T_1=&\frac{2Q\mathrm{Le}_{\mathcal{R}}(1-\mathrm{Le}_{\mathcal{R}})q^{(0)}q^{(1)}m_+^2Y_{\mathcal{F}}^{R*}}{(m_+-m_-)(\mathrm{Le}_{\mathcal{R}}q^{(0)}+2m_+)(m_+^2+q^{(0)}m_+)^2}\exp\bigl(-q^{(0)}(\xi-\xi_0)\bigr)\\&-\left(q^{(1)}(T_{\times 2}-T^{R*})+\frac{Q\mathrm{Le}_{\mathcal{R}}q^{(0)}q^{(1)}Y_{\mathcal{F}}^{R*}}{(m_+-m_-)(m_-^2+m_-q^{(0)})}\right)(\xi-\xi_0)\exp\bigl(-q^{(0)}(\xi-\xi_0)\bigr)\\&+\frac{Q\mathrm{Le}_{\mathcal{R}}^2m_-q^{(0)}q^{(1)}Y_{\mathcal{F}}^{R*}}{(m_+-m_-)(\mathrm{Le}_{\mathcal{R}}q^{(0)}+2m_-)(m_-^2+q^{(0)}m_-)}(\xi-\xi_0)\exp(m_-(\xi-\xi_0))\\&+\left(\frac{2Q\mathrm{Le}_{\mathcal{R}}(1-\mathrm{Le}_{\mathcal{R}})q^{(0)}q^{(1)}m_-^2Y_{\mathcal{F}}^{R*}}{(m_+-m_-)(\mathrm{Le}_{\mathcal{R}}q^{(0)}+2m_-)(m_-^2+q^{(0)}m_-)^2}\right.\\&\left.\quad+\frac{Q\mathrm{Le}_{\mathcal{R}}B}{\mathrm{Le}_{\mathcal{F}}(m_-^2+q^{(0)}m_-)}\right)\bigl(\exp(m_-(\xi-\xi_0))-\exp\bigl(-q^{(0)}(\xi-\xi_0)\bigr)\bigr).\end{aligned} \tag{A.21a}$$

$$Y_{\mathcal{F}1}=B\exp\bigl(-\mathrm{Le}_{\mathcal{F}}q^{(0)}(\xi-\xi_0)\bigr)+Y_{\mathcal{F}}^{R*}q^{(1)}\mathrm{Le}_{\mathcal{F}}(\xi-\xi_0)\exp\bigl(-\mathrm{Le}_{\mathcal{F}}q^{(0)}(\xi-\xi_0)\bigr), \tag{A.21b}$$

$$\begin{aligned}Y_{\mathcal{R}1}=&-\frac{\mathrm{Le}_{\mathcal{R}}}{\mathrm{Le}_{\mathcal{F}}}B\exp(m_-(\xi-\xi_0))\\&-\frac{\mathrm{Le}_{\mathcal{R}}^2m_-q^{(0)}q^{(1)}Y_{\mathcal{F}}^{R*}}{(m_+-m_-)(\mathrm{Le}_{\mathcal{R}}q^{(0)}+2m_-)}(\xi-\xi_0)\exp(m_-(\xi-\xi_0)).\end{aligned} \tag{A.21c}$$

Behind the branching zone, in region IV, we find that

$$\begin{aligned}T_1=&\frac{Q\mathrm{Le}_{\mathcal{R}}^2m_+q^{(0)}q^{(1)}Y_{\mathcal{F}}^{R*}}{(m_+-m_-)(\mathrm{Le}_{\mathcal{R}}q^{(0)}+2m_+)(m_+^2+q^{(0)}m_+)}(\xi-\xi_0)\exp(m_+(\xi-\xi_0))\\&+\left(\frac{2Q\mathrm{Le}_{\mathcal{R}}(1-\mathrm{Le}_{\mathcal{R}})q^{(0)}q^{(1)}m_+^2Y_{\mathcal{F}}^{R*}}{(m_+-m_-)(\mathrm{Le}_{\mathcal{R}}q^{(0)}+2m_+)(m_+^2+q^{(0)}m_+)^2}\right)\exp(m_+(\xi-\xi_0)).\end{aligned} \tag{A.22a}$$

$$Y_{\mathcal{F}1}=0, \tag{A.22b}$$

$$Y_{\mathcal{R}1}=-\frac{\mathrm{Le}_{\mathcal{R}}^2m_+q^{(0)}q^{(1)}Y_{\mathcal{F}}^{R*}}{(m_+-m_-)(\mathrm{Le}_{\mathcal{R}}q^{(0)}+2m_+)}(\xi-\xi_0)\exp(m_+(\xi-\xi_0)). \tag{A.22c}$$

The solutions (A.21) and (A.22) are written in terms of $q^{(1)}$ and $B$. We now use (A.20) to identify an expression for $q^{(1)}$ in terms of the dimensionless parameters listed in

Table 2.2, the temperature, $T^{R*}$, and mass fraction, $Y_{\mathcal{F}}^{R*}$, of fuel ahead of the flame. Substituting (A.21) and (A.22) into (A.20), and making use of (2.78), we find

$$B = -\frac{\mathrm{Le}_{\mathcal{F}} q^{(1)} Y_{\mathcal{F}}^{R*}}{m_+}\left(1 - \frac{(\mathrm{Le}_{\mathcal{R}} q^{(0)})^2}{(m_+ - m_-)^2}\right). \tag{A.23}$$

With (A.10) and (A.23), we have found two equations for $B$ in terms of $q^{(1)}$, $A$, $\hat{C}_1$, $\hat{C}_2$ and $\hat{Y}_{\mathcal{R}0}$. From (A.13) and (A.21a), we recognise that

$$\hat{C}_1 = \frac{2Q\mathrm{Le}_{\mathcal{R}}(1-\mathrm{Le}_{\mathcal{R}}) q^{(0)} q^{(1)} m_+^2 Y_{\mathcal{F}}^{R*}}{(m_+ - m_-)(\mathrm{Le}_{\mathcal{R}} q^{(0)} + 2m_+)(m_+^2 + q^{(0)} m_+)^2}. \tag{A.24}$$

Now, eliminating $A$, $B$, $\hat{C}_1$, $\hat{C}_2$ and $\hat{Y}_{\mathcal{R}0}$ from (2.87), (2.91), (A.9), (A.10), (A.23) and (A.24), we find, after some algebraic manipulation, that $q^{(1)}$ satisfies

$$\begin{aligned}\frac{1}{q^{(1)}}\left(\gamma_c - \frac{1}{2}\log\left(\frac{m_+^2(m_+ - m_-)(T_{\times 2} - T^{R*} - QY_{\mathcal{F}}^{R*})^2}{\mathrm{Le}_{\mathcal{R}}\mathrm{Le}_{\mathcal{F}} q^{(0)} Y_{\mathcal{F}}^{R*} T_{\times 2}^4}\right)\right) &= \frac{Q\mathrm{Le}_{\mathcal{R}}(1-\mathrm{Le}_{\mathcal{R}}) q^{(0)} m_+^2 Y_{\mathcal{F}}^{R*}}{(m_+ - m_-)(\mathrm{Le}_{\mathcal{R}} q^{(0)} + 2m_+)(m_+^2 + q^{(0)} m_+)^2 T_{\times 2}^2} \\ &\quad + \frac{T_{\times 2} - T^{R*} - QY_{\mathcal{F}}^{R*}}{2q^{(0)} T_{\times 2}^2}\left(1 - \frac{(\mathrm{Le}_{\mathcal{R}} q^{(0)})^2}{(m_+ - m_-)^2}\right),\end{aligned} \tag{A.25}$$

where $q^{(0)}$ is the solution to (2.88), and $m_\pm$ are given by (2.78). The form of (A.25) has been chosen for ease of presentation across multiple lines; we can easily rearrange (A.25) for an explicit expression for $q^{(1)}$.

# References


[1] ASTM. *D2700-13b Standard Test Method for Motor Octane Number of Spark-Ignition Engine Fuel*. 2013.

[2] ASTM. *D2699-19 Standard Test Method for Research Octane Number of Spark-Ignition Engine Fuel*. 2019.

[3] G. A. Batley, A. C. McIntosh and J. Brindley. 'The time evolution of interactions between ultra short length pressure disturbances and premixed flames'. In: *Combustion Science and Technology* 92 (1993), pp. 367–388. DOI: 10.1080/00102209308907679.

[4] L. Bauwens. *Email conversation with J. P. Harris*. June 2022.

[5] L. Bauwens, C. R. L. Bauwens and I. Wierzba. 'Oscillating flames: multiple-scale analysis'. In: *Proceedings of the Royal Society A* 465 (2009), pp. 2089–2110. DOI: 10.1098/rspa.2008.0388.

[6] C. M. Bender and S. A. Orszag. *Advanced Mathematical Methods for Scientists and Engineers I. Asymptotic Methods and Pertubation Theory*. Springer, 1999.

[7] R. B. Bird, W. E. Stewart and E. N. Lightfoot. *Transport Phenomena*. Revised 2nd ed. John Wiley & Sons, Inc., 2007.

[8] P. A. Blythe and D. G. Crighton. 'Shock-generated ignition'. In: *Proceedings of the Royal Society A* 426 (1989), pp. 189–209. DOI: 10.1098/rspa.1989.0123.

[9] P. A. Blythe, A. K. Kapila and M. Short. 'Homogeneous ignition for a three-step chain-branching reaction model'. In: *Journal of Engineering Mathematics* 56 (2006), pp. 105–128. DOI: 10.1007/s10665-006-9055-0.

[10] P. A. Blythe, A. K. Kapila and M. Short. 'Shock-induced chain-branched ignition'. In: *Proceedings of the Combustion Institute*. Vol. 32. 2009, pp. 2371–2377. DOI: 10.1016/j.proci.2008.05.071.

[11] D. Bradley. 'Autoignitions and detonations in engines and ducts'. In: *Philosophical Transactions of the Royal Society A* 370 (2012), pp. 689–714. DOI: 10.1098/rsta.2011.0367.

[12] I. Brailovsky and G. I. Sivashinsky. 'On deflagration-to-detonation transition'. In: *Combustion Science and Technology* 130 (1997), pp. 201–231. DOI: 10.1080/00102209708935743.

[13] J. Buckmaster, P. Clavin, A. Liñán, M. Matalon, N. Peters, G. Sivashinsky and F. A. Williams. 'Combustion theory and modeling'. In: *Proceedings of the Combustion Institute*. Vol. 30. 2005, pp. 1–19. DOI: 10.1016/j.proci.2004.08.280.

[14] J. D. Buckmaster. 'The contribution of asymptotics to combustion'. In: *Physica D: Nonlinear Phenomena* 20 (1986), pp. 91–108. DOI: 10.1016/0167-2789(86)90098-9.

[15] J. D. Buckmaster and G. S. S. Ludford. *Lectures on Mathematical Combustion*. Society for Industrial and Applied Mathematics, 1983.

[16] J. D. Buckmaster and G. S. S. Ludford. *Theory of Laminar Flames*. Cambridge University Press, 1982.

[17] V. V. Bychkov and M. A. Liberman. 'Dynamics and stability of premixed flames'. In: *Physics Reports* 325 (2000), pp. 115–237. DOI: 10.1016/S0370-1573(99)00081-2.

[18] L. Cai and H. Pitsch. 'Optimized chemical mechanism for combustion of gasoline surrogate fuels'. In: *Combustion and Flame* 162 (2015), pp. 1623–1637. DOI: 10.1016/j.combustflame.2014.11.018.

[19] Z. Chen, M. P. Burke and Y. Ju. 'Effects of Lewis number and ignition energy on the determination of laminar flame speed using propagating spherical flame'. In: *Proceedings of the Combustion Institute*. Vol. 32. 2009, pp. 1253–1260. DOI: 10.1016/j.proci.2008.05.060.

[20] J. F. Clarke. 'On changes in the structure of steady plane flames as their speed increases'. In: *Combustion and Flame* 50 (1983), pp. 125–138. DOI: 10.1016/0010-2180(83)90056-1.

[21] J. F. Clarke. 'Finite amplitude waves in combustible gases'. In: *The Mathematics of Combustion*. Ed. by J. D. Buckmaster. Society for Industrial and Applied Mathematics, 1985. Chap. 5.

[22] J. F. Clarke, D. R. Kassoy and N. Riley. 'On the direct initiation of a plane detonation wave'. In: *Proceedings of The Royal Society A* 408 (1986), pp. 129–148. DOI: 10.1098/rspa.1986.0113.

[23] P. Clavin and G. Searby. *Combustion Waves and Fronts in Flows*. Cambridge University Press, 2016. DOI: 10.1017/CBO9781316162453.

[24] J. D. Cole. *Perturbation Methods in Applied Mathematics*. Blaisdell Publishing Company, 1968.

[25] R. Courant and K. O. Friedrichs. *Supersonic Flow and Shock Waves*. Interscience Publishers, Inc., 1948.

[26] T. P. Davies. 'Schlieren photography — short bibliography and review'. In: *Optics & Laser Technology* 13 (1981), pp. 37–42. DOI: 10.1016/0030-3992(81)90089-X.

[27] J. W. Dold. 'Dynamic transition of a self-igniting region'. In: *Mathematical Modeling in Combustion and Relaled Topics*. Ed. by C.-M. Brauner and C. Schmidt-Lainé. Martinus Nijlwff Publishers, 1988, pp. 461–470.

[28] J. W. Dold. 'Induction period generation of a supersonic flame'. In: *Numerical Combustion*. Ed. by A. Dervieux and B. Larrouturou. Springer, 1989, pp. 245–256.

[29] J. W. Dold. 'Premixed flames modelled with thermally sensitive intermediate branching kinetics'. In: *Combustion Theory and Modelling* 11 (2007), pp. 909–948. DOI: 10.1080/13647830701294599.

[30] J. W. Dold and A. K. Kapila. 'Comparison between shock initiations of detonation using thermally-sensitive and chain-branching chemical models'. In: *Combustion and Flame* 85 (1991), pp. 185–194. DOI: 10.1016/0010-2180(91)90186-F.

[31] J. W. Dold, A. K. Kapila and M. Short. 'Theoretical description of direct initiation of detonation for one-step chemistry'. In: *Dynamic Structure of Detonation in Gaseous and Dispersed Media*. Ed. by A. A. Borissov. Kluwer Academic Publishers, 1991, pp. 109–141.

[32] W. Döring. 'Über den Detonationsvorgang'. In: *Annalen der Physik* 435 (1943), pp. 421–436. DOI: 10.1002/andp.19434350605.

[33] T. A. Driscoll, N. Hale and L. N. Trefethen, eds. *Chebfun Guide*. [Online; Accessed 04/03/2024]. Pafnuty Publications, 2014. URL: https://www.chebfun.org/docs/guide/.

[34] G. Emanual. *Gasdynamics: Theory and Applications*. American Institute of Aeronautics and Astronautics, 1986.

[35] Engineering ToolBox. *Gases — ratios of specific heat*. https://www.engineeringtoolbox.com/specific-heat-ratio-d_608.html. [Online; Accessed 03/11/2024]. 2003.

[36] Engineering ToolBox. *Universal and individual gas constants*. https://www.engineeringtoolbox.com/individual-universal-gas-constant-d_588.html. [Online; Accessed 02/11/2021]. 2004.

[37] F. F. Fachini and L. Bauwens. 'Oscillatory flame propagation: coupling with the acoustic field'. In: *Proceedings of the Combustion Institute*. Vol. 34. 2013, pp. 2043–2048. DOI: 10.1016/j.proci.2012.05.032.

[38] T. M. Foong, K. J. Morganti, M. J. Brear, G. Da Silva, Y. Yang and F. L. Dryer. 'The octane numbers of ethanol blended with gasoline and its surrogates'. In: *Fuel* 115 (2014), pp. 727–739. DOI: 10.1016/j.fuel.2013.07.105.

[39] P. Ghosh, K. J. Hickey and S. B. Jaffe. 'Development of a detailed gasoline composition-based octane model'. In: *Industrial and Engineering Chemistry Research* 45 (2006), pp. 337–345. DOI: 10.1021/ie050811h.

[40] I. Glassman, R. A. Yetter and N. Glumac. *Combustion*. 5th ed. Elsevier Science & Technology, 2015.

[41] H. Guénoche. 'Flame propagation in tubes and closed vessels'. In: *Nonsteady Flame Propagation*. Ed. by G. H. Markstein. Pergamon Press, 1964. Chap. E, pp. 107–181.

[42] P. Hartman. *Ordinary Differential Equations*. 2nd ed. Society for Industrial and Applied Mathematics, 2002.

[43] B. Heid, C. Martens and A. Orthofer. *How hydrogen combustion engines can contribute to zero emissions*. https://www.mckinsey.com/industries/automotive-and-assembly/our-insights/how-hydrogen-combustion-engines-can-contribute-to-zero-emissions. [Online; Accessed 14/07/2022]. 2021.

[44] J. B. Heywood. *Internal Combustion Engine Fundamentals*. McGraw-Hill Book Company, 1988.

[45] J. B. Heywood. *Internal Combustion Engine Fundamentals*. 2nd ed. McGraw-Hill Education, 2018.

[46] E. J. Hinch. *Perturbation Methods*. Cambridge University Press, 1991.

[47] G. Hutchings, M. Davidson et al. *Sustainable synthetic carbon based fuels for transport: Policy breifing*. Royal Society, 2019. ISBN: 978-1-78252-422-9.

[48] T. L. Jackson, A. K. Kapila and D. S. Stewart. 'Evolution of a reaction center in an explosive material'. In: *SIAM Journal of Applied Mathematics* 49 (1989), pp. 432–458. DOI: 10.1137/0149027.

[49] L. Kagan and G. Sivashinsky. 'Hydrodynamic aspects of end-gas autoignition'. In: *Proceedings of the Combustion Institute*. Vol. 34. 2013, pp. 857–863. DOI: 10.1016/j.proci.2012.06.038.

[50] A. K. Kapila. 'Homogeneous branched-chain explosion: Initiation to completion.' In: *Journal of Engineering Mathematics* 12 (1978), pp. 221–235. DOI: 10.1007/BF00036460.

[51] A. K. Kapila. 'Reactive-diffusive system with Arrhenius kinetics: dynamics of ignition'. In: *SIAM Journal of Applied Mathematics* 39 (1980), pp. 21–36. DOI: 10.1137/0139004.

[52] A. K. Kapila and J. W. Dold. 'A theorectical picture of shock-to-detonation transition in a homogenous explosive'. In: *Proceedings: Ninth Symposium (International) on Detonation*. Vol. 1. 1989, pp. 219–227.

[53] A. K. Kapila, D. W. Schwendeman, J. J. Quirk and T. Hawa. 'Mechanisms of detonation formation due to a temperature gradient'. In: *Combustion Theory and Modelling* 6 (2002), pp. 553–594. DOI: 10.1088/1364-7830/6/4/302.

[54] D. R. Kassoy. 'Perturbation methods for mathematical models of explosion phenomena'. In: *The Quarterly Journal of Mechanics and Applied Mathematics* 28 (1975), pp. 63–74. DOI: 10.1093/qjmam/28.1.63.

[55] D. R. Kassoy. 'The response of a compressible gas to extremely rapid transient, spatially resolved energy addition: an asymptotic formulation'. In: *Journal of Engineering Mathematics* 68 (2010), pp. 249–262. DOI: 10.1007/s10665-010-9402-z.

[56] D. R. Kassoy. 'Mechanical disturbances arising from thermal power deposition in a gas'. In: *AIAA Journal* 52 (2014), pp. 2328–2335. DOI: 10.2514/6.2013-567.

[57] D. R. Kassoy. 'What Zeldovich did not tell us about spontaneous reaction wave propagation'. In: *52nd Aerospace Sciences Meeting*. 1507. AIAA, 2014. DOI: 10.2514/6.2014-1507.

[58] D. R. Kassoy, A. K. Kapila and D. S. Stewart. 'A unified formulation for diffusive and nondiffusive thermal explosion theory'. In: *Combustion Science and Technology* 63 (1989), pp. 33–43. DOI: 10.1080/00102208908947116.

[59] D. R. Kassoy and J. Poland. 'The thermal explosion confined by a constant temperature boundary: II—the extremely rapid transient'. In: *SIAM Journal of Applied Mathematics* 41 (1981), pp. 231–246. DOI: 10.1137/0139035.

[60] D. R. Kassoy and K. Wojciechowski. 'Thermomechanical response of reactive gas to rapid transient, spatially distributed energy addition: an asymptotic formulation'. In: *50th AIAA Aerospace Sciences Meeting including the New Horizons Forum and Aerospace Exposition*. 2012. DOI: 10.2514/6.2012-973.

[61] J. Kevorkian. 'Passage through resonance for a one-dimensional oscillator with slowly varying frequency'. In: *SIAM Journal of Applied Mathematics* 20 (1971), pp. 364–373. DOI: 10.1137/0120039.

[62] G. König, R. R. Maly, D. Bradley, A. K. C. Lau and C. G. W. Sheppard. 'Role of exothermic centres on knock initiation and knock damage'. In: *SAE Transactions* 99 (1990), pp. 840–861. DOI: 10.4271/902136.

[63] G. König and C. G. W. Sheppard. 'End gas autoignition and knock in a spark ignition engine'. In: *SAE Transactions* 99 (1990), pp. 820–839. DOI: 10.4271/902135.

[64] J. H. S. Lee. 'Initiation of gaseous detonation'. In: *Annual Review of Physical Chemistry* 28 (1977), pp. 75–104. DOI: 10.1146/annurev.pc.28.100177.000451.

[65] J. Li, Z. Zhao, A. Kazakov and F. L. Dryer. 'An updated comprehensive kinetic model of hydrogen combustion'. In: *International Journal of Chemical Kinetics* 36 (2004), pp. 566–575. DOI: 10.1002/kin.20026.

[66] M. A. Liberman, V. V. Bychkov, S. M. Golberg and L. E. Eriksson. 'Numerical study of curved flames under confinement'. In: *Combustion Science and Technology* 136 (1998), pp. 221–251. DOI: 10.1080/00102209808924172.

[67] M. A. Liberman, A. D. Kiverin and M. F. Ivanov. 'Regimes of chemical reaction waves initiated by nonuniform initial conditions for detailed chemical reaction models'. In: *Physical Review E* 85 (2012), p. 056312. DOI: 10.1103/PhysRevE.85.056312.

[68] A. C. McIntosh. 'Deflagration fronts and compressibility'. In: *Philosophical Transactions of the Royal Society A* 357 (1999), pp. 3523–3538. DOI: 10.1098/rsta.1999.0507.

[69] J. G. Mutzke. 'Abnormal combustion in spark ignition engines'. DPhil Thesis. University of Oxford, 2018.

[70] J. von Neumann. *Theory of detonation waves*. Office of Scientific Research and Development Report 549. 1942. 'Theory of detonation waves'. In: *John von Neumann Collected Works*. Ed. by A. H. Taub. Vol. 6. Pergamon Press, 1963, pp. 203–218.

[71] H. Ockendon and J. R. Ockendon. *Waves and Compressible Flow*. 2nd ed. Springer, 2015.

[72] J. Ockendon, S. Howison, A. Lacey and A. Movchan. *Applied Partial Differential Equations*. Revised ed. Oxford University Press, 2003.

[73] F. W. J. Olver. 'Bessel functions of integer order'. In: *Handbook of Mathematical Functions With Formulas, Graphs and Tables*. Ed. by M. Abramowitz and I. A. Stegun. 10th ed. National Bureau of Standards, United States of America, 1972. Chap. 9.

[74] S. V. Pantakar. *Numerical Heat Transfer and Fluid Flow*. Hemisphere Publishing Corporation, 1980.

[75] M. Parang and M. C. Jischke. 'Adiabatic ignition of homogeneous systems'. In: *AIAA Journal* 13 (1975), pp. 405–408. DOI: 10.2514/3.49716.

[76] C. J. Parkins, P. A. Blythe and D. G. Crighton. 'Hot spot ignition: the Newtonian limit'. In: *Proceedings of the Royal Society A* 456 (2000), pp. 2857–2882. DOI: 10.1098/rspa.2000.0644.

[77] J. Poland and D. R. Kassoy. 'The induction period of a thermal explosion in a gas between infinite parallel plates'. In: *Combustion and Flame* 50 (1983), pp. 259–274. DOI: 10.1016/0010-2180(83)90069-X.

[78] G. J. Sharpe and N. Maflahi. 'Homogeneous explosion and shock initiation for a three-step chain-branching reaction model'. In: *Journal of Fluid Mechanics* 566 (2006), pp. 163–194. DOI: 10.1017/S0022112006001844.

[79] M. Short. 'The initiation of detonation from general non-uniformly distributed initial conditions'. In: *Philosophical Transactions of the Royal Society A* 353 (1995), pp. 173–203. DOI: 10.1098/rsta.1995.0097.

[80] M. Short and J. W. Dold. 'Weak detonations, their paths and transition to strong detonation'. In: *Combustion Theory and Modelling* 6 (2002), pp. 279–296. DOI: 10.1088/1364-7830/6/2/308.

[81] M. Short, A. K. Kapila and J. J. Quirk. 'The chemical-gas dynamic mechanisms of pulsating detonation wave instability'. In: *Philosophical Transactions of the Royal Society A* 357 (1999), pp. 3621–367. DOI: 10.1098/rsta.1999.0513.

[82] M. Short and J. J. Quirk. 'On the nonlinear stability and detonability limit of a detonation wave for a model three-step chain-branching reaction'. In: *Journal of Fluid Mechanics* 339 (1997), pp. 89–119. DOI: 10.1017/S002211209700503X.

[83] A. A. Sileem, D. R. Kassoy and A. K. Hayashi. 'Thermally initiated detonation through deflagration to detonation transition'. In: *Proceedings of the Royal Society A* 435 (1991), pp. 459–482. DOI: 10.1098/rspa.1991.0156.

[84] G. I. Sivashinsky. 'Hydrodynamic theory of flame propagation in an enclosed volume'. In: *Acta Astronautica* 6 (1979), pp. 631–645. DOI: 10.1016/0094-5765(79)90023-7.

[85] G. I. Sivashinsky. 'Some developments in premixed combustion modeling'. In: *Proceedings of the Combustion Institute*. Vol. 29. 2002, pp. 1737–1761. DOI: 10.1016/S1540-7489(02)80213-9.

[86] U. Spicher, H. Kröger and J. Ganser. 'Detection of knocking combustion using simultaneously high-speed schlieren cinematography and multi optical fiber technique'. In: *SAE Transactions* 100 (1991), pp. 569–588. DOI: 10.4271/912312.

[87] S. Szwaja and J. D. Naber. 'Dual nature of hydrogen combustion knock'. In: *International Journal of Hydrogen Energy* 38 (2013), pp. 12489–12496. DOI: 10.1016/j.ijhydene.2013.07.036.

[88] P. A. Urtiew and A. K. Oppenhiem. 'Experimental observations of the transition to detonation in an explosive gas'. In: *Proceedings of the Royal Society A* 295 (1966), pp. 13–28. DOI: 10.1098/rspa.1966.0223.

[89] Z. Wang, H. Liu and R. D. Reitz. 'Knocking combustion in spark-ignition engines'. In: *Progress in Energy and Combustion Science* 61 (2017), pp. 78–112. DOI: 10.1016/j.pecs.2017.03.004.

[90] Z. Wang, Y. Qi, X. He, J. Wang, S. Shuai and C. K. Law. 'Analysis of pre-ignition to super-knock: hotspot-induced deflagration to detonation'. In: *Fuel* 144 (2015), pp. 222–227. DOI: 10.1016/j.fuel.2014.12.061.

[91] H. Wei, Y. Shang, C. Chen, D. Gao and D. Feng. 'A numerical study on pressure wave-induced end gas auto-igntion near top dead center of a downsized spark ignition engine'. In: *International Journal of Hydrogen Energy* 39 (2014), pp. 21265–21274. DOI: 10.1016/j.ijhydene.2014.10.008.

[92] C. M. White, R. R. Steeper and A. E. Lutz. 'The hydrogen-fueled internal combustion engine: a technical review'. In: *International Journal of Hydrogen Energy* 31 (2006), pp. 1292–1305. DOI: 10.1016/j.ijhydene.2005.12.001.

[93] F. A. Williams. *Combustion Theory*. 2nd ed. CRC Press, 1985.

[94] F. Yang, H. Zhang, Z. Chen and W. Kong. 'Interaction of pressure wave and propagating flame during knock'. In: *International Journal of Hydrogen Energy* 38 (2013), pp. 15510–15519. DOI: 10.1016/j.ijhydene.2013.09.078.

[95] H. Yu and Z. Chen. 'End-gas autoignition and detonation development in a closed chamber'. In: *Combustion and Flame* 162 (2015), pp. 4102–4111. DOI: 10.1016/j.combustflame.2015.08.018.

[96] Y. B. Zeldovich. 'K teorii rasprostranenia detonatsii v gasoobraznykh systemakh'. In: *Zhurnal Experimentalnoi i Teoreticheskoi Fiziki* 10 (1940). *On the theory of the propagation of detonation in gaseous systems*. National Advisory Committee for Aeronautics Technical Memorandum 1261. 1950.

[97] Y. B. Zeldovich. 'Regime classification of an exothermic reaction with nonuniform initial conditions'. In: *Combustion and Flame* 39 (1980), pp. 211–214. DOI: 10.1016/0010-2180(80)90017-6.

[98] X. Zhen, Y. Wang, S. Xu, Y. Zhu, C. Tao, T. Xu and M. Song. 'The engine knock analysis — an overview'. In: *Applied Energy* 92 (2012), pp. 628–636. DOI: 10.1016/j.apenergy.2011.11.079.